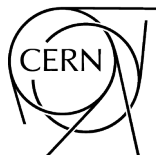


# **Radiation effects in the LHC experiments**


**Impact on detector performance and operation**

Editor: I. Dawson



CERN Yellow Reports: Monographs  
Published by CERN, CH-1211 Geneva 23, Switzerland

ISBN 978-92-9083-590-5 (paperback)  
ISBN 978-92-9083-591-2 (PDF)  
ISSN 2519-8068 (Print)  
ISSN 2519-8076 (Online)  
DOI <https://doi.org/10.23731/CYRM-2021-001>

Copyright © CERN, 2021  
 Creative Commons Attribution 4.0

This volume should be cited as:

Radiation effects in the LHC experiments: Impact on detector performance and operation,  
Ian Dawson (ed.)  
CERN Yellow Reports: Monographs, CERN-2021-001 (CERN, Geneva, 2021)  
<https://doi.org/10.23731/CYRM-2021-001>.

A contribution in this report should be cited as:

[Chapter editor name(s)], in Radiation effects in the LHC experiments: Impact on detector performance  
and operation, Ian Dawson (ed.)  
CERN-2021-001 (CERN, Geneva, 2021), pp. [first page]–[last page],  
<http://doi.org/10.23731/CYRM-2021-001>. [first page]

Corresponding editor: [Ian.Dawson@cern.ch](mailto:Ian.Dawson@cern.ch).

Accepted in March 2021, by the [CERN Reports Editorial Board](#) (contact [Carlos.Lourenco@cern.ch](mailto:Carlos.Lourenco@cern.ch)).

Published by the CERN Scientific Information Service (contact [Jens.Vigen@cern.ch](mailto:Jens.Vigen@cern.ch)).

Indexed in the [CERN Document Server](#) and in [INSPIRE](#).

Published Open Access to permit its wide dissemination, as knowledge transfer is an integral part of the mission of CERN.

# **Radiation effects in the LHC experiments: Impact on detector performance and operation**

*Editor: I. Dawson*

*Section editors: M. Bindi, M. Bomben, E. Butz, P. Collins, A. de Cosa, I. Dawson, S. Mallows, M. Moll B. Nachman, J. Sonneveld*

## **Abstract**

This report documents the knowledge and experiences gained by the LHC experiments in running detector systems in radiation environments during 2010–2018, with a focus on the inner detector systems. During this time, the LHC machine has delivered a large fraction of the design luminosity to the experiments and the deleterious effects of radiation on detector operation are being observed and measured. It is timely to review the findings from across the experiments. Questions we aim to answer include: Are the detector systems operating and performing as expected? How reliable are the radiation damage models and predictions? How accurate are the Monte Carlo simulation codes? Have there been unexpected effects? What mitigation strategies have been developed? A major goal of this report is to provide a reference for future upgrades and for future collider studies, summarizing the experiences and challenges in designing complex detector systems for operation in harsh radiation environments.

## **Keywords**

Radiation effects; LHC experiments; radiation environments; simulation; modelling; detectors; electronics.



## Contents

1	Introduction . . . . .	1
2	Overview of radiation effects on detector systems . . . . .	3
2.1	Sensors . . . . .	3
2.2	Electronics . . . . .	14
2.3	Optoelectronics . . . . .	18
3	The LHC machine and experiments . . . . .	23
3.1	Luminosity delivered to the experiments . . . . .	23
3.2	The large LHC experiments . . . . .	25
4	Simulation of radiation environments . . . . .	35
4.1	Event generation . . . . .	35
4.2	Particle transport codes . . . . .	36
4.3	Radiation damage estimators . . . . .	39
4.4	Experiment simulations and predictions . . . . .	39
4.5	Discussion and outlook . . . . .	56
5	Measurements of radiation damage on silicon sensors . . . . .	59
5.1	Measurement considerations . . . . .	60
5.2	Radiation damage modelling . . . . .	62
5.3	Results . . . . .	65
5.4	Discussion and outlook . . . . .	82
6	Impact of radiation on electronics and opto-electronics . . . . .	87
6.1	ATLAS . . . . .	87
6.2	CMS . . . . .	108
6.3	Discussion and outlook . . . . .	117
7	Simulating radiation effects and signal response in silicon sensors . . . . .	123
7.1	ATLAS . . . . .	125
7.2	CMS . . . . .	133
7.3	LHCb . . . . .	139
7.4	Discussion and outlook . . . . .	141
8	Conclusions . . . . .	147



## 1 Introduction

*I. Dawson*

Queen Mary University of London, United Kingdom

This report documents the knowledge and experiences gained by the LHC experiments in running vertex and tracker detector systems in extreme radiation environments and concludes a series of workshops held at CERN [1–3]. By the time of the workshops, the last one held on February 2019, the LHC machine had delivered a large fraction of the design luminosity to the experiments and the deleterious effects of radiation on detector performance and operation were being observed and measured. It was timely to review the situation across the LHC experiments and answer questions such as: Are the detector systems operating and performing as expected? How reliable are the radiation damage models and predictions? How accurate are the Monte Carlo simulation codes? Have there been unexpected effects? What mitigation strategies have been developed? Since the workshops, additional radiation studies have been undertaken and published, the results of which are also referenced in this report.

Our understanding and modelling of radiation effects in the LHC detector systems was originally tested in irradiation facilities. However, such facilities do not reproduce the more complex radiation reality of the LHC experiments and there is strong motivation to cross-check and validate. Previous collider experiments were designed for operation in much less severe radiation environments and extrapolating their experiences to the LHC experiments has been limited, partly due to the higher collision energies of the LHC, but mainly because of the much higher proton–proton collision rates.

The scope of the report is focused on the measurements and observations made in Run 1 (2010–2012) and Run 2 (2015–2018), and, where feasible, their comparison with predictions. We discuss predictions for Run 3 (2022–2024) and the Phase II upgrades only in the context of where lessons learned from Runs 1 and 2 have directly impacted design or strategy. The many crucial LHC Phase II upgrade design studies currently being qualified in irradiation test facilities are not considered in this report.

A major goal of this report is to provide a reference for future upgrade and collider studies, summarizing the experiences and challenges of designing complex detector systems for operation in harsh radiation environments. We begin in Section 2 with a general introduction into the physics of radiation effects on silicon sensors and electronic systems. In Section 3 a brief description of the LHC detector systems relevant for this report is given, along with the important machine parameters, such as the collision luminosity delivered to the experiments. In Section 4 we describe how the experiments simulate their complex radiation backgrounds, crucial in the design of experiments, using Monte Carlo event generators and particle transport codes. From such simulations radiation quantities of interest, such as particle fluence and ionizing dose, can be determined. Also included in this section are the results of validation studies to establish the accuracy of the simulated predictions. In Sections 5 and 6 we give a detailed description of the many radiation related measurements and observations made by the detector sensor and electronic systems, respectively, along with comparisons with simulated predictions. In Section 7 we show how the LHC radiation damage measurements are being integrated into detector simulation and digitization software to allow increasingly accurate predictions of sensor design and performance. Finally, we present the conclusions of this inter-experiment work in Section 8.

---

This chapter should be cited as: Introduction, I. Dawson, DOI: [10.23731/CYRM-2021-001.1](https://doi.org/10.23731/CYRM-2021-001.1), in: Radiation effects in the LHC experiments: Impact on detector performance and operation, Ed. Ian Dawson, CERN Yellow Reports: Monographs, CERN-2021-001, DOI: [10.23731/CYRM-2021-001](https://doi.org/10.23731/CYRM-2021-001), p. 1. © CERN, 2021. Published by CERN under the [Creative Commons Attribution 4.0 license](https://creativecommons.org/licenses/by/4.0/).

## References

- [1] Radiation effects in the LHC experiments and impact on operation and performance, CERN, 11–12 February 2019, <https://indico.cern.ch/event/769192/>.
- [2] Radiation effects in the LHC experiments and impact on operation and performance, CERN, 23–24 April 2018, <https://indico.cern.ch/event/695271/>.
- [3] 31st RD50 Workshop, CERN, 20–22 November 2017, <https://indico.cern.ch/event/663851/>.



## 2 Overview of radiation effects on detector systems

*I. Dawson<sup>a</sup>, F. Faccio<sup>b</sup>, M. Moll<sup>b</sup>, A. Weidberg<sup>c</sup>*

<sup>a</sup>Queen Mary University of London, United Kingdom

<sup>b</sup>CERN, Geneva, Switzerland

<sup>c</sup>University of Oxford, United Kingdom

In this section we give an overview of the effects of radiation on silicon detector systems in the LHC experiments. We divide the sections into: sensors; electronics; optoelectronics; services. While the physics of the energy loss between these categories is similar, the radiation quantities of interest used to evaluate damage are usually different. As an example, sensor radiation studies typically focus on the effects of bulk displacement damage, whereas degradation in electronics is generally more concerned with ionizing dose effects.

### 2.1 Sensors

The various sensor types employed in the LHC experiments suffer from radiation induced performance degradation that is mostly originating from displacement damage effects occurring in the silicon bulk of the devices. In this section, we present a general overview of displacement damage effects with relevance for all silicon sensor types. The given data were mainly obtained on very simple sensor structures, so-called pad detectors with single electrodes on the top and bottom of a silicon layer, that allow for an in-depth investigation of the bulk damage effects. For more complex sensor geometries with surface passivation layers or AC-coupled readout, additional damage effects might have to be considered. These are described in the experiment specific sections. This section starts with an introduction to the non-ionizing energy loss theorem and a description of the properties of electrically active radiation induced defects in the framework of the Shockley–Read–Hall theory. Then, the main macroscopic damage effects observed as increase of leakage current, change of effective doping concentration, and loss of charge collection efficiency are presented. Finally, a brief introduction to the radiation induced change of the sensor internal electrical field shape is given, pointing towards the full complexity of the understanding of radiation damage effects in segmented silicon sensors.

#### 2.1.1 Non-ionizing energy loss

The non-ionizing energy loss (NIEL) gives the portion of energy lost by a traversing particle which does not go into ionization and eventually leads to displacement damage. However, only a fraction of the NIEL leads to displacements as part of the energy is dissipated in phonons. This fraction depends on the energy of the impinging particle. NIEL is defined in units of  $\text{MeVcm}^2/\text{g}$  or as NIEL cross-section (displacement damage function  $D$ ) in units of  $\text{MeVmb}$ . A reference value of 1 MeV neutron equivalent ( $n_{\text{eq}}$ ) has been fixed to 95 MeVmb. Calculated values of the NIEL cross-sections for various particles are shown in Fig. 1. The NIEL hypothesis assumes that radiation damage effects scale linearly with NIEL, irrespective of the distribution of the primary displacements over energy and space. For the simulated examples shown in Fig. 2 the number of vacancies should give a measure of the damage irrespective of their distribution, whether homogeneously scattered over a relatively wide volume (as for the case of low energetic proton or gamma-ray damage) or clustered in high density in small regions (as in the case of neutron damage). Consequently, the damage produced by different particles or particles with

---

This chapter should be cited as: Overview of radiation effects on detector systems, Eds. I. Dawson, M. Moll, F. Faccio, A. Weidberg, DOI: [10.23731/CYRM-2021-001.3](https://doi.org/10.23731/CYRM-2021-001.3), in: Radiation effects in the LHC experiments: Impact on detector performance and operation, Ed. Ian Dawson,

CERN Yellow Reports: Monographs, CERN-2021-001, DOI: [10.23731/CYRM-2021-001](https://doi.org/10.23731/CYRM-2021-001), p. 3.

© CERN, 2021. Published by CERN under the [Creative Commons Attribution 4.0 license](https://creativecommons.org/licenses/by/4.0/).

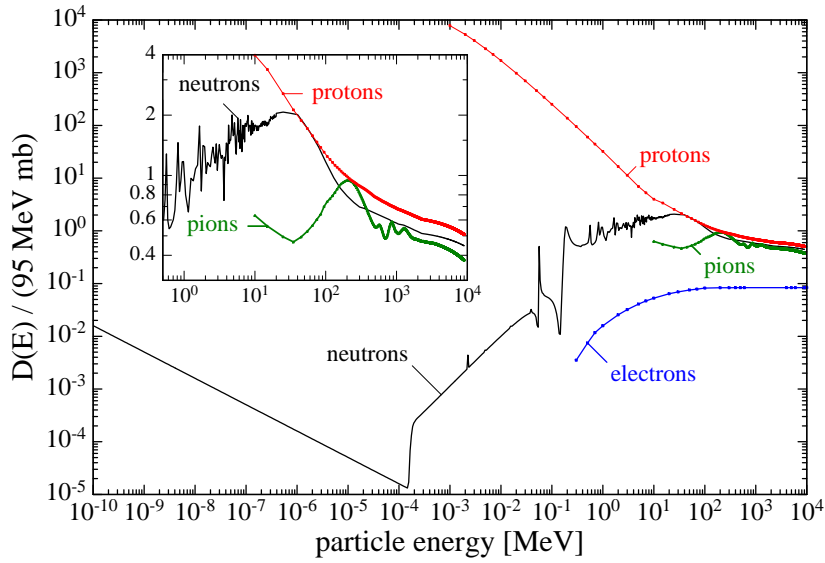


**Fig. 1:** Non-ionizing energy loss (NIEL) cross-sections normalized to 95 MeV mb. Data collected by A. Vasilescu and G. Lindström [1] based on [2–5] and private communications.

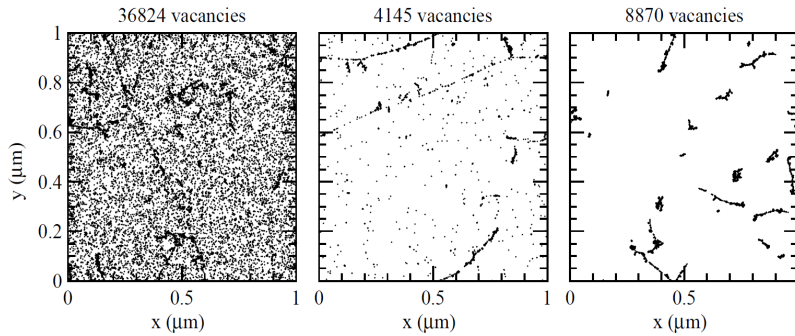


**Fig. 2:** Initial distribution of vacancies produced by 10 MeV protons (left), 23 GeV protons (middle), and 1 MeV neutrons (right). The plots are projected over 1  $\mu\text{m}$  depth ( $z$ ) and correspond to a fluence of  $10^{14}$  particles/ $\text{cm}^2$ . Figure taken from Ref. [6].

different energies should be scalable via their NIEL (i.e., the number of displacements) and the data given in Fig. 1 should allow us to normalize the damage from different particles or particles with different energies. As will be shown below, NIEL scaling is a powerful method for coping with displacement damage predictions in complex radiation fields. It allows us to predict many device damage parameters in fast hadron dominated radiation fields (such as, e.g., the leakage current) but also has shortcomings arising, for example, from the fact that point-like and clustered defects contribute differently to some device damage parameters such as, e.g., the effective space charge (see Section 2.1.2). The displacement damage functions shown in Fig. 1 are presently used to calculate the 1 MeV neutron equivalent fluence radiation fields in the experiments of the LHC and HL-LHC. It has, however, been shown that, for protons and electrons, an *effective NIEL* [7, 8] or the *equivalent displacement damage dose* concept [8–10] can deliver better linearity between some damage parameters and the calculated NIEL (see e.g., Ref. [11]). A revision of the used damage functions for the 1 MeV neutron equivalent fluence calculation is thus of interest.

### 2.1.2 Radiation induced defects

Radiation induced electrically active defects with energy levels in the silicon bandgap impact on the device performance in various ways. Generally, the impact on the detector performance can be described in the framework of the Shockley–Read–Hall (SRH) statistics and, in principle, the impact of each defect can be calculated if the capture cross-sections for holes  $\sigma_p$  and electrons  $\sigma_n$ , the position in the bandgap, the type of defect (acceptor or donor), and the concentration of the defect  $N_t$  are known (see, e.g., Ref. [12]). On the device performance level, three main effects can be identified and are discussed in the following with their formulation in the SRH framework.

**Leakage current:** The leakage current is most effectively produced by defect levels close to the middle of the bandgap. It follows the NIEL hypothesis scaling for high energy hadron induced damage, meaning as well that defect engineering (i.e., the impurity content of the silicon) has in this case no impact on the leakage current (see e.g., Ref. [14]). Increase of leakage current leads to an increase of noise in the amplifiers and to an increase of power consumption. As the leakage current depends exponentially on the temperature, cooling is a very effective means to mitigate the detrimental effects. To calculate the leakage current, we need to determine the defect occupancy with electrons  $f_t$  given by

$$f_t = \frac{c_n n + e_p}{c_n n + e_n + c_p p + e_p}, \quad (1)$$

where  $c_n$  and  $c_p$  are the capture coefficients for electrons and holes,  $n$  and  $p$  are the electron and hole densities, and  $e_n$  and  $e_p$  the emission rates for electrons and holes. The value of  $c_n$  is given by  $c_n = \sigma_n v_{th,n}$ , with  $v_{th,n}$  being the thermal velocity for electrons and  $e_n$  being given by  $e_n = c_n n_i \exp((E_t - E_i)/k_B T)$ , with  $n_i$  being the intrinsic carrier density,  $E_i$  the intrinsic Fermi level, and  $k_B$  the Boltzmann constant. In the space charge region (SCR) of a detector the carrier densities are very low and can often be neglected, simplifying Eq. 1 to

$$f_t = e_p / (e_n + e_p). \quad (2)$$

Defect levels produce leakage current by the subsequent emission of electrons and holes (i.e., the transfer of electrons from the valence to the conduction band). The generation rate  $G_t$  of a single defect type  $t$  in the case of neglectable free carrier concentrations is given by

$$G_t = N_t f_t e_n = N_t (1 - f_t) e_p = N_t \frac{e_n e_p}{e_n + e_p}. \quad (3)$$

Summing over all defect types and taking into account the active volume of a sensor (depletion width  $w$  and area  $A$ ) results in the total leakage of the device

$$I = q_0 w A \sum_{\text{defects}} G_t, \quad (4)$$

with  $q_0$  being the elementary charge.

**Effective space charge:** In undamaged sensors, the bulk doping (e.g., phosphorus or boron) constitutes the effective space charge. Radiation induced changes to the effective space charge lead to a change of the electric field distribution within the device and shift the depletion voltage to lower or higher values. In the latter case, higher operation voltages might have to be applied to establish an electric field throughout the full sensor volume in order to avoid under-depletion and loss of active volume and therefore signal. If sufficiently high voltage cannot be applied or breakdown of the sensor is at risk, sensors will have to be operated under-depleted with the corresponding loss in signal heights. Inhomogeneous distribution of the space charge might lead to double junction effects or the shift of the highest electric field towards regions that are unprofitable for segmented sensors. High local fields can lead furthermore to impact ionization effects or breakdown. It has been shown that the change of the space charge in silicon is strongly material dependent (e.g., oxygen content) and depends on the particle type used for the irradiation experiment (e.g., neutron vs. proton damage). This implies that this damage effect does not directly scale with NIEL

and can be altered or mitigated by defect engineering approaches (e.g., change of impurity content). Defects can contribute positive (donors) or negative (acceptors) charge to the space charge and thus alter the electric field distribution and the depletion voltage of a device. The effective space charge  $N_{\text{eff}}$  (neglecting free carriers) is then given by the sum of all positively charged donors  $N_D$  and all negatively charged acceptors  $N_A$

$$N_{\text{eff}} = \sum_{\text{donors}} (1 - f_t)N_t - \sum_{\text{acceptors}} f_t N_t, \quad (5)$$

where the index  $t$  is running over all donor and acceptor like defect type  $t$  with concentration  $N_t$ .

**Trapping:** Charge carriers generated by ionizing particles or photons in the SCR travel towards the electrodes and constitute the sensor signal. Defect levels can capture (trap) charge carriers and, if the release (detrapping) time of the charge carriers is long compared to the collection time of the system or if the concentration of defects (trapping centres) is very high, the overall signal of the sensor is reduced. Trapping becomes the limiting factor for high fluence applications. Mitigation of this problem is possible through device modifications leading to faster collection times (i.e., device engineering). In segmented sensors, the collection of electrons instead of holes at the sensing electrodes can be an advantage due to the higher mobility of electrons and the possibility of exploiting charge multiplication by impact ionization at lower fields and without device breakdown. The trapping is characterized by a trapping time (inverse capture rate)  $\tau_e$  for electrons and  $\tau_h$  for holes that are calculated as

$$1/\tau_e = c_n(1 - f_t)N_t \text{ and } 1/\tau_h = c_p f_t N_t. \quad (6)$$

Summing over all defects contributing to the trapping results in the effective trapping times  $\tau_{\text{eff}}$  for electrons and holes

$$\frac{1}{\tau_{\text{eff},e}} = \sum_{\text{defects}} c_{(n,t)}(1 - f_t)N_t \quad (7)$$

$$\frac{1}{\tau_{\text{eff},h}} = \sum_{\text{defects}} c_{(p,t)} f_t N_t. \quad (8)$$

Equations 1 to 8 allow us to estimate the impact of defects (with known parameters of donor/acceptor,  $\sigma_n$ ,  $\sigma_p$ ,  $E_t$  and  $N_t$ ) on the space charge, current generation, and trapping. For precise calculations, the defect parameters have to be properly embedded in the Poisson and transport equations, as done for example in technology computer aided design (TCAD) device simulations (see Chapter 7). This allows us to determine the device geometry, spatial distribution of defect concentrations, free carrier densities, field strength, and other semiconductor effects such as, for example, impact ionization.

### 2.1.3 Impact of radiation on sensor performance

Silicon particle detectors are basically reverse biased silicon diode structures. Correspondingly, the most simple test structure to investigate radiation damage effects on silicon detectors is the a so-called *pad detector*. It consists of a large front electrode (with respect to the thickness of the silicon bulk) surrounded by one or a series of guard rings (to protect the collecting electrodes from unwanted currents originating from the edges and to precisely define the active volume) and a homogeneous electrode covering all back side. For n-type bulk structures, the front contact and guard rings are  $p^+$  implants and the backside implant is an  $n^+$  implant. Typical dimensions are 5 mm  $\times$  5 mm for the front electrode and 300  $\mu\text{m}$  for the thickness of the silicon bulk. Most of the results presented in the following sections are based on measurements on pad detectors. Segmented sensors add more complexity to the impact of bulk (and surface) radiation damage and will be treated at the end of the section and in the following chapters.

The principle radiation effects originating from displacement damage in the silicon bulk of the detectors are an increase in the leakage current (dark current), a change of the effective doping concentration (change of depletion voltage), and a decrease of the charge collection efficiency (i.e., a reduction

of the signal due to trapping effects). These effects are strongly interlinked and partly depend on the material parameters such as impurities in the silicon and/or do not follow the NIEL scaling concept. Therefore, the parameterization and damage parameters presented in the following section have to be carefully benchmarked against the experimental situation for which the modelling is applied. Especially after exposure to very high particle fluences, when the electric field inside the sensor is no longer a linear function of the distance from the collecting electrode, parameters like the depletion voltage can no longer serve to straightforwardly calculate the electric field and the charge collection efficiency.

### 2.1.3.1 Leakage current

#### Leakage current: Fluence dependence

After exposure to highly energetic particles having sufficient energy to produce so-called defect clusters (see e.g., Ref. [13]), the radiation induced increase of the leakage current is proportional to the particle fluence and independent of the type, resistivity, and impurity content of the used silicon material [14, 15]. This is shown in Fig. 3 (left) for various silicon detectors [16]. The proportionality factor is called *current related damage factor*  $\alpha$  and is defined by

$$\alpha = \frac{\Delta I}{V\phi_{\text{eq}}}, \quad (9)$$

where  $\Delta I$  is the leakage current increase caused by irradiation,  $V$  the volume contributing to the current, and  $\phi_{\text{eq}}$  the 1 MeV neutron equivalent particle fluence. The data shown in Fig. 3 (left) result in a value of  $\alpha(80 \text{ min}, 60^\circ\text{C}) = (3.99 \pm 0.03) \times 10^{-17} \text{ A/cm}$  for the measurements taken at  $20^\circ\text{C}$ . It shall be

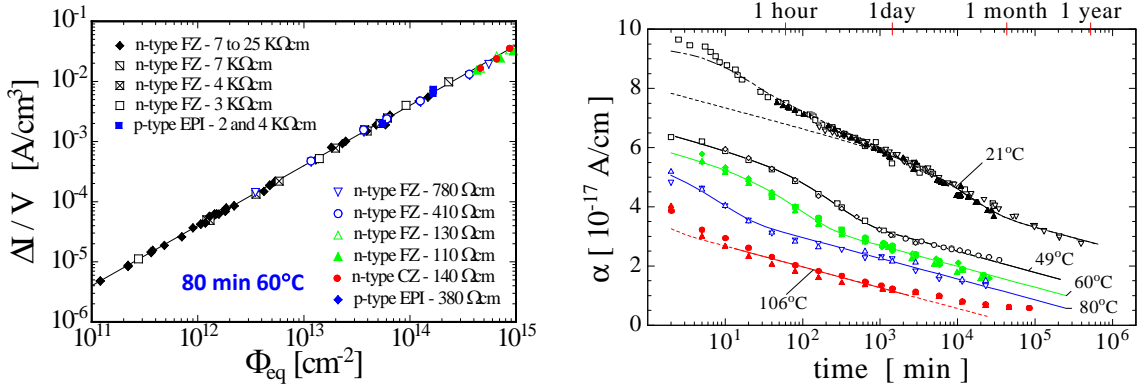


**Fig. 3:** Left: Radiation induced leakage current increase as a function of particle fluence for various silicon detectors made from silicon materials produced by various process technologies with different resistivities and conduction types. The current was measured at room temperature ( $20^\circ\text{C}$ ) after irradiation in a neutron field with 5.2 MeV mean energy and a dedicated annealing of 80 min at  $60^\circ\text{C}$ . Figure taken from Ref. [16]. Right: Current related damage rate  $\alpha$  as a function of cumulated annealing time at different temperatures. Solid lines represent fits to the data (see text). Figure taken from Ref. [17].

mentioned that for irradiations producing predominantly point defects (e.g.,  $^{60}\text{Co}$ -gamma) a non-linear dependence on the particle fluence and a strong dependence on the impurity content are observed [18]. This case is not further treated here as in the LHC context the defect cluster induced leakage is the dominant one; more details regarding point-defect induced leakage can be found in Ref. [19].

#### Leakage current: Temperature dependence

The temperature dependence of the leakage current is dominated by the position of the energy levels in the band gap, their cross-sections, their concentrations, and the temperature dependence of the bandgap

itself. The most efficient generation centres are the ones at the intrinsic energy level. In this case, the leakage current temperature dependence will follow that of the intrinsic carrier concentration  $n_i$ . In a recent work, experimental results obtained on several different irradiated silicon particle detectors using the parameterization

$$I(T) \propto T^2 \exp(-E_{\text{eff}}/2k_B T) \quad (10)$$

were compared and resulted in a value of  $E_{\text{eff}} = 1.214 \pm 0.014$  eV [20]. This value is presently the reference in the HEP community for temperature correction (scaling) of the leakage current. In practice, this value translates into a reduction of the leakage current by 8–10% per degree centigrade in the temperature range from RT to  $-20^\circ\text{C}$ .

#### *Leakage current: Annealing effects and parameterization*

The annealing behaviour of the current related damage factor  $\alpha$  after irradiation is displayed in Fig. 3 (right) for various annealing temperatures ranging from 21–106 °C [17]. The annealing temperature is the temperature at which the samples are stored or heated to accelerate the defect reactions in the silicon bulk. This temperature shall not be confused with the measurement temperature of the leakage current, which, in the given example, is 20 °C. The  $\alpha$  value is continuously decreasing with increasing annealing time. In Refs. [16, 17] a parametrization of the data with an exponential and logarithmic term is proposed

$$\alpha = \alpha_1 \cdot \exp(-t/\tau_1) + \alpha_0 - \alpha_2 \cdot \ln(t/t_0), \quad (11)$$

and has been used in the figure to fit the data (solid lines). The complete parameter set ( $\alpha_0$ ,  $\alpha_1$ ,  $\alpha_2$ ,  $\tau_1$ , and  $t_0$ ) and a discussion on the physical meaning of the parameters can be found in Refs. [16, 17].

#### *2.1.3.2 Depletion voltage – space charge – effective doping concentration*

The radiation induced defects lead to a change in the effective space charge  $N_{\text{eff}}$  that is reflected in a change of the depletion voltage  $V_{\text{dep}}$  of silicon detectors. The depletion voltage  $V_{\text{dep}}$  is given by

$$V_{\text{dep}} = \frac{q \cdot |N_{\text{eff}}| \cdot d^2}{2 \cdot \epsilon \epsilon_0}, \quad (12)$$

where  $d$  is the thickness of the device,  $q$  the elementary charge,  $\epsilon$  the relative permittivity of silicon, and  $\epsilon_0$  the vacuum permittivity. It shall be noted that Eq. 12 assumes a constant space charge over the volume of the damaged detector, which is not always the case [21]. Furthermore, the depletion voltage is usually determined from capacitance vs. voltage (CV) measurements at  $\approx 10$  kHz and a temperature between  $+20^\circ\text{C}$  and  $-20^\circ\text{C}$  depending on measurement limits set by the high leakage currents, while a dependence of the depletion voltage on the measurement frequency and temperature has been reported for damaged detectors [22]. It is thus understood that the following parameterizations give precise values for the prediction of the depletion voltage (i.e., the kink in the CV measurement of a diode), while the translation into  $N_{\text{eff}}$  via Eq. 12 might be afflicted with systematic errors. It shall be mentioned that, in highly irradiated detectors, contrary to undamaged detectors, the space charge is no longer identical to the free carrier concentration in thermal equilibrium. Results of characterization methods determining the free carrier density or the low voltage resistivity are therefore not easily correlated with the space charge determined from full depletion voltage.

#### *Depletion voltage: Fluence dependence*

Figure 4 (left) shows an example of the evolution of the effective space charge (i.e., depletion voltage) for an n-type sensor with particle fluence [23]. Before irradiation the sensor was of high resistivity n-type (phosphorus doped) base material resulting in a positive space charge of some  $10^{11} \text{ cm}^{-3}$ . Irradiation of the sensor results in the formation of negative space charge, which compensates the initial positive

space charge. With increasing particle fluence, the net space charge decreases and reaches very low values corresponding to almost intrinsic silicon. This point is called *type inversion* or *space charge sign inversion (SCSI)*, as the space charge sign changes from positive to negative. Increasing the particle fluence beyond the SCSI point leads to more and more negative space charge values. The depletion voltage rises accordingly and eventually reaches values that cannot be applied to the detector any more without causing breakdown. The applied voltage will have to be kept below the depletion voltage and the detector is operated “underdepleted”.

For high resistivity p-type sensors no “type inversion” is usually observed as the initial space charge is already negative before irradiation. It should, however, be mentioned that, after neutron and charged hadron irradiations, cases have been observed in non-standard silicon materials where type inversion occurs from negative to positive space charge [16] or the effective space charge remains positive in n-type sensors up to very high particle fluences [24, 25].

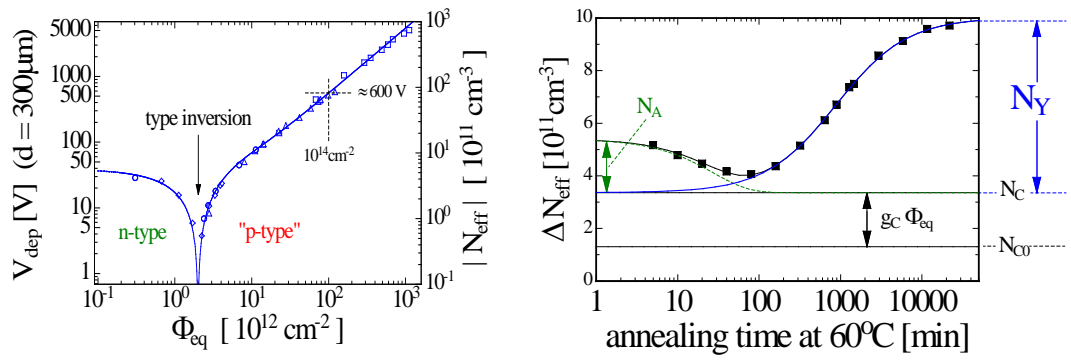


**Fig. 4:** Left: Effective doping concentration (depletion voltage) as a function of particle fluence for a standard float zone (FZ) n-type silicon detector. Data were measured directly after exposure and are taken from Ref. [23]. Right: Evolution of the effective doping concentration as function of annealing time. The data shown here were taken at room temperature while the annealing took place at 60 °C. Taken from Ref. [16].

#### Depletion voltage: Annealing and parameterization

The effective doping concentration after irradiation is changing with time. This so-called annealing can be accelerated at elevated temperatures and decelerated or frozen when going to lower temperatures. Figure 4 (right) gives an example for a typical annealing behaviour after high fluence irradiation. The change of the effective doping concentration with irradiation  $\Delta N_{\text{eff}}$  is given by

$$\Delta N_{\text{eff}} = N_{\text{eff},0} - N_{\text{eff}}(t), \quad (13)$$

where  $N_{\text{eff},0}$  is the value before irradiation and  $N_{\text{eff}}(t)$  the value after irradiation. The fact that  $\Delta N_{\text{eff}}$  is positive for the data shown in Fig. 4 (right) demonstrates that the radiation induced change of  $N_{\text{eff}}$  has a negative sign, i.e., the overall produced space charge due to radiation is a negative one, in accordance with the data shown in Fig. 4 (left). The time dependence of  $N_{\text{eff}}$  can be parameterized as

$$\Delta N_{\text{eff}}(t) = N_A(t) + N_C + N_Y(t), \quad (14)$$

where  $N_C$  is the so-called *stable damage* component, which is not changing with time after irradiation,  $N_A$  is the *short term* or *beneficial annealing* component, and  $N_Y$  the *reverse annealing* component. They are parameterized as

$$N_A(t) = g_a \phi_{\text{eq}} \exp(-t/\tau_a) \quad (15)$$

$$N_C = N_{C,0} (1 - \exp(-c\phi_{\text{eq}})) + g_c\phi_{\text{eq}} \quad (16)$$

$$N_Y(t) = g_y\phi_{\text{eq}}(1 - \exp(-t/\tau_y)). \quad (17)$$

Here,  $N_{C,0}$  represents the fact that often an incomplete doping removal is observed (i.e.,  $N_{C,0}$  represents only a fraction of the initial doping concentration, see e.g., Ref. [26]),  $c$  is the removal coefficient, and  $g_a$ ,  $g_c$ , and  $g_y$  are the introduction rates for the space charge defined as the beneficial annealing, the stable damage, and the reverse annealing above (e.g.,  $N_Y = g_y\phi_{\text{eq}}$ ). The temperature dependence of the time constants for the beneficial ( $\tau_a$ ) and the reverse annealing ( $\tau_y$ ) has been found to follow an Arrhenius equation with activation energies of 1.09 eV and 1.33 eV, respectively [16]. Note as well that there are different parameterizations for the reverse annealing represented here by Eq. 17 (see e.g., Refs. [16, 24, 26]).

#### *Depletion voltage: Material and particle dependence*

Material and defect engineering techniques have been extensively studied by the RD48 [28] and RD50 [29] research collaborations in order to explore the potential for radiation hardening of silicon sensors. A wide range of sensors produced on different silicon base materials (e.g., different growth methods or different impurity content), exposed to different types of particles (e.g., electrons, pions, protons, and neutrons), and tested under various operational conditions (e.g., different temperatures and/or applied voltages during and after irradiation) have been studied. Particularly the enrichment of silicon with oxygen was studied in detail and found to be a key element for the radiation hardness of silicon sensors [27]. These studies demonstrated that the impurity content of the used silicon and the type of particle used for the irradiation experiment have a strong impact on the observed radiation damage and specifically on the space charge and the electric field distribution within the sensor. These findings demonstrate a weakness of the NIEL hypothesis, as the damage is no longer scaling for all silicon materials in the same way with the 1 MeV neutron equivalent fluence. An example is given in Fig. 5 (from Ref. [27]) showing data obtained on various n-type silicon detectors in a so-called *CERN scenario measurement* technique [30] where individual samples are successively exposed to radiation with annealing steps and measurements in between each irradiation step. The minimum in the curves for  $|N_{\text{eff}}|$  displays the fluence for which the material undergoes space charge sign inversion from positive to negative space charge from whereon the increase at higher fluence values is almost linear. The slope of this branch can be seen as a measure of the radiation hardness. Although oxygenated material does not exhibit any benefit for neutron irradiation (see Fig. 5 (left)), it clearly leads to superior results with respect to standard FZ silicon in the case of proton or pion induced damage. Following the developments of the RD48 collaboration and the positive results on oxygen enriched silicon, the ATLAS and CMS pixel detectors at the LHC have been made from oxygen enriched silicon [31].

#### *Depletion voltage: Donor removal*

By the term donor removal we understand the transformation of electrically active shallow donors (usually phosphorus) into defect complexes that no longer have the properties of those shallow dopants. The positive space charge contributed by the shallow dopants is therefore lost and the overall space charge is altered. In the context of the depletion voltage, the donor removal is parameterized in the parameter  $N_C$  in Eq. 16), where an exponential function with a removal parameter  $c$  describes the fluence dependence. The removal of phosphorus and boron by irradiation with fast neutrons has been measured by Wunstorf *et al.* [32] using different high resistivity silicon wafers that were partly doped by the neutron transmutation doping (NTD) technique. From the measurement of the resistivity change as a function of the neutron fluence, removal coefficients were determined to be  $c_D = 2.4 \times 10^{-13} \text{ cm}^2$  for phosphorus in very high resistivity n-type material ( $> 1 \text{ k}\Omega\text{cm}$ ). A systematic investigation of the dependence of the donor removal coefficient determined from space charge measurements on the phosphorus content (material resistivity) [26] revealed that the product of removal coefficient and phosphorus concentration



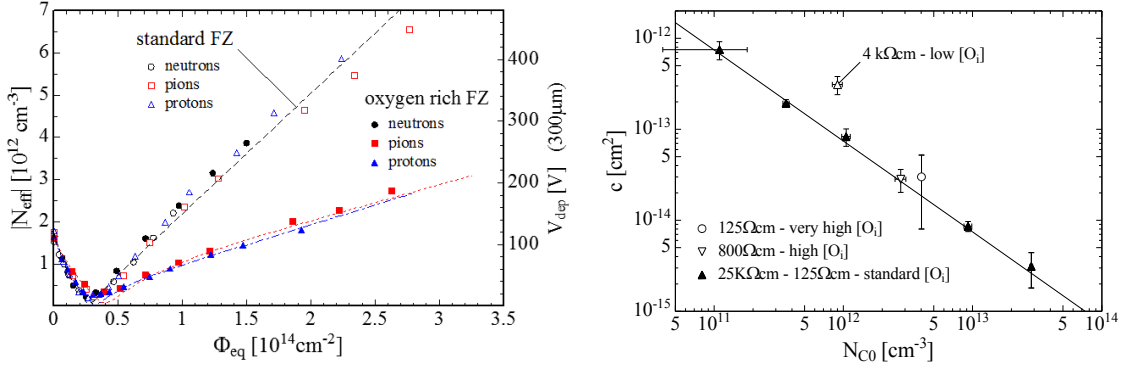


**Fig. 5:** Left: Dependence of  $N_{\text{eff}}$  on the accumulated 1 MeV neutron equivalent fluence for standard and oxygen enriched FZ silicon irradiated with reactor neutrons (Ljubljana), 24 GeV protons (CERN PS), and 192 MeV pions (PSI). Data of the RD48 collaboration taken from Ref. [27]. Right: Donor removal coefficient  $c$  plotted versus the donor concentration  $N_{c0}$  [26].

gives a constant value for materials varying over several orders of magnitude in resistivity. This is shown in Fig. 5 (right) and allows us to simulate this effect after neutron irradiations. For charged particle irradiations less data are available, but based on the nature of the removal mechanism and recent experiments on the acceptor removal in p-type silicon [33], a higher removal coefficient with respect to the one after neutron irradiation is expected.

### 2.1.3.3 Charge carrier trapping

The charge carriers generated by ionizing particles or photons in the depleted bulk of the silicon sensor travel towards the electrodes and constitute the sensor signal. If a charge carrier is trapped into a defect level and not released within the signal collection time of the sensor, the charge is lost and the corresponding sensor signal reduced.

#### Charge carrier trapping: Fluence dependence

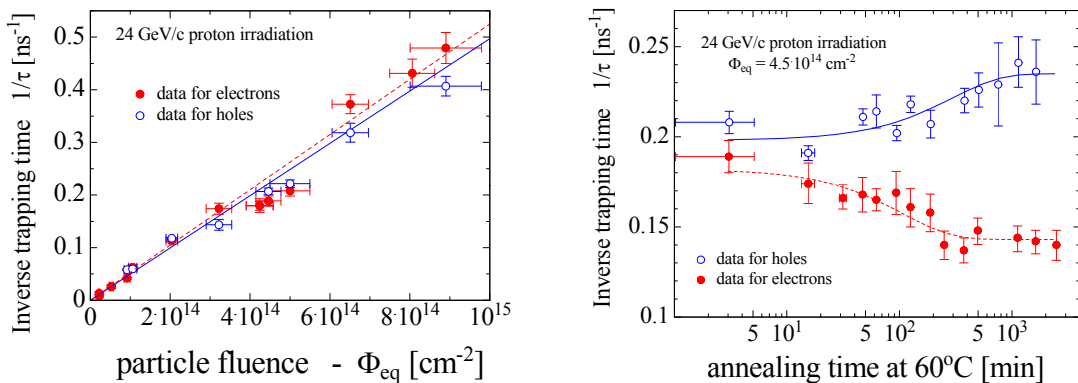


**Fig. 6:** Left: Inverse trapping time as a function of particle fluence as measured at  $0^\circ \text{C}$  after an annealing of 30 to 60 min at  $60^\circ \text{C}$ . Right: Evolution of the inverse trapping time as a function of annealing time at  $60^\circ \text{C}$ . Data for both plots taken from Ref. [34].

With increasing particle fluence (increasing number of trapping centres) more and more charge carriers get trapped during signal formation, leading to a decrease of the charge collection efficiency

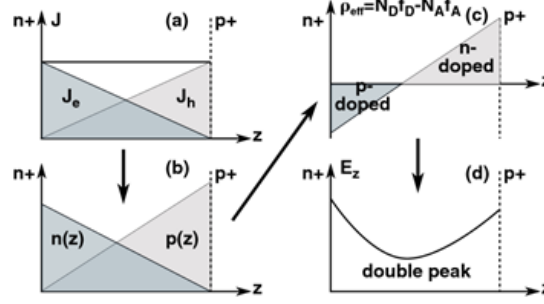


**Fig. 7:** The diagrams illustrate the polarization effect leading to a double peak electric field distribution in a sensor with a high defect concentration. (a) Current density distribution due to the generation of leakage current. (b) Carrier density distribution with higher hole concentration due to lower hole mobility. (c) Distribution of space charge due to predominant trapping of electrons close to the  $n^+$  contact and holes close to the  $p^+$  contact. (d) Distribution of electric field strength arising out of space charge distribution given in (c) (see Ref. [21] for more details).

(CCE) i.e., signal height of the sensor. The effective trapping time  $\tau_{\text{eff}}$  can be used to describe this effect, assuming that the loss of charge depends uniquely on the transport time of the charge carriers inside the sensor:  $Q(t) = Q_0 \exp(-t/\tau_{\text{eff}})$ . The effective trapping time can be separately measured for electrons and holes [34, 35]. As shown in Fig. 6, a linear dependence of the inverse effective trapping time on the particle fluence is observed and can be described as

$$1/\tau_{\text{eff}} = 1/\tau_{(\text{eff},0)} + \beta\phi_{\text{eq}}, \quad (18)$$

where  $\beta$  is the proportionality factor (effective trapping damage constant) and  $\tau_{\text{eff},0}$  the effective carrier lifetime before irradiation, which in standard silicon already after very moderate radiation levels can be neglected. Similar values for various silicon materials (float zone (FZ) [35], diffusion oxygenated FZ (DOFZ) [35], magnetic Czochralski (MCZ) [37], and epitaxial (EPI) [38]) and different heavy particle irradiations [35, 36] have been observed, resulting in  $\beta$  values of 4 to  $6 \times 10^{-16} \text{ cm}^2/\text{ns}$  for electrons and 5 to  $8 \times 10^{-16} \text{ cm}^2/\text{ns}$  for holes. In a more recent work focusing on high fluence irradiations, deviations from the linear behaviour shown in Fig. 6 (left) for particle fluences above about  $3 \times 10^{14} \text{ n}_{\text{eq}}\text{cm}^{-2}$  were reported [39]. The inverse trapping time (trapping rate) increased slower than expected from the linear extrapolation from low fluence data and gave e.g., a two to three times lower value at  $3 \times 10^{15} \text{ n}_{\text{eq}}\text{cm}^{-2}$ .

#### Charge carrier trapping: Annealing

As for the leakage current and the depletion voltage (effective doping concentration), the effective trapping damage constant depends on the annealing status of the sensor after irradiation. This is depicted in Fig. 6 (right) for a proton irradiated sensor. While for electrons a reduction in  $\beta_e$  (decrease in  $1/\tau_{\text{eff},e}$ , less trapping) with annealing time is observed, for holes (damage parameter  $\beta_h$ ) an increase of trapping with time has been measured. The trapping damage constant  $\beta$  has been parameterized for electrons and holes as

$$\beta(t) = \beta_0 \exp(-t/\tau_a) + \beta_\infty(1 - \exp(-t/\tau_a)), \quad (19)$$

where  $\beta_0$  and  $\beta_\infty$  denote the trapping rates  $\beta$  at the beginning and end of the annealing process that is governed by the time constant  $\tau_a$  [40].

#### 2.1.4 The electric field and double junction effects

In the previous sections, and most importantly, in the transformation of the measured depletion voltage into effective space charge by Eq. 12, it is assumed that the space charge is homogeneously distributed

over the sensor bulk and constant. The electric field is thus assumed to be a linear function of the depth in the sensor. However, in reality this is often not the case and all results on the effective space charge as deduced from e.g., CV curves in form of depletion voltage characterization have to be treated with care. Only for non-irradiated sensors or low irradiation fluences can the space charge be assumed to be constant throughout the depleted sensor volume. For higher fluences, above about  $10^{14}$   $n_{\text{eq}}/\text{cm}^2$ , more complex field structures are observed. “Type inversion” or “space charge sign inversion (SCSI)” in an n-type sensor (see Section 2.1.3.2) was naively assumed to shift the space charge from positive to negative sign throughout the full sensor volume and consequently should lead to an electric field that starts to grow from the back electrode when rising the reverse bias over the sensor. While a strong electric field growing from the backside of the device is indeed observed, also a field growing from the front side is observed at the same time. The formation of such a double peak field structure can be explained by a polarization effect [21] and is illustrated in Fig. 7. The free carriers (electrons and holes) generated by radiation induced defects constitute the radiation induced leakage current. As electrons are drifting towards the  $n^+$  electrode and holes towards the  $p^+$  electrode, the electron density is highest at the  $n^+$  contact while the hole density is highest at the  $p^+$  contact (see Fig. 7b). The free carriers (electrons and holes) are partly trapped at radiation induced defect levels (acceptors and donors) and thus build up additional space charge. This space charge is predominantly negative at the  $n^+$  contact and positive at the  $p^+$  contact (see Fig. 7c). Finally, if the total effective space charge is negative at the  $n^+$  contact and positive at the  $p^+$  contact, a double peak electric field distribution is observed (see Fig. 7d).

The transient current technique (TCT) allows us to characterize and visualize the electric field distribution [41–43]. An example for a non-irradiated and highly irradiated sensor, as measured with edge TCT, is given in Fig. 8 [44]. The depth profiles of the sum of the drift velocities of electrons ( $\nu_e$ ) and holes ( $\nu_h$ ) as created in the indicated depth of the sensor is shown. This parameter relates to the electric field strength  $E$  via  $\vec{\nu}_e + \vec{\nu}_h = \mu_e(E)\vec{E} + \mu_h(E)\vec{E}$  where  $\mu_{e,h}$  are the carrier mobilities. In cases where the drift velocity has not saturated as a function of electric field strength, the sum of the drift velocities gives an image of the electric field strength within the sensor. It is clearly visible that the electric field in the non-irradiated sensor is growing from the front side while in the irradiated sensor fields are growing from both sides with rising reverse bias voltage. While many measurements on the electric field distribution

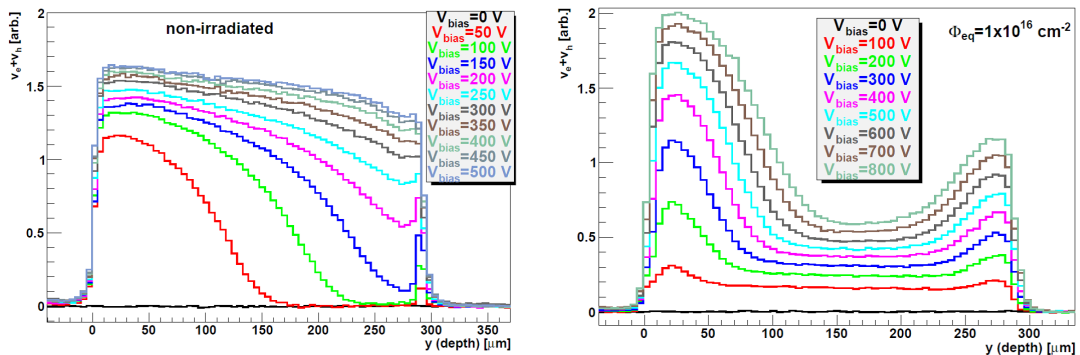


**Fig. 8:** Drift velocity profiles with varying bias voltages for a non-irradiated (left) and a neutron irradiated ( $10^{16}$   $\text{cm}^{-2}$ ) (right) p-type micro-strip detector made from float zone silicon (5  $\text{k}\Omega\text{cm}$ , 300  $\mu\text{m}$ ,  $V_{\text{dep}}=180$  V). Figures taken from Ref. [44].

of irradiated sensors exist, a parameterization of the electric field distribution as a function of silicon material, particle fluence and type, sensor thickness, temperature, and annealing time does not exist to the same comprehensive level as e.g., for the effective space charge distribution presented in Section 2.1.3.2. A proposal on how to parameterize the electric field distribution has been made [44], but needs to be completed with a bigger set of measured data. Another approach to predict the electric field distribution as a function of the above mentioned parameters is to use TCAD simulations. Here, the defect levels

are parameterized and the electric field is calculated, offering the advantage that the parameterization becomes sensor geometry independent (see Chapter 7).

### 2.2 Electronics

It is of paramount importance to understand how radiation impacts the operation of microelectronic systems in the LHC experiment radiation environments so that electronics satisfying the reliability requirements can be designed, tested and qualified. Furthermore, the selection and qualification of commercial-off-the-shelf (COTS) electronics requires a good understanding of how they will perform in radiation environments for which they were not necessarily designed. The radiation quantities, listed below, are obtained from the Monte Carlo simulations described in Section 4. A difficulty arises, however, in that the radiation response of CMOS and bipolar electronics can depend strongly on the particle type and energy, dose rate, temperature, and bias. Reproducing all these conditions in test facilities is not feasible so the challenge is to relate the results to the real life application. The performance of microelectronic devices is impacted by radiation in several ways.

1. Total ionizing dose (TID) effects. This kind of damage accumulates over time causing device degradation and even failure. TID damage is associated with the build up of trapped charge states, either in an oxide layer or at the oxide–bulk ( $\text{SiO}_2\text{-Si}$ ) interface, which leads to the modification of the electric fields in the device, thus impacting the electrical characteristics. In metal-oxide-semiconductor (MOS) transistors, the main parameters influenced by TID are the threshold voltage, charge mobility and leakage current. An example of a MOS transistor device structure is shown in Fig. 9. TID is measured in Grays (Gy) and values for the LHC experiments range from a few Gy up to several MGy. The discussion of TID effects in electronics at the LHC is continued below in Section 2.2.1.
2. Single event effects (SEE). When an ionizing particle deposits sufficient charge in a sensitive node, for example the drain in Fig. 9, then its normal function can be disrupted. A simple example is when a ‘1’ is changed to a ‘0’ (or vice versa) in a logic circuit or memory cell. Unlike TID and NIEL effects, SEEs are instantaneous and correlate strongly with the particle flux, itself proportional in LHC to the beam collision rate. The SEE sensitivity of a chip to radiation is defined by a cross-section, or the ratio between the events and the particle integrated flux triggering them, that is measured in an irradiation facility with the appropriate particle type and energy. At the LHC this cross-section is combined with the hadron fluence rate  $> 20$  MeV to predict the rate of SEEs during operation [47]. The discussion of SEE effects in electronics at the LHC is continued below in Section 2.2.2
3. Non-ionizing energy loss effects, a cumulative degradation effect also known as displacement damage. Particles interacting in the semiconductor material cause atoms to be displaced, creating defects and clusters of defects in the crystal lattice and changes to the device electrical and optical properties. The accumulation of NIEL defects gives rise to effects such as increased leakage currents and changes in the effective doping concentrations. CMOS devices are typically less sensitive to NIEL effects compared with TID, mainly due to the high level of majority charge carrier doping. However, in some MOS devices with low doping features such as LDMOS (laterally diffused MOS), the impact of NIEL can play an important role. Bipolar electronics are typically more sensitive to bulk defects than CMOS. A full overview of displacement damage in silicon devices was given previously in Section 2.1.3.

#### 2.2.1 TID effects

Electrons and holes are generated (in pairs) by ionizing radiation and normally transported in a device through the usual mechanisms of diffusion and drift. However, in the insulating oxide layers charges are

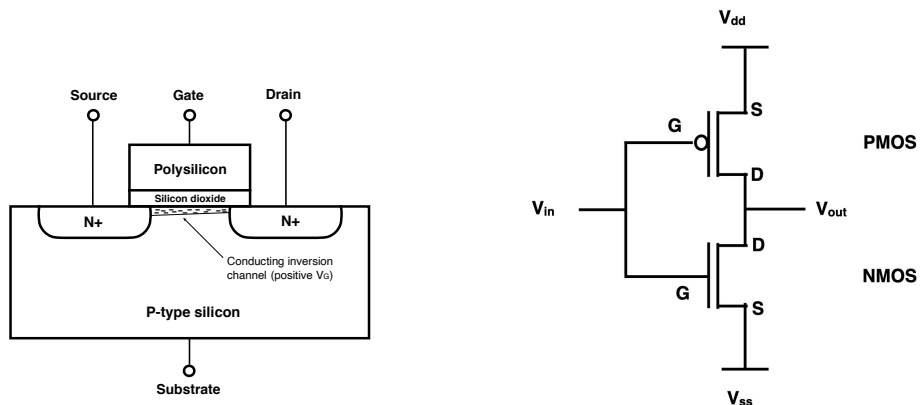


**Fig. 9:** Left: Schematic 2D representation of an NMOS transistor with N-type implants in a P-type body, creating two PN junctions. The  $\text{SiO}_2$  is a thin insulating layer separating the P-type silicon bulk from the conductive polysilicon where the gate voltage is applied. A positive gate voltage induces the formation of a conduction n-channel at the  $\text{SiO}_2$  interface where current can flow between source and drain in the presence of a horizontal electric field. The accumulation of radiation induced charged traps near the interface can significantly modify the conduction channel behaviour. Right: The combination of one NMOS and one PMOS transistor yields the simplest digital circuit: CMOS inverter. (G = gate; S = source; D = Drain.) When  $V_{in}$  is high, the NMOS transistor is switched on and current flows between the source and drain, and  $V_{out}$  takes the value of  $V_{ss}$ . When  $V_{in}$  is low, the NMOS transistor is off and  $V_{out}$  takes the value of  $V_{dd}$ . Both TID and SEE effects in either of the transistors can drastically impact circuit functionality.

less mobile than in the doped semiconductor regions. This is especially true for holes, which become trapped by defects in the oxide layer, resulting in an accumulation of positive charge during irradiation. The impact on CMOS and bipolar devices includes shifts in threshold voltages, opening of parasitic conductive paths (leakage currents) and decreased current gains. In CMOS structures (see Fig. 9) the migrating holes initiate a second class of defects close to the oxide–bulk interface which also leads to the degradation of the electrical performance. The physics behind oxide and interface charge trapping and annealing is complex, involving holes, protons ( $\text{H}^+$ ), and the breaking of Si–H bonds at the oxide–bulk interface [45]. The build up and annealing of these two kinds of effects is not the same and device performance is usually dose-rate and temperature dependent. An (infamous) example of the different kinetics of the two defects is the evolution of the leakage current during TID exposure. In many CMOS technologies the evolution of the leakage flowing between the drain and the source of the NMOS transistors has a non-monotonic behaviour, appearing as a ‘bump’ in a plot of leakage vs. TID (Fig. 10). After an initial increase, observed at low and moderate doses, the leakage current recovers when the TID is increased further. The height of the leakage current bump depends on the temperature and dose rate of the test, as well as the applied bias voltage. The peak of the bump is normally larger when the devices are kept cold. Because of this non-monotonic behaviour, it is strongly recommended to constantly monitor the evolution of the electrical characteristics of the circuits during radiation hardness assurance (RHA) irradiation tests, or at least to perform step-by-step irradiations. A case where this procedure was not followed is illustrated in Section 6.1.1, and as a consequence the increase of the system power consumption during data taking appeared as a surprise.

Ideally, when qualifying electronic components for TID in LHC radiation environments, whether ASIC or COTS, tests would be performed in similar radiation and environmental conditions. While this may be possible for temperature and biasing, irradiations have to be done on much shorter timescales than the lifetime of the detector systems, which means much higher dose rates. The consequence of

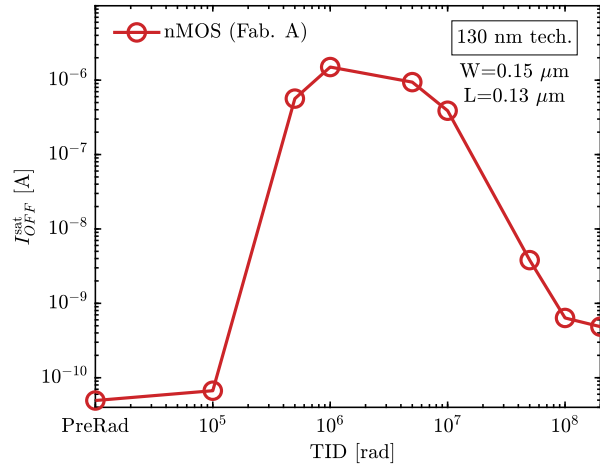


**Fig. 10:** Evolution of the source–drain leakage current in an NMOS transistor in 130 nm CMOS during a TID exposure. The position (in TID) and amplitude of the leakage depends on the temperature, bias, and dose rate.

using high dose rates on device performance is discussed below in Section 2.2.1.1. In addition to low dose-rate (LDR) effects, experiments also need to consider the sensitivity of TID response in different wafer production batches, which is discussed in Section 2.2.1.2. As a final comment on TID effects to electronics, we consider in Section 2.2.2.1 radiation effects on more recent technologies being used for the experiment upgrades.

### 2.2.1.1 LDR effects

The LDR effect refers to the fact that, for many components, the damage due to TID depends not only on the total dose, but also on the dose rate. The lifetime of a detector system may be up to ten years, which means TID testing at irradiation facilities has to be done with dose rates much higher than those found in the LHC radiation environments. In bipolar transistors, and in particular the older linear bipolar technologies, TID damage is typically larger for lower dose rates. This is a real LDR effect, named ELDRS (enhanced LDR sensitivity), that cannot be understood in terms of time evolution of defects and which makes it difficult to relate the laboratory results to the real life application. On the contrary, CMOS components were considered immune to real LDR effects, and by applying a post irradiation annealing procedure, known as a rebound test (168 h at 100 °C under bias), a reasonable prediction of the long term behaviour at lower dose rates could be established. An example of dose rate dependence in a CMOS device is illustrated in Fig. 11. Irradiating at high dose rates tends to lead to a negative shift in the threshold voltage because the build up of oxide-trap charge dominates. Irradiating at lower dose rates allows the oxide traps more time to anneal and at very low dose rates the impact of the interface-raps becomes dominant along with positive shifts in the threshold voltage.

Test methods have been developed for radiation hardness assurance (RHA) to take into account LDR effects [45]. Because of ELDRS, qualification of bipolar components is more challenging and the required test procedures more complex. In ATLAS, for example, testing on CMOS devices was derived from the MIL-STD 883-D Test Method 1019.4, a relatively straightforward method which includes the ‘rebound test’ (168 h at 100 °C with the device biased). The general idea of MIL-STD 883-D is to give a conservative upper bound to the effect of both oxide trapped charge and interface defects on the CMOS devices described above. Recommendations on test sample sizes are also given.

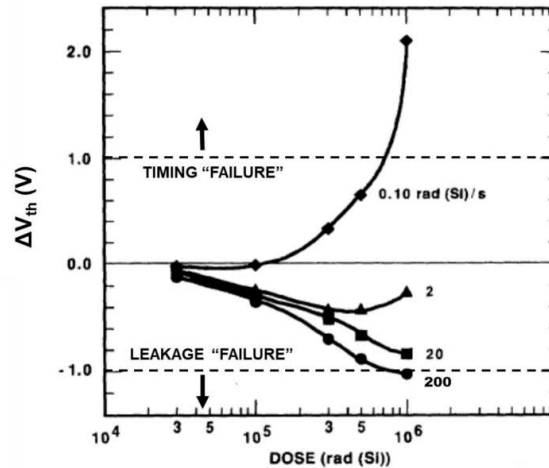


**Fig. 11:** Example of dose-rate dependence. Plot taken from Ref. [46].

### 2.2.1.2 Lot-to-lot effects

ASICs are designed in a specific technology process and can only be manufactured by a single company, although in several production plants (foundries). This decreases the possible variability in their radiation resistance, especially because it is typically possible to request fabrication at a specific plant. On the contrary, COTS components are most often purchased via a distributor and purchasing lots are constituted of samples of unknown origin. Unless specific agreements are concluded with the supplier to ensure a common and known origin of the components, a purchase lot has thus to be assumed inhomogeneous, i.e., components can come from different production lots. Measurements of samples coming from different manufacturing plants, or even from different lots produced at the same production site (Fab), have shown that relevant differences in the radiation damage might exist [49]. On top of the natural variability in their characteristics, normal even in very tightly controlled processes because of the incredible complexity of modern CMOS technologies, modifications to the processing sequence can be introduced by the manufacturer without warning. It is thus risky to assume comparable radiation response even for ASICs manufactured in the same Fab at different times. For COTS, of unknown origin, large variation can be found within the same purchase lot. It is therefore important to sample test for each batch or lot.

### 2.2.2 Single event effects

Single event effects (SEE) is the umbrella acronym covering a range of radiation effects on electronic circuits triggered by the transit of a single particle in the device [48]. These include single event upset (SEU), single event latch-up (SEL), single event gate rupture (SEGR), and single event burnout (SEB). For practical purposes we can also categorize the SEEs in terms of their impact on a system:

- soft SEEs (also called soft SEUs) are radiation induced bit flips that corrupt data or system configurations. They are not permanent effects as they can be dealt with by resetting the system or rewriting data in a memory. For example, a ‘1’ can be changed into a ‘0’ (or vice versa) in a combinatorial logic circuit, or in a register, or in a memory;
- hard SEEs (also called hard SEUs) are radiation induced bit flip that corrupts data or system configurations. They are permanent effects (they are not cancelled by resetting the system or rewriting data in a memory), such as a bit stuck to ‘1’ in a memory cell;
- destructive SEEs (SEs, SEBs, SEGRs) lead to permanent damage. SELs are destructive SEEs, unless a robust architectural solution protects the circuit against thermal destruction resulting from latch-up. SEBs and SEGRs are always destructive SEEs typically affecting high-power and/or high-voltage circuits.

SEEs are caused by a single particle depositing a large amount of ionizing energy in a small sensitive region of the chip. For SEUs, the sensitive region is typically the drain of a transistor and the amount of charge required for the event is smaller than for the destructive SEEs. Since the sensitive region is very small, only particles with large linear energy transfer (LET) can trigger an event. In the CMOS generations used in LHC experiments, only nuclear fragments originating from hadronic collisions of the incoming particles (protons, neutrons, pions) with atoms composing the circuit can lead to a sufficient charge deposition. These fragments have a range of only a few micrometres in silicon, and they must hence be produced very close to the sensitive region.

With continuously decreasing feature size and lower operating voltages integrated circuits become sensitive to smaller amount of deposited charge. In terms of SEU rates, this, however, is compensated by the fact that the size of the sensitive region also decreases. Thus both the probability of a fragment traversing the sensitive region and its path length within this, decrease. As a net effect, the SEU cross-section per unit of digital value stored in the chip (for instance, per memory cell) has been observed to rather decrease with decreasing feature size. There is, however, another effect that should be considered: with a smaller charge needed to create the upset it is possible that fragments with lower energy or charge are sufficient to induce it. This might increase the SEU vulnerability of modern chips more sensitive to low-energy neutron interactions. Finally, even if the SEU cross-section per node decreases, the SEU cross-section per chip will increase drastically due to the increasing node density.

### 2.2.2.1 *Evolution of electronics*

Microelectronics has advanced enormously over the past 20 years, with feature sizes and oxide thicknesses having become much smaller. The original LHC ASICs that are now participating in the data taking were designed and manufactured mainly in a commercial-grade 250 nm process or in the dedicated radiation-tolerant DMILL technology. The LHC upgrades are now adopting more advanced commercial-grade CMOS technologies for the development of ASICs needing an order of magnitude more radiation tolerance, and a large effort in the characterization of the radiation effects in CMOS nodes ranging from 250 to 28 nm has been recently made. New effects have been reported, in particular (but not only) in 130 and 65 nm technologies exposed to ultra-high TID levels. Time-, bias-, and temperature-driven effects have been better understood, along with ELDR effects, and the systematic observation of effects in test structures manufactured in several production plants has provided essential data on the variability of the radiation effects. This new knowledge drives the need for modifying aspects of testing components at the LHC upgrades [49–51].

## 2.3 Optoelectronics

The effects of radiation on optoelectronics used at the LHC can be divided into radiation damage degrading the performance of optical links and single event effects (SEE).

### 2.3.1 *Radiation damage and optoelectronics*

The effects of radiation damage mechanisms in p-i-n diodes (p-type - insulator - n-type) are similar to those in semiconductor detectors (e.g., silicon microstrip sensors) as described in the subsections above). The creation of mid-band states in the depleted region of the p-i-n diode leads to an increase in leakage current. As the volume of the p-i-n diode is very much smaller than that of a silicon strip, this leakage current is not expected to create a significant problem for LHC optoelectronics. The radiation damage will create defects which can lead to charge trapping. As the thickness of the depletion layer in the p-i-n diode is much less than that of typical silicon detectors this effect is also not expected to lead to significant signal loss for LHC applications. Finally the radiation damage will create defects in the active region of the p-i-n diode which will lead to the creation of acceptor states and therefore change the effective charge



carrier density which will cause the full depletion voltage to increase. However, if the bias voltage can be maintained at a value greater than the full depletion voltage this effect will not cause any signal loss.

The radiation damage in a Vertical Cavity Surface Emitting Laser (VCSEL) arises from bulk damage leading to defects which act as non-radiative recombination centres [52]. These decrease the minority carrier lifetime and hence the fraction of radiative transitions. This is a small effect for VCSELs operated above laser threshold as in this region they are dominated by stimulated emission with a correspondingly short lifetime. However, this is a significant effect below laser threshold because of the much longer lifetimes for spontaneous emission. This therefore can result in a significant increase in laser threshold. Complex annealing processes occur in the VCSELs and this can be accelerated by the electron-hole currents [52]. This injection annealing can lead to a very large fraction of the initial radiation damage being removed. Very significant radiation damage effects have been observed in VCSELs and Edge Emitting Lasers (EEL) from test beam studies.

### 2.3.2 Single event effects

As already discussed in Section 2.2.2, an SEE occurs when a high energy particle deposits a sufficiently large amount of energy in a small volume of electronics. In principle the effect can lead to a catastrophic failure but more commonly it can cause a bit to flip in a Single Event Upset (SEU). SEUs have been observed in LHC operation. The most vulnerable component to SEU in optical links is the p-i-n photodiode as a small amount of energy deposited in the active region of this type of device is indistinguishable from the signal from the infra-red photons in the optical link.

In a typical application the energy deposited by a minimum ionizing particle (MIP) passing through a p-i-n photodiode will be below threshold for causing an SEU. The main origin of SEUs at the LHC is high energy hadrons making nuclear interactions upstream close to the p-i-n photodiode and the combination of the energy deposition from the secondary particles is sufficient to cause an SEU. This requires very detailed simulations to make predictions for SEU rates at LHC, see for example Ref. [5]. Note that this is very different to space applications in which SEUs arise mainly from slow moving heavy ions which can have large enough LET to create SEUs. SEUs in optical links can therefore be studied either with beams of high energy protons or pions or with heavy ion beams. Estimates of the SEU rates in LHC operation have been made and compared to extrapolations from test beam data. This report also discusses some simple mitigation strategies that have been used to minimize the loss of data from SEUs and gives estimates for the fraction of data lost due to SEUs. More sophisticated mitigation strategies are planned for the HL-LHC detector upgrades.

## References

- [1] A. Vasilescu and G. Lindström, [Displacement damage in silicon](#), last accessed July 15 2020.
- [2] P.J. Griffin *et al.*, SNL RML recommended dosimetry cross section compendium, SAND92-0094 (Sandia Natl. Lab., Albuquerque, NM, 1993), [doi:10.2172/10115441](#).
- [3] G.P. Summers *IEEE Trans. Nucl. Sci.* **40** (1993) 1372, [doi:10.1109/23.273529](#).
- [4] A.Yu. Konobeyev *et al.*, *J. Nucl. Mater.* **186** (1992) 117, [doi:10.1016/0022-3115\(92\)90328-I](#).
- [5] M. Huhtinen and P.A. Aarnio, *Nucl. Instrum. Meth.* **A335** (1993) 580, [doi:10.1016/0168-9002\(93\)91246-J](#).
- [6] M. Huhtinen, *Nucl. Instrum. Meth.* **A491** (2002) 194, [doi:10.1016/S0168-9002\(02\)01227-5](#).
- [7] C. Inguibert *et al.*, *IEEE Trans. Nucl. Sci.* **57** (2010) 1915, [doi:10.1109/TNS.2010.2049581](#).
- [8] C. Inguibert and S.R. Messenger, *IEEE Trans. Nucl. Sci.* **59** 3117, [doi:10.1109/TNS.2012.2221477](#).
- [9] S.R. Messenger *et al.*, *Prog. Photovolt. Res. Appl.* **9** (2001) 103, [doi:10.1002/pip.357](#).
- [10] S.R. Messenger *et al.*, *IEEE Trans. Nucl. Sci.* **58** (2011) 3118, [doi:10.1109/TNS.2011.2172957](#).

- [11] R. Radu *et al.*, *Appl. Phys.* **117** (2015) 164503, doi:10.1063/1.4918924.
- [12] S.M. Sze, *Semiconductor Devices: Physics and Technology*, 3rd ed. (Wiley, New York, NY, 2012), see chapter 3 for a brief summary of the Shockley-Read-Hall theory.
- [13] M. Moll, *IEEE Trans. Nucl. Sci.* **65** (2018) 1561, doi:10.1109/TNS.2018.2819506.
- [14] M. Moll *et al.*, *Nucl. Instrum. Meth.* **A426** (1999) 87, doi:10.1016/S0168-9002(98)01475-2.
- [15] J.R. Srouf and J.W. Palko, *IEEE Trans. Nucl. Sci.* **60** (2013) 1740, doi:10.1109/TNS.2013.2261316.
- [16] M. Moll, [Radiation damage in silicon particle detectors: Microscopic defects and macroscopic properties](#), PhD thesis: Hamburg University, 1999.
- [17] M. Moll *et al.*, *Nucl. Instrum. Meth.* **B186** (2002) 100, doi:10.1016/S0168-583X(01)00866-7.
- [18] I. Pintilie *et al.*, *Nucl. Instrum. Meth.* **A514** (2003) 18, doi:10.1016/j.nima.2003.08.079, [DESY-02-199D](#).
- [19] I. Pintilie *et al.*, *Nucl. Instrum. Meth.* **A611** (2009) 52, doi:10.1016/j.nima.2009.09.065, [arXiv:0907.3050](#) [physics.ins-det].
- [20] A. Chilingarov, *JINST* **8** (2013) P10003, doi:10.1088/1748-0221/8/10/P10003.
- [21] V. Eremin *et al.*, *Nucl. Instrum. Meth.* **A476** (2002) 556, doi:10.1016/S0168-9002(01)01642-4.
- [22] D. Campbell *et al.*, *Nucl. Instrum. Meth.* **A492** (2002) 402, doi:10.1016/S0168-9002(02)01353-0.
- [23] R. Wunstorf, [Systematische Untersuchung zur Strahlenresistenz von Silizium-Detektoren für die Verwendung in Hochenergiephysik-Experimenten](#), PhD thesis, Hamburg University, 1992.
- [24] G. Lindström *et al.*, *Nucl. Instrum. Meth.* **A556** (2006) 451, doi:10.1016/j.nima.2005.10.103.
- [25] N. Pacifico *et al.*, *Nucl. Instrum. Meth.* **A658** (2011) 55, doi:10.1016/j.nima.2011.03.026.
- [26] M. Moll *et al.*, *Nucl. Instrum. Meth.* **A439** (2000) 282, doi:10.1016/S0168-9002(99)00842-6.
- [27] G. Lindström *et al.*, *Nucl. Instrum. Meth.* **A466** (2001) 308, doi:10.1016/S0168-9002(01)00560-5.
- [28] [The ROSE Collaboration: CERN RD48](#), last accessed July 15 2020; F. Lemeilleur; [Proposal for further work on radiation hardening of silicon detectors](#), CERN-LHCC-96-023, LHCC-P-62 (CERN, Geneva, 1996).
- [29] D. Mauro De Palma *et al.* [RD50 Collaboration], [Radiation hard semiconductor devices for very high luminosity colliders](#), CERN-LHCC-2002-003, LHCC-P-6 (CERN, Geneva, 2002).
- [30] A. Ruzin [RD48 Collaboration], *Nucl. Instrum. Meth.* **A447** (2000) 116, doi:10.1016/S0168-9002(00)00179-0.
- [31] F. Hartmann, *Evolution of Silicon Sensor Technology in Particle Physics*, 2nd ed. (Springer, Berlin, 2017), doi:10.1007/978-3-319-64436-3.
- [32] R. Wunstorf *et al.*, *Nucl. Instrum. Meth.* **A377** (1996) 228, doi:10.1016/0168-9002(96)00217-3.
- [33] M. Moll, *PoS Vertex2019* (2020) 027, doi:10.22323/1.373.0027.
- [34] O. Krasel *et al.*, *IEEE Trans. Nucl. Sci.* **51** (2004) 3055, doi:10.1109/TNS.2004.839096.
- [35] G. Kramberger, *Nucl. Instrum. Meth.* **A481** (2002) 297, doi:10.1016/S0168-9002(01)01263-3.
- [36] G. Kramberger, Solid state detectors for high radiation environments, in *Detectors for Particles and Radiation. Part 2: Systems and Applications, Landolt-Börnstein - Group I: Elementary Particles, Nuclei and Atoms, vol. 21B2*, Eds. C.W. Fabjan and H. Schopper (Springer, Berlin, 2011), chap. 7.2, doi:10.1007/978-3-642-14142-3\_7.
- [37] A.G. Bates and M. Moll, *Nucl. Instrum. Meth.* **A555** (2005) 113, doi:10.1016/j.nima.2005.09.020.
- [38] J. Lange *et al.*, *Nucl. Instrum. Meth.* **A624** (2010) 405, doi:10.1016/j.nima.2009.11.082.
- [39] W. Adam *et al.* [CMS Tracker Group], *JINST* **11** (2016) P04023, doi:10.1088/1748-0221/11/04/P04023.
- [40] G. Kramberger, [Signal development in irradiated silicon detectors](#), Ph.D. thesis, University of Ljubljana, 1998.

- [41] V. Eremin *et al.*, *Nucl. Instrum. Meth.* **A372** (1996) 388, [doi:10.1016/0168-9002\(95\)01295-8](https://doi.org/10.1016/0168-9002(95)01295-8).
- [42] G. Kramberger *et al.*, *IEEE Trans. Nucl. Sci.* **57** (2010) 2294, [doi:10.1109/TNS.2010.2051957](https://doi.org/10.1109/TNS.2010.2051957).
- [43] M. Fernández García *et al.*, *JINST* **12** (2017) C01038, [doi:10.1088/1748-0221/12/01/C01038](https://doi.org/10.1088/1748-0221/12/01/C01038).
- [44] G. Kramberger *et al.*, *JINST* **9** (2014) P10016, [doi:10.1088/1748-0221/9/10/P10016](https://doi.org/10.1088/1748-0221/9/10/P10016).
- [45] J.R. Schwank *et al.*, *IEEE Trans. Nucl. Sci.* **55** (2008) 1833, [doi:10.1109/TNS.2008.2001040](https://doi.org/10.1109/TNS.2008.2001040).
- [46] D.M. Fleetwood and H.A. Eisen, *IEEE Trans. Nucl. Sci.* **50** (2003) 552, [doi:10.1109/TNS.2003.813130](https://doi.org/10.1109/TNS.2003.813130).
- [47] M. Huhtinen and F. Faccio, *Nucl. Instrum. Meth.* **A450** (2000) 155, [doi:10.1016/S0168-9002\(00\)00155-8](https://doi.org/10.1016/S0168-9002(00)00155-8).
- [48] Edward Petersen, [Single event effects in aerospace](#), Wiley-IEEE Press, 2011.
- [49] F. Faccio *et al.*, *IEEE Trans. Nucl. Sci.* **62** (2015) 2933 [doi:10.1109/TNS.2015.2492778](https://doi.org/10.1109/TNS.2015.2492778).
- [50] F. Faccio *et al.*, *IEEE Trans. Nucl. Sci.* **65** (2018) 164 [doi:10.1109/TNS.2017.2760629](https://doi.org/10.1109/TNS.2017.2760629).
- [51] G. Borghello *et al.* *IEEE Trans. Nucl. Sci.* **65** (2018) 1482 [doi:10.1109/TNS.2018.2828142](https://doi.org/10.1109/TNS.2018.2828142).
- [52] Teng, P. K. *et al.*, *Nucl. Instrum. Meth.* **A497** (2003) 294, [doi:10.1016/S0168-9002\(02\)01922-8](https://doi.org/10.1016/S0168-9002(02)01922-8).



### 3 The LHC machine and experiments

A. Alici<sup>a</sup>, M. Bomben<sup>b</sup>, I. Dawson<sup>c</sup>, J. Sonneveld<sup>d</sup>

<sup>a</sup>University of Bologna, Italy

<sup>b</sup>LPNHE & University of Paris, France

<sup>c</sup>Queen Mary University of London, United Kingdom

<sup>d</sup>Nikhef, Amsterdam, Netherlands

The Large Hadron Collider is a 26.7 km circular accelerator based on a twin aperture superconducting magnet design with a design proton beam energy of 7 TeV [1]. The four particle physics experiments ALICE, ATLAS, CMS, and LHCb are located at the positions indicated in Fig. 12.

The LHC was first operated with beams for short periods in 2008 and 2009. In 2010, a first experience with the machine was gained at a beam energy of 3.5 TeV, with moderate beam intensities of  $1.1 \times 10^{11}$  protons per bunch (ppb) and up to  $\sim 200$  bunches. In 2011, the beam intensity was increased to  $\sim 1400$  bunches of  $1.4 \times 10^{11}$  ppb, while 2012 was dedicated to luminosity production with higher bunch intensities ( $1.6 \times 10^{11}$  ppb) and a beam energy of 4 TeV. The running years 2010–2013 are commonly referred to as Run 1. In early 2013 beam operation was stopped for a 2 year long shutdown (LS1) to complete work on the magnets in view of reaching the design beam energy. Beam operation resumed in 2015 with beam energies of 6.5 TeV following a dipole training campaign that took place at the end of LS1 [2]. The LHC experiments had expressed a strong preference for beams with 25 ns bunch spacing, as opposed to the 50 ns spacing used in 2011–2012, as this would result in too many inelastic collisions per crossing (pile-up). On the machine side, this posed additional challenges, so 2015 became a learning year dedicated to preparing the machine for full luminosity production in 2016–2018 (Run 2). Further details of machine operation during Run 2 can be found in Ref. [3].

In addition to the proton beams, one month per year is dedicated to running with heavy ions, providing either Pb–Pb or p–Pb collisions. The first two years of Run 1 provided Pb–Pb collisions to the experiments, and the final year was dedicated to p–Pb. Run 2 (2015–2018) again saw a mix of Pb–Pb and p–Pb set-ups, except in 2017- when Xe–Xe collisions were provided for the first time to the experiments.

#### 3.1 Luminosity delivered to the experiments

The main driver of radiation backgrounds in the experiments is from the collisions, although beam backgrounds can play a role too. The rate of collisions  $R$  in an experiment is given simply by the product of the particle interaction cross-section  $\sigma_{\text{int}}$  and the instantaneous luminosity  $L$ :

$$R = L \times \sigma_{\text{int}}, \quad L = \frac{kN^2f}{4\pi\sigma_x^*\sigma_y^*}F, \quad (20)$$

where  $k$  is the number of colliding bunch pairs,  $N$  the particle number of each bunch, and  $f$  is the LHC revolution frequency ( $= 11.25$  kHz). Here,  $\sigma_x^*$  and  $\sigma_y^*$  are the horizontal and vertical beam sizes at the interaction point and  $F$  ( $\leq 1$ ) is a geometric reduction factor which takes into account the reduced luminosity due to beam crossing angles at the interaction point.

Shown in Fig. 13 is the delivered integrated luminosity in 2018 for all four LHC experiments. The delivered luminosity is the important quantity for radiation background considerations, and not the ‘recorded’ luminosity, which is when the experiment starts taking data during a run. ATLAS has multiple

---

This chapter should be cited as: The LHC machine and experiments, Eds. A. Alici *et al.*, DOI: [10.23731/CYRM-2021-001.23](https://doi.org/10.23731/CYRM-2021-001.23), in: Radiation effects in the LHC experiments: Impact on detector performance and operation, Ed. Ian Dawson, CERN Yellow Reports: Monographs, CERN-2021-001, DOI: [10.23731/CYRM-2021-001](https://doi.org/10.23731/CYRM-2021-001), p. 23.  
© CERN, 2021. Published by CERN under the [Creative Commons Attribution 4.0 license](https://creativecommons.org/licenses/by/4.0/).

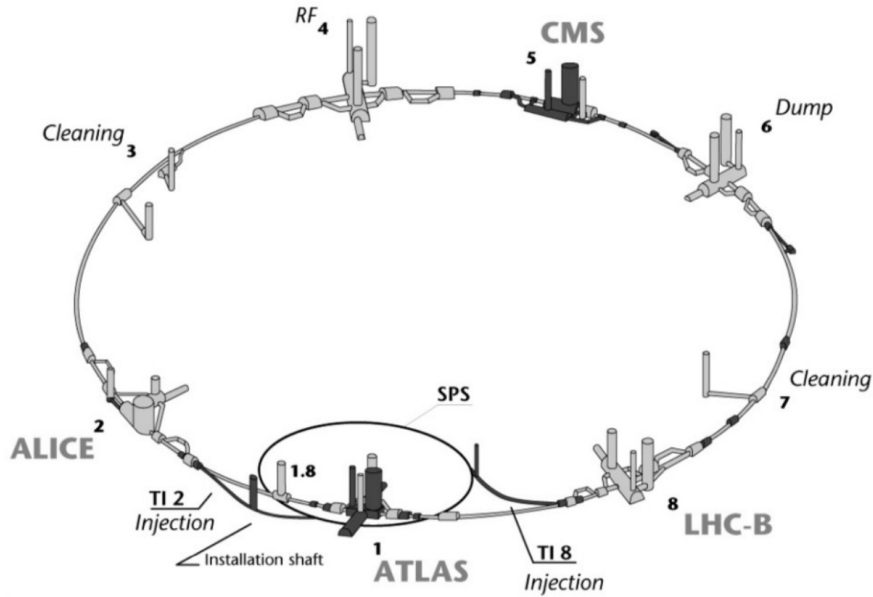


**Fig. 12:** The LHC layout

luminosity monitors, with the primary luminosity measurement performed by the LUCID-2 detector [4]. Additional detectors and dedicated LHC runs are used to achieve an uncertainty of 1.7% for Run 2 [5]. Similarly to ATLAS, CMS makes use of several luminosity monitors to measure the LHC delivered luminosity. All systems contribute to improve the accuracy of the measurement, reaching for the Run 2 an uncertainty of 1.8%.

The example of the total integrated luminosity delivered to the CMS experiment over the period 2010–2018 is shown in Fig. 14. The situation for ATLAS is similar. The gaps in the measurements correspond either to machine winter technical stops or the long shutdown LS1 (2013–2014). The total integrated luminosities delivered to experiments for pp, p–Pb, and Pb–Pb collisions are given in Table 1.

The particle collision rates inside the experiments are determined by the luminosity and the interaction cross-sections (Eq. 20). In particular, it is the inelastic component of the total cross-section that generates the dominant component of the radiation backgrounds in and around the LHC experiments. The particles from low angle elastic scattering disappear down the beam line, eventually interacting with elements of the machine. Measurements of the inelastic proton–proton cross-section have now been measured by all the experiments, and an example of how these compare for different centre of mass energies is given in Fig. 15. The ATLAS measured value at  $\sqrt{s} = 13$  TeV is  $78.1 \pm 2.9$  mb.

**Table 1:** Total integrated luminosities delivered to each of the experiments for the different particle collisions.

	pp (fb <sup>-1</sup> )		Pb–Pb (nb <sup>-1</sup> )		p–Pb (nb <sup>-1</sup> )	
	Run 1	Run 2	Run 1	Run 2	Run 1	Run 2
ATLAS	28.0	157.0	0.176	2.37	31.2	183.8
CMS	29.4	162.9	0.184	2.49	36.14	188.3
LHCb	3.47	6.35	-	0.24	2.14	34.1
ALICE	0.015	0.067	0.153	1.34	31.9	43.3

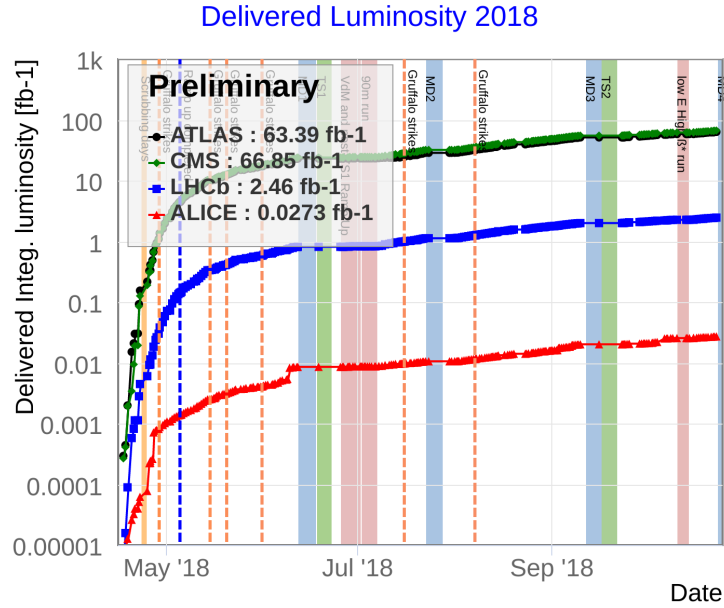


**Fig. 13:** LHC delivered integrated luminosity in 2018 for all four LHC experiments. The luminosity of ALICE was levelled to achieve moderate collision rates. Figure from Ref. [6].

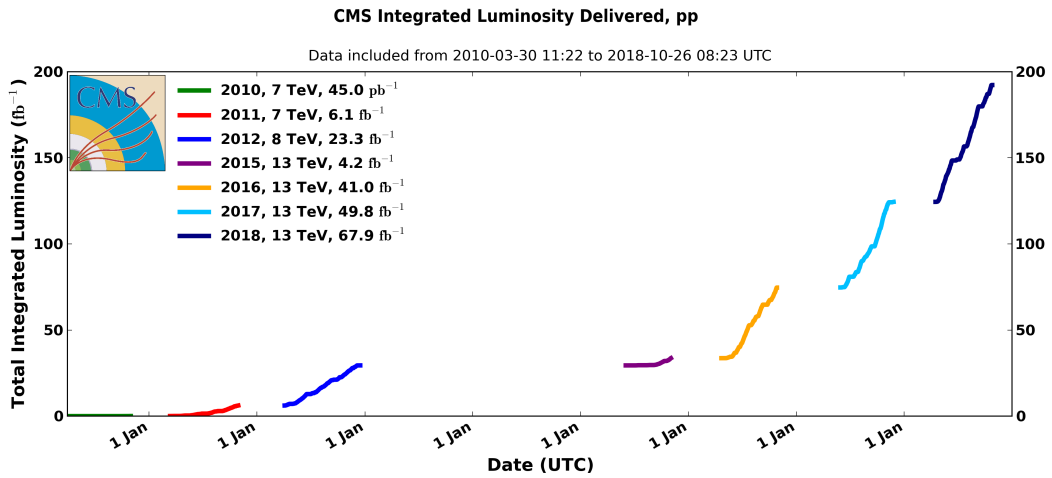


**Fig. 14:** CMS cumulative integrated luminosity versus day delivered to CMS during stable beams for pp collisions at nominal centre of mass energy. The CMS strip tracker has seen a total of  $192.3 \text{ fb}^{-1}$ ; the original CMS pixel detector was exposed to  $74.6 \text{ fb}^{-1}$ , the Phase-1 pixel detector, installed in 2017, has seen  $117.7 \text{ fb}^{-1}$ . Figure from Ref. [7].

### 3.2 The large LHC experiments

The LHC hosts a multitude of experiments. This report focuses on the four largest, namely ALICE, ATLAS, CMS, and LHCb. The inner tracking system of each of these experiments described below is affected most by radiation damage. All experiments use a right-handed coordinate system with its origin at the nominal interaction point (IP) of each of the experiments and the  $z$ -axis coincides with the axis of the beam pipe. The  $x$ -axis points from the IP towards the centre of the LHC ring, and the  $y$ -axis points upward. Cylindrical coordinates  $(r, \phi)$  are used in the transverse plane,  $\phi$  being the azimuthal angle around the  $z$ -axis. The pseudorapidity is defined in terms of the polar angle  $\theta$  as  $\eta = -\ln \tan(\theta/2)$ .

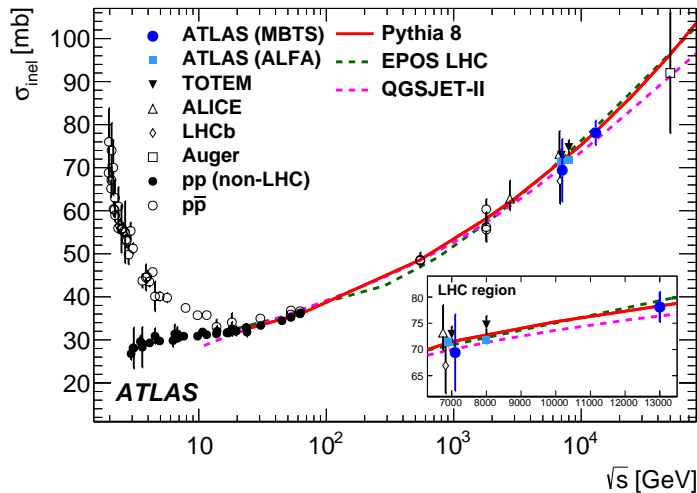


**Fig. 15:** Measurements and predictions of the inelastic proton–proton cross-sections. Figure from Ref. [8].

### 3.2.1 ATLAS

The ATLAS detector [9] was built and installed at the LHC interaction point 1 in the years 2000 to 2008. Since November 2009, when LHC first became operational, the experiment has collected  $185 \text{ fb}^{-1}$  of proton–proton collisions at 7, 8, and then 13 TeV centre of mass energy. The inner detector (ID) was designed to provide hermetic and robust pattern recognition, excellent momentum resolution, and both primary and secondary vertex measurements for charged tracks within the pseudorapidity range  $|\eta| < 2.5$ . The ID layout, described in Ref. [9], reflects the performance requirements: the ID is contained within a cylindrical envelope of length 3512 mm and of radius 1150 mm, within a solenoidal magnetic field of 2 T. The ID consists of three independent but complementary subdetectors: at inner radii, high-resolution pattern recognition capabilities are available using discrete space points from the silicon Pixel detector ( $r < 122.5 \text{ mm}$ ) and stereo pairs of silicon microstrips from the semiconductor tracker (SCT) ( $299 < r < 514 \text{ mm}$ ); at larger radii ( $563 < r < 1066 \text{ mm}$ ), the transition radiation tracker (TRT) comprises several layers of gaseous straw tube elements interleaved with transition radiation material.

The performance of the ATLAS experiment depends critically on the innermost layer of the Pixel detector. For this reason, at the beginning of 2013, during the LS1, a fourth pixel layer was added to the Pixel detector. Based on a new technology, the insertable B-layer (IBL) [10] was inserted between a new, narrower beryllium beam pipe and the pre-existing Pixel B-layer (the former innermost layer). Figure 16 shows the  $r - z$  layout of the upgraded ID before the start of Run 2. At the same time, the Pixel services were replaced by new ones (new Service Quarter Panel, or nSQP upgrade), making repairs of the opto-electrical converters possible without extraction of the Pixel detector in the future.

After resuming data taking in 2015, ATLAS has successfully operated the ID during Run 2 at  $\sqrt{s} = 13 \text{ TeV}$  and instantaneous luminosities surpassing the design value of  $1 \times 10^{34} \text{ cm}^{-2} \text{ s}^{-1}$ . The total integrated luminosity collected till 2019 by the Pixel, SCT, and TRT detectors is  $\sim 190 \text{ fb}^{-1}$  whilst the IBL detector, operating only during Run 2, collected a luminosity of  $\sim 159 \text{ fb}^{-1}$ . The ATLAS SCT received a maximum fluence of  $\Phi_{\text{eq}} \sim 4.5 \cdot 10^{13} / \text{cm}^2$  in its innermost layer, whereas the ATLAS pixel detector received a factor 20 more fluence  $\Phi_{\text{eq}}, \sim 1 \cdot 10^{15} / \text{cm}^2$ .



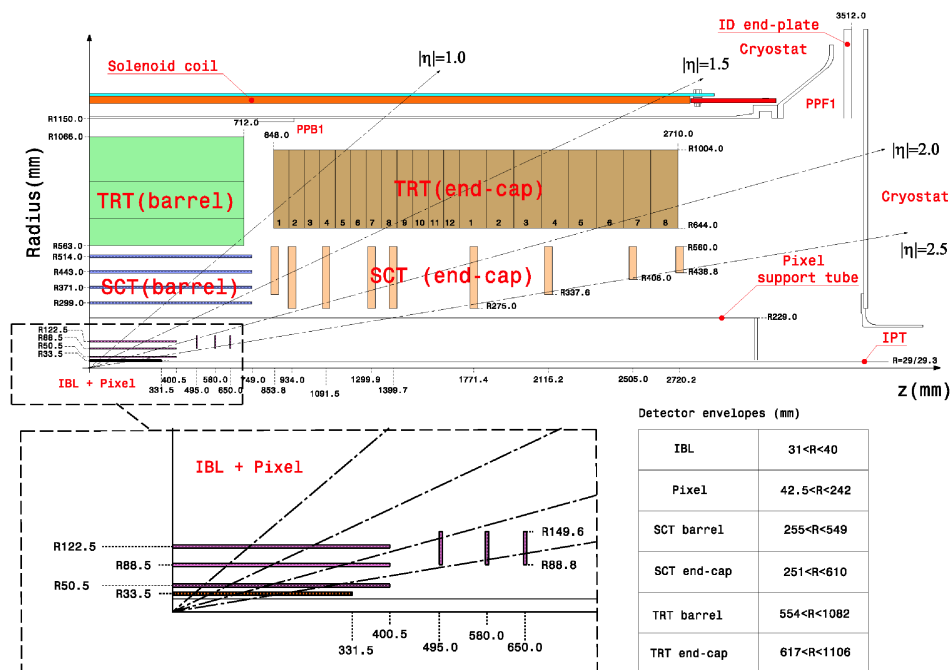


**Fig. 16:** Layout of the ATLAS inner detector, including the IBL installed before LHC Run 2. The top panel shows the whole inner detector, whereas the bottom panel shows a magnified view of the Pixel detector.

### 3.2.1.1 The ATLAS pixel detector

The ATLAS pixel detector [10–12] consists of four barrel layers and a total of six disc layers, three at each end of the barrel region. The four barrel layers are composed of  $n^+$ -in- $n$  planar oxygenated [13, 14] silicon sensors (p-type implants in n-type silicon) at radii of 33.5, 50.5, 88.5, and 122.5 mm from the geometric centre of the ATLAS detector. The IBL sensors are  $200 \mu\text{m}$  thick while the sensors in the other layers are  $250 \mu\text{m}$  thick. At high  $|z|$  on the innermost barrel layer, there are  $n^+$ -in-p 3D sensors [15] that are  $230 \mu\text{m}$  thick. The IBL pixel pitch is  $50 \times 250 \mu\text{m}^2$ ; everywhere else the pixel pitch is  $50 \times 400 \mu\text{m}^2$ . The IBL is cooled with two-phase  $\text{CO}_2$  cooling [16] with a nominal set temperature of  $-20^\circ\text{C}$ . The sensors are around  $-13^\circ\text{C}$  with the front-end electronics powered during data taking. Charged particles traversing the sensors deposit energy by ionizing the silicon bulk; for typical LHC energies, such particles are nearly minimum-ionizing particles (MIP). The deposited charge drifts through the sensor and the analogue signal recorded by the electrode is digitized, buffered, and read out using an FE-I4B [17] (IBL) or FE-I3 [12] (all other layers) chip.

### 3.2.1.2 The ATLAS SCT detector

The ATLAS SCT consists of four concentric silicon strip barrel layers, and two endcaps, each with nine disks, as indicated in Fig. 16. All the silicon strip sensors are 285 mm thick and are constructed of high-resistivity n-type bulk silicon with p-type implants. The barrel system is built from 2112 modules [18], and each endcap from 988 modules. Barrel modules consists of four rectangular silicon-strip sensors [19] with strips with a constant pitch of 80 mm. The SCT has a particle rapidity coverage of  $|\eta| < 2.5$ . Each barrel or disk provides two strip measurements at a stereo angle which are combined to build space-points. The SCT typically provides eight strip measurements (four space-points) to reconstruct particles coming from the proton-proton interactions.

### 3.2.1.3 The ATLAS TRT detector

The main detector component of the TRT is a cylindrical 4 mm diameter straw of thin-wall proportional chamber. Charged particles passing through the straw cause ionization of the gas atoms by exchange of either virtual photons from Coulomb interactions or real photons from transition radiation created in radiator material surrounding the straw. The liberated electrons drift according to the electric field applied, and are collected by the centre anode wire in the straw. The secondary electron drift time ranges up to 70 ns depending on the distance from a hit to the wire. The detector consists of a barrel and two endcaps; the barrel has 52 544 axial straws of about 144 cm length with anode wires read out by both ends independently; the endcaps situated on both sides of the barrel contain 122 880 straws each; giving 350 848 straws in total.

### 3.2.2 CMS

The Silicon Tracker of the Compact Muon Solenoid (CMS) [20] is the largest silicon tracker in the world. It is operated in a magnetic field of 3.8 T and reconstructs charged particle trajectories (tracks) that originate from the proton–proton collisions delivered by the LHC. The CMS tracker consists of a hybrid pixel detector as innermost part and a silicon strip tracker at larger radii. The CMS pixel detector [21] (also called the Phase-0 pixel detector) was running during the years 2009–2012 and 2015–2016 and was replaced with the CMS Phase-1 pixel detector [22] during the extended year-end technical stop 2016–2017. The strip tracker and the Phase-0 pixel detector cover(ed) the pseudo-rapidity range  $|\eta| < 2.5$ , the coverage of the Phase-1 pixel detector extends up to  $|\eta| = 3.0$ . A schematic of the CMS tracker is shown in Fig. 17.

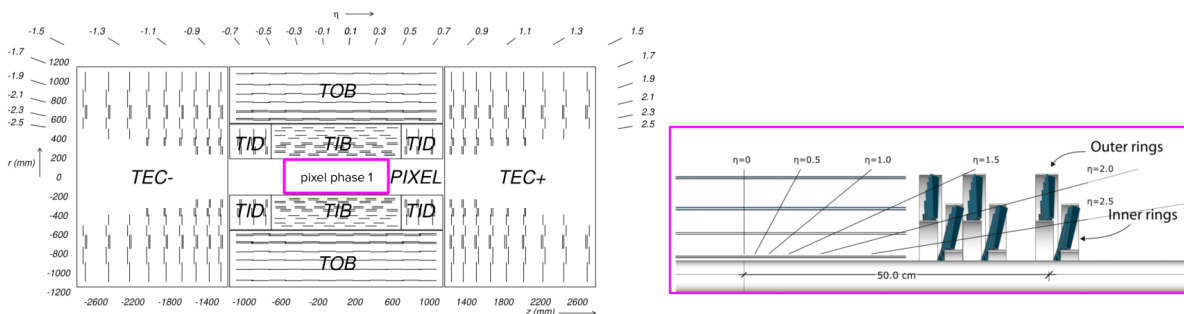


**Fig. 17:** The layout of the CMS tracker. Left: overview of the entire CMS tracker, with the CMS strip tracker detailed. It consists of 10 barrel layers and 12 disks on each detector end. Right: the layout of the CMS Phase-1 pixel detector that was installed in 2017. It consists of 4 layers and 3 endcap disks on each detector end. Figures from Ref. [22].

#### 3.2.2.1 The CMS pixel detector

The pixel Phase-1 (Phase-0) system consists of a barrel part with four (three) layers and two endcaps with three (two) disks each on either side of the interaction point. The pixel detector uses 285  $\mu\text{m}$  thick  $n^+$  in  $n$  sensors with  $100 \times 150 \mu\text{m}^2$  pixels. The sensors are bump bonded to the readout chips (ROC). Its innermost layer is located 2.9 cm (4.4 cm for the Phase-0 detector) from the beamline. At this distance the particle rates reach 600 MHz/cm<sup>2</sup> and the dose and fluence reach in excess of 100 Mrad or  $1 \times 10^{15} n_{\text{eq}}$ , respectively over the lifetime of the detector.

The detector modules were read out by the PSI46 chip in the original detector and by the PSI46dig [23, 24] for the upgraded detector apart from the innermost barrel layer, which is read out by the PROC600 ASIC [25], specifically designed to cope with the very high particle rates in this region.

**Table 2:** Operational bias voltages and maximum fluence for the CMS pixel detector at  $z = 0$  in the barrel and the module part closest to the beam line for the endcaps at the end of Run 2 in 2018. The distance from the beam line is also shown. This distance varies over modules on rings in the endcaps. The fluence variation in the endcaps results from the different distances in  $z$  from the interaction point of the 3 disks on each end of the detector.

Layer/ring	Operational bias	Radius	Maximum fluence $\Phi_{\text{eq}}$
layer 1	450 V	2.9 cm	$7.9 \times 10^{14}/\text{cm}^2$
layer 2	300 V	6.6 cm	$1.8 \times 10^{14}/\text{cm}^2$
layer 3	250 V	10.9 cm	$9 \times 10^{13}/\text{cm}^2$
layer 4	250 V	16.0 cm	$5 \times 10^{13}/\text{cm}^2$
ring 1	350 V	4.5–11 cm	$2.92\text{--}3.32 \times 10^{14}/\text{cm}^2$
ring 2	300 V	9.5–16 cm	$1.09\text{--}1.15 \times 10^{13}/\text{cm}^2$

The other components of the pixel module are the high-density interconnect (HDI) printed circuit and the token bit manager (TBM) ASIC [26]. The ROCs read out the individual pixels in a double-column structure with a global threshold per ROC. The TBM controls the programming and orchestrates the readout of the ROCs upon the receipt of a Level-1 accept (L1A) signal by passing a readout token to the group of ROCs it is connected to. Most of the auxiliary electronics for the pixel detector are located on the service cylinders outside of the active detector volume. Module power is regulated with DCDC converters [27] using the CERN FEAST2 ASIC [28] that is controlled with command and control units (CCUs) [29] similar to those used in the CMS strip tracker (see below). A detailed description of the CMS Pixel DAQ is given in Ref. [30]

The sensors of the Phase-1 pixel detector are cooled with bi-phase  $\text{CO}_2$  cooling [31–33] at a temperature of  $-22^\circ\text{C}$ . The effective temperature on the carbon fibre support structure of the modules ranges from  $-14$  to  $-8^\circ\text{C}$  when the modules are powered ( $-18^\circ\text{C}$  when unpowered), with higher temperatures at the start and lower temperatures at the end of cooling loops.

The original CMS pixel detector was exposed to  $74.6 \text{ fb}^{-1}$  while the Phase-1 detector has seen  $117.7 \text{ fb}^{-1}$ . The operational bias voltage in the pixel system is adjusted during the run to compensate the effects of radiation. This is done taking into account the fluence a detector part has been exposed to. The operational voltage and approximate fluence for the individual detector parts is summarized in Table 2.

### 3.2.2.2 The CMS strip detector

The CMS strip tracker contains 15 148 modules with more than 9.3 million silicon strips covering a total active area of silicon of  $198 \text{ m}^2$ . It is organized in large substructures: the inner barrel (TIB) with four layers, the inner disks (TID) with three disks on each end of the TIB volume in the forward region, the outer barrel (TOB) which completely surrounds the TIB and TID and consists of 6 layers, and the two large endcaps (TEC) with 9 disks each that complement the strip tracker on either side of the interaction point. The first two layers of the TIB and TOB and rings 1 and 2 (1, 2, and 5) of the TIB(TEC) contain stereo modules with silicon modules mounted back to back for 3D space point reconstruction. The strip tracker sensors are of n-type silicon with 512 or 768  $\text{p}^+$  single-sided strips with a thickness of  $320 \mu\text{m}$  up to a radius of 600 mm, and  $500 \mu\text{m}$  at larger radii. The charge on each microstrip is read out and amplified by a  $0.25 \mu\text{m}$  analogue pipeline voltage (APV25) chip [34]. A module contains either 4 or 6 APV25 chips. The APV chips are located on the so-called front-end hybrid which also houses auxiliary chips like a multiplexer (APVMUX), a PLL chip and a detector control unit (DCU) which allows readout of slow-control monitoring data like low voltage levels, temperatures, and the leakage current of the silicon sensors. The module is connected via a cable to the analogue-opto hybrid (AOH) which houses a linear laser driver (LLD). The control of the detector modules happens through token or control-ring

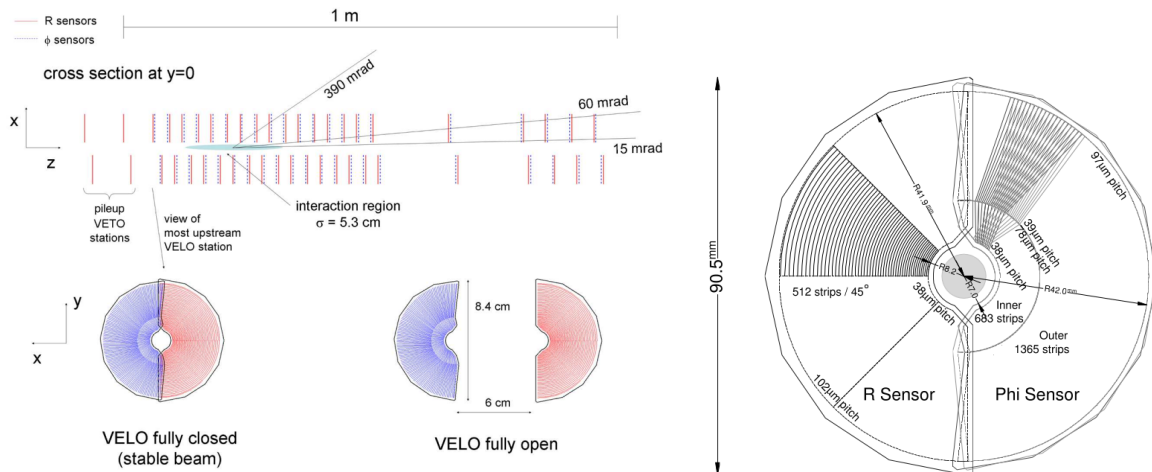


**Fig. 18:** Left top: cross-section of the LHCb VELO modules when fully closed around the beam line at  $y = 0$ . Left bottom: front face of first VELO modules when VELO is fully closed (left) and fully opened (right). Right: the different types of sensors in the LHCb VELO detector. Figures from Ref. [35].

networks of clock and control units (CCU). The token rings are connected via bidirectional optical links to the front-end controllers (FEC) located in the service cavern outside the radiation zone. The FECs send clock, trigger, and fast commands to the modules and transmit configuration data to them. The link allows for a readback of the configuration parameters and the communication with the DCU.

Upon receipt of an L1A the charge of a pipeline cell is read out by an analogue pulse shape processor (APSP) that can operate in two modes. In *peak mode* a single cell is read out, timed to be at the peak of the analogue pulse. In *deconvolution mode*, three samples are read out and the output is the weighted sum of all three. The shaper of the APV has a pulse shape with a length of 200 ns which is much longer than the LHC bunch spacing of 25 ns. In deconvolution mode the pulse is reshaped to peak after 25 ns resulting in a pulse length of about 50 ns; this happens at the expense of increased noise. The signal from two chips is time multiplexed in the APVMUX and converted to an optical signal on the AOH. The signal is then transferred via optical fibres of 60–100 m length to the service cavern to the front-end drivers (FED).

The strip tracker uses a mono-phase  $C_6F_{14}$  cooling system. The coolant temperature was  $+4^\circ\text{C}$  during Run 1 and was lowered to  $-15^\circ\text{C}$  during the running years 2015–2017 and to  $-20^\circ\text{C}$  during 2018.

### 3.2.3 LHCb

The LHCb tracking system (Run 1 and Run 2) is comprised of two silicon detectors, the LHCb vertex locator (VELO), and the silicon tracker (ST) [35]. The LHCb VELO detector consists of two retractable halves, each with 21 modules containing a pair of n-on-n silicon sensors of  $300\ \mu\text{m}$  thickness. A cross-section of the VELO modules when closed in around the beam line is shown on the left in Fig. 18.

Each module contained two sensor types, R-type sensors with 2048 concentric strips and  $\phi$ -type with 2048 radial strips as shown on the right in Fig. 18. The innermost active channels were placed at approximately 8 mm from the proton beams during the stable data taking conditions.

The sensor pitch ranged from  $35\ \mu\text{m}$  closest to the beam line to  $101\ \mu\text{m}$  furthest away from the beam line. Strip isolation was achieved through p-spray and a minimum pitch of  $35\ \mu\text{m}$  for the sensors at the innermost radius for optimal vertex resolution.

The VELO detector is operated in a secondary vacuum, separated from the primary LHC vacuum by a  $300\ \mu\text{m}$  thick aluminium radio-frequency (RF) foil. It is cooled with two-phase  $\text{CO}_2$  cooling with

a nominal set temperature of  $-30^{\circ}\text{C}$ . The sensors are at around  $-8^{\circ}\text{C}$  with the front-end electronics powered during data taking.

The vertex locator has operated since the start of the LHC and has since collected  $3\text{ fb}^{-1}$  of proton–proton collision data in Run 1 and  $9\text{ fb}^{-1}$  in Run 2. With their proximity to the beam line at a distance of only 8 mm, the innermost VELO sensors have been exposed fluences up to about  $\Phi_{\text{eq}} \sim 6.5 \times 10^{14}/\text{cm}^2$ .

The ST is part of the LHCb main tracking system which consists of four tracking stations, one upstream and three downstream of the LHCb dipole magnet. The trigger tracker or tracker turicensis (TT) constitutes the first tracking station while the inner tracker (IT) covers and cross-shaped region around the beam pipe in the three downstream tracking stations. The TT is a planar station with dimensions about 130 cm in height and 150 cm in width. The IT is about 120 cm wide and 40 cm high. Both the IT and TT have four silicon detection layers using silicon microstrip sensors. The first and last layer of each station has the strips in the vertical direction. The two middle layers of each station have a stereo angle compared to the vertical with the first station rotated by  $-5^{\circ}$  and the third station by  $+5^{\circ}$ . The TT uses  $500\text{ }\mu\text{m}$  p<sup>+</sup>-in-n sensors with a strip pitch  $183\text{ }\mu\text{m}$ . The IT uses p<sup>+</sup>-in-n sensors with a strip pitch of  $198\text{ }\mu\text{m}$ . The modules in the horizontal plane have  $410\text{ }\mu\text{m}$  thickness and a strip length of 22 cm through daisy chaining of two individual sensors. The sensors at the top and bottom are of  $320\text{ }\mu\text{m}$ . In the latter case a single sensor is used resulting in a strip length of 11 cm.

### 3.2.4 ALICE

The ALICE inner tracking system (ITS) [36] operated in Run 1 and Run 2 consisted of six cylindrical layers of silicon detectors placed coaxially around the beam pipe, based on different technologies, and located at radii between 3.9 and 43 cm (Fig. 19). It provided a rapidity coverage  $|\eta| < 0.9$  for all vertices located within the length of the interaction diamond ( $\pm 1\sigma$ , i.e.,  $\pm 5.3\text{ cm}$  along the beam direction). The number, position, and segmentation of the layers were optimized for efficient track finding and high impact parameter resolution. In particular, the inner radius is the minimum allowed by the radius of the beam pipe, while the outer radius is determined by the necessity to match tracks with those from the time projection chamber (TPC).

Table 3 summarizes the main characteristics of each layer. Due to the high particle density expected in heavy-ion collisions at LHC (as many as 50 particles per  $\text{cm}^2$  have been predicted for the inner layer), and in order to achieve the required impact parameter resolution, silicon pixel detectors (SPD) have been chosen for the innermost two layers, and silicon drift detectors (SDD) for the following two layers. The two outer layers, where the track density is expected to be below one particle per  $\text{cm}^2$ , are equipped with double-sided silicon micro-strip detectors (SSD). The four outer layers have analogue readout and therefore can be used for particle identification via  $dE/dx$  measurement in the non-relativistic ( $1/\beta^2$ ) region. The analogue readout has a dynamic range large enough to provide the  $dE/dx$  measurement for low-momentum highly ionizing particles, down to the lowest momentum at which tracks can still be reconstructed. This feature gives the ITS standalone capability as a low- $p_{\text{T}}$  particle spectrometer. The ITS provided the reconstruction of the collision point (primary vertex), with a resolution of  $10\text{ }\mu\text{m}$  in central Pb–Pb collisions, and the displaced vertices (secondary vertices), with a resolution better than  $100\text{ }\mu\text{m}$  [37].

#### 3.2.4.1 The silicon pixel detector

The two innermost layers making the silicon pixel detector (SPD), were based on hybrid pixel detectors with binary output consisting of  $200\text{ }\mu\text{m}$  thick silicon sensor matrix and  $150\text{ }\mu\text{m}$  thick bump-bonded readout chips. The matrix had  $256 \times 160$  reversely biased (50 V) p-n diodes, forming cells  $50\text{ }\mu\text{m}$  wide ( $r\phi$ ) and  $425\text{ }\mu\text{m}$  long ( $z$ ). The binary output is readout at 10 MHz. The detector is equipped with a  $\text{C}_4\text{F}_{10}$ -based evaporative cooling system.

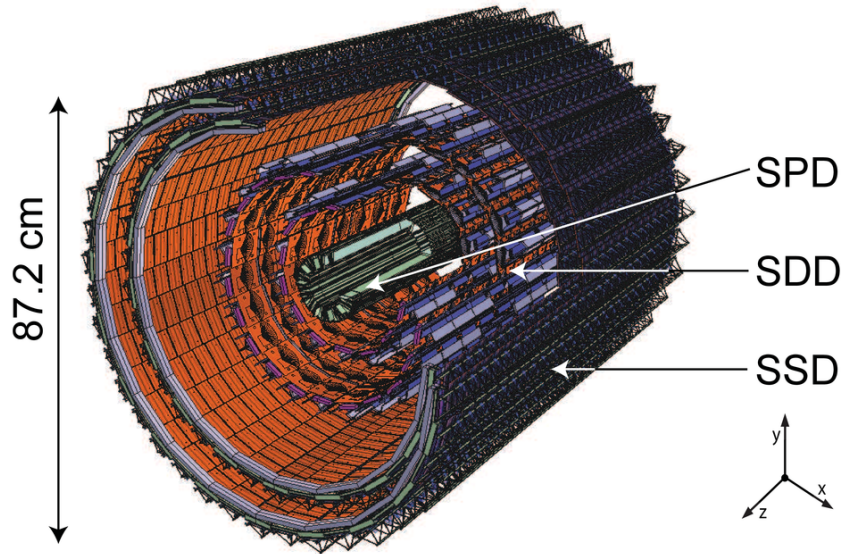


**Fig. 19:** The ALICE inner tracking system before 2019 from the start of the LHC up to long shutdown 2 (LS2). Figure from Ref. [36].

**Table 3:** Characteristics of the ITS, layer by layer. Res. is the resolution, along the bending direction ( $r\phi$ ) and the beam axis ( $z$ ). M.B. is the material budget, expressed in terms of radiation lengths ( $X_0$ ).

Layer	Detector	Radius	Length	Channels	Area	Res. ( $\mu\text{m}$ )		M.B. (% $X_0$ )
		(cm)	(cm)		( $\text{m}^2$ )	$r\phi$	$z$	
1	SPD	3.9	28.2	3.3 M	0.07	12	100	1.14
2		7.6	28.2	6.5 M	0.14			1.14
3	SDD	15.0	44.4	43 k	0.42	35	25	1.13
4		23.9	59.4	90 k	0.89			1.26
5	SSD	38.0	86.2	1.1 M	2.20	20	830	0.83
6		43.0	97.8	1.5 M	2.80			0.83

#### 3.2.4.2 The silicon drift detector

The silicon drift detector (SDD) equipped the two intermediate layers of the ITS and was based on  $300\ \mu\text{m}$  thick drift sensor and custom hybrid readout boards. The sensitive area of the module was divided into two drift regions along the bending direction ( $r\phi$ ) by the central cathode at  $-1.8\ \text{kV}$ . In each drift region and on both detector surfaces,  $\text{p}^+$  cathode strips ( $120\ \mu\text{m}$  pitch) were used to fully deplete the detector and generate a uniform electric drift field ( $500\ \text{V/cm}$ ), parallel to the module surface, towards collection anodes ( $294\ \mu\text{m}$  pitch) aligned with the beam axis. The drift speed was about  $6.7\ \mu\text{m/s}$  and was monitored by means of MOS charge injectors. The analogue SDD information was digitized by 10-bit ADCs at 20 MHz at the level of the front-end electronics developed on CMOS  $0.25\ \mu\text{m}$ . The SDD was equipped with a leakless water cooling system.

#### 3.2.4.3 The silicon strip detector

The two outermost layers of the ITS consisted of double-sided strip sensors, with a thickness of  $300\ \mu\text{m}$ , connected with two HAL25 front-end chips, making the silicon strip detector (SSD). The analogue signals were digitized by 12-bit ADCs directly in the readout electronics placed outside the ALICE solenoid magnet. The  $\text{p}^+$  reverse bias was optimized in the range 20–80 V. The SSD was provided with a leakless

water cooling system shared with the SDD, and, due to the sensitivity of the detector to the air humidity, an air dryer system was also used to keep the absolute humidity between 1 and 1.5 g/kg.

Because of lower collision rates, the ALICE ITS saw less fluence and dose than the ATLAS, CMS, and LHCb detectors. The fluence and dose seen by the ALICE ITS subsystems in Run 1 and Run 2 are summarized in Table 4 for the innermost layer of each system.

**Table 4:** ALICE fluence and dose levels after Run 1 and Run 2 at the end of 2018 in its inner tracking system (ITS). Only the maximum fluence of the innermost layer of each subsystem is shown.

ITS subdetector	Radius	Maximum TID	Maximum hadron fluence $\Phi_{\text{eq}}$
SPD	3.9 cm	19.3 krad	$3.2 \times 10^{11}/\text{cm}^2$
SDD	15 cm	1.65 krad	$4.0 \times 10^{10}/\text{cm}^2$
SSD	38 cm	0.37 krad	$1.8 \times 10^{10}/\text{cm}^2$

## References

- [1] O.S. Brüning *et al.* (Eds.), LHC design report, CERN-2004-003-V-1 (CERN, Geneva, 2004), [doi:10.5170/CERN-2004-003-V-1](https://doi.org/10.5170/CERN-2004-003-V-1).
- [2] A. Verweij, Circuit performance at 6.5 TeV and beyond, LHC Performance Workshop, Chamonix, France, 2016, [Indico](#).
- [3] J. Wenninger, *PoS CHARGED2018* (2019) 001, [doi:10.22323/1.339.0001](https://doi.org/10.22323/1.339.0001).
- [4] G. Avoni *et al.*, *JINST* **13** (2018) P07017, [doi:10.1088/1748-0221/13/07/P07017](https://doi.org/10.1088/1748-0221/13/07/P07017).
- [5] ATLAS Collaboration, [Luminosity determination in  \$pp\$  collisions at  \$\sqrt{s} = 13\$  TeV using the ATLAS detector at the LHC](#), ATLAS-CONF-2019-021 (CERN Geneva, 2019).
- [6] LHC Program Coordination [Performance plots for  \$pp\$  collisions, May–Sep 2018](#).
- [7] CMS Collaboration, [CMS luminosity public results](#).
- [8] ATLAS Collaboration *Phys. Rev. Lett.* **117** (2016) 182002, [doi:10.1103/PhysRevLett.117.182002](https://doi.org/10.1103/PhysRevLett.117.182002).
- [9] ATLAS Collaboration, *JINST* **3** (2008) S08003, [doi:10.1088/1748-0221/3/08/S08003](https://doi.org/10.1088/1748-0221/3/08/S08003).
- [10] ATLAS Collaboration, [ATLAS insertable B-layer: technical design report](#), CERN-LHCC-2010-013, ATLAS-TDR-19 (CERN, Geneva, 2010).
- [11] ATLAS Collaboration, *JINST* **13** (2018) T05008, [doi:10.1088/1748-0221/13/05/T05008](https://doi.org/10.1088/1748-0221/13/05/T05008).
- [12] ATLAS Collaboration, *JINST* **3** (2008) P07007, [doi:10.1088/1748-0221/3/07/P07007](https://doi.org/10.1088/1748-0221/3/07/P07007).
- [13] ROSE Collaboration, [3rd RD48 status report: the ROSE collaboration \(R&D on silicon for future experiments\)](#), CERN-LHCC-2000-009 (CERN, Geneva, 2000).
- [14] ROSE Collaboration, *Nucl. Instrum. Methods Phys. Res.* **A465** (2000) 60, [doi:10.1016/S0168-9002\(01\)00347-3](https://doi.org/10.1016/S0168-9002(01)00347-3).
- [15] S.I. Parker, C.J. Kenney, J. Segal, *Nucl. Instrum. Methods Phys. Res.* **A395** (1997) 328, [doi:10.1016/S0168-9002\(97\)00694-3](https://doi.org/10.1016/S0168-9002(97)00694-3).
- [16] B. Verlaat *et al.*, *JINST* **12** (2017) C02064, [doi:10.1088/1748-0221/12/02/C02064](https://doi.org/10.1088/1748-0221/12/02/C02064).
- [17] M. Garcia-Sciveres *et al.*, *Nucl. Instrum. Methods Phys. Res.* **A636** (2011) S155, [doi:10.1016/j.nima.2010.04.101](https://doi.org/10.1016/j.nima.2010.04.101).

- [18] A. Abdesselam *et al.*, *Nucl. Instrum. Methods Phys. Res.* **A568** (2006) 642, doi:[10.1016/j.nima.2006.08.036](https://doi.org/10.1016/j.nima.2006.08.036).
- [19] A. Ahmad *et al.*, *Nucl. Instrum. Methods Phys. Res.* **A578** (2007) 98, doi:[10.1016/j.nima.2007.04.157](https://doi.org/10.1016/j.nima.2007.04.157).
- [20] CMS Collaboration, [The CMS tracker system project : technical design report](#), CERN-LHCC-98-06, CMS-TDR-5 (CERN, Geneva, 1998); [Addendum](#), CERN-LHCC-2000-016, CMS-TDR-5-add-1 (CERN, Geneva, 2000).
- [21] CMS Collaboration, *JINST* **3** (2008) S08004, doi:[10.1088/1748-0221/3/08/S08004](https://doi.org/10.1088/1748-0221/3/08/S08004).
- [22] CMS Collaboration, [CMS technical design report for the pixel detector upgrade](#), CERN-LHCC-2012-016, CMS-TDR-11 (CERN, Geneva, 2012).
- [23] H. C. Kästli, *Nucl. Instrum. Methods Phys. Res.* **A731**, (2013) 88, doi:[10.1016/j.nima.2013.05.056](https://doi.org/10.1016/j.nima.2013.05.056).
- [24] H. C. Kästli *et al.*, *Nucl. Instrum. Methods Phys. Res.* **A565** (2006) 188, doi:[10.1016/j.nima.2006.05.038](https://doi.org/10.1016/j.nima.2006.05.038), [arXiv:physics/0511166](https://arxiv.org/abs/physics/0511166).
- [25] A. Starodumov, P. Berger, M. Meinhard, *JINST* **12** (2017) C01078, doi:[10.1088/1748-0221/12/01/C01078](https://doi.org/10.1088/1748-0221/12/01/C01078).
- [26] E. Bartz, [The token bit manager chip for the CMS pixel readout](#), Proc. Int. Workshop on Semiconductor Pixel Detectors for Particles and X-Rays (PIXEL2002), Carmel (CA), USA, Ed. S.C. Loken (SLAC, Stanford, 2002).
- [27] L. Feld *et al.*, *JINST* **11** (2016) C02033, doi:[10.1088/1748-0221/11/02/C02033](https://doi.org/10.1088/1748-0221/11/02/C02033).
- [28] F. Faccio *et al.*, FEAST2: a radiation and magnetic field tolerant point-of-load buck DC/DC converter, Proc. 2014 IEEE Radiation Effects Data Workshop (REDW), Paris, France, 14–18 Jul. 2014, Eds. F. Irom, S Metzger, pp. 1–7, doi:[10.1109/REDW.2014.7004569](https://doi.org/10.1109/REDW.2014.7004569).
- [29] C. Paillard, C. Ljuslin and A. Marchioro, The CCU25: a network oriented communication and control unit integrated circuit in a 0.25  $\mu\text{m}$  CMOS technology, Proc. 8th Workshop on Electronics for LHC Experiments Colmar, France, Sep. 9–13, 2002, Eds. P. Sharp, C. Isabella (CERN, Geneva, 2002), pp.174–178 doi:[10.5170/CERN-2002-003.174](https://doi.org/10.5170/CERN-2002-003.174).
- [30] The Tracker Group of the CMS Collaboration, *JINST* **14** (2019) P10017, doi:[10.1088/1748-0221/14/10/P10017](https://doi.org/10.1088/1748-0221/14/10/P10017).
- [31] J. Daguin *et al.*, Evaporative CO<sub>2</sub> cooling system for the upgrade of the CMS pixel detector at CERN, Proc. 13th InterSociety Conference on Thermal and Thermomechanical Phenomena in Electronic Systems, San Diego (CA), USA, 30 May–1 Jun. 2012, pp. 723–731, doi: [10.1109/ITHERM.2012.6231499](https://doi.org/10.1109/ITHERM.2012.6231499).
- [32] P. Tropea *et al.*, *Nucl. Instrum. Methods Phys. Res.* **A824** (2016), doi:[10.1016/j.nima.2015.08.052](https://doi.org/10.1016/j.nima.2015.08.052).
- [33] B. Verlaat, M. Van Beuzekom, A. Van Lysebetten, CO<sub>2</sub> cooling for HEP experiments, Proc. Topical Workshop on Electronics for Particle Physics, Naxos, Greece, 15–19 Sep. 2008, Eds. E. Dho, F. Vasey (CERN, Geneva, 2008), pp.328–336, doi:[10.5170/CERN-2008-008.328](https://doi.org/10.5170/CERN-2008-008.328).
- [34] M. Raymond *et al.*, The CMS tracker APV25 0.25 $\mu\text{m}$  CMOS readout chip, Proc. 6th Workshop on Electronics for LHC Experiments, Krakow, Poland, 11–15 Sep. 2000 (CERN, Geneva, 2000), pp. 130–134, doi:[10.5170/CERN-2000-010.130](https://doi.org/10.5170/CERN-2000-010.130).
- [35] LHCb Collaboration, *JINST* **3** (2008) S08005, doi:[10.1088/1748-0221/3/08/S08005](https://doi.org/10.1088/1748-0221/3/08/S08005).
- [36] ALICE Collaboration, *JINST* **3** 08 (2008) S08002, doi:[10.1088/1748-0221/3/08/s08002](https://doi.org/10.1088/1748-0221/3/08/s08002).
- [37] ALICE Collaboration, *Int. J. Mod. Phys.* **A29** (2014) 1430044, doi:[10.1142/S0217751X14300440](https://doi.org/10.1142/S0217751X14300440).



## 4 Simulation of radiation environments

*Editors:* I. Dawson<sup>a</sup>, S. Mallows<sup>b</sup>.

*Contributing authors:* A. Alici<sup>c</sup>, I. Azhgirey<sup>d</sup>, I. Dawson<sup>a</sup>, M. Huhtinen<sup>e</sup>, V. Ivantchenko<sup>f</sup>, D. Kar<sup>g</sup>, M. Karacson<sup>e</sup>, S. Mallows<sup>b</sup>, T. Manouos<sup>e</sup>, I. Mandić<sup>h</sup>, A. Di Mauro<sup>e</sup>, S. Menke<sup>i</sup>, P.S. Miyagawa<sup>a</sup>, A. Oblakowska-Mucha<sup>j</sup>, S. Pospisil<sup>k</sup>, T. Szumlak<sup>j</sup>, V. Vlachoudis<sup>e</sup>.

<sup>a</sup>Queen Mary University of London, United Kingdom

<sup>b</sup>Karlsruhe Institute of Technology, Germany

<sup>c</sup>University of Bologna, Italy

<sup>d</sup>IHEP, Protvino, Russia

<sup>e</sup>CERN, Geneva, Switzerland

<sup>f</sup>Tomsk State University, Russia

<sup>g</sup>University of the Witwatersrand, Johannesburg, South Africa

<sup>h</sup>Jozef Stefan Institute, Ljubljana, Slovenia

<sup>i</sup>Max Planck Institute for Physics, Munich, Germany

<sup>j</sup>AGH University of Science and Technology, Kraków, Poland

<sup>k</sup>Czech Technical University in Prague, Czech Republic

Simulating radiation environments is crucial in the design phase of new hadron collider experiments or upgrades, especially when extrapolating to new centre of mass collision energies where previous experience cannot be relied on. The generation of radiation fields in the LHC experiments is dominated by proton–proton collisions, with contributions from beam–gas interactions and other machine losses [1]. It is therefore essential to first reproduce the proton–proton collisions, using Monte Carlo event generators such as PYTHIA8 [2] and DPMJET-III [3]. This part of the simulation chain is discussed in Section 4.1.

The particles originating from the proton–proton collisions interact with the detector and machine material, causing electromagnetic and hadronic showers which give rise to the complex radiation fields seen in the LHC experiments. This second part of the simulation is dealt with using advanced Monte Carlo particle transport codes such as FLUKA [4,5], MARS [6], or GEANT4 [7]. An overview of these codes is given in Section 4.2.

Key radiation quantities of interest are extracted from the simulations, such as 1 MeV neutron equivalent fluence and total ionizing dose, and these are discussed in Section 4.3. It is these quantities that are needed by the detector systems for evaluating radiation damage and predicting sensor and electronic performance over the lifetime of the experiment. In Section 4.4, the simulated predictions of radiation backgrounds for each of the experiments is presented. Finally, in Section 4.5, we offer general conclusions and recommendations for the future.

### 4.1 Event generation

The physics processes in inelastic proton–proton collisions are dominated by soft (low- $p_T$ ) QCD interactions, but hard (high- $p_T$ ) parton–parton scatters can play an important role too in radiation background studies. Experimental physicists often refer to these events as ‘minimum bias’, reflecting the minimally biased trigger system required to study these events. Although the hard scattering processes are well described by perturbative QCD, this breaks down for low- $p_T$  interactions and a wide variety of models with distinct theoretical concepts have been developed to describe this regime.

---

This chapter should be cited as: Simulation of radiation environments, Eds. I. Dawson, S. Mallows, DOI: [10.23731/CYRM-2021-001.35](https://doi.org/10.23731/CYRM-2021-001.35), in: Radiation effects in the LHC experiments and impact on detector performance and operation, Ed. Ian Dawson, CERN Yellow Reports: Monographs, CERN-2021-001, DOI: [10.23731/CYRM-2021-001](https://doi.org/10.23731/CYRM-2021-001), p. 35.

© CERN, 2021. Published by CERN under the [Creative Commons Attribution 4.0 license](https://creativecommons.org/licenses/by/4.0/).

A good minimum-bias event generator describes accurately both the soft and hard physics processes, including diffractive disassociation of one or both protons. The cross-sections for these processes should be provided too so that event rates can be calculated. Another desirable feature is a smooth transition between the soft and hard processes up to the highest centre-of-mass collision energies. PHOJET [8] (part of the DPMJET-III package) was used extensively during the design phase of the ATLAS experiment, and implements the dual parton model [9] to describe particle production in low- $p_T$  processes. PYTHIA6 was also used in the original design studies on ATLAS and LHCb to provide an estimate of systematic uncertainties in the event generator predictions. PYTHIA6 implements leading-order QCD matrix elements with a very low transverse momentum cutoff to model the low- $p_T$  (non-diffractive) physics, and incorporates different approaches for dealing with the resulting divergences. Other well-known Monte Carlo event generators at the time, such as ISAJET and HERWIG, had not been fully developed for minimum-bias event generation.

Collision data taking began in earnest at the LHC experiments in 2010, and comparisons with the Monte Carlo predictions have been made. Measurements of event distributions such as  $dN_{\text{ch}}/d\eta$  and  $dN_{\text{ch}}/dp_T$  have been made for centre-of-mass energies 900 GeV, 7 TeV, and 13 TeV. Examples of measurements compared with event generator predictions from ATLAS [10] and LHCb [11] are shown in Figs. 20 and 21, respectively. Examples of measurements from CMS compared with event generator predictions are found in Ref. [12].

Corresponding measurements of the proton–proton cross-sections have also been made, allowing the rise of the inelastic cross-sections to be studied [13]. Shown in Table 5 is a comparison of the predicted and measured proton–proton cross-sections between the experiments. The ATLAS and LHCb experiments use mainly PYTHIA8 for minimum-bias event generation. This is because the code is fully supported by the LHC experiments and the code authors, with continuous development and improvement of the physics models. DPMJET-III is integrated into the FLUKA transport code and is used by CMS.

**Table 5:** Inelastic proton–proton cross-sections (mb) measured by the LHC experiments. These are compared with the PYTHIA8 cross-sections used by ATLAS for MC event generation. The DPMJET-III prediction for  $\sqrt{s} = 13$  TeV is 84 mb.

	LHC measurements			PYTHIA8
	ATLAS	CMS	LHCb	(ATLAS tune)
$\sqrt{s} = 13$ TeV	$78.1 \pm 2.9$	$71.3 \pm 3.5$	$75.4 \pm 5.4$	78.4
$\sqrt{s} = 7$ TeV	$69.1 \pm 2.4$	$64.5 \pm 3.2$	$66.9 \pm 5.3$	71.4

## 4.2 Particle transport codes

Monte Carlo particle transport codes are essential in simulating and studying the radiation fields. The main workhorse codes for ATLAS during the design phase were FLUKA and GCALOR, but today (2020) most radiation background studies are performed with FLUKA and GEANT4. CMS continues to use both FLUKA and MARS for radiation background studies. Both LHCb and ALICE have relied principally on FLUKA for radiation particle transport since early design studies.

### 4.2.1 FLUKA

The FLUKA code [4,5] is well established for studies of hadronic and electromagnetic cascades induced by high-energy particles and it is the baseline code for radiation background simulations at CERN and the LHC experiments. Electrons, photons, and muons can be interacted and transported up to 1000 TeV, and hadrons up to 20 TeV. Lower transport limits are typically at the keV level, except for low-energy

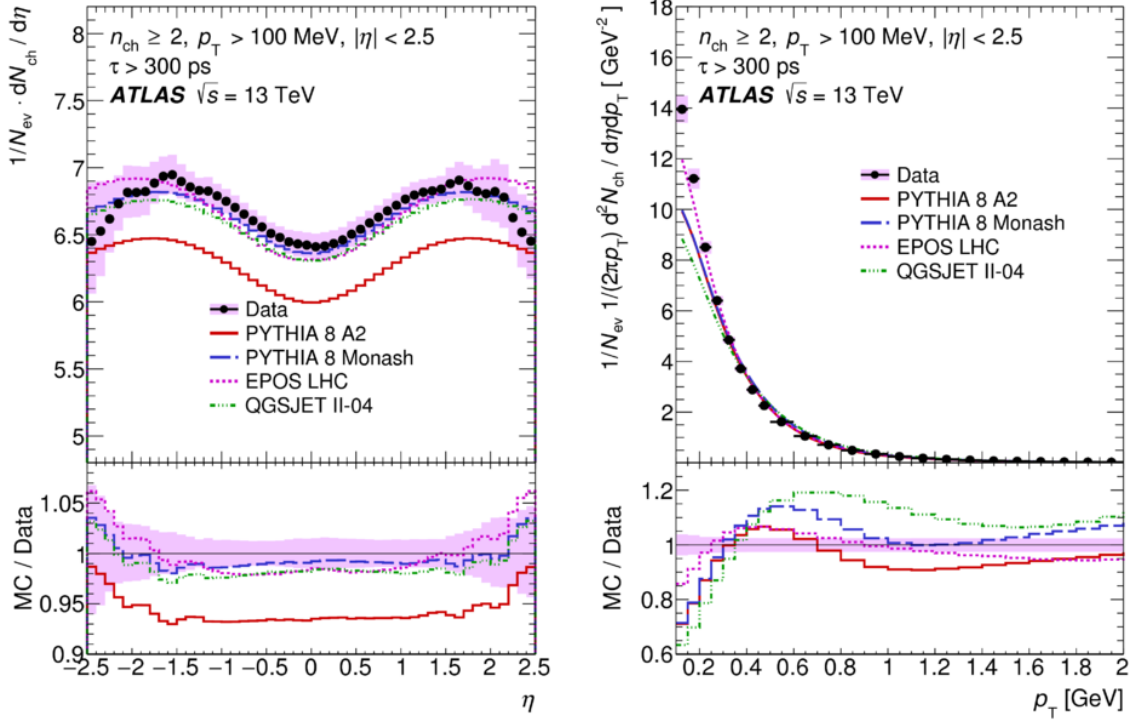


**Fig. 20:** Primary charged particle multiplicities as a function of (left) pseudorapidity  $\eta$  and (right) transverse momentum  $p_T$  for events with at least two primary charged particles with  $p_T > 100$  MeV and  $|\eta| < 2.5$ , each with a lifetime  $> 300$  ps. The black dots represent the data and the coloured curves the different MC model predictions. The plots are taken from Ref. [10].

neutrons which can be transported to thermal energies. Anti-particles, heavy ions, and residual nuclei production are also treated by FLUKA.

Microscopic physics modelling is adopted in FLUKA when possible and conservation laws are enforced at each interaction step. Results are benchmarked against experimental data at the single interaction level. An advantage of this methodology is that the simulated predictions are based on a minimal set of free parameters which are fixed for all projectile energies and target materials. This makes simulations more reliable when extrapolating to complex cases where no experimental data exists, and correlations within interactions and shower components are preserved.

A complete description of FLUKA's physics models and capabilities can be found in Ref. [14] and references therein. As an example, inelastic hadron interactions are described by different physics models depending on the energy. For inelastic hadron–hadron interactions above 5 GeV the dual parton model (DPM) [15] is used, and below 5 GeV the resonance production and decay model [16]. For hadron–nucleus inelastic interactions greater than 5 GeV, Glauber–Gribov multiple scattering followed by generalized intranuclear cascade (GINC) is employed. Below 5 GeV, the pre-equilibrium-cascade model PEANUT is used [17, 18]. All the above hadron interaction models include evaporation and gamma deexcitation of the residual nucleus [19, 20]. Light residual nuclei are not evaporated but fragmented into a maximum of 6 bodies according to a Fermi break-up model.

For the geometry and material description, FLUKA uses a ‘combinatorial geometry’ which combines bodies (defined by surfaces) into regions using boolean operations (union, subtraction, etc.). The transport and interaction of particles in FLUKA are also designed to accurately track charged particles in the presence of magnetic or electric fields. Although intrinsically an analogue code, FLUKA can be

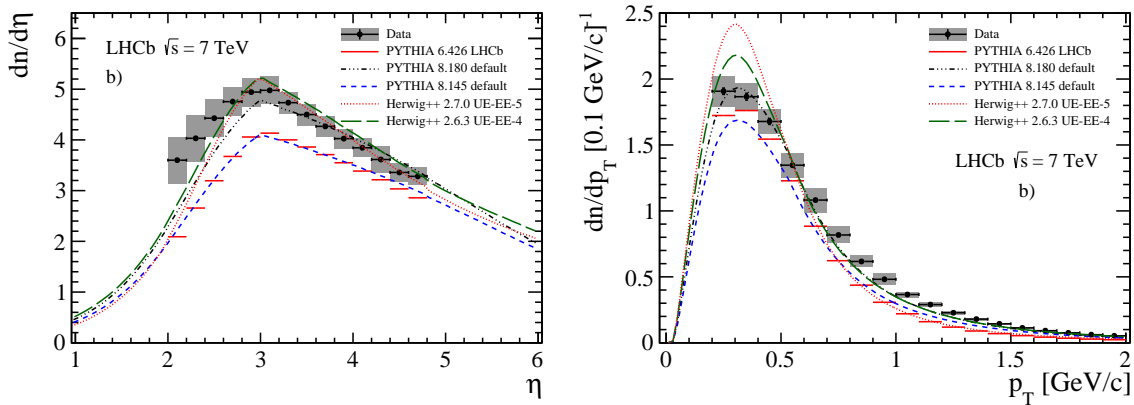


**Fig. 21:** Charged particle density as a function of  $\eta$  (left) and  $p_T$  (right). The LHCb data are shown as points. The grey bands are the combined systematic and statistical uncertainties. The measurements are compared to several Monte Carlo generator predictions. The plots are taken from Ref. [11].

run in biased mode (variance reduction) for a variety of deep penetration applications.

#### 4.2.2 MARS

The Monte Carlo simulation package MARS [6] is occasionally used to calculate the radiation levels in the CMS cavern, and was used by ATLAS in the very early days of shielding design. MARS is similar to FLUKA, but the main difference is that it is an inclusive code, so that a fixed number of secondary particles is generated in one step, with weights according to the averaged multiplicities of such particles. MARS uses a 28-group library for low-energy ( $< 14.5$  MeV) neutron reactions and transport, while photon production in low-energy neutron-induced reactions is described in a 15-group approximation.

#### 4.2.3 GEANT4

GEANT4 [7] is a toolkit for simulating the passage of particles through matter and is used by all the LHC experiments for studying detector performance. It is the outcome of an international collaboration of physicists and software engineers, exploiting the advantages of modern object-oriented programming and, in contrast FLUKA and MARS, constructed to allow easy access to the physics models.

However, the use of GEANT4 for radiation background studies in the past has been limited. Radiation transport codes such as FLUKA and MARS were more established in accurately modelling both high- and low-energy nuclear physics processes. Today, the situation has changed and the increasingly mature GEANT4 is now considered a credible alternative for HEP radiation background studies.

Physics lists are used to configure the physics processes to be enabled in the simulation. The default physics simulation list (since version 9.6) is the so-called FTFP\_BERT, but for radiation background studies either the FTFP\_BERT\_HP or SHIELDING lists are recommended as they enable high precision neutron transport. Users can also customize lists to their needs, for example adding a radioactive decay package.

An interesting development ( $\sim 2018$ ) by the ATLAS experiment was to run their full GEANT4 physics simulation framework, which uses a very detailed description of the ATLAS detector, with physics settings appropriate for radiation background studies. In the past this was not feasible due to CPU and memory issues, but today running on the GRID has made this possible.

#### 4.2.4 GCALOR

The GCALOR package [21] was used extensively for ATLAS radiation background studies during the initial design phase. It was developed and maintained by the Oak Ridge National Laboratory, and was one of the recommended detector simulation codes to support the development of detector designs for the Superconducting Super Collider project in the 1990s.

By the time of LHC upgrade studies, the support for CALOR and GEANT3 maintenance and development was limited, and FLUKA, MARS and GEANT4 became the preferred choice for radiation background studies. We also make the point that radiation background expertise tends to be limited, so sometimes it is better to be agnostic when it comes to choosing simulation strategies.

### 4.3 Radiation damage estimators

The radiation environments at the LHC experiments are complex, covering a wide range of particle types and energies. In practice, only a few derived quantities are needed to predict detector damage and performance. The physics of radiation effects on sensors and electronics is described in Section 2. The three main radiation quantities of interest are:

- the 1 MeV neutron equivalent fluence ( $\Phi_{\text{eq}}^{\text{Si}}$ ), allowing studies of bulk damage in silicon and the impact on electrical and optical properties, such as leakage currents, depletion voltages, and charge collection efficiency. The particle type and energy is obtained from the simulations and scaled by the hardness factors described in Section 2. The hardness factors have been experimentally determined only over limited energy ranges for neutrons, protons and pions, and the associated uncertainties are estimated to be  $\sim 30\%$ ;
- total ionizing dose (TID), defined as the amount of ionizing energy deposited per unit mass of material. In the design and qualification of electronics the ionizing radiation can lead to charges trapped in the device oxide layers. The accumulated charge can induce shifts in device threshold voltages and increased parasitic currents. In addition, scintillating materials and optical fibres also suffer from damage that to good approximation is proportional to the ionizing dose. The damage manifests itself as a reduction of the light transmission, as induced phosphorescence, or changes of the scintillating properties;
- hadron fluence  $> 20$  MeV ( $\Phi_{20}^{\text{had}}$ ). This characterization of the radiation field is used for predicting single event upsets (SEU) estimates at the LHC [22]. Single event effects (SEE) in electronic circuits are caused by large energy depositions close to sensitive regions of the chips. The released charge can be sufficient to flip the logic state of a transistor, and in extreme cases cause permanent or destructive damage. The amount of ionization needed to cause a SEE can be only deposited by heavy ions, which at the LHC can be created in the chip itself from high-energy hadron interaction with the target nuclei.

## 4.4 Experiment simulations and predictions

### 4.4.1 ATLAS

The radiation environment in the ATLAS inner detector is complex and comprises a full spectrum of particles (pions, protons, neutrons, photons, etc.), with energies ranging from TeV down to thermal for neutrons. Close to the interaction point the environment is dominated by particles coming directly from the proton–proton collisions, but at larger radii albedo neutrons from high-energy hadron and electromagnetic cascades in the calorimeters can play a major role. The use of advanced Monte Carlo event generators and particle transport codes is the principle method for accurately simulating and studying such complex radiation environments.

The deleterious effects of radiation in silicon sensor systems include: increased leakage currents; charge accumulation in silicon oxide layers; decreasing signal-to-noise; changing depletion voltages;

single event effects impacting electronics; and radiation-induced activation of components. Both sensors and electronics are impacted by radiation and the measurements and observations made in these two areas are discussed in detail in Sections 5 and 6, respectively.

Radiation background simulations on ATLAS have been performed mainly using the FLUKA particle transport code since the first design studies, with GCALOR playing a big role too. More recently GEANT4 simulations have been performed successfully for radiation background studies which uses the same simulation framework as for the physics performance studies and thus exploits the full detailed ATLAS geometry description. See Section 4.2 for a description of these codes.

PYTHIA8 is used to generate the inelastic proton–proton collisions (including single and double diffractive processes) which feed into the FLUKA and GEANT4 simulations. In particular, PYTHIA8 is tuned to LHC minimum-bias data [23] and events are generated according to the LHC centre of mass energies (7, 8, and then 13 TeV). The ATLAS PYTHIA8 tune predicts a fiducial inelastic cross-section of 69.9 mb at 13 TeV, which compares well with the measured value of  $68.1 \pm 1.4$  mb. In the original FLUKA studies, the PHOJET event generator was used. The predictions for the fluences in the inner detector are typically  $\sim 5\%$  higher with PYTHIA8 than for PHOJET. More details about the event generators are given in Section 4.1.

FLUKA simulation studies are typically performed on CPU farms, with the codes installed locally on Unix based workstations. The ever increasing CPU capacity has benefitted ATLAS simulations enormously over the past 20 years allowing faster turnaround times and increasing detector description complexity. The situation was similar for the original GCALOR and MARS simulation effort. Eventually, around 2014, FLUKA started using the SVN repository, and later GIT, to allow shared collaboration and file versioning between the different groups performing FLUKA simulations. GEANT4 simulation studies take advantage of the ATLAS GeoModel detector description [24] and jobs are run on the GRID. Simulation results are shared with the various experiment groups through Web tools and TWiki pages.

#### 4.4.1.1 ATLAS detector geometry and material description

For the accurate simulation of radiation environments, a well-defined geometry model is needed which includes the detector systems, shielding elements, services, and beam-line material. Details of the inner detector system are described in Section 3.2.1. An overview of the full ATLAS experiment can be found in Ref. [25]. Shown in Fig. 22 is the inner detector region as described in the FLUKA geometry. A complete description of the surrounding calorimeters is also important to reproduce the neutron albedo. For the most part the FLUKA geometry is simplified, describing for example detector barrel layers as cylinders. This is sufficient (in most cases) as long as the material radiation and interaction lengths are reproduced accurately. In contrast, the GEANT4/GeoModel detector description is built for physics performance simulations and contains millions of geometry volumes. In the past such simulations were prohibitively CPU expensive for radiation background studies, but these days running on the LHC computing Grid has made this feasible.

Running simulations with more than one simulation package allows comparisons to be made and investigations into simulation uncertainties. This is especially useful in regions where the geometry description is complex. Radiation background studies comparing FLUKA and GEANT4 suggest that differences in the physics models are small for the quantities of interest ( $\Phi_{eq}^{Si}$ , TID,  $\Phi_{20}^{had}$ ) and that in most cases it is the geometric uncertainties that are most important.

#### 4.4.1.2 FLUKA fluence and dose predictions

FLUKA simulations of  $\Phi_{eq}^{Si}$  and TID in the ATLAS inner detector  $\phi$  region are shown in Fig. 23. Such  $r$ - $z$  colour plots are common in ATLAS, superimposed on a quarter slice of the FLUKA geometry and illustrating how fluence and dose profiles vary across different regions. The fluence and dose values are averaged over  $\phi$ . The radius  $r$  is measured from the beam line, and  $z$  from the interaction point. Similar

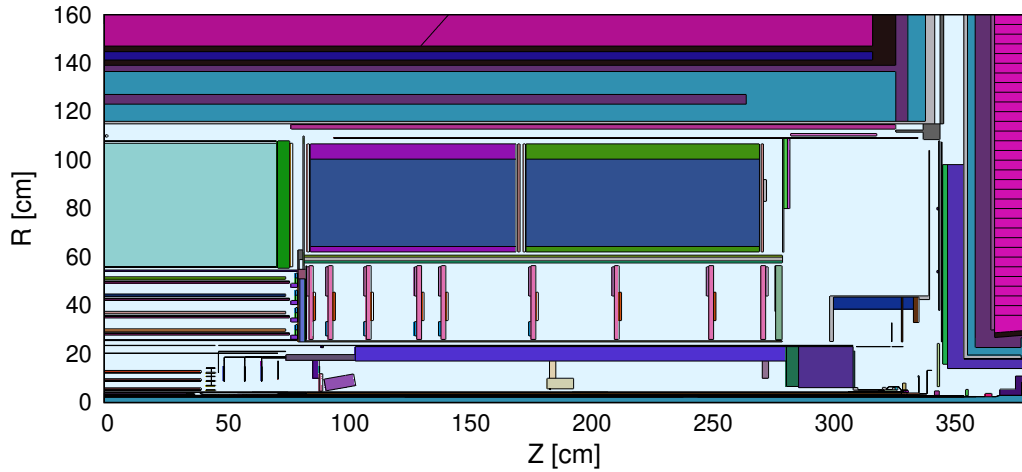


**Fig. 22:** ATLAS geometry described in FLUKA focusing on the inner detector regions, including part of the surrounding calorimeter (magenta).

plots are generated for  $\Phi_{20}^{\text{had}}$  to allow SEE estimates. The locations of the IBL (insertable B-layer), pixels, SCT (semi-conductor tracker), and TRT (transition radiation tracker) are indicated.

Illustrated in Fig. 24 is the neutron component of  $\Phi_{\text{eq}}^{\text{Si}}$  in the central region ( $z=0$ ) as a function of the radius  $r$ . In the IBL and pixel systems,  $\Phi_{\text{eq}}^{\text{Si}}$  is dominated by charged pions from the IP, but once we reach the radii of the SCT it is the neutrons ‘back splashing’ from the calorimeters that matter. In the absence of scattering and a magnetic field, the particles emerging from the IP with a flat  $\eta$ -distribution<sup>1</sup> would result in a fluence independent of  $z$  and dropping as  $r^{-2}$ . Figure 24 shows that this radial dependence is well described up to  $r \sim 20$  cm, but in the SCT region the fluence shows a much slower decrease, which is due to the particle interactions and showering, as well as the effect of the 2 T inner detector solenoid field. Also shown is the FLUKA to GEANT4 ratio, where it can be seen that the GEANT4 predictions are some  $\sim 20\%$  higher in the regions  $r > 20$  cm, which is ascribed mainly to differences in the geometry and material description between the two codes.

While the colour plots and histograms illustrated above are useful for information dissemination within the collaboration, more important to the detector sub-systems are tables of values. As an example, given in Table 6 are the  $\Phi_{\text{eq}}^{\text{Si}}$ , TID and  $\Phi_{20}^{\text{had}}$  values in the different module locations of the IBL.

#### 4.4.1.3 Comparison of simulated predictions with measurements

The FLUKA and GEANT4 simulations on ATLAS provide crucial input into modelling radiation effects. Comparisons with measurements gives an indication of the simulation uncertainties which in turn allows future simulation accuracies to be evaluated. Section 5 describes in detail some of the measurements made on ATLAS and their comparison with model predictions. As an example, leakage current measurements from some four thousand SCT detector modules are combined to produce the plot given in Fig. 25. Differences between the predictions and measurements are typically less than 20%. However, larger differences are being observed in the outer Pixel barrel layers, some  $\sim 50\%$  higher than the

<sup>1</sup>A reasonable approximation for pp collisions at the LHC and  $|\eta| < 3$ .

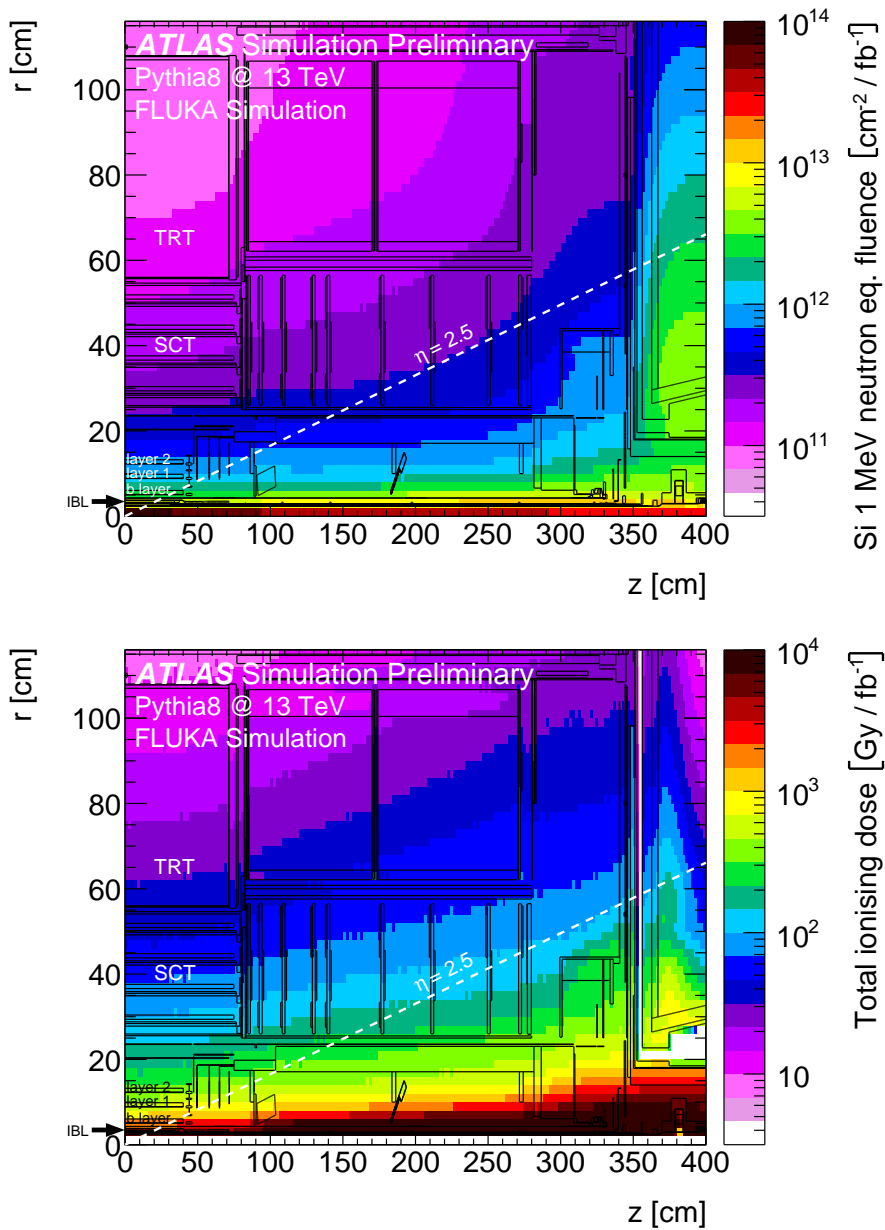


**Fig. 23:** The 1 MeV neutron equivalent fluence (top) and total ionizing dose (bottom) in the ATLAS inner detector. The minimum-bias pp events are simulated with ATLAS tuned Pythia8 at 13 TeV centre-of-mass energy and a predicted inelastic cross-section of 78.4 mb. Particle tracking and interactions with material are simulated with the FLUKA 2011 code using the Run 2 geometry description of the ATLAS detector.

simulated predictions. In general this is more of a concern to experiments, when the simulations under predict the impact of radiation. The IBL and Pixel measurements and comparison with simulations are described in Section 5.

In addition to the Pixel and SCT sensor measurements, ATLAS also installed a radiation monitoring system. The so-called RadMon system [26, 27] consists of sensors at 14 locations inside the ID volume. In addition to  $\Phi_{\text{eq}}^{\text{Si}}$ , measurements of TID are made with the RadMons, which cannot be done with the silicon detector systems. These measurements and comparisons with simulated predictions are shown in Fig. 26. It can be seen that the FLUKA and GEANT4 predictions agree with each other,



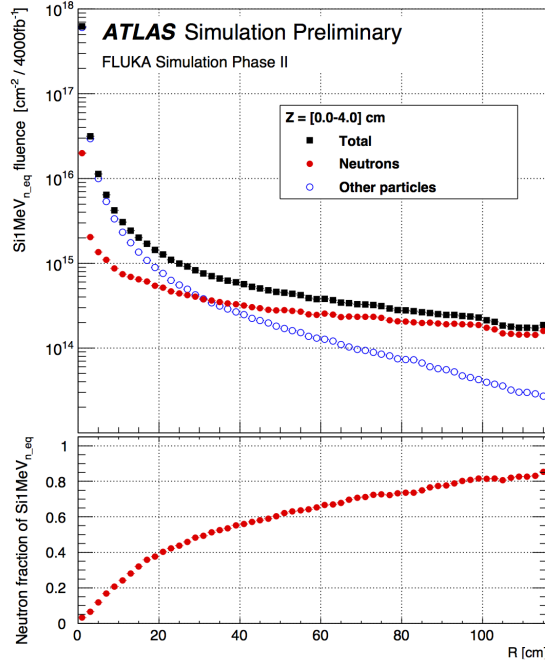


**Fig. 24:** Radial dependence of  $\Phi_{\text{eq}}^{\text{Si}}$  at  $z = 0$  as predicted by FLUKA. The total  $\Phi_{\text{eq}}^{\text{Si}}$  is separated into the contribution from neutrons and all other particles.

**Table 6:** Fluence and dose values in the ATLAS IBL detector system predicted by FLUKA, based on 50 000 events. For  $\Phi_{20}^{\text{had}}$ , the assumed instantaneous luminosity is  $10^{34} \text{ cm}^{-2} \text{ s}^{-1}$ .

IBL module	Sensor type	$z$ position (cm)	$\Phi_{\text{eq}}^{\text{Si}}$ ( $\times 10^{11} \text{ cm}^{-2} / \text{fb}^{-1}$ )	TID ( $\text{Gy} / \text{fb}^{-1}$ )	$\Phi_{20}^{\text{had}}$ ( $\times 10^6 \text{ cm}^{-2} \text{ s}^{-1}$ )
0	planar	2.08	$62.5 \pm 0.4$	$2897 \pm 24$	$83.4 \pm 0.4$
1	planar	6.23	$61.2 \pm 0.3$	$2901 \pm 23$	$85.0 \pm 0.4$
2	planar	10.38	$59.7 \pm 0.3$	$2917 \pm 23$	$87.5 \pm 0.4$
3	planar	14.53	$58.0 \pm 0.3$	$2983 \pm 26$	$89.0 \pm 0.5$
4	planar	18.68	$56.6 \pm 0.3$	$3015 \pm 25$	$89.6 \pm 0.5$
5	planar	22.83	$55.6 \pm 0.4$	$3083 \pm 27$	$89.4 \pm 0.5$
6	3D	25.94	$55.2 \pm 0.4$	$3126 \pm 32$	$89.8 \pm 0.6$
7	3D	28.00	$55.5 \pm 0.4$	$3182 \pm 34$	$90.6 \pm 0.6$
8	3D	30.07	$55.0 \pm 0.4$	$3191 \pm 34$	$90.4 \pm 0.6$
9	3D	32.13	$55.7 \pm 0.4$	$3308 \pm 36$	$91.0 \pm 0.6$

but overestimate compared with the measurements. Given the measurement uncertainties, the level of agreement is considered reasonable, being somewhat worse for the RadMon in the cryostat location.

In the original ATLAS design studies, ‘safety factors’ were introduced to reflect the uncertainties in simulating radiation backgrounds at the unprecedented centre-of-mass collision energy and luminosities. These were used for the testing and qualification of technologies for application in radiation environments. For example, in the testing and procurement of electronics, safety factors of 3.5 (5.0) were applied to the simulated radiation levels for TID ( $\Phi_{\text{eq}}^{\text{Si}}$ ,  $\Phi_{20}^{\text{had}}$ ). A taskforce review in 2013 concluded it was reasonable to reduce these safety factors to 1.5 for all three radiation quantities.

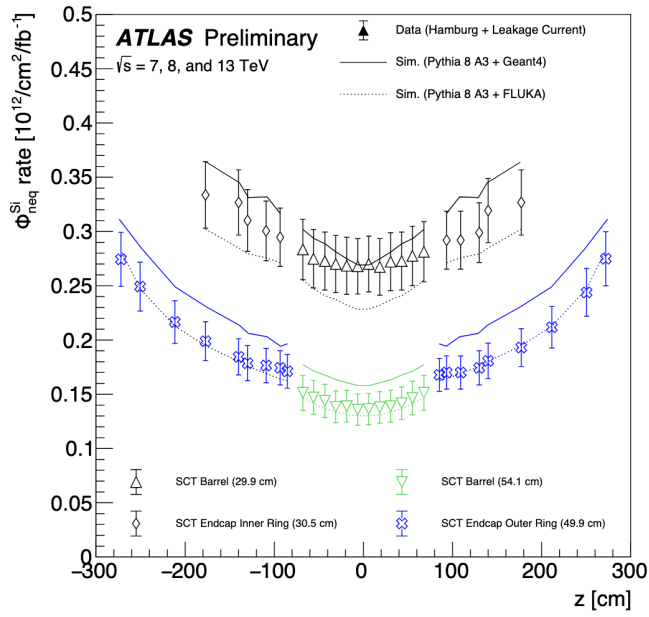


**Fig. 25:** Comparison of measured and simulated leakage current in the innermost and outermost SCT barrel and endcap layers. The simulations are based on FLUKA or GEANT with the Hamburg annealing model.

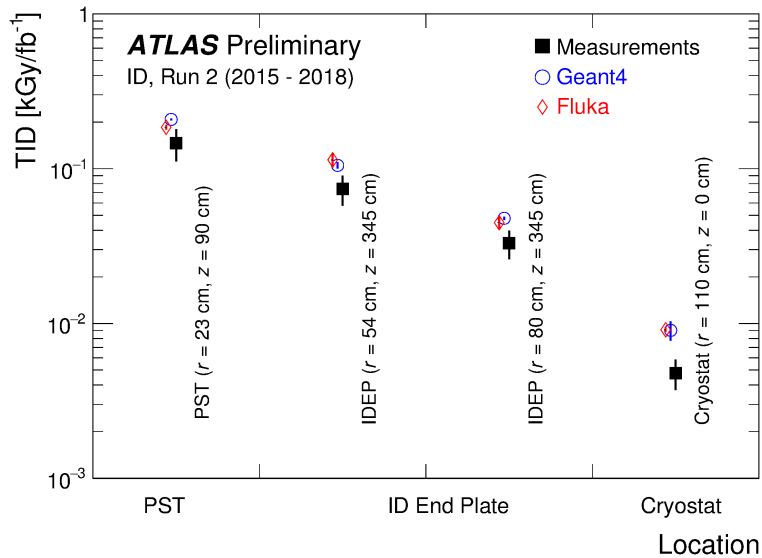


**Fig. 26:** Comparison of measurements with RadMon monitors and simulated TID at several locations inside the ID volume. One set of monitors is close to the IP, fixed on the pixel support tube (PST). Two sets are at different radii on the ID end plate, next to the endcap calorimeter, and a fourth set on the wall of the cryostat of the solenoid.

## 4.4.2 CMS

### 4.4.2.1 CMS simulation set-up

CMS typically uses FLUKA for radiation background simulations although MARS is used on occasion when quick turnaround simulations are required. The FLUKA simulation infrastructure is maintained by the Beam Radiation Instrumentation and Luminosity (BRIL) Project. FLUKA simulations are performed using the CERN Batch Service.

### 4.4.2.2 CMS FLUKA geometry description

In order to predict the radiation levels inside the CMS detectors, the complete detector and experimental cavern must be represented. The CMS FLUKA model includes the detector systems, shielding elements, services and beam-line components, the cavern floor and walls, and basic representations of cavern elements (main supports structures and electronics racks). The level of detail for the CMS FLUKA model inner detectors in terms of material composition and spatial resolution of regions is similar to that of the ATLAS FLUKA model.

Figure 27 shows the inner detector region as described in the FLUKA geometry. The central detectors are constructed with cylindrical shapes, and simulation results are therefore typically symmetric around the azimuthal angle  $\phi$ , reducing necessary simulation time to obtain results with a small statistical uncertainty. For most predictions related to radiation damage, accurate results are produced so long as the total material radiation and interaction lengths are correctly implemented. However, an increasingly detailed representation of various structures is required so that localized effects are simulated in regions near the damage threshold. This often includes the implementation of  $\phi$  asymmetric structures, for example, near the tracker bulkhead and LHC vacuum equipment. Advances in computing and use of batch computing means that corresponding results produced in a finer spatial binning structure are still possible within a reasonable time frame.

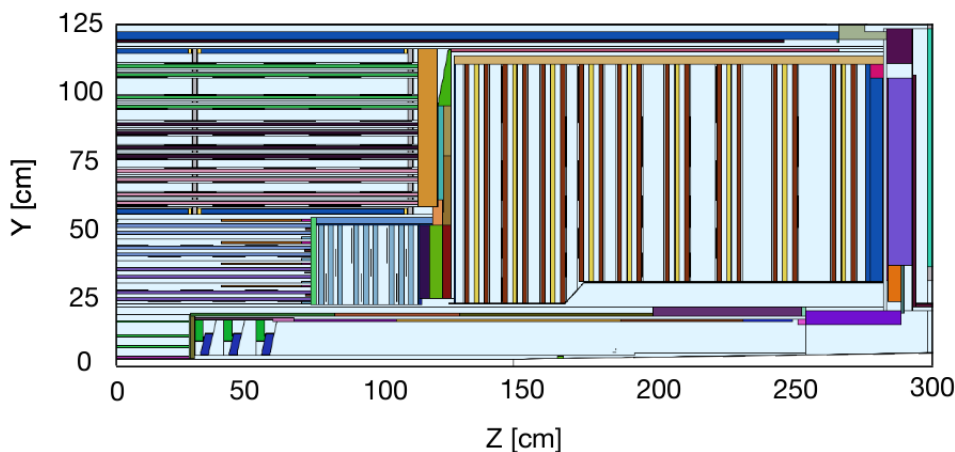


**Fig. 27:** A  $Z - Y$  cut of the tracker region in the CMS FLUKA model

The CMS FLUKA geometry is frequently updated to include actual changes to the detector configurations, such as new shielding and beam pipe elements as well as to make general improvements to the representation of existing components. Future detector geometries are updated as upgrade designs evolve and several geometry models for past detector configurations are maintained for benchmarking purposes.

## 4.4.2.3 CMS FLUKA fluence and dose predictions

Figure 28 shows all particle contributions to the  $\Phi_{\text{eq}}^{\text{Si}}$  and absorbed dose in the CMS inner detector resulting from proton–proton collisions. Here,  $R$  is the radial distance from the beamline and  $Z$  the distance from the IP following the direction of the beamline, and the results are averaged over the full  $\phi$  range. In standard operation, collisions are the main source of radiation in the CMS central detectors and contributions from the LHC beam halo, or ‘beam induced background’, can be considered negligible. At the time of writing, estimates of the  $\Phi_{\text{eq}}^{\text{Si}}$  use the in-built weighting factors for NIEL damage included in the FLUKA code.

The radiation field in the tracker volume is influenced by the 3.8 T magnetic field, the scattering on tracker material and vacuum chamber elements, as well as the backscattering from the surrounding

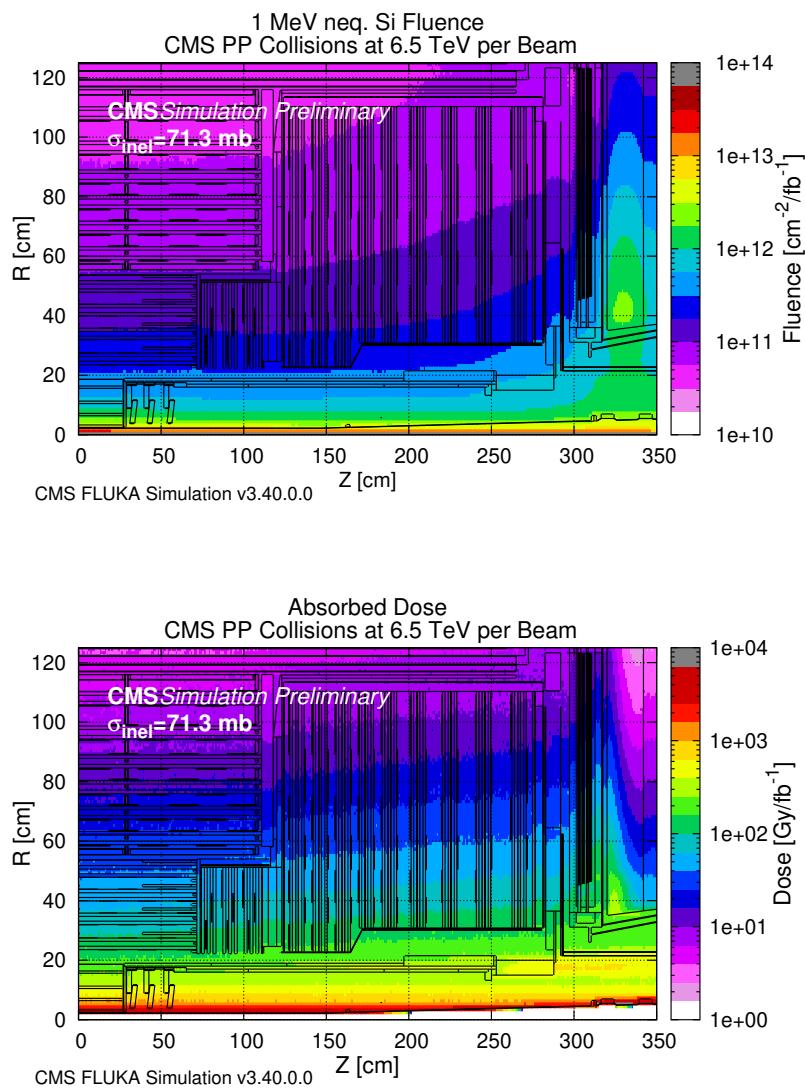


**Fig. 28:** The 1 MeV neutron equivalent fluence (top) and absorbed dose (bottom) in the CMS inner detector. The minimum-bias pp events are simulated with DPMJET-III at 13 TeV centre-of-mass energy and results are normalized to 71.3 mb inelastic cross-section. Simulations were performed with the FLUKA 2011 code using a Run 2 geometry model of CMS representing the 2018 configuration.

heavier detector elements, in particular the electromagnetic calorimeter crystals of the ‘ECAL endcap’ situated at approximately 3.2 m in  $Z$ . Figure 29 shows the relative contributions of various particle types to the  $\Phi_{\text{eq}}^{\text{Si}}$  as a function of radius at two  $Z$  locations. The detectors exposed to the highest levels of total  $\Phi_{\text{eq}}^{\text{Si}}$  are the pixel barrel which is situated around the IP and extends from a radius of 3.0 cm to 16.0 cm and the forward pixel regions which are situated between 29 cm and 60 cm in  $Z$  from the IP and extend into the  $|\eta| > 2.5$  range. Here,  $\Phi_{\text{eq}}^{\text{Si}}$  is dominated by the pion component. In the remaining tracker region, the high eta range in the tracker endcap (TEC) and layers close to the ECAL endcap at low radius are exposed to the highest  $\Phi_{\text{eq}}^{\text{Si}}$  rates.

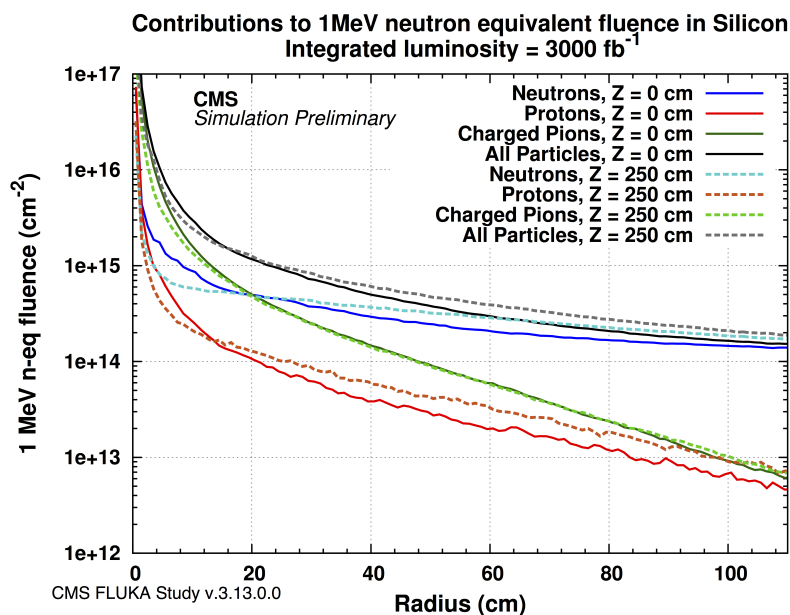


**Fig. 29:** Value of “ $\Phi_{\text{eq}}^{\text{Si}}$ ” in the CMS tracker region estimated using the 2011 FLUKA code and a Run 2 geometry model. The minimum-bias pp events are simulated with DPMJET-III at 14 TeV centre-of-mass energy and results are normalized to 71.3 mb inelastic cross-section. The “All Particles” curve shows the total amount of  $\Phi_{\text{eq}}^{\text{Si}}$ . The Neutrons, Protons, and Charged Pions curves show the contribution to the  $\Phi_{\text{eq}}^{\text{Si}}$  only from the respective particles.

#### 4.4.2.4 Comparison of simulated predictions with measurements

Data that can be used for comparison with simulation include measurements of detector degradation; direct data from the subdetectors, which require special triggers and more complex analysis; measurements with passive and active radiation monitoring systems installed by the CMS BRIL project or other CERN groups; and measurements of the residual radiation field from activated components.

Section 5 describes measurements of the leakage current and depletion voltage in the CMS pixel and strip detectors and their comparisons with predictions based on FLUKA simulations and damage models. The leakage current, measured for each layer in the strip detector, and predictions agree with the data within 20%. For depletion voltage data and corresponding predictions, agreement is generally within 10%.

Whilst not the optimal for benchmark of  $\Phi_{\text{eq}}^{\text{Si}}$ , successful comparisons of FLUKA predictions with measurements of the residual radiation field from activated material in the tracker and central beampipe regions [28, 29] provide confidence in the relevant parts of the simulation set up for fluence and dose predictions, i.e., the production and transport of prompt radiation and the representation of materials in the CMS geometry model.

RAMSES ionization chamber monitors [30] installed by the HSE/RP group have been used successfully to benchmark energy deposition at various locations in the CMS experimental cavern with predictions and measurements being well within a factor 2 [28], a reasonable agreement for the outer cavern locations. Comparisons of FLUKA predictions with measurements from LHC RadMons installed by the EN/STI group for the high energy hadron (HEH) fluence, TID, and  $\Phi_{\text{eq}}^{\text{Si}}$  at the cavern walls seem promising. However, remote switching ability between two modes for measuring either HEH or thermal neutron fluence is necessary for provision of independent data which currently require some FLUKA input. This will be available for Run 3.

### 4.4.3 LHCb

The LHCb experiment uses FLUKA for simulating radiation background in the spectrometer and detector cavern. The geometry description is simplified compared to the real detector, but contains the most relevant parts of all subdetectors, the LHC tunnel (with magnets) and support structures. The geometry has been continually updated and improved since its first implementation in the early phase of the experiment.

A set of radiation detectors were installed in the LHCb experimental area to measure different aspects of its radiation environment, allowing comparisons with the FLUKA predictions for TID and 1 MeV neutron fluence equivalent ( $\Phi_{\text{eq}}^{\text{Si}}$ ). The neutron equivalence fluence simulated in the inner part of the detector is shown in Fig. 30. The main source of particle radiation is prompt production of particles in proton–proton collisions. This component is dominant in silicon VELO sensors which are situated at 8 mm from the interaction point. Further away from the interaction point particles produced in secondary interactions in the detector material become more dominant.

The radiation field in the LHCb spectrometer has a strong radial dependence. This is especially visible in the VELO sensors, where the fluence increases by an order of magnitude across the sensor radius, see Fig. 31 (left). During Run 1 and Run 2 the LHCb spectrometer collected an amount of data corresponding to  $3.22 \text{ fb}^{-1}$  and  $6 \text{ fb}^{-1}$  of integrated luminosity, respectively. The evolution of  $\Phi_{\text{eq}}^{\text{Si}}$  is depicted in Fig. 31 (right). This distribution shows the differences between sensors situated at different  $z$  positions along the beam line. Considering the strong  $\Phi_{\text{eq}}^{\text{Si}}$  dependence on radius  $r$ , it was noted that the fluence in the inner part of the sensors reached almost  $6.7 \times 10^{14} \text{ cm}^{-2}$ .

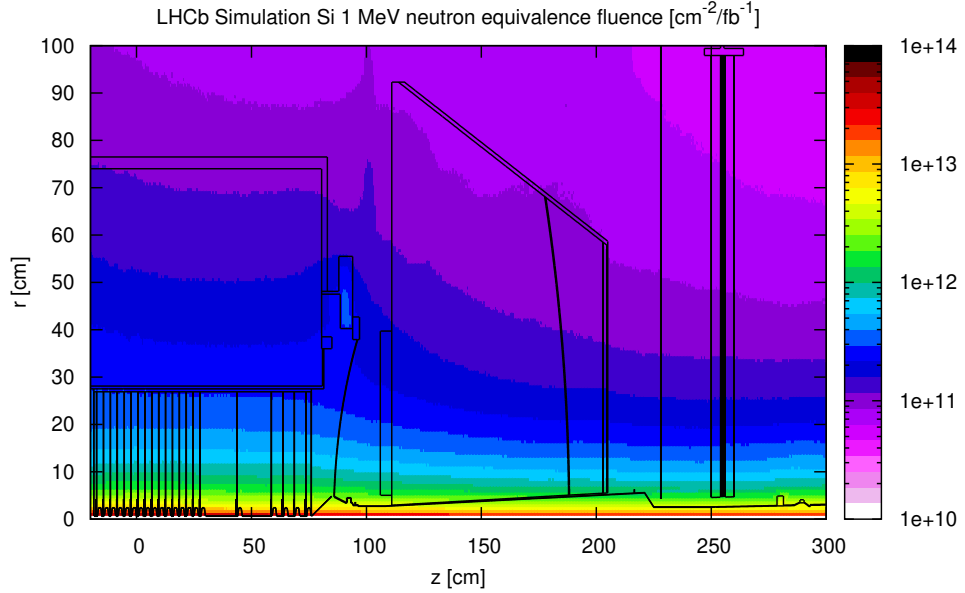


**Fig. 30:** Value of  $\Phi_{\text{eq}}^{\text{Si}}$  in the LHCb trackers. The VELO sensors are perpendicular to the beam line and are visible in the bottom left corner.

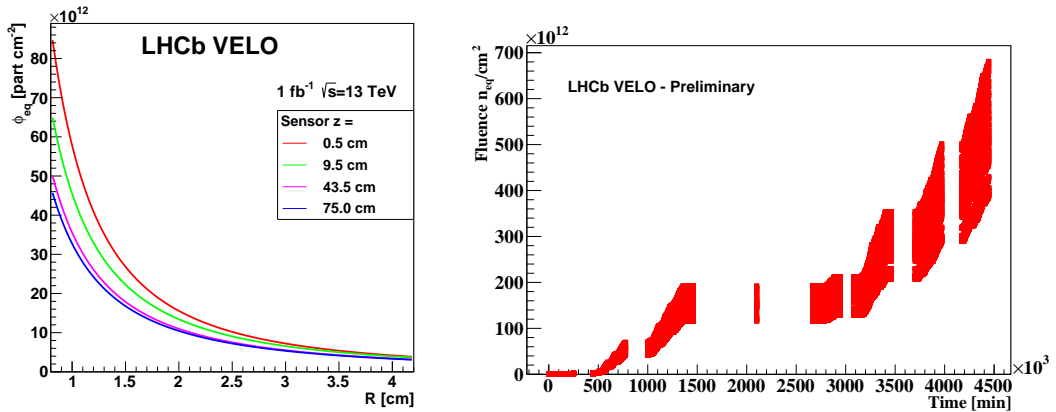


**Fig. 31:** Left: Radial dependency of the FLUKA simulation of  $\Phi_{\text{eq}}^{\text{Si}}$  at a few representative LHCb VELO sensor positions. Right: Simulation of the evolution of  $\Phi_{\text{eq}}^{\text{Si}}$  in the inner part ( $0.8 < R < 1.1$  mm) in the LHCb VELO sensors during Run 1 and Run 2. Points represent the sensors situated at different  $z$  positions. The integrated luminosity delivered to the LHCb spectrometer reached  $10 \text{ fb}^{-1}$  of data.

#### 4.4.4 ALICE

Given the requirement to run at reduced luminosity, the fluence seen by the innermost layer of the ALICE pixel detector, placed at a radius of  $R = 3.9$  cm from the beam axis, was significantly lower with respect to the other LHC pixel detectors ( $\Phi_{\text{eq}}^{\text{Si}} \sim 3.2 \times 10^{11}/\text{cm}^2$  integrated throughout Run 1 and Run 2). Although these levels are not very severe, compared, for instance, with the levels in ATLAS and CMS, all components used in the ALICE inner tracking system (ITS) design were tested for their radiation hardness to levels exceeding significantly the expected doses, and full radiation tolerant technologies have been used throughout the system for critical components, such as the front-end electronics. In particular, the chips of the two innermost layers of the ITS detector were qualified for a radiation in excess of 10 Mrad [31]; this explains the extremely low failure rate observed, even though radiation effects were not completely absent, as reported in Ref. [32].

Single event upset (SEU) events have also been observed in the silicon strip detector, in particular affecting the SRAM FPGA of the front-end read out modules (FEROM) [32]. Figure 32 shows the integrated number of SEUs since 2015, together with the integrated fluence of high-energy hadrons (HEH), measured by a RadMon sensor installed near the FEROM crate. No SEUs were expected, since the FEROM modules are located in the experiment cavern in a region where the TID at the end of Run 2 was 0.34 krad. Anyway, the linear correlation between SEU occurrences and fluence indicates that the SEU cross-section did not increase during Run 2. As mitigation measures, after LS1 a radiation tolerant PROM was used and a firmware upgrade allowing faster FPGA reload was implemented.

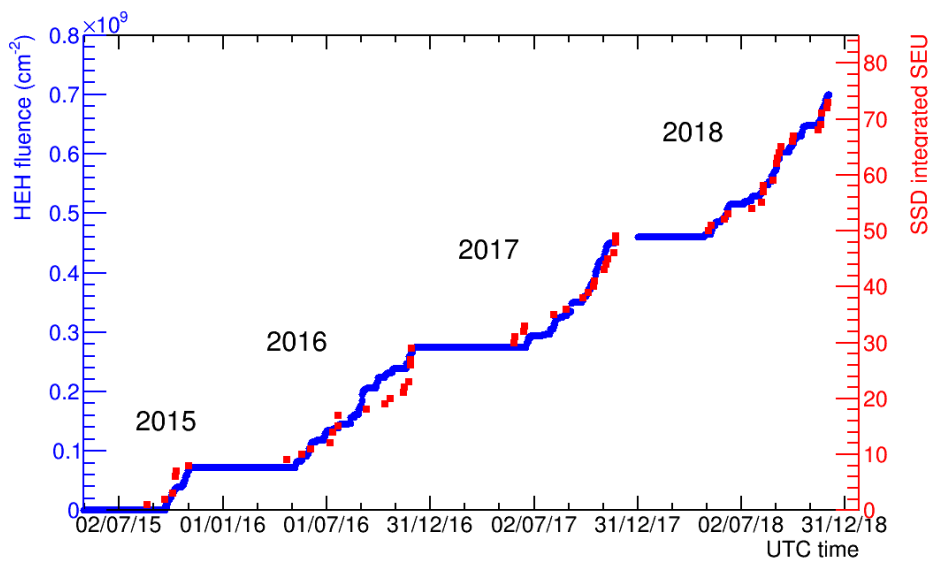


**Fig. 32:** Observed SEU occurrences in the SSD front-end readout modules and high-energy hadron fluence at the modules position, as a function of time

Simulations of the radiation environments were focused initially only on beam losses, in particular during injection, since ALICE is close to the Beam 1 transfer line from the SPS into the LHC. During Run 1, however, as explained in Section 4.4.4.1 below, a degradation of the vacuum conditions in the Long Straight Section 2 led to a new detailed study of the beam-induced background [33]. More recently, in view of the comprehensive upgrade planned for Run 3, when the experiment will face increasing collision rates, new studies have been performed [34], in particular to assess the radiation load of the new ITS, the first large scale application of the monolithic active pixel sensor in a HEP experiment. The radiation simulations for the ALICE experiment are performed within the AliRoot [35] framework, which provides a detailed geometry and material description of all detector layers, support structures, and beamline elements inside the experimental area. Electric and magnetic field maps are processed



as well. Particle transport is performed with FLUKA [4, 5]. The transport cuts for the particle species are adjusted region by region according to their importance in order to optimize the computing time. The lowest cuts are used in the central barrel detectors, while in the outer regions these cuts are raised considerably in order to save CPU time. The lowest kinetic energy cutoff for photon, electron, neutral, and charged hadron and muon transport is set to 1 keV and down to thermal energies of 293 K for neutron. The threshold for electron and muon delta-ray production is 30 keV, as well as for electron and muon bremsstrahlung and for electron pair production by muons.

The simulations are based on 50 000 minimum-bias proton–proton events at a centre-of-mass energy of 5.5 TeV, simulated using the PYTHIA6 event generator (Perugia-2011 tune). The 1 MeV neutron equivalent fluence ( $\Phi_{\text{eq}}^{\text{Si}}$ ) and the TID are the numbers that determine the long-term radiation damage of sensors and electronics. The rate of hadrons with a kinetic energy  $> 20$  MeV determines the rate of stochastic failures, like single event upsets in the microelectronics circuitry. The fluence of all the charged particles is not directly linked to radiation-induced effects; nevertheless, it determines the detector occupancy and influences track reconstruction and particle identification and was therefore calculated along with the above mentioned quantities. The FLUKA USRBIN function, that allows the distribution of one or several quantities of interest to be scored in a regular spatial structure independent from the geometry, is used in the calculations. All results were obtained by superimposing a  $r - z$  cylindrical mesh, with the cylinder axis parallel to the  $z$ -axis, on top of the ALICE geometry; the scored quantities are averaged along the azimuthal angle  $\varphi$ . Results from the USRBIN function are normalized per unit volume and per unit primary weight. Different meshes were defined to score the relevant quantities with the appropriate granularity. The bin size ranges from  $1 \text{ mm} \times 5 \text{ mm}$  for the innermost layers of the silicon detectors to  $1 \text{ cm} \times 2.5 \text{ cm}$  for the outermost ALICE detectors.

The dose and the neutron equivalence fluence simulated in the inner part of the detector are shown in Fig. 33 for the whole Run 1 and Run 2 physics program. At positions with  $-100 < z < 250 \text{ cm}$ , the radiation numbers are dominated by primary tracks originating from the interaction point. At  $z < -100 \text{ cm}$  the front absorber of the muon spectrometer is stopping hadrons that are pointing towards the muon system, which leads to a decrease of the TID but an increase of the hadron fluence due to the lateral escape of neutrons. The innermost ALICE detectors are exposed to a TID close to a few tens of krad and a fluence up to  $10^{11} \text{ cm}^{-2}$ .

#### 4.4.4.1 Contribution of beam-gas background

The moderate interaction rates in Run 1 and Run 2 meant that ALICE had the most unfavourable ratio of collision rate over background rate. In addition, after the beam intensity ramp up in 2011, a degradation of vacuum upstream of the UX25 was observed, producing a large beam-gas background reaching  $\sim 20\%$  of the collision rates.

The machine-induced background is mainly ascribed to inelastic interactions of beam protons with residual gas molecules in the so-called long straight section (LSS2). The observed nearly linear correlation between background rates measured in ALICE and the product of the bunch intensity times the average vacuum pressure in the LSS2 provides a further confirmation of this assumption. The pressure in the LSS2 easily exceeded the  $10^{-8}$  mbar both in the 2011 and 2012 pp fills with more than 1000 circulating bunches. In the UX25 cavern, on the contrary, it has been measured to be constantly around  $1\text{--}0.5 \times 10^{-10}$  mbar, below  $10^{13}$  molecules/m<sup>3</sup> hydrogen-equivalent gas density. The contribution of beam-gas interactions inside the cavern can therefore be neglected for the computation of the beam background simulations. Due to the proportionality of the dynamic gas pressure and the TDI outgassing to the beam intensity, their relevance for Pb–Pb as well for p–Pb runs is orders of magnitude lower than for pp, as confirmed by ALICE measurements. Beam-gas interactions were simulated by distributing proton–H<sub>2</sub> inelastic interactions along the LSS2 according to a detailed pressure profile provided by the CERN TE-VSC group in 2012 and based on the pp reference fill 2736. So far, only the machine-induced background from the IR2 left side of ALICE has been simulated; however, due to the presence of the beam 1 injection

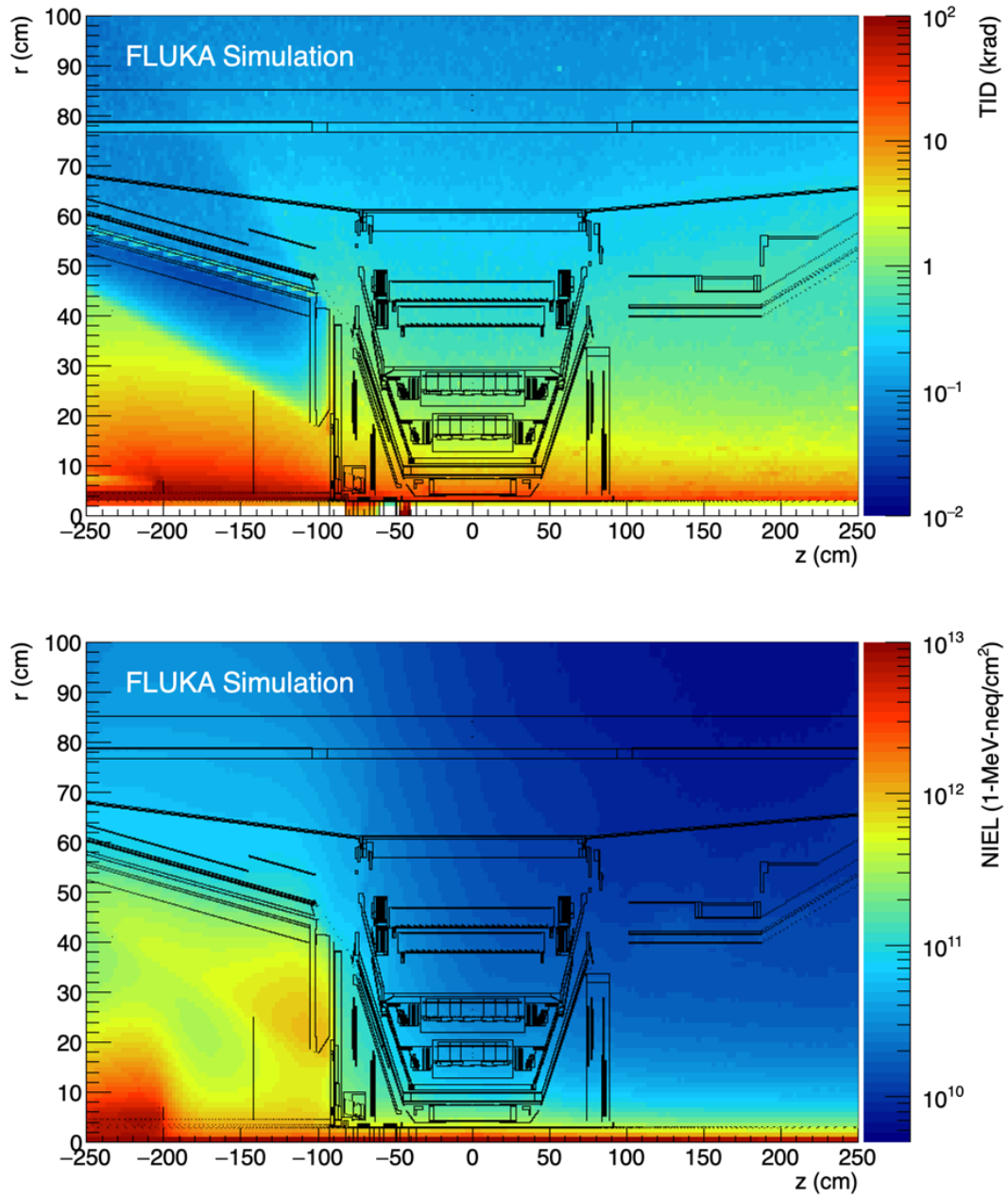


**Fig. 33:** TID (top) and  $\Phi_{\text{eq}}^{\text{Si}}$  (bottom) in ALICE. The values correspond to the Run 1 and Run 2 physics programs.

line and the TDI, this background is by far the most dominant one in ALICE.

The p–H<sub>2</sub> interactions were computed with DPMJET [9] and the total rate of inelastic interactions in the LSS2 was calculated from the integral of the pressure profile. The cascade of the p–H<sub>2</sub> collisions were calculated using a detailed FLUKA modelling of the LSS2 (from UJ23 until ALICE cavern) performed by the LHC FLUKA Group in 2012 with a very accurate vacuum layout. A transport cutoff of 20 MeV has been applied in order to save CPU time. All the particles reaching the scoring plane 20 m away from the IP2 are then transported using FLUKA. In the present simulation 50 000 primary beam-gas interactions have been considered.

#### 4.4.4.2 Comparison of simulated predictions with measurements

A comparison between simulated and measured dose in ALICE was performed by means of radiation monitors (RadMon) in order to validate the radiation calculations. The RadMon system has been developed by the CERN Engineering (EN) department; it includes RadFETs for TID measurements, silicon p–i–n diodes for the 1 MeV equivalent neutron fluence, and SRAM memories for the high-energy hadron and thermal neutron fluence. In Fig. 34, the trend versus time of the TID measured during the 2017 pp fills by the RadMon sensor called D12, located 480 cm away from the IP2 and 34 cm from the beam axis, is reported and compared with prediction from simulation. The expected TID is obtained by multiplying the ALICE delivered luminosity by the inelastic pp cross-section at  $\sqrt{s} = 13$  TeV and the simulated TID per pp collision at the sensor location scaled for the average charged-particle multiplicity density ratio  $(dN_{\text{ch}}/d\eta(13\text{TeV})) / (dN_{\text{ch}}/d\eta(5.5\text{TeV}))$ . The measured TID is well reproduced by the expected dose due to genuine pp collisions at IP2, thus implying a negligible contribution from machine-induced background to the total dose, which is expected considering the low beam-gas rates measured in ALICE throughout the 2017 and the RadMon sensor location.

A further comparison was performed with 2018 pp data after having moved the D12 sensor closer to the beam axis and downstream of the massive vacuum equipment at  $z \sim 4$  m from IP2 (new location at 340 cm away from the IP2 and at 20 cm from the beam axis). The comparison is reported in Fig. 35. To evaluate the radiation load due to the machine-induced background, an estimation of the total number of primary beam-gas interactions in the LSS2 (left side) throughout the 2018 pp fills is needed. This is estimated as the integral of the trend versus time of the average vacuum pressure in the LSS2, evaluated as the arithmetic average of pressure in the TDI and in the inner triplet ITL2, multiplied by the beam 1 intensity, the LHC revolution frequency, and the probability that a proton traversing the LSS2 has an inelastic nuclear interaction with a residual gas nucleus. The latter was obtained based on p–H<sub>2</sub> interactions computed with DPMJET and on the Run 1 pressure profile normalized to the Run 2 average vacuum pressure. The expected dose was then derived by multiplying the expected total beam-gas interactions in 2018 by the simulated dose per beam-gas interaction at the sensor location. The measurements can be reproduced by simulation including pure pp collisions at the IP and beam gas from LSS2. The dose of  $2.0 \times 10^{-13}$  krad per pp collision shown in Fig. 35 is the value that better reproduces the TID measured by the D12 sensor during the 2018 Pb–Pb fills, where the contribution of beam gas to the total dose is expected to be negligible because of the low intensity of the Pb beams, while  $2.0 \times 10^{-13}$  krad per beam-gas interaction is the outcome of our simulation. The overall contribution from beam gas in 2018 is, however, expected to be very low, thus making it difficult to draw firm conclusions on the reliability of our beam-gas simulation since the measurements can be also reproduced assuming a negligible contribution from machine-induced background even during the pp fills. However, such comparison suggests that the aforementioned calculations can be interpreted as an upper limit for machine-induced background contribution to the total dose.

#### 4.4.4.3 Detector specifications for Run 3 and Run 4

After the second LHC Long Shutdown, the luminosity with lead beams will gradually increase to an interaction rate of 50 kHz, leading to a data rate that the current ALICE electronics and detectors cannot process. The upgrade of the experiment is mainly focused on increasing the readout rate capability to record the full 50 kHz of Pb–Pb interactions. A fundamental element of the upgrade strategy is the new, high-resolution, ultra-light ITS based on MAPS (monolithic active pixel sensor) [36]. The ALPIDE chip is a 15 mm  $\times$  30 mm large MAPS, implemented in a 180 nm CMOS imaging sensor process by TowerJazz<sup>2</sup>. Material budget constraints require the usage of sensors thinned to 50  $\mu\text{m}$  in the IB, while 100  $\mu\text{m}$  thick sensors are employed in the outermost layers. The novel implementation of deep p-well in the process allows full CMOS circuitry within the pixel matrix, still keeping full charge collection efficiency [37–39]. A very low power consumption of less than 40 mW/cm<sup>2</sup> has been achieved thanks to

<sup>2</sup>Tower Jazz, <http://www.jazzsemi.com>

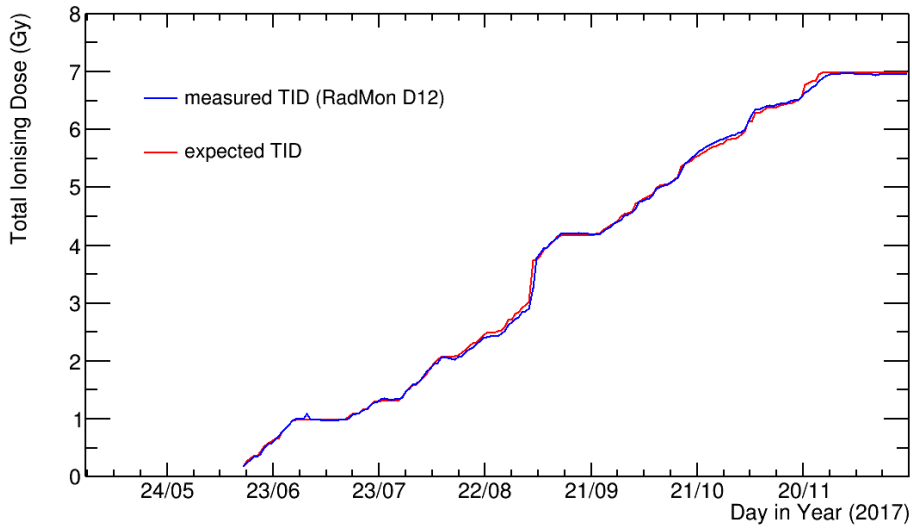


**Fig. 34:** Trend of the accumulated TID during 2017 from measurements by RadMon sensor (blue line) and simulations (red line).

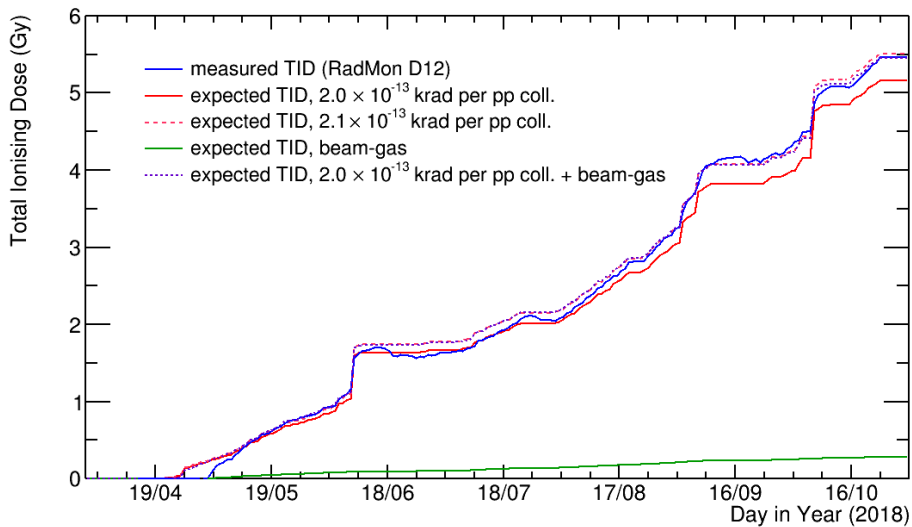


**Fig. 35:** Trend of the accumulated TID during 2018 from measurements by RadMon sensor (blue line) and simulations.

the integration of continuously active low-power front end into each pixel and in-matrix zero suppression circuit ('Priority encoder'). The sensor is segmented into  $512 \times 1024$  pixels of  $29 \mu\text{m} \times 27 \mu\text{m}$ ; a periphery circuit region of  $1.2 \text{ mm} \times 30 \text{ mm}$  implements control, and readout functionalities.

From the doses and fluences simulated for IP collisions and the background assumptions, the specifications for the ALICE detector systems in Run 3 and Run 4, including safety factors, can be derived, taking into account the recent results on measured multiplicities for Pb–Pb, pp, and p–Pb collisions. Results for different colliding systems and energies are derived by scaling the simulated values by the average charged-particle multiplicity density reported in Table 7, where an extended running scenario for

**Table 7:** Extended running scenario for the ALICE operation after LS2;  $\int \mathcal{L}$  and  $L_{\text{peak}}$  stand for integrated and peak luminosity respectively,  $\sigma_t$  for inelastic cross-section, and  $\eta$  for pseudorapidity.

	<b>pp</b>	<b>p-Pb</b>	<b>Pb-Pb</b>
	14 TeV	5.5 TeV/NN	5.5 TeV/NN
$\int \mathcal{L}(\text{nb}^{-1})$	$2.5 \cdot 10^5$	1000	13
$L_{\text{peak}}(\text{cm}^{-2}\text{s}^{-1})$	$6.0 \cdot 10^{30}$	$1.0 \cdot 10^{29}$	$6.25 \cdot 10^{27}$
$\sigma_t$ (mb)	80	2000	8000
Peak rate ( $\text{s}^{-1}$ )	$4.2 \cdot 10^5$	$2.0 \cdot 10^5$	$5 \cdot 10^4$
Events	$2 \cdot 10^{13}$	$2.0 \cdot 10^{12}$	$10.4 \cdot 10^{10}$
$dN_{\text{ch}}/d\eta$	6.46	18.4	492.5
peak rate of tracks $N_{\text{ch}}/\eta$ ( $\text{s}^{-1}$ )	$2.7 \cdot 10^6$	$3.7 \cdot 10^6$	$25 \cdot 10^6$
total Nr. of tracks $N_{\text{tot}}/\eta$	$129.2 \cdot 10^{12}$	$36.8 \cdot 10^{12}$	$51.2 \cdot 10^{12}$

Run 3 and Run 4 even more ambitious than the plan reported in the ALICE Upgrade LOI [40] is shown, under the assumption that the shape of the  $dN_{\text{ch}}/d\eta$  distribution does not differ significantly for the different colliding systems. The charged-particle multiplicity densities at midrapidity have been obtained by scaling the ALICE measured multiplicities [41–44]. A scaling factor of  $s_{NN}^{0.15}$  ( $s_{NN}^{0.11}$ ) has been applied to Pb–Pb (p–Pb and pp) to obtain the values for the centre-of-mass energy of  $\sqrt{s_{NN}} = 5.5$  TeV. The last row in Table 7 represents the expected total number of charged particles per unit of pseudorapidity integrated for Run 3 and Run 4. Since the radiation load is directly correlated with the total number of produced particles, in this scenario the pp collisions would represent 59% of the total ionizing dose and high-energy hadron fluence, while p–Pb and Pb–Pb collisions account for 17% and 24%, respectively.

The sum of the two contributions (IP collisions and beam gas) gives the best estimate for the radiation load of ALICE, on top of which a safety factor ten was multiplied. Concerning the beam-gas collisions, an improvement of the vacuum conditions by a factor of 10 with respect to Run 1 is assumed, i.e., an average vacuum pressure of  $< 2.3 \times 10^{-9}$  mbar in the LSS2 around ALICE. The resulting numbers are shown in Table 8. With the extended running scenario, the TID contributions from collisions and beam-gas background are quite similar, while the NIEL is dominated by collisions. This is not surprising considering that the background consists almost entirely of electromagnetic radiation (mostly photons, then electrons).

**Table 8:** Specified radiation numbers for the 7 layers of the new ALICE ITS for a physics program of  $13 \text{ nb}^{-1}$  Pb–Pb +  $1 \text{ pb}^{-1}$  p–Pb +  $6 \text{ pb}^{-1}$  pp at 5.5 TeV +  $250 \text{ pb}^{-1}$  pp at 14 TeV collisions, assuming an operational efficiency of 77%, a vacuum pressure of  $2.3 \times 10^{-9}$  mbar in the Long Straight Sections around ALICE, and a safety factor of 10.

<b>Element</b>	<b>TID</b>	<b>1-MeV-neq</b>
	<b>(krad)</b>	<b>(<math>\text{cm}^{-2}</math>)</b>
ITS L0	5602	$5.78 \times 10^{13}$
ITS L1	3810	$3.97 \times 10^{13}$
ITS L2	2310	$2.58 \times 10^{13}$
ITS L3	130	$2.46 \times 10^{12}$
ITS L4	106	$2.17 \times 10^{12}$
ITS L5	36	$1.44 \times 10^{12}$
ITS L6	33	$1.40 \times 10^{12}$

## 4.5 Discussion and outlook

In this chapter we have shown how Monte Carlo particle event generators and particle transport codes have been used to successfully simulate radiation backgrounds in and around the LHC experiments. We showed how the proton–proton collisions are now well described by Monte Carlo events generators such as PYTHIA, with inelastic cross-sections and particle productions rates described at levels of precision typically less than 10%. The validation of the simulations by comparison with measurements has led to an improved understanding of the uncertainties involved. For example, in the initial design phase of ATLAS, factors of 2–5 were applied by some of the experiments to reflect the uncertainties in the simulations. Today, a factor 1.5 on simulated predictions of fluence and dose is used in HL-LHC upgrade studies. This in turn has enormous implications on the choice of technologies that can be used in the LHC experiment upgrades, which in turn has enormous cost benefits. An important caveat to this, however, is that the reliability and accuracy of the simulation results are highly dependent on the geometry and material description of the experiment implemented in the simulations. For radiation background studies the fine detail is often not required, but it is crucial to reproduce accurately the radiation and interaction lengths. A final comment on ‘lessons learned’ is relevant for detector upgrades in an experiment. It is vital to study the impact of introducing new detector systems and services into an existing experiment, otherwise unintended increases in radiation background levels can occur in some of the other systems leading to a reduction in detector lifetime.

## References

- [1] ATLAS Collaboration, *JINST* **13** (2018) P12006, doi:10.1088/1748-0221/13/12/P12006.
- [2] T. Sjöstrand, S. Mrenna, P. Skands, *JHEP* **05** (2006) 026, doi:10.1088/1126-6708/2006/05/026; *Comput. Phys. Comm.* **178** (2008) 852–867, doi:10.1016/j.cpc.2008.01.036.
- [3] S. Roesler, R. Engel, J. Ranft, The Monte Carlo Event Generator DPMJET-III, International Conference on Advanced Monte Carlo for Radiation Physics, Particle Transport Simulation and Applications (Springer, Berlin, 2001), pp. 1033–1038, doi:10.1007/978-3-642-18211-2\_166, arXiv:hep-ph/0012252.
- [4] G. Battistoni *et al.*, *Ann. Nucl. Energy* **82** (2015) 10, doi:10.1016/j.anucene.2014.11.007.
- [5] T.T. Bohlen *et al.*, *Nucl. Data Sheets* **120** (2014) 211, doi:10.1016/j.nds.2014.07.049.
- [6] I.L. Azhgirey and V.V. Talanov, MARS software package status, Proc. 17. Conference on Charged Particle Accelerators ([s.n.], Protvino, 2000), vol. 2, p. 184.
- [7] S. Agostinelli *et al.* [GEANT4 Collaboration], *Nucl. Instrum. Methods Phys. Res.* **A506** (2003) 250, doi:10.1016/S0168-9002(03)01368-8; J. Allison *et al.*, *IEEE Trans. Nucl. Sci.* **53** (2006) 270, doi:10.1109/TNS.2006.869826; J. Allison *et al.*, *Nucl. Instrum. Methods Phys. Res.* **A835** (2016) 186, doi:10.1016/j.nima.2016.06.125.
- [8] R. Engel, *Z.Phys.* **C66** 203 1995, doi:10.1007/BF01496594; R. Engel, J. Ranft, *Phys.Rev.* **D54** (1996) 4244, doi:10.1103/PhysRevD.54.4244, arXiv:hep-ph/9509373.
- [9] J. Ranft, *Phys. Rev.* **D51** (1995) 64, doi:10.1103/PhysRevD.51.64.
- [10] ATLAS Collaboration, *Eur. Phys. J.* **C76** (2016) 502, doi:10.1140/epjc/s10052-016-4335-y.
- [11] LHCb Collaboration, *Eur. Phys. J.* **C74** 2014 2888, doi:10.1140/epjc/s10052-014-2888-1.
- [12] CMS Collaboration, *Eur. Phys. J.* **C78** (2018) 697, doi:10.1140/epjc/s10052-018-6144-y.
- [13] ATLAS Collaboration, *Phys. Rev. Lett.* **117** (2016) 182002, doi:10.1103/PhysRevLett.117.182002.
- [14] [FLUKA web site](#), (CERN, Geneva), last accessed July 15 2020.
- [15] A. Capella *et al.*, *Phys. Rep* **236** (1994) 225, doi:10.1016/0370-1573(94)90064-7.
- [16] A. Ferrari and P.R. Sala, The physics of high energy reactions, Proc. Workshop on Nuclear Reaction Data and Nuclear Reactors Physics, Design and Safety, Eds. A. Gandini, G. Reffo (World Scientific, Singapore, 1998), pp. 424–532, doi:10.1142/9789814530385, ATL-PHYS-97-113.

- [17] A. Ferrari, P.R. Sala, A new model for hadronic interactions at intermediate energies for the FLUKA code, Proc. MC93 Int. Conf. on Monte Carlo Simulation in High Energy and Nuclear Physics Eds. P. Dragovitsch *et al.* (World Scientific, Singapore 1994), pp. 277-288, doi:10.1142/9789814534833.
- [18] A. Fassò *et al.*, **FLUKA: performances and applications in the intermediate energy range**, Proc. OECD / NEA Specialists' Meeting on Shielding Aspects of Accelerator, Targets and Irradiation Facilities, (OECD, Paris 1995), pp. 287-304.
- [19] A. Ferrari *et al.*, *Z. Phys.* **C71** (1996) 75, doi:10.1007/s002880050149, arXiv:nucl-th/9603010.
- [20] A. Ferrari *et al.*, *Z. Phys.* **C70** (1996) 413, doi:10.1007/s002880050119, arXiv:nucl-th/9509039.
- [21] C. Zeitnitz and T.A. Gabriel, *Nucl. Instrum. Meth.* **A349** (1994) 106, doi:10.1016/0168-9002(94)90613-0.
- [22] M. Huhtinen and F. Faccio, *Nucl. Instrum. Meth.* **A450** (2000) 155, doi:10.1016/S0168-9002(00)00155-8.
- [23] ATLAS Collaboration, **Summary of ATLAS Pythia 8 Tunes**, ATL-PHYS-PUB-2012-003 (CERN, Geneva, 2012).
- [24] J. Boudreau *et al.*, The GeoModel Toolkit for detector description, Proc. Computing in High Energy Physics and Nuclear Physics 2004, Eds. A. Aymar, J. Harvey, N. Knoors (CERN, Geneva, 2005), p. 353 doi:10.5170/CERN-2005-002.353.
- [25] ATLAS Collaboration *JINST* **3** (2008) S08003, doi:10.1088/1748-0221/3/08/S08003.
- [26] I. Mandić *et al.*, *IEEE Trans.Nucl.Sci.* **54** (2007) 1143, doi:10.1109/TNS.2007.895120.
- [27] I. Mandić *et al.*, First results from the online radiation dose monitoring system in ATLAS experiment, 2011 IEEE Nuclear Science Symposium Conference Record, Valencia, 2011, pp. 1107-1112, doi: 10.1109/NSSMIC.2011.6154582.
- [28] J. Wańczyk, **Measurements and estimates of the radiation levels in the CMS experimental cavern using Medipix and RAMSES monitors, and the FLUKA Monte Carlo code**, Master thesis, AGH Univ. Sci. Tech., Kraków, 2019.
- [29] D. Bozzato, **Simulations for the CMS radiation field: results for shutdown scenarios and benchmarks**, Laurea, Polytech. Univ. Milan, 2019.
- [30] G. Segura *et al.*, **RAMSES: the LHC radiation monitoring system for the environment and safety**, Proc. 10th Int. Conf. on Accelerator and Large Experimental Physics Control Systems (JACoW, Geneva, 2005), TH3B.1-3O.
- [31] ALICE Collaboration, *JINST* **3** (2008) S08002, doi:10.1088/1748-0221/3/08/S08002.
- [32] E. Botta, *PoS Vertex2019* (2020) 002, doi:10.22323/1.373.0002.
- [33] ALICE Collaboration, Performance of the ALICE Experiment at the CERN LHC, *Int. J. Mod. Phys. textbfA29* (2014) 1430044, doi:10.1142/S0217751X14300440.
- [34] A. Alici *et al.*, **Radiation dose and fluence in ALICE after LS2**, ALICE-PUBLIC-2018-012 (CERN, Geneva, 2018).
- [35] **ALICE Software Reference Manual**, (CERN, Geneva), last accessed July 25 2020.
- [36] ALICE Collaboration, *J. Phys.* **G41** (2014) 087002 doi:10.1088/0954-3899/41/8/087002.
- [37] G. Aglieri Rinella, *Nucl. Instrum. Methods Phys. Res.* **A845** 2017 583 doi:10.1016/j.nima.2016.05.016.
- [38] A. Di Mauro, *Nucl. Instrum. Methods Phys. Res.* **A936** 2019 625, doi:10.1016/j.nima.2018.10.047.
- [39] M. Šuljić, *JINST* **11**(2016) C11025, doi:10.1088/1748-0221/11/11/C11025.
- [40] ALICE Collaboration, *J. Phys.* **G41** (2014) 087001, doi:10.1088/0954-3899/41/8/087001.
- [41] ALICE Collaboration, *Eur. Phys. J.* **C68** (2010) 345, doi:10.1140/epjc/s10052-010-1350-2.
- [42] ALICE Collaboration, *Phys. Rev. Lett.* **110** (2013) 032301, doi:10.1103/PhysRevLett.110.032301.

- [43] ALICE Collaboration, *Phys. Rev. Lett.* **105** (2010) 252301, [doi:10.1103/PhysRevLett.105.252301](https://doi.org/10.1103/PhysRevLett.105.252301).  
[44] ALICE Collaboration, *Phys. Rev. Lett.* **116** (2016) 222302, [doi:10.1103/PhysRevLett.116.222302](https://doi.org/10.1103/PhysRevLett.116.222302).



## 5 Measurements of radiation damage on silicon sensors

*Editors:* A. De Cosa<sup>a</sup>, B. Nachman<sup>b</sup>, P. Collins<sup>c</sup>.

*Contributing authors:* J. L. Agram<sup>d</sup>, W. Barter<sup>e</sup>, M. Baselga<sup>f</sup>, M. Battaglia<sup>g</sup>, J. Beyer<sup>h</sup>, H. M. Borecka-Bielska<sup>i</sup>, D. Brzhechko<sup>j</sup>, A. De Cosa<sup>a</sup>, I. Dawson<sup>k</sup>, F. Djama<sup>l</sup>, F. Feindt<sup>m</sup>, A. Grummer<sup>n</sup>, M. Hoefkamp<sup>n</sup>, J. Hunt<sup>f</sup>, T. Kondo<sup>p</sup>, V. Lima<sup>q</sup>, A. Macchiolo<sup>j</sup>, J. Llorente Merino<sup>s</sup>, K. Mochizuki<sup>t</sup>, B. Nachman<sup>b</sup>, G. Sarpis<sup>u</sup>, S. Seidel<sup>n</sup>, J. Sonneveld<sup>v</sup>, S. Tsuno<sup>p</sup>, M. Vignali<sup>m</sup>, R. Wang<sup>w</sup>.

<sup>a</sup>ETH Zurich, Switzerland

<sup>b</sup>Lawrence Berkeley National Laboratory, USA

<sup>c</sup>CERN, Geneva, Switzerland

<sup>d</sup>Hubert Curien Pluridisciplinary Institute (IPHC) Strasbourg - Univ. de Haute-Alsace, France

<sup>e</sup>Imperial College London, United Kingdom

<sup>f</sup>Karlsruhe Institute of Technology, Germany

<sup>g</sup>University of California, Santa Cruz, USA

<sup>h</sup>Ludwig Maximilian University of Munich, Germany

<sup>i</sup>University of Liverpool, United Kingdom

<sup>j</sup>University of Zurich, Switzerland

<sup>k</sup>Queen Mary University of London, United Kingdom

<sup>l</sup>CPPM, Marseille, France

<sup>m</sup>Hamburg University, Germany

<sup>n</sup>University of New Mexico, USA

<sup>p</sup>KEK, Tsukuba, Japan

<sup>s</sup>Institute of High Energy Physics, Beijing, China

<sup>t</sup>University of Montreal, Canada

<sup>u</sup>University of Manchester, United Kingdom

<sup>v</sup>Nikhef, Amsterdam, Netherlands

<sup>w</sup>Argonne National Laboratory, USA

Non-ionizing energy loss introduces defects in the silicon lattice that modify the electronic properties of the bulk material. See Section 2.1 for a detailed discussion. As a result, the sensor leakage current increases and the electric field from an applied bias voltage is distorted. Electron–hole pairs from a minimum ionizing particle traverse the modified electric field and can be trapped in the silicon lattice defects. Measuring and modelling these effects is essential for informing detector operations, monitoring the radiation environment near the detector, tuning offline simulation algorithms, and making performance predictions for the future.

Sensor damage is characterized by the particle fluence  $\Phi$  and the goal of this section is to present measurements of a number of observables  $X$  and their response to  $\Phi$ ,  $dX/d\Phi$ . Comparing the responses of  $X$  across time is complicated by annealing effects and thermal histories across the detector systems can vary significantly. An additional complication is that the particle composition and energy spectra of the radiation backgrounds, discussed in Section 4, can vary substantially across different detector layers. Radiation damage in silicon is typically scaled to the 1 MeV neutron equivalent fluence ( $\Phi_{eq}^{Si}$ ), but this assumes the NIEL hypothesis, see Section 2.1.1, which is not always respected. Additional challenges with sensor measurements and their interpretation are discussed in Section 5.4. Below are the observables that have been studied by one or more of the LHC experiments.

---

This chapter should be cited as: Measurements of radiation damage on sensors, Eds. A. De Cosa, B. Nachman, P. Collins, DOI: [10.23731/CYRM-2021-001.59](https://doi.org/10.23731/CYRM-2021-001.59), in: Radiation effects in the LHC experiments: Impact on detector performance and operation, Ed. Ian Dawson,

CERN Yellow Reports: Monographs, CERN-2021-001, DOI: [10.23731/CYRM-2021-001](https://doi.org/10.23731/CYRM-2021-001), p. 59.

© CERN, 2021. Published by CERN under the [Creative Commons Attribution 4.0 license](https://creativecommons.org/licenses/by/4.0/).

1. *Leakage current*: the current measured across the sensor when applying a bias voltage independent of ionization from charged particles. The leakage current contributes to the noise and is relevant for module power consumption. This power will heat the module, which further increases the leakage current. In extreme cases, this can lead to *thermal runaway*, whereby the sensors quickly reach electrical breakdown.
2. *Depletion voltage*: the bias voltage such that nearly the entire sensor is depleted. After irradiation, the electric field can have regions of low field, so this concept is less well defined. It is usually measured by performing a high voltage scan and finding the point at which the collected charge, cluster size, or hit efficiency saturate. Unlike the leakage current, measuring the depletion voltage therefore usually requires active collisions in order to measure the collected charge. This is true for all subsequent measurements as well.
3. *Hit/Cluster efficiency*: the probability of minimum ionizing particle producing a signal in the sensor that is registered above threshold. Charge trapping shifts the deposited charge distribution to lower values and thus reduces the efficiency. The hit efficiency is the probability in a single sensor and the cluster efficiency is the probability for a particle going through a detector layer. Clusters are composed of multiple hits. It is more likely that hits on the periphery of a cluster goes below threshold than that the whole cluster is lost.
4. *Collected charge*: a direct measurement of the induced charge. Track reconstruction efficiency is most affected by the cluster efficiency, but the track parameters can also be impacted by the amount of collected charge. Furthermore, the charge itself is often used for particle identification, making use of the fact that heavier/slower particles ionize more than lighter/faster particles.
5. *Position resolution*: one of the direct consequences of losing hits on the periphery of a cluster is the degradation in the position resolution.
6. *Lorentz angle*: ionized electrons and holes drift in both the sensor electric field and the detector magnetic field. The track incidence angle that corresponds to the minimum transverse cluster size that results from the balance between these fields is called the Lorentz angle. The angle is largely insensitive to charge trapping, but can be used to study deformations in the sensor electric field.

This chapter is organized as follows. Section 5.1 introduces, for each experiment, aspects of the detector set-up and measurement methods particularly relevant for the measurements. Next, the models used to interpret the data are summarized in Section 5.2. Then, in Section 5.3, we present the measurements for the above observables. The chapter ends with discussion and outlook in Section 5.4.

### 5.1 Measurement considerations

#### 5.1.1 ATLAS

Particle fluence cannot be measured directly. Instead, the luminosity is measured as explained in Section 3.2 and Monte Carlo simulations are used to convert this to a 1 MeV neutron equivalent fluence ( $\Phi_{\text{eq}}^{\text{Si}}$ ). Another important input to many of the measurements and their interpretation is the sensor temperature. Temperatures are measured per module and stored in a conditions database. While these temperatures are measured as close as possible to the sensors, there is a potential offset. A summary of the operating conditions for the ATLAS pixel detector during Run 2 can be found in Fig. 36. The high voltage was slowly increased throughout the run in order to compensate for the raising depletion voltage (see Section 5.3).

#### 5.1.2 CMS

Similarly to ATLAS, the fluence is inferred from the measured luminosity using FLUKA simulations, (CMS FLUKA study v3.23.1.0). Luminosity values are translated into charged and neutral particle

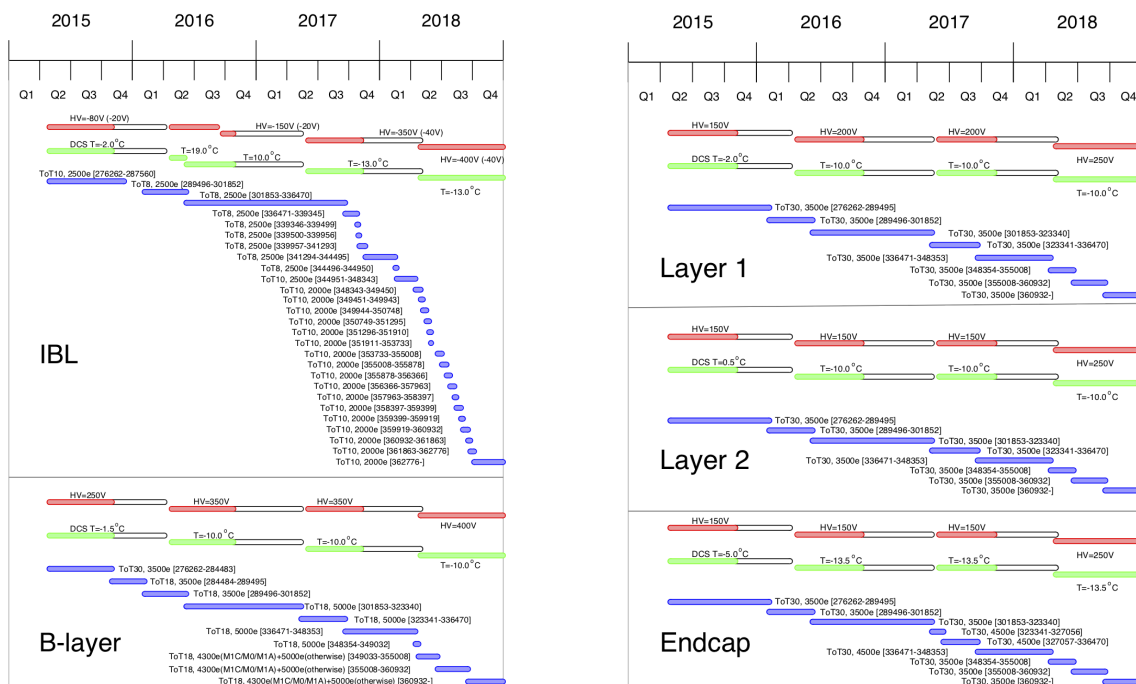


**Fig. 36:** The operating conditions of the ATLAS pixel detector during the LHC Run 2. The red bars indicate the high voltage setting, the green lines are the temperatures, and the blue bars represent the charge thresholds and periods where these were recalibrated. ToT stands for time over threshold, which is a digitized version of the deposited charge using either 4 (innermost layer) or 5 (outer layers) bits.

fluences at a given position in the CMS detector taking into account the proton–proton cross-section at the respective beam energy.

The other main source of uncertainty for the radiation damage tracker modelling is the measurement of the silicon sensor temperatures. In the pixel barrel, temperature measurements are taken along the cooling pipes, with temperature sensors mounted on the carbon fibre support structure at the edges of the barrel. The on-sensor temperature is estimated to be about 2–5 K higher than the temperatures measured on the support structures from studies on a thermal mockup. More details on the mock-up system and on the studies performed are discussed in Ref. [2]. The temperature in the CMS pixel detector is controlled by an evaporative CO<sub>2</sub> cooling system. During 2017 and 2018, the operation point of the cooling plant was set to  $-22$  °C. The coolant temperature decreases along the cooling lines due to a drop in the CO<sub>2</sub> pressure. This feature of the cooling system results in a temperature gradient inside the detector of up to 6 °C. This spread in temperature translates in a spread in leakage current values for modules placed at the same distance from the beam line: measurements for modules placed on a same layer differ up to a factor of 2. This effect was verified on the thermal mock-up as well, where a similar spread in temperature and leakage current measurements was observed. The forward pixel detector has on-module temperature sensors that provide measurements for each readout group (ROG).

Sensor temperature and leakage current measurements for the CMS strip detector are provided with high granularity: one measurement per module. Measurements can be retrieved from the detector control unit (DCU), an ASIC mounted on the front-end hybrid PCB. Figure 37 shows a map of the sensor temperatures within the CMS strip detector as measured during 2017 data taking from the DCUs.

The detector was operated at  $-15^{\circ}\text{C}$  during 2015–2017, and the temperature was lowered to  $-20^{\circ}\text{C}$  at the beginning of 2018 in order not to reach the power supply current limits in detector regions with degraded cooling contacts or passive cooling. During Run 3 several modules are expected to experience thermal runaway. Reducing further the coolant temperature to  $-25^{\circ}\text{C}$  will allow us to decrease this number by almost a factor of 2. Preliminary studies indicate that the detector will be able to provide good performance throughout Run 3.

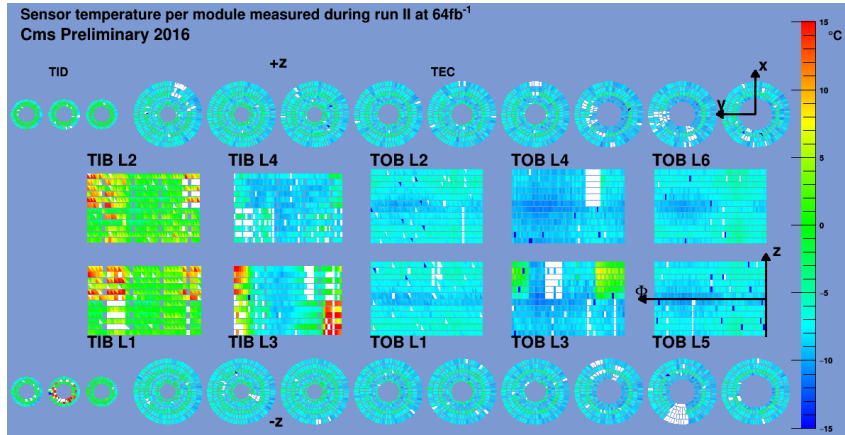


**Fig. 37:** Map of silicon temperature per module for the CMS strip detector, measured in 2017 at  $68.4\text{ fb}^{-1}$  with coolant temperature at  $-15^{\circ}\text{C}$ . White spots arise from modules which are not read out, or for which DCU readings are missing. Detector regions with missing direct cooling, or degraded cooling contacts show visibly higher temperatures with respect to the average.

### 5.1.3 LHCb

The LHCb VELO operated throughout Run 1 and Run 2 of the LHC (2011–2018) without changes to the sensor hardware. Due to its proximity to the proton beam, the sensors were exposed to a fluence of up to approximately  $6.5 \times 10^{14} \text{ 1MeV n}_{\text{eq}} \text{ cm}^2$ . As expected, this extreme radiation environment caused changes to the sensor material and performance via radiation damage effects.

To quantify the radiation damage effects, the estimated fluence accumulated by each sensor is calculated. This can be done by measuring the leakage currents in the silicon sensors, as they are expected to vary linearly with fluence [4]. The fluence is estimated from the simulation, known radiation damage factors and luminosity. A single current is measured for each VELO sensor, corresponding to the current drawn by the entire sensor. The difference of the measured currents amongst sensors is dominated by the variation in sensor temperatures, and to a lesser degree, by their distance to the interaction region.

## 5.2 Radiation damage modelling

There are two types of microscopically motivated effective radiation damage models used to interpret the measurements presented in subsequent sections. One set of models include annealing effects (Hamburg and Sheffield models) and the other set of models make predictions for deformations in the electric field inside the sensor. This second set of models are developed in the framework of technology computer aided design (TCAD) simulations. At the moment, there is no one framework for modelling both annealing and a non-trivial electric field inside the sensor bulk. Traditionally, annealing models are used to interpret the leakage current and depletion voltage data while TCAD simulations are used for observables that are related to track reconstruction. Integrating TCAD models into full detector systems is further discussed in Chapter 7.

### 5.2.1 Leakage current modelling

For a given instantaneous irradiation with fluence  $\Phi$ , the leakage current changes as  $\Delta I_{\text{leak}} = \alpha V \Phi$ , where  $V$  is the depleted volume of the sensor and  $\alpha$  is approximately independent of the damaging particle energies and flavours. After some time  $t$  at a temperature  $T$ , the leakage current changes from defect annealing, so  $\alpha = \alpha(t, T)$ . Different models vary in their treatment of  $\alpha$ , including  $n_{\text{states}}$  effective defect states whose contribution to the leakage current evolves with time. In all models, the leakage current starting from zero current is given by

$$I_{\text{leak}} = (\Phi/L_{\text{int}}) \cdot \sum_{i=1}^n V_i \cdot L_{\text{int},i} \left[ \sum_{j=1}^{n_{\text{states}}} \alpha_j((T_i, t_i), (T_{i+1}, t_{i+1}), \dots, (T_n, t_n)) \right], \quad (21)$$

where  $L_{\text{int},i}$  is the integrated luminosity,  $V_i$  is the depleted volume,  $t_i$  is the duration, and  $T_i$  is the temperature in time interval  $i$ . The three most common forms for the  $\alpha_j$  are as follows:

$$\begin{aligned} \alpha_1^A &= \alpha_I \exp \left( - \sum_{j=i}^n \frac{t_j}{\tau(T_j)} \right) \\ \alpha_2^A &= \alpha_0^* - \beta \log \left( \sum_{j=i}^n \frac{\Theta(T_j) \cdot t_j}{t_0} \right), \end{aligned} \quad (22)$$

$$\begin{aligned} \alpha_1^B &= \alpha_1^A \\ \alpha_2^B &= \alpha_0 + \frac{1}{\sum_{j=1}^n t_j} \sum_{j=1}^n \frac{t_j}{T_j} - \beta \log \left( \sum_{j=i}^n \frac{t_j}{t_0} \right), \end{aligned} \quad (23)$$

$$\alpha_k^C = \alpha(T_{\text{ref}}) \frac{A_k \tau_k}{\Theta(T_i) t_i} \left[ 1 - \exp \left( - \frac{\Theta(T_i) t_i}{\tau_k} \right) \right] \exp \left( - \frac{1}{\tau_k} \sum_{j=1}^n \Theta(T_j) t_j \right), \quad (24)$$

where Eqs. 22 and 23 are called the Hamburg model [4] and Eq. 24 is called the Sheffield model [5]. Both Eqs. 22 and 23 assume that the annealing over time  $t$  with fixed temperature  $T$  is given by  $\alpha \exp(-t/\tau) + \alpha_0 - \beta \log(t/t_0)$ ; they differ in how to treat periods with varying temperature. The unspecified functions in the above equations are  $1/\tau(T) = k_{I,0} \exp(-E_i/k_B T)$  and  $\Theta(T) = \exp(-E_i/k_B(1/T - 1/T_{\text{ref}}))$ . Typical parameters are given in Tables 9 and 10. These are the values used by both the ATLAS and CMS pixel and strip detector groups [4, 6, 16]. Other values used in some measurements from LHCb can be found in Ref. [7]. An example implementation of the code can be found at this link: <http://cern.ch/go/mDb9>.

The resulting prediction is then valid for leakage currents measured at a value  $T_{\text{ref}}$ . In order to compare the data directly with this prediction, the data are corrected to correspond to the same constant reference temperature. This is done by using the following scaling factor:

$$\left( \frac{T_{\text{ref}}}{T} \right)^2 \exp \left( - \frac{E_{\text{eff}}}{2k_B} \left( \frac{1}{T_{\text{ref}}} - \frac{1}{T} \right) \right), \quad (25)$$

where  $E_{\text{eff}}$  is the effective band-gap energy in silicon. The most commonly used value of  $E_{\text{eff}}$  is 1.21 eV [8], but some studies have suggested that a lower value (e.g., 1.12 eV [6]) may lead to a better fit with collider data.

**Table 9:** Leakage current model parameters from Eq. 22 using Ref. [4].

Parameter	Value	Units
$\alpha_I$	$(1.23 \pm 0.06) \times 10^{-17}$	A/cm
$k_{I,0}$	$1.2^{+5.3}_{-1.0} \times 10^{13}$	Hz
$E_I$	$1.11 \pm 0.05$	eV
$\alpha_0^*$	$7.07 \times 10^{-17}$	A/cm
$\beta$	$3.29 \times 10^{-18}$	A/cm
$E_I^*$	$1.30 \pm 0.14$	eV
$t_0$	1	min.
$T_{\text{ref}}$	21	°C

**Table 10:** Leakage current model parameters from Eq. 24 using Ref. [5] using  $T_{\text{ref}} = 20^\circ\text{C}$ . The value for  $\alpha(T_{\text{ref}})$  is  $(4.81 \pm 0.13) \times 10^{-17}$  A/cm.

$k$	$\tau_k$ (min)	$A_k$
1	$(1.2 \pm 0.2) \times 10^6$	$0.42 \pm 0.11$
2	$(4.1 \pm 0.6) \times 10^4$	$0.10 \pm 0.01$
3	$(3.7 \pm 0.3) \times 10^3$	$0.23 \pm 0.02$
4	$124 \pm 2.5$	$0.21 \pm 0.02$
5	$8 \pm 5$	$0.04 \pm 0.03$

### 5.2.2 Full depletion voltage modelling

Aside from the  $V_i$  term in Eq. 21, modelling the leakage current is largely insensitive to the doping concentration spatial distribution inside the sensor. In contrast, the full depletion voltage becomes poorly defined when the electric field profile inside the sensor has a non-linear shape. For unirradiated sensors, one can relate the full depletion voltage and the effective doping concentration:

$$V_{\text{depl}} = |N_{\text{eff}}| \cdot \frac{ed^2}{2\epsilon\epsilon_0}, \quad (26)$$

where  $d$  is the sensor thickness,  $e$  is the unit charge,  $\epsilon$  is the dielectric constant, and  $\epsilon_0$  is the vacuum permittivity. There currently does not exist a model that can account for both the spatial inhomogeneity of  $N_{\text{eff}}$  and its annealing. For predicting the operational full depletion voltage, experiments typically focus on the thermal effects. The most widely used model for this goal is the Hamburg model<sup>3</sup>:

$$N_{\text{eff}}(t, T) = N_{\text{D}}^{\text{non-removable}}(0) + N_{\text{D}}^{\text{removable}}(t) - N_{\text{A}}^{\text{stable}}(t) - N_{\text{A}}^{\text{beneficial}}(t, T) - N_{\text{A}}^{\text{reverse}}(t, T), \quad (27)$$

where  $N_{\text{D}}^{\text{(non)-removable}}(0)$  is the initial concentration of (non)-removable donors and the other terms are defined below. The fraction of removable donors for the typical concentrations used for LHC silicon sensors is predicted to be all of the initial doping concentration for charged-particle irradiation. Irradiation by charged particles dominates the damage on the innermost layers of the LHC experiments. The components of Eq. 27 are governed by coupled system of differential equations:

$$\begin{aligned} \frac{d}{dt} N_{\text{D}}^{\text{removable}}(t) &= -c\phi(t) N_{\text{D}}^{\text{removable}}(t) && \text{removal of donors for } n\text{-type during irradiation,} \\ \frac{d}{dt} N_{\text{A}}^{\text{stable}}(t) &= g_{\text{C}}\phi(t) && \text{addition of stable acceptors during irradiation,} \\ \frac{d}{dt} N_{\text{A}}^{\text{beneficial}}(t, T) &= g_{\text{A}}\phi(t) - k_{\text{A}}(T) N_{\text{A}}^{\text{beneficial}}(t, T) && \text{beneficial annealing,} \\ \frac{d}{dt} N_{\text{N}}^{\text{reverse}}(t, T) &= g_{\text{Y}}\phi(t) - k_{\text{Y}}(T) N_{\text{N}}^{\text{reverse}}(t, T) && \text{reverse annealing – neutrals,} \\ \frac{d}{dt} N_{\text{A}}^{\text{reverse}}(t, T) &= k_{\text{Y}}(T) N_{\text{N}}^{\text{reverse}}(t, T) && \text{reverse annealing – acceptors,} \end{aligned} \quad (28)$$

<sup>3</sup>Both the leakage current and full depletion voltage models are typically referred to as ‘the’ Hamburg model [4], but the physical parameters of the two models are not related.

where  $\phi(t)$  is the irradiation rate in  $n_{\text{eq}}/\text{cm}^2/\text{s}$  ( $\Phi = \int dt\phi(t)$ ). The introduction rates have been measured by the ROSE collaboration [9] and typical values for the other parameters can be found in Ref. [4]. One challenge is that the ROSE collaboration measurements do not report uncertainties and also do not include charged hadron damage for  $g_A$ . Even though the damage is different for charged and neutral hadrons, typically experiments pick one value when simulating Eq. 27. An example implementation of the code can be found at this link: <http://cern.ch/go/mDb9>.

## 5.3 Results

### 5.3.1 Leakage current

#### 5.3.1.1 ATLAS pixels

The ATLAS pixel system consists of four parts: the insertable B-layer (IBL), the outer barrel layers, and the endcaps. The IBL was added to the ATLAS detector at the start of Run 2, but has already accumulated more fluence than any other layer due to its close proximity to the interaction point (3.3 cm). Figure 38 presents the measured and simulated leakage current on the IBL as a function of the integrated luminosity during Run 2. The simulations have been fit with an overall scale factor ( $\Phi/L_{\text{int}}$  in Eq. 21). The IBL is composed of four equally spaced module groups along the beam direction,  $z$ . The current is highest for the innermost module group and decreases monotonically to the fourth group. The outermost module group is composed of 3D sensors [10] which require a much lower bias voltage to be fully depleted. The right plot of Fig. 38 is the ratio of the innermost module groups to the 3D module group. The ratio is expected to be constant and proportional to the ratio of fluences. During 2016 (around  $20 \text{ fb}^{-1}$ ), the innermost module groups were under-depleted, which is observed as a dip in the leakage current ratio.

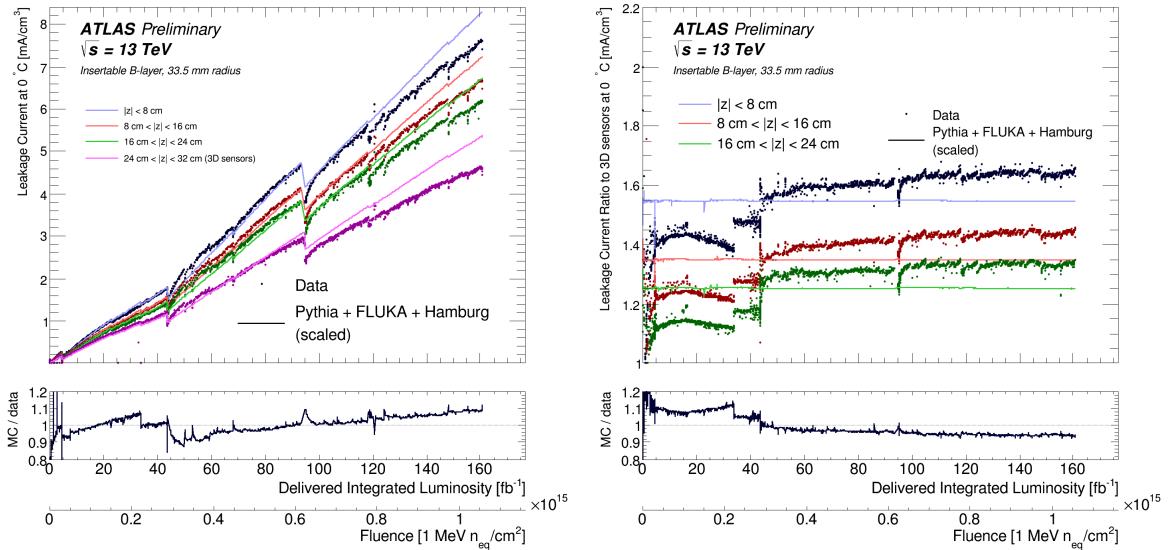


**Fig. 38:** The leakage current as a function of the integrated luminosity in Run 2 for the ATLAS IBL [6]. The left plot shows the absolute current normalized to  $0^\circ\text{C}$  and the right plot shows the current in the innermost three module groups normalized to the outermost module group that is composed of 3D sensors. The predictions in the left plot are after a  $\chi^2$  fit to the  $\Phi/L_{\text{int}}$  scaling factor for each of the four module groups (represented by different colours). The  $z$  ranges of each group are indicated in the plots.

Similar figures for the outer three pixel layers ( $B$ -layer, L1, and L2) are presented in Fig. 39. Unlike the IBL, the outer layers have been active since the start of the LHC and so the current history spans nearly  $200 \text{ fb}^{-1}$ . The ratio between the various layers (right plot of Fig. 39) is nearly constant with time, as expected when both layers are fully depleted.

The fitted  $\Phi/L_{\text{int}}$  scale factors for the IBL and the outer pixel layers are shown in Fig. 40 as a

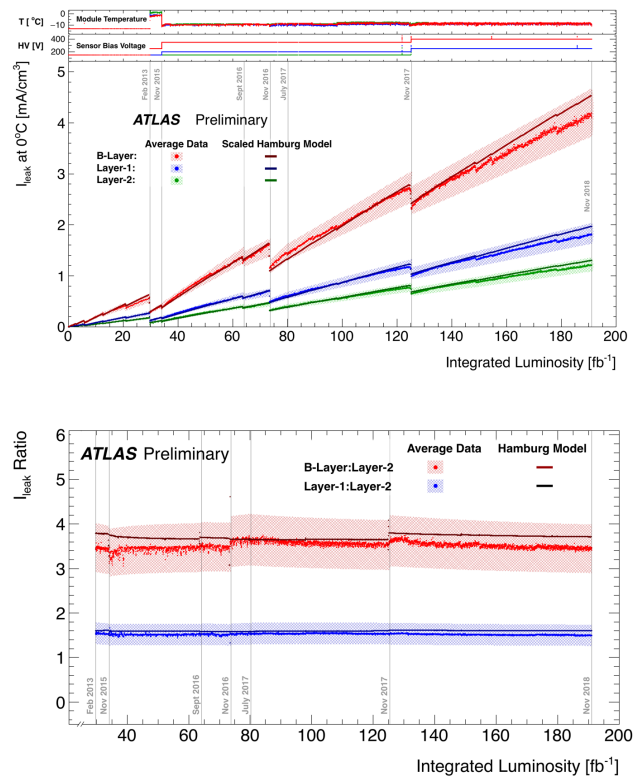


**Fig. 39:** The leakage current as a function of the integrated luminosity in Run 2 for the outer pixel layers of the ATLAS detector [11]. The top plot is the absolute current and the bottom plot shows the ratio between the inner layers and the outer layer. The predictions in the left plot are after a  $\chi^2$  fit to the overall  $\Phi/L_{\text{int}}$  scaling factor per layer.

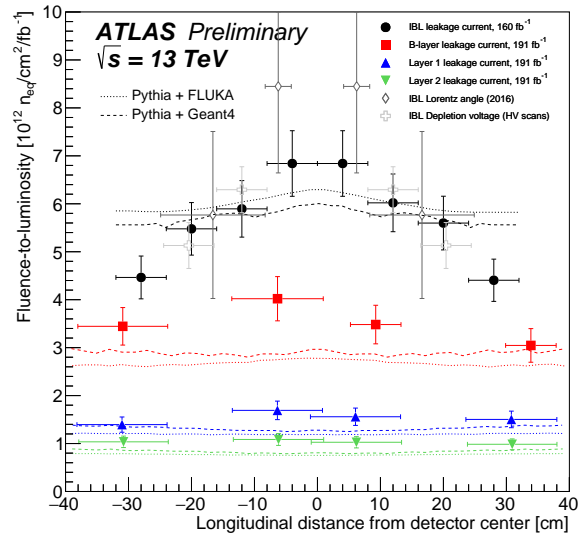


**Fig. 40:** The predicted fluence rates compared with the measured  $\Phi/L_{\text{int}}$  scale factors [6, 11]. The different marker colours correspond to the four pixel layers. Extractions with other methods are presented and will be discussed in subsequent sections.



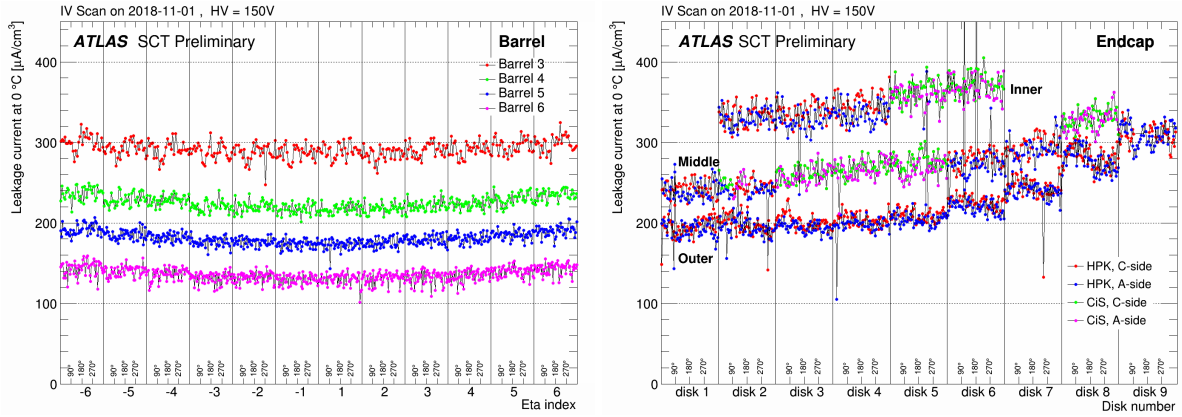


**Fig. 41:** A measurement of the leakage current on the ATLAS strip detector in the barrel (left) and disks (right) [12].

function of  $z$ . The innermost layers have acquired the most fluence and so are at the top of the plot. A large  $|z|$ -dependence in the IBL is observed in data that is not reproduced by the simulation. Furthermore, the overall fluence is about 50% higher in the outer layers compared with the simulation while the average fluence is approximately correct for the IBL. For reference, the IBL is at 3.3 cm while the  $B$ -layer is at 5.1 cm and the outer two layers are at 8.9 and 12.3 cm, respectively.

### 5.3.1.2 ATLAS strips

Leakage current measurements with the ATLAS strip detector are presented in Fig. 41. The current is nearly independent of  $z$  in the barrel detector while a significant increase in fluence is observed in the outermost disks. A comparison between the measured current in each barrel layer and predictions are shown in Fig. 42. The Hamburg and Sheffield models agree well with each other and with the data without a scale factor.

An increasing leakage current contributes to the module heating. As the leakage current itself depends strongly on the module temperature, this leads to a feedback loop. If this feedback loop does not converge from moderation with active or passive cooling, then thermal runaway can cause module failures. A study of thermal runaway is presented in Fig. 43. So far there is no indication of thermal runaway, but it may be necessary to operate the detector colder in Run 3.

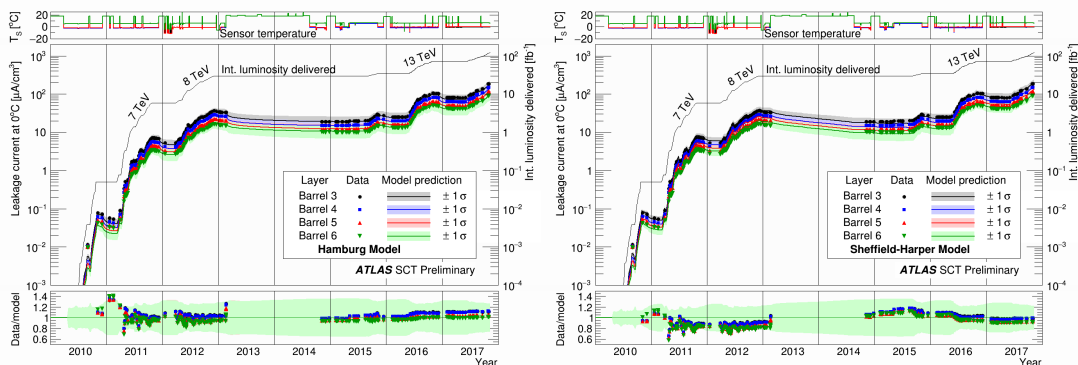


**Fig. 42:** A comparison of the measured and predicted leakage current as a function of time in the ATLAS strip detector [12] for the Hamburg model (left) and the Sheffield model (right). No scaling factor is applied to the leakage current predictions.

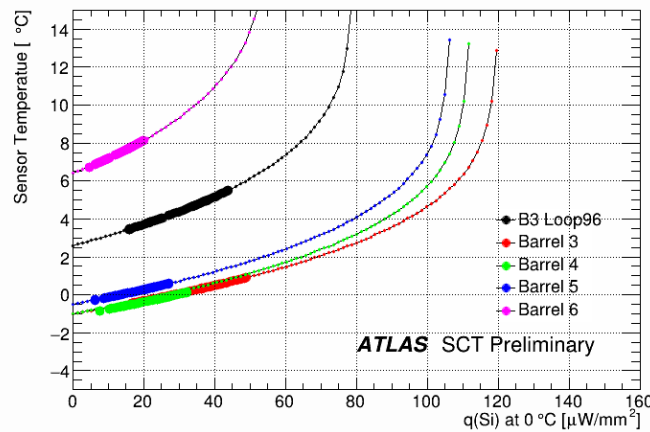


**Fig. 43:** A study of thermal runaway in the ATLAS strip detector [12]. The horizontal axis is the power per area while the vertical axis is the sensor temperature. The data points are large markers and the predictions are in small markers, extending to the expected conditions in 2023.

### 5.3.1.3 CMS pixels

The CMS pixel detector was replaced half-way through Run 2. Measurements and predictions of the leakage current for the new four-layer pixel detector are presented in Fig. 44. The measurements are taken for each LHC fill, 20 minutes into stable beam, excluding short or fills with small number of bunches. They are taken for all sectors and averaged for each layer excluding not operated modules. The averaged current corresponds to one module with a volume of  $0.0285 \times 6.48 \times 1.62 \text{ cm}^3 \approx 0.3 \text{ cm}^3$ . The simulations for each layer are performed for  $z = 0$  and  $r = 2.898, 6.757, 10.8725,$  and  $15.9805 \text{ cm}$  for Layers 1 to 4, respectively. The simulated leakage currents are scaled to the temperatures at which the measurements were taken using Eq. 25 [8]. Scale factors are applied to the simulation to match the data. This scale factor is 1.0 for the innermost layer, 2.2 on the second layer, 2.0 on the third layer, and 1.8 on the outermost layer. After applying these scaling factors, the simulation provides an excellent model of the time dependence of the leakage current. The final fluences, derived using FLUKA, are 79, 18, 9 and  $5 \times 10^{13} \text{ n}_{\text{eq}}\text{cm}^{-2}$  for Layers 1 to 4, respectively.

Unlike ATLAS, the HV channels in CMS are grouped together in  $z$  so it is not possible to determine the  $z$  dependence of the leakage current during detector operations. Studies with the forward pixel detector (Fig. 45) do not show a  $|z|$  dependence in either data or simulation which is approximately consistent with the outer pixel layer results from ATLAS. While the comparison of the  $|z|$  dependence is inconclusive, the larger-than-expected fluence on the outer barrel layers is observed by CMS as well as ATLAS.

### 5.3.1.4 CMS strips

In the CMS strip detector leakage current, together with sensor temperature, is monitored at module level using the DCU on the front-end hybrid PCB. The leakage current of each module in the CMS strip detector in the middle of Run 2 is shown in Fig. 46. Inhomogeneities are due to degraded cooling in some parts of the detector. Measured values of leakage current are corrected for temperature variations and compared with Hamburg model predictions. The computed evolution is based on the global temperature and luminosity history. It takes into account the increase of the temperature expected from the increase in power dissipation with leakage current. Leakage current measured and predicted values are compared for each layer as a function of time and luminosity (Fig. 47). The predictions agree with the data within 20% and there is only a slight difference between Run 1 and Run 2. Differences are compatible with the uncertainties.

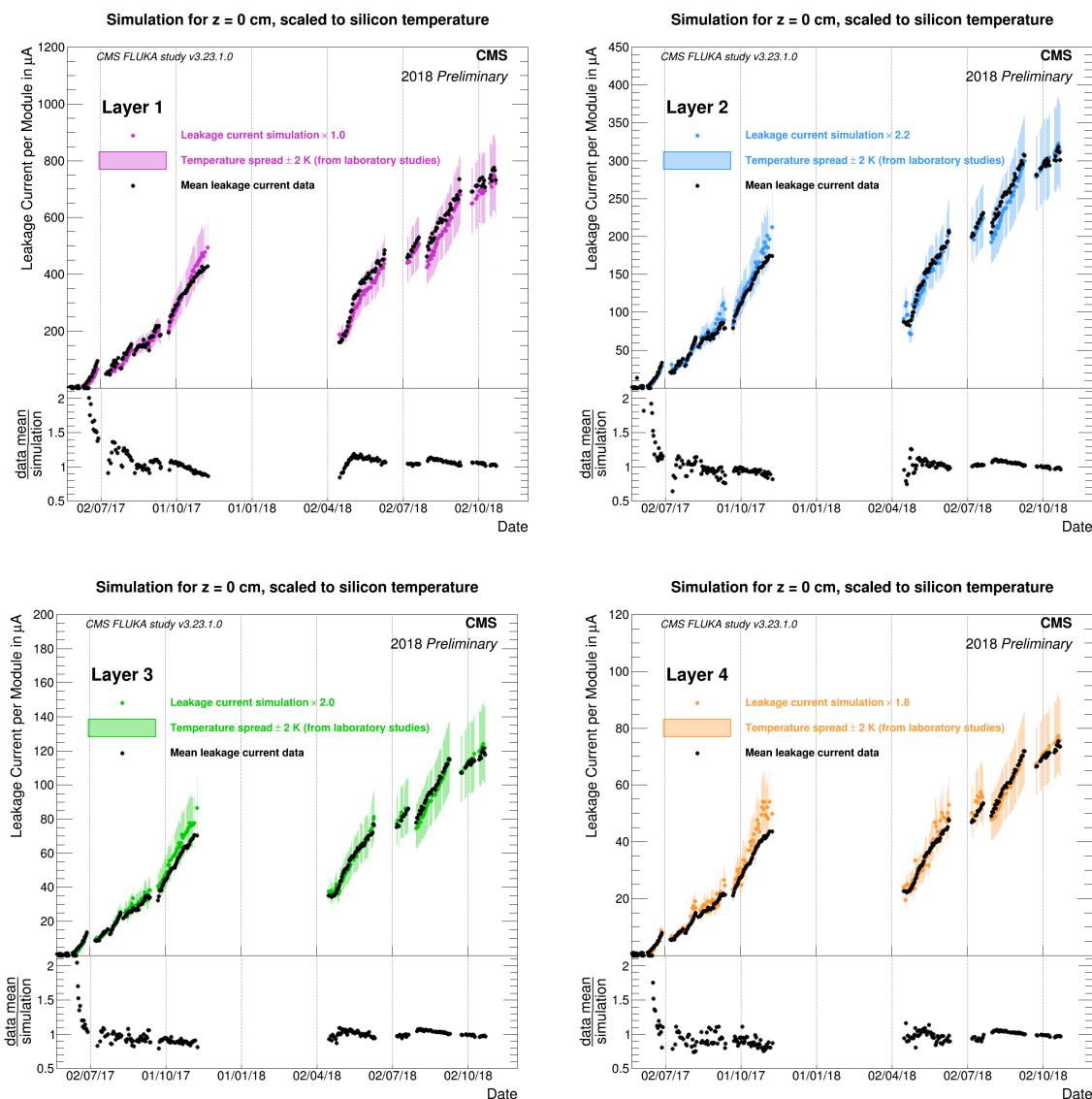


**Fig. 44:** Comparison of the measured leakage current per sensor module (approximately  $0.3 \text{ cm}^3$  of silicon) with simulation for the four layers of the CMS barrel pixel detector. For Layers 2 to 4 the simulated values are scaled by a factor of about 2, as indicated on each of the three plots.

CMS has also investigated thermal runaway. A small number of modules already in Run 2 experienced thermal runaway due to degraded cooling contacts and relatively large fluences. In the example in Fig. 48 the currents from two HV channels connected to sets of modules from a double-sided layer are shown. When both channels are switched on thermal runaway occurs until one of the two channels trips due to reaching its current limit. One of the two HV channels can, however, continue to operate. The occurrence of further thermal runaways was limited in the last year of Run 2 by decreasing the baseline temperature between 15 and  $-20^\circ\text{C}$ .

### 5.3.1.5 LHCb vertex detector

Even though the LHCb detector has received about a factor of 10 fewer collisions than ATLAS or CMS, the fluence on the VELO is comparable to the innermost pixel layers of ATLAS and CMS ( $\sim 10^{15} \text{ n}_{\text{eq}}/\text{cm}^2$  after Run 2) due to the closer proximity to the collision point. Figure 49 shows the

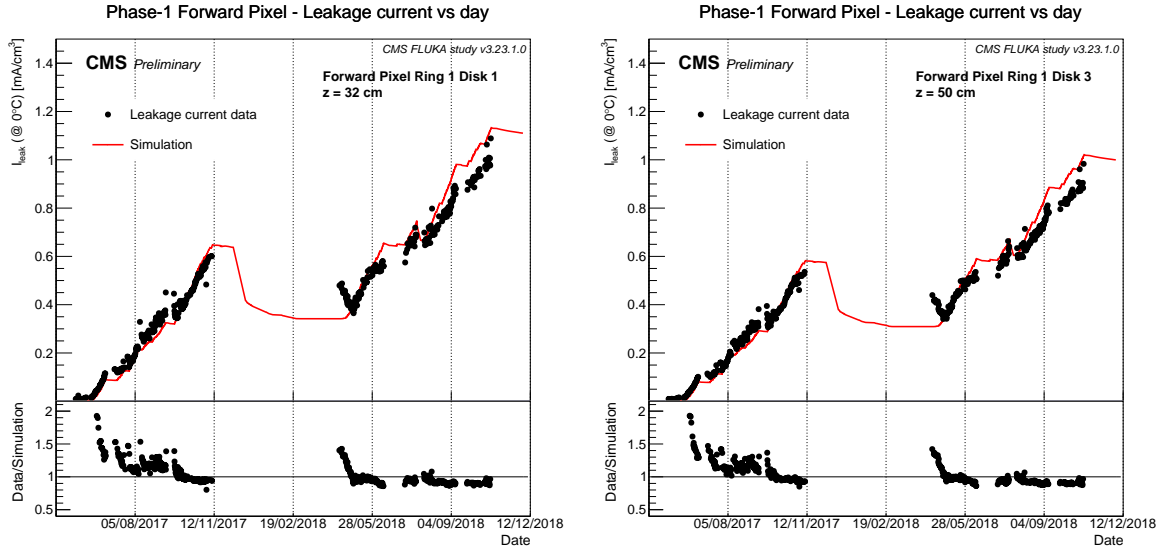


**Fig. 45:** A comparison of the measured and simulated leakage currents on the CMS forward pixels in 2017 and 2018 with a total of  $120 \text{ fb}^{-1}$ . The plots are for the inner ring (average radius 7.8 cm) and for the closest disk to the interaction (left) and the furthest disk from the interaction (right). No fluence-to-luminosity scaling factors are applied to the simulation.

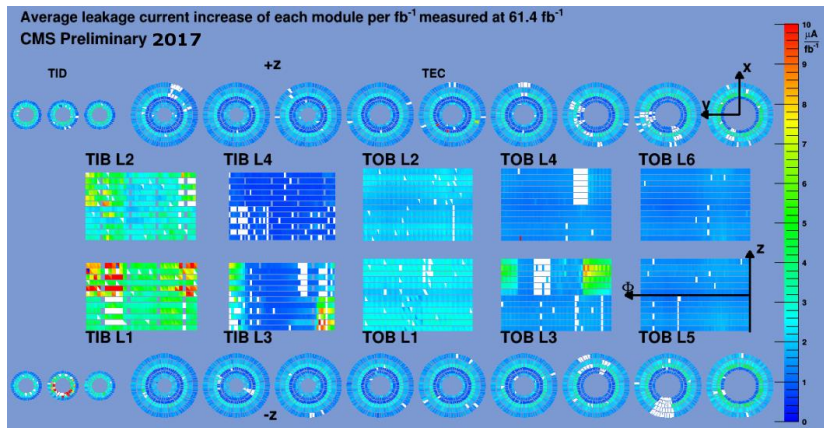


**Fig. 46:** The leakage current per module for the CMS strip detector in the middle of Run 2 (after  $61.4 \text{ fb}^{-1}$ ). The middle rectangles show the barrel region and the disks are above and below. The currents shown here are not corrected for variations in the module temperature.

measured and predicted currents from the beginning of Run 1 through the end of Run 2. The Hamburg model provides an excellent model of the data across the entire VELO lifetime.

### 5.3.1.6 LHCb tracker turicensis

The current drawn by each HV channel in the LHCb tracker turicensis (TT) is monitored with a resolution of  $1.0 \mu\text{A}$ , and a maximum interval of 120 minutes allowed between consecutive readings. The current for a given channel is defined as the maximum observed during a given LHC fill (typically several hours). Figure 50 shows how the measured leakage currents vary along the beam direction in  $z$ . Figure 51 presents the measured and predicted leakage current using the Hamburg model. The simulation provides an excellent model for the data across the entire TT lifetime.

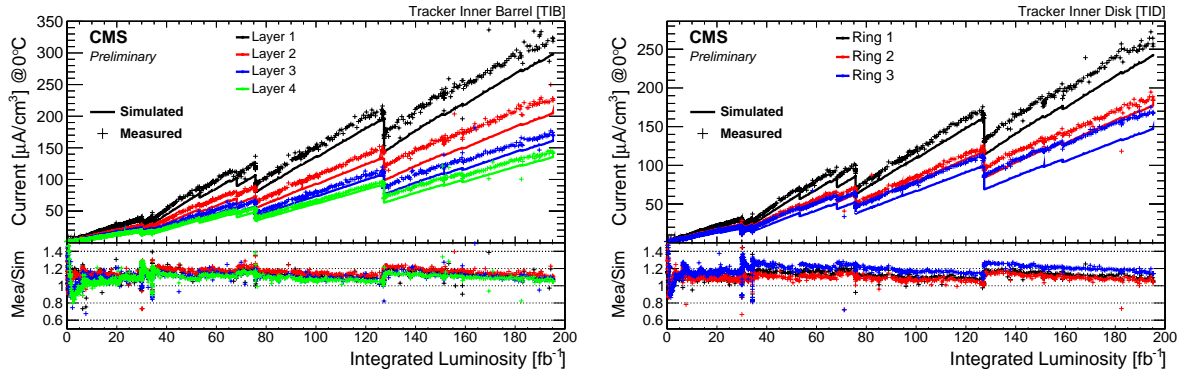


**Fig. 47:** The measured and predicted leakage current as a function of the integrated luminosity since early Run 1 for TIB (left) and TOB (right). The predictions are not scaled to match the data.

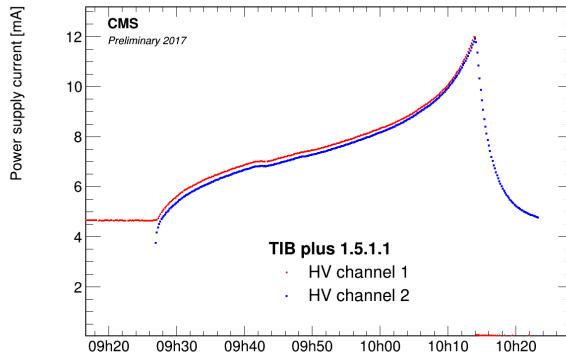


**Fig. 48:** An example of thermal runaway in Run 2 in one power group of the CMS strip detector

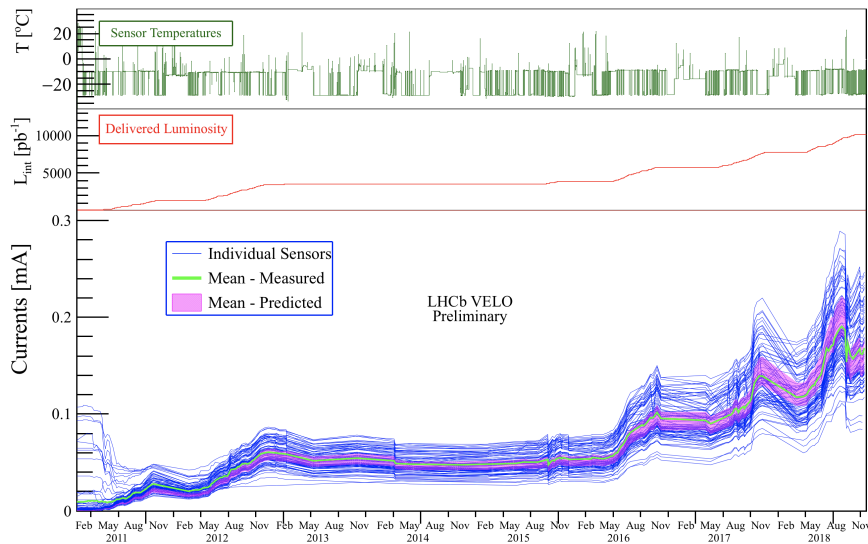


**Fig. 49:** The leakage current for the VELO sensors as a function of time scaled to 0 °C. The average measured and Hamburg model predicted currents are also shown.

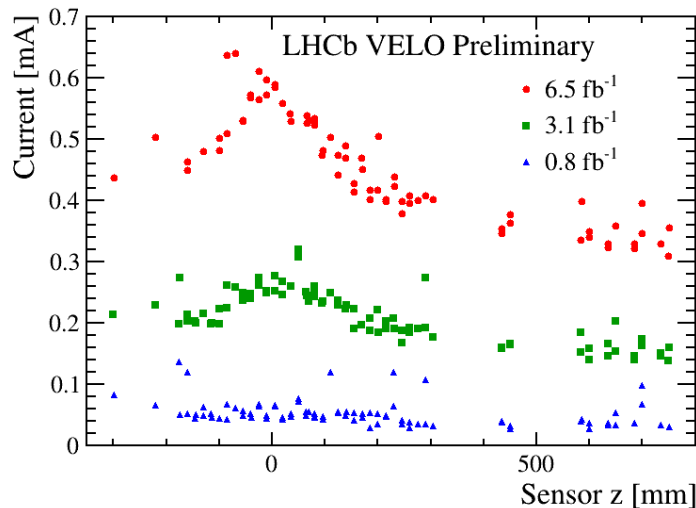


**Fig. 50:** The leakage current at various locations along the beam direction ( $z$ )

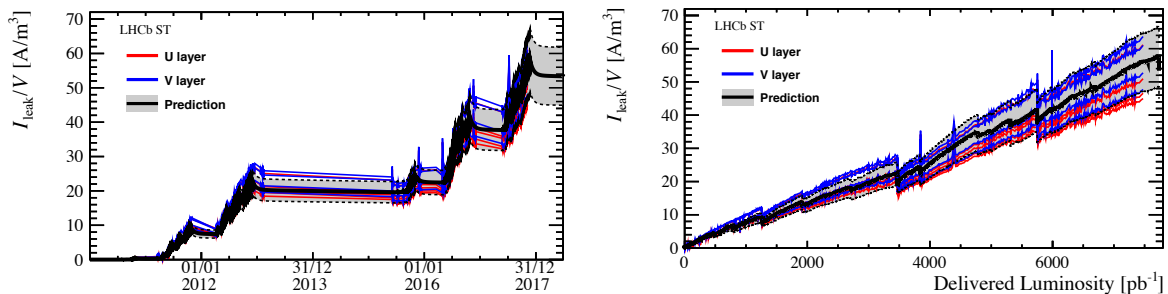


**Fig. 51:** The measured and predicted leakage current as a function of time (left) and integrated luminosity (right) for the innermost sensors in the second and third detection layers, indicated as U and V layers, respectively [7]. Currents are normalized to  $8^\circ\text{C}$ . The grey uncertainty band includes uncertainty on the Hamburg model parameters, on the input FLUKA simulation, and on the temperature measurements. The effective band gap energy is set to 1.21 eV.

### 5.3.2 Depletion voltage

The depletion voltage is often determined by performing a scan of the collected charge or hit/cluster efficiency with applied high voltage. Unlike for leakage current, this requires that the depletion voltage be measured during collisions (or integrate for a long time with cosmic runs).

#### 5.3.2.1 ATLAS pixels

Depletion voltage measurements and predictions from the Hamburg model in the innermost two layers of the ATLAS pixel detector are presented in Fig. 52. The IBL measurement includes the full Run 2 dataset while the  $B$ -layer measurement includes data from early Run 1 up to the middle of Run 2. The first measurements before space-charge-sign inversion were performed with cross-talk scans since the pixels were isolated. These scans are particularly useful because no active collisions are required. However, once the pixels are non-isolated following type inversion, this method is no longer available. Following space-charge-sign inversion, the depletion voltage is determined from charge collection efficiency scans. The measured charged versus high voltage is fit to a square root and linear function. The point where these two functions intersect is defined as the depletion voltage.

The introduction rates were fit to the Run 1 and early Run 2 data [6]. In order to fit these data, the

introduction rates  $g_Y$  and  $g_C$  were increased for the IBL with respect to the ROSE Collaboration values. While this fit provides a reasonable model of the Run 1 and early Run 2 data, it fails to describe the full Run 2 IBL leakage current. Various *ad hoc* modifications to the Hamburg model were investigated, but none resulted in global agreement with the data.

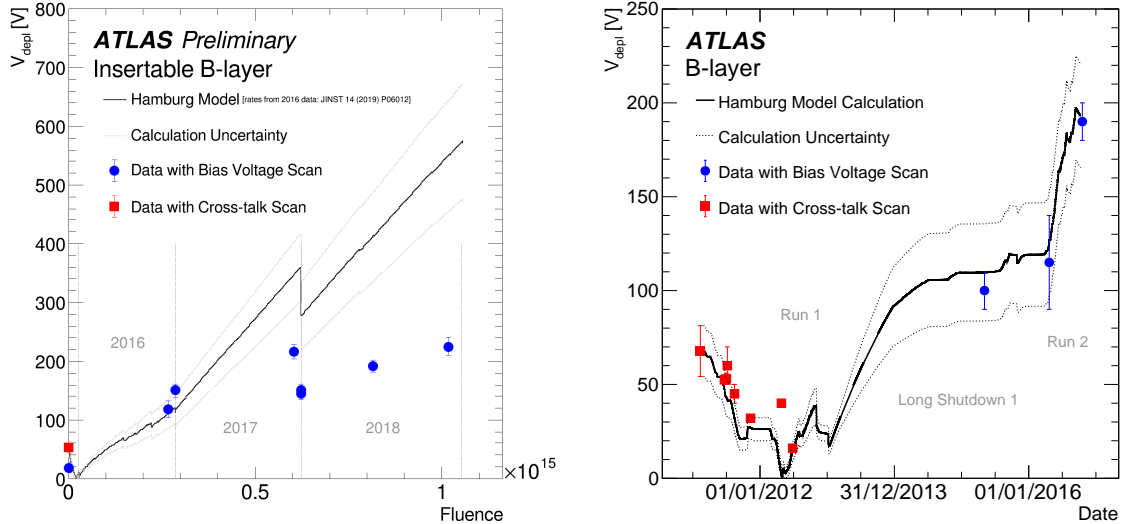


**Fig. 52:** Measurements and Hamburg model predictions for the ATLAS IBL (left) and  $B$ -layer (right). Circular points indicate measurements of the depletion voltage using the bias voltage scan method while square points display earlier measurements using cross-talk scans. The uncertainty band results from the fitted uncertainty in the introduction rates.

### 5.3.2.2 ATLAS strips

The ATLAS strip detector has a binary readout, so a charge collection scan cannot be used to determine the depletion voltage. Instead, a hit efficiency scan can be used (also studied with the average cluster size), as indicated in the left plot of Fig. 53. The increasing depletion voltage from the scans conducted in April and September of 2018 indicate that the sensors have passed space-charge-sign inversion. However, the efficiency starts to drop when going from high to low voltage at a much higher voltage (100 V) than the expected full depletion voltage (about 50 V).

### 5.3.2.3 CMS pixels

The average cluster charge and size are used to determine the full depletion voltage for the CMS pixel detector. Figure 54 presents measurements and Hamburg model predictions for the second half of Run 2 for the new pixel detector. For both measurement approaches, the full depletion voltage is estimated from the kink in the respective curves. The two measurement approaches show similar trends with time, but the actual measured full depletion voltage tends to be higher for the cluster charge determination than for the cluster size method. The depletion voltage was measured frequently during 2018 (about once/month) and the simulation under-predicts the outer layers and over-predicts the inner layer (similar to the ATLAS IBL).

Analogously, the full depletion voltage for the CMS forward pixel detector is determined from the average cluster charge. Figure 55 shows the evolution of the expected full depletion voltages for the forward pixel tracker disks based on the full temperature and irradiation history, as simulated using the Hamburg model. In this case the Hamburg model is fitted to 2018 data leaving  $g_C$  parameter as a free parameter. The  $g_Y$  parameter is fixed to  $7 \times 10^{-2} \text{ cm}^{-1}$  and  $g_A$  to  $1.4 \times 10^{-2} \text{ cm}^{-1}$ . The simulation

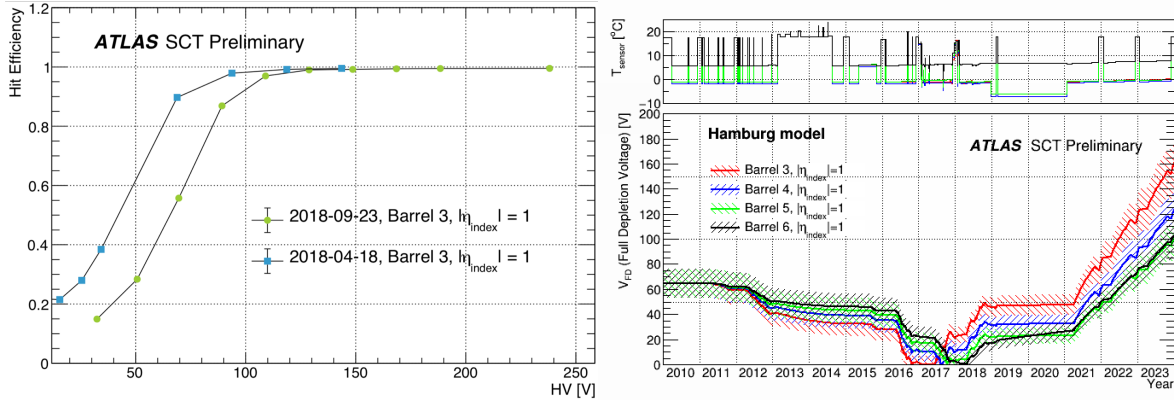


**Fig. 53:** A scan of the hit efficiency versus the sensor high voltage (left) and the simulated full depletion voltage using the Hamburg model for the four barrel layers [12]. Space-charge-sign inversion is predicted to have occurred during 2016.

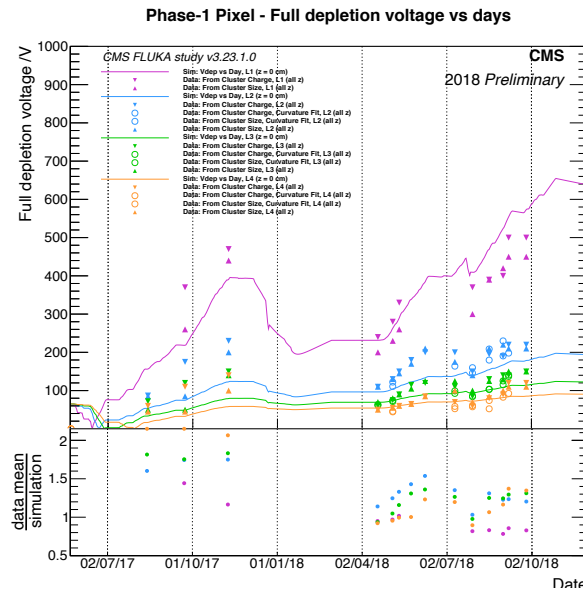


**Fig. 54:** Measurements and simulations of the full depletion voltage as a function of time since the start of 2017, when the new pixel detector was installed for the barrel layers 1 (purple), 2 (blue), 3 (green), and 4 (orange). Both cluster charge and cluster size measurements are used to determine the full depletion voltage.

well predicts the measurements in both the closer and farer disk from interaction point, except for the end of the Run 2, where predictions overestimate measurements. Figure 56 presents the comparison of the fit to the data following the Hamburg model performed assuming a linear or logarithmic dependence of the effective doping concentration on the fluence. This study shows that for the end of Run 2, a logarithmic trend better describes measurements. The fit method has been tested also on the barrel Layer 1 pixel detector, comparing the linear and logarithmic model, as presented in Fig. 57. For the Layer 1 the logarithmic model describes data much better, except for the period before type inversion.

#### 5.3.2.4 CMS strips

As with the CMS pixel detector, both the cluster charge and width are used to determine the full depletion voltage for the CMS strip detector. It was found that the cluster width has a better sensitivity to low



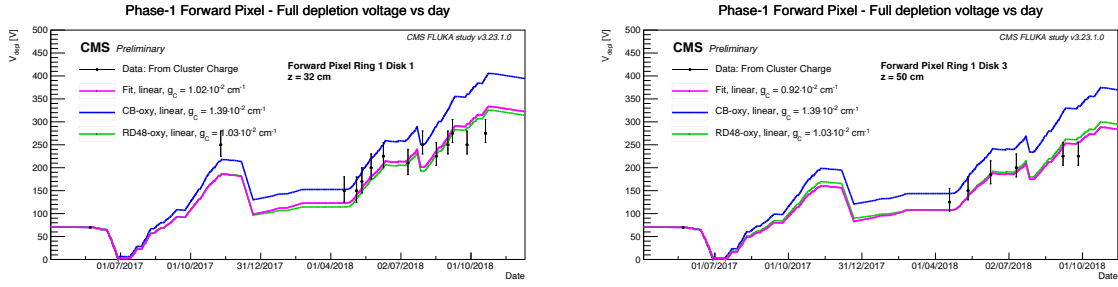


**Fig. 55:** Measurements and simulations of the full depletion voltage as a function of time since the start of 2017, when the new pixel detector was installed, for the inner ring (Ring 1) of two endcap disks (Disk 1 and Disk 3). Cluster charge measurements are used to determine the full depletion voltage. The resulting prediction (magenta line) is compared to the Hamburg model using two sets of Hamburg parameters for oxygenated Si (DOFZ): CB-oxy (blue line) and RD48-oxy (green line).

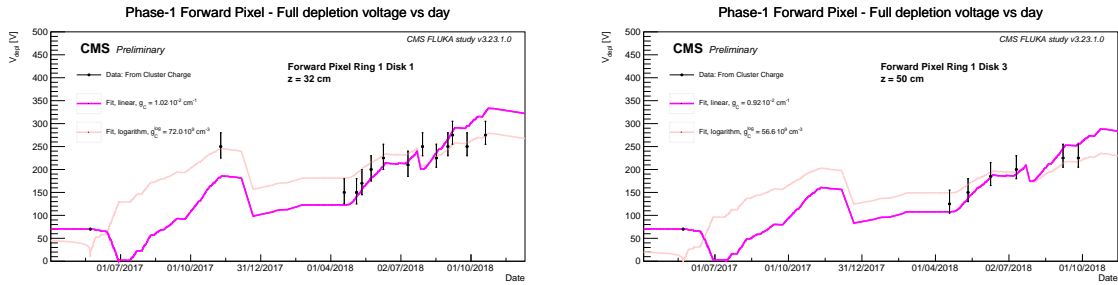


**Fig. 56:** Comparison of the fit to the data following the Hamburg model, with a linear (magenta) and a logarithmic (pink) dependence of the effective doping concentration on the fluence for the CMS forward pixel detector.

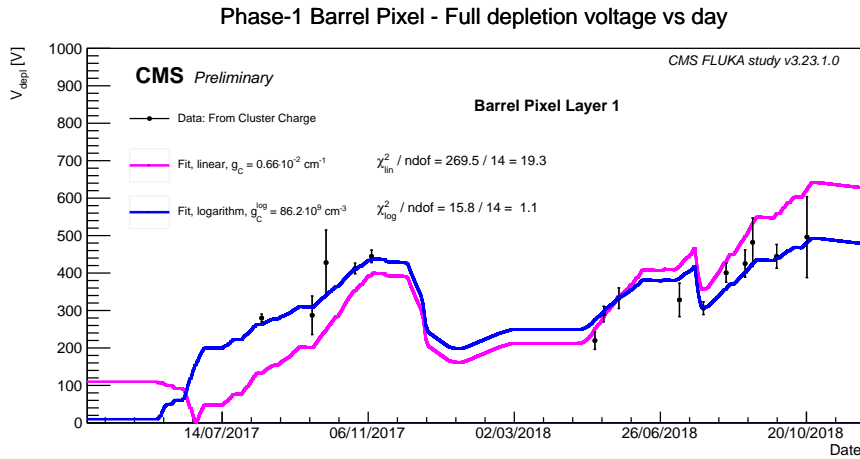


**Fig. 57:** Comparison of the fit to the data following the Hamburg model, with a linear (magenta) and a logarithmic (blue) dependence of the effective doping concentration on the fluence for Layer 1 CMS barrel pixel detector.

depletion voltages and is thus used for the baseline results presented in Figs. 58 and 60. The point of full depletion itself is determined by fitting the trend of average cluster width versus bias voltage to two linear curves. The point of intersection is the estimated bias voltage (Fig. 59). Scans are performed approximately four times per year.

A comparison between data and simulation for one module on the innermost strip layer is presented in Fig. 60 (left). At the end of Run 2, the sensors have just begun space-charge-sign inversion. Overall, the agreement between the data and the prediction are excellent, agreeing within about 10%. The experimental method loses sensitivity on the full depletion voltage at low values where many clusters cannot be reconstructed and very few steps are below the full depletion voltage. Most of the sensors start reaching doping inversion around the end of 2017. The evolution averaged over sensors of the same layers are provided until the end of 2017. As presented in Fig. 60 (right), the evolution scales with fluence and depends on the sensor thickness as the depletion voltage directly depends on the thickness.

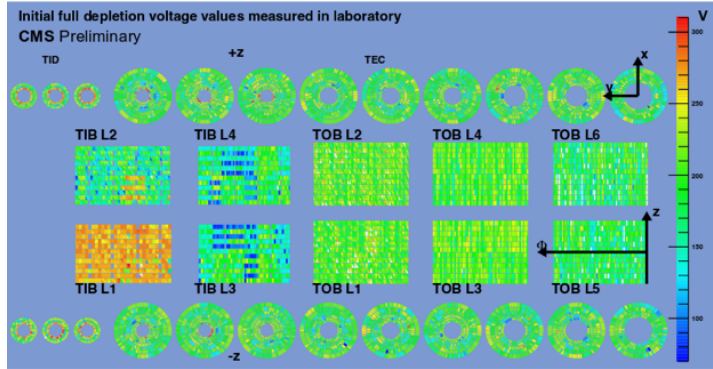


**Fig. 58:** The measured full depletion voltage for all CMS strip modules using CV curves prior to any irradiation.

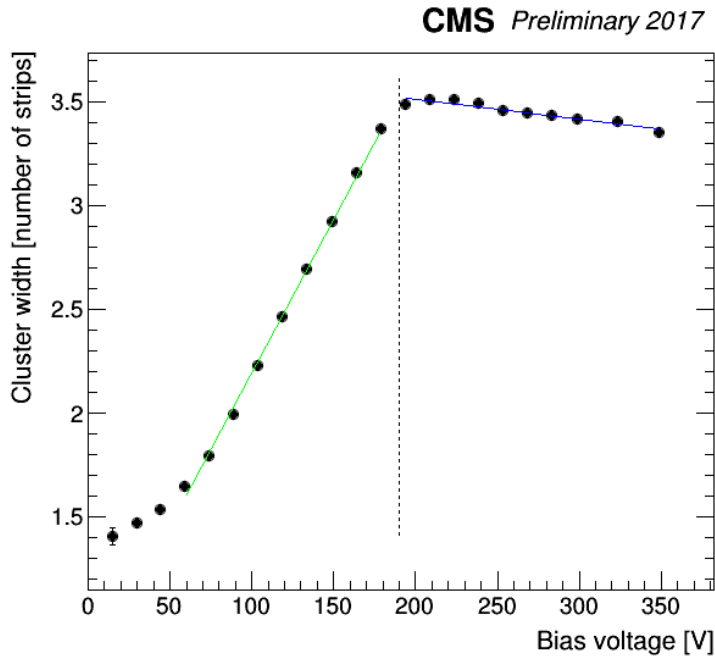


**Fig. 59:** Evolution of the cluster width as a function of the bias voltage. The saturation point is extracted from linear fits of the two regimes of the curve indicated in green and blue. Their crossing point gives the position of the full depletion voltage. See Ref. [3].

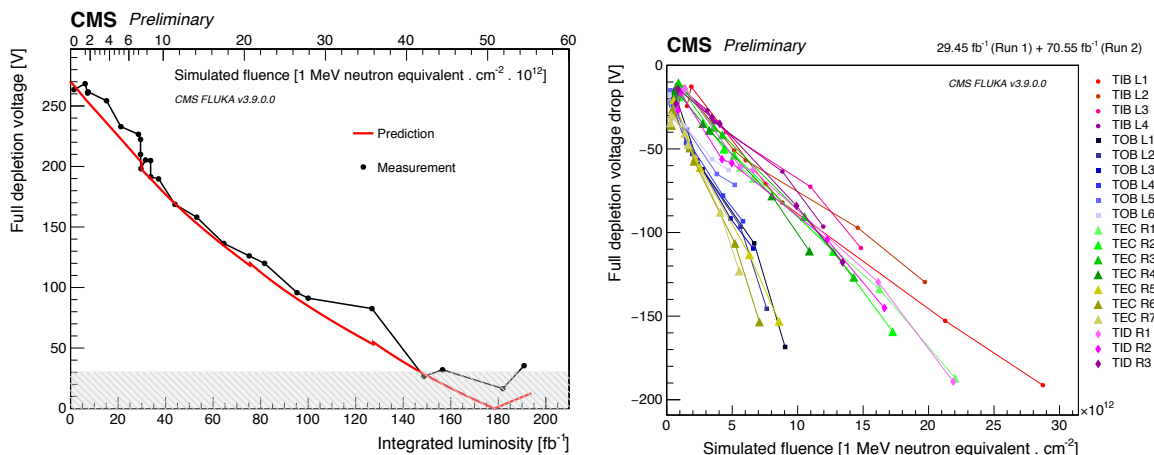


**Fig. 60:** Left: the measurement and prediction of the full depletion voltage in the CMS strip detector for a single module. The break in the simulation at about  $30 \text{ fb}^{-1}$  is due to an extended period at room temperature due to the opening of the CMS detector and cooling plant maintenance. Additional breaks at  $75$  and  $130 \text{ fb}^{-1}$  occur during winter shutdown periods. The grey area denotes regions where the signal-to-noise is too low so that no clusters are reconstructed in the rising part of the average cluster width curve. Right: the measured full depletion voltage including all power supplies of the CMS strip detector, with scans taken twice per year. The two sets of curves correspond to the two groups of sensors with different thicknesses ( $320 \mu\text{m}$  and  $500 \mu\text{m}$ ).

### 5.3.2.5 LHCb vertex detector

Since 2015, there have been 16 charge collection efficiency scans with 13 voltage steps each. These scans are performed during the normal data taking by varying the bias voltage on only every fifth sensor. Most sensors are in their standard operating voltage and thus the normal tracking algorithms can be executed, excluding the sensors with a varied bias voltage. The actual charge collection efficiency is estimated by fitting the distribution of analogue-to-digital counts to a convolution of a Landau and Gaussian. The *effective depletion voltage* is defined as the voltage at which the most probable value of the fitted probability density reaches 80% of its maximum value. Figure 61 shows the evolution of the effective depletion voltage as a function of time since the start of Run 1. The VELO was kept cold during all of the shutdown, which is why the depletion voltage is predicted to be constant. The sensors were purposefully heated near the end of Run 2 by changing the temperature from  $-30$  to  $-25 \text{ }^\circ\text{C}$  for three days (during a technical stop). This engineered beneficial annealing reduced the effective depletion voltage by about  $70 \text{ V}$ , as indicated in Fig. 62. Decreasing the depletion voltage with purposeful heating is a potentially powerful technique, but also requires high-fidelity simulation tools.

### 5.3.2.6 LHCb tracker turicensis

The full depletion voltage for the LHCb TT detector is determined from charge collection efficiency scans. Such scans are performed two to four times per year, including just before the winter shutdown and at the beginning of the LHC operations in the spring. The whole scan takes 2–3 hours, with eleven different bias voltage steps. The actual charge used for the extraction is determined as the most probable value from a fit of two Gaussian distributions and two Landau distributions all convolved with each other and fit to the analogue-to-digital-conversion values. The second Landau is used to account for  $e^+e^-$  pairs from photon conversions that deposit twice as much charge as a single minimum ionizing particle. Integrating these most probable values over different time samplings results in an estimate of the total charge. The actual depletion voltage is determined using a fifth-order spline with a constant plateau. Figure 63 reports the predicted and measured full depletion voltage (defined as the voltage

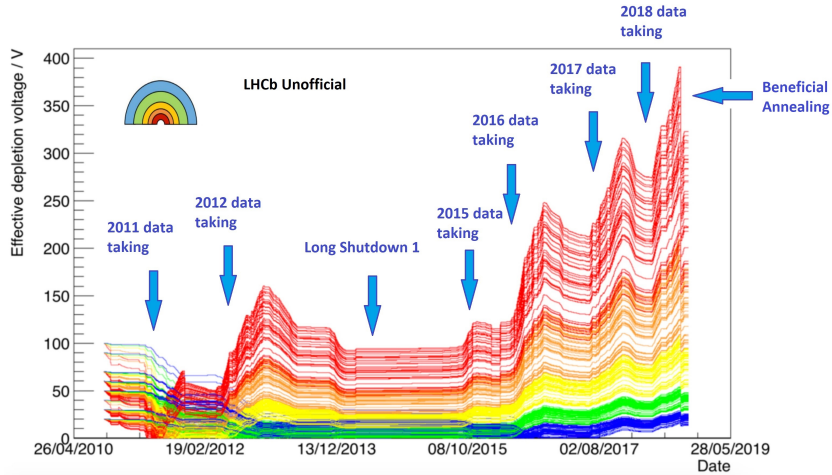


**Fig. 61:** The predicated full depletion voltage as a function of time since the beginning of Run 1 until the end of Run 2. Annotated arrows indicate LHC events, including periods of data taking and the long shutdown between Runs 1 and 2.

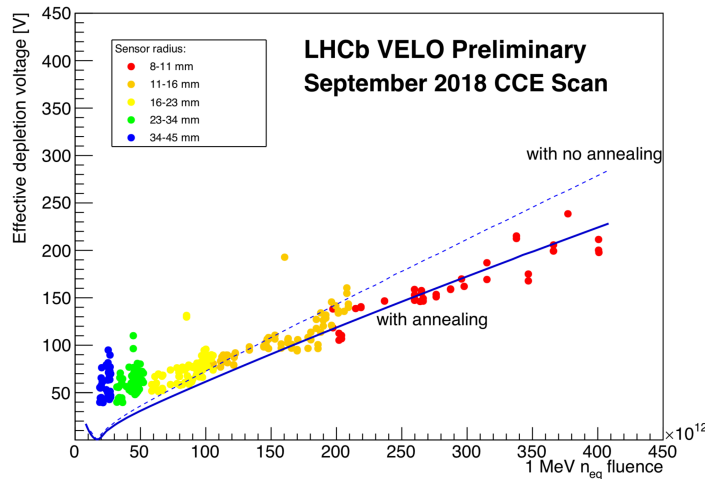


**Fig. 62:** The full depletion voltage as a function of fluence. Measurements are coloured based on their proximity to the interaction point. The impact of annealing is shown in the dashed line.

corresponding to 94% of the plateau value). Measurements and predictions as a function of fluence are presented in Fig. 64. At the time of the reported measurement, the sensors had not yet undergone space-charge-sign inversion.

Additional observables have been studied to probe the detector response to non-ionizing energy loss. modelling these observables is more complicated than for the leakage current and full depletion voltage because they require a simulation of the electric field profile inside the sensor bulk. While all of the silicon systems in ATLAS, CMS, and LHCb have measured the leakage current and depletion voltage, the catalogue of additional measurements is not as complete. Therefore, many of the following sections show measurement highlights from only one or two experiments.

### 5.3.3 Hit/cluster efficiency

The charge and hit efficiencies are often studied only during bias voltage scans, but can also be monitored during normal data taking conditions. Figure 65 shows the measured hit efficiency in the innermost layer

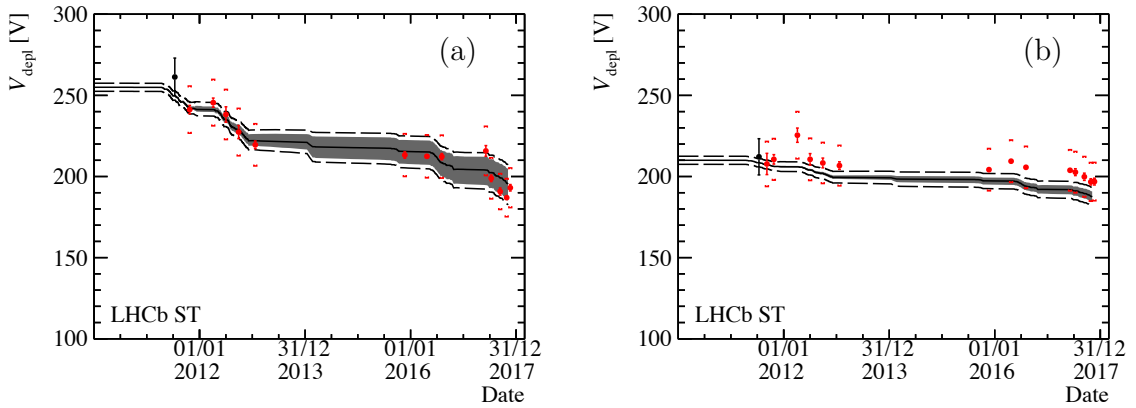


**Fig. 63:** The full depletion voltage in the LHCb tracker turicensis as a function of time [7]. The left plot is for sensors closer to the beam pipe (left) and further away from the beam pipe (right). The uncertainty band on the Hamburg model prediction corresponds to uncertainty in the model parameters while the black dashed band represents the uncertainty in the initial depletion voltage.

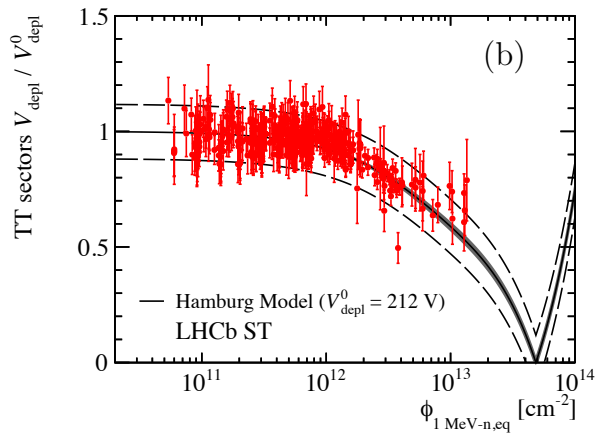


**Fig. 64:** The measured and predicted depletion voltage as a function of fluence in the LHCb tracker turicensis [7]. The black solid curve shows the predictions from the stable damage part of the Hamburg model and the band represents the model parameter uncertainty. This prediction is averaged over all sensors and the dashed line shows the standard deviation of the distribution of the initial full depletion voltages.

of the ATLAS strip detector in 2018. A 1% drop in the efficiency was recovered when the high voltage was adjusted from 150 V to 250 V after about  $45 \text{ fb}^{-1}$ .

The LHCb VELO community has also extensively studied the efficiency. One surprise, shown in Fig. 65 is that there are regions of low efficiency in the regions furthest away from the collisions (lowest fluence) that form after irradiation. This loss in efficiency has been connected with the second metal layer effect (see Ref. [13] for details). LHCb also took advantage of a unique opportunity at the end of Run 2. Since the VELO operation ended in Run 2 (replaced with a new detector for Run 3), potentially destructive high voltage scans were performed to determine how much the cluster finding efficiency could be recovered as well as probe for thermal runaway. The design voltage of the power supplies is only 500 V, but scans were conducted up to 700 V. The results of this study are shown in the right plot of Fig. 66. There is a drop in the efficiency for the innermost part of the detector that is recovered when the high voltage is increased. Going from 500 to 700 V actually increases the efficiency by about 2%.

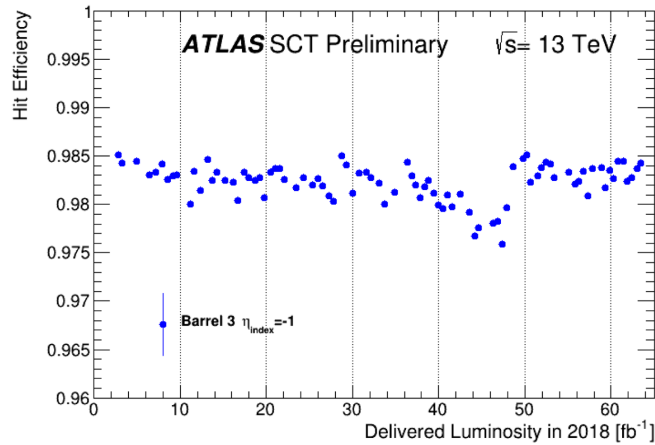


**Fig. 65:** The measured hit efficiency on the innermost barrel layer of the CMS strip detector in 2018 just before and after the high voltage was increased.

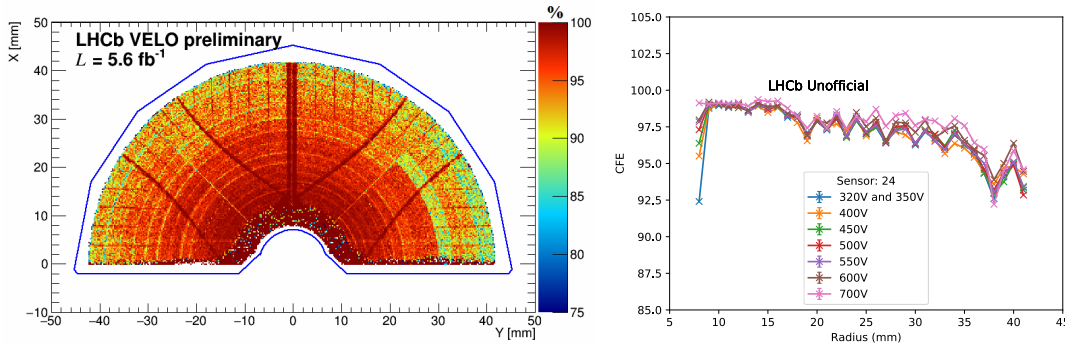


**Fig. 66:** Left: the cluster finding efficiency map as a function of location inside one of the VELO sensors. The position of the straight dark lines agree with the position of routing lines. Right: the cluster finding efficiency during the final high voltage scan at the end of Run 2 as a function of radius inside the LHCb VELO sensors.

### 5.3.4 Collected charge

While the impact of charge trapping on the hit efficiency is  $\mathcal{O}(1\%)$  over Run 2, the impact on the collected charge can be much larger,  $\mathcal{O}(10\%)$ . Figure 67 presents a measurement of the measured charge and cluster size throughout Run 2 for the innermost layer of the ATLAS pixel detector. Jumps in the pixel cluster properties are due to changes in the operational conditions, most notably the high voltage. During periods of constant conditions, the charge and cluster size decreases with integrated luminosity. About 30% of the charge is now lost after the full Run 2.

### 5.3.5 Lorentz angle

The Lorentz angle depends strongly on temperature, but is also sensitive to deformations in the electric field within a sensor. One benefit of the Lorentz angle over other quantities like the charge collection efficiency is that the Lorentz angle is largely insensitive to charge trapping and instead directly probes the bulk electric field. Figure 68 shows the measured Lorentz angle for the ATLAS IBL detector throughout Run 2. During periods of constant temperature, the Lorentz angle is observed to be approximately proportional to the fluence. The fitted values of the response  $\partial\theta_L/\partial\Phi$  are presented in Table 11. When

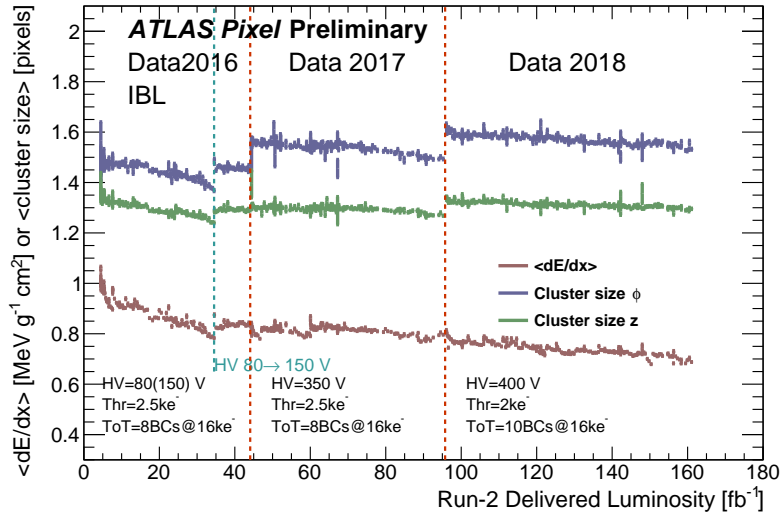


**Fig. 67:** The measured charge, longitudinal cluster size ( $z$ ), and transverse cluster size ( $\phi$ ) as a function of the delivered integrated luminosity in Run 2 for the ATLAS IBL.

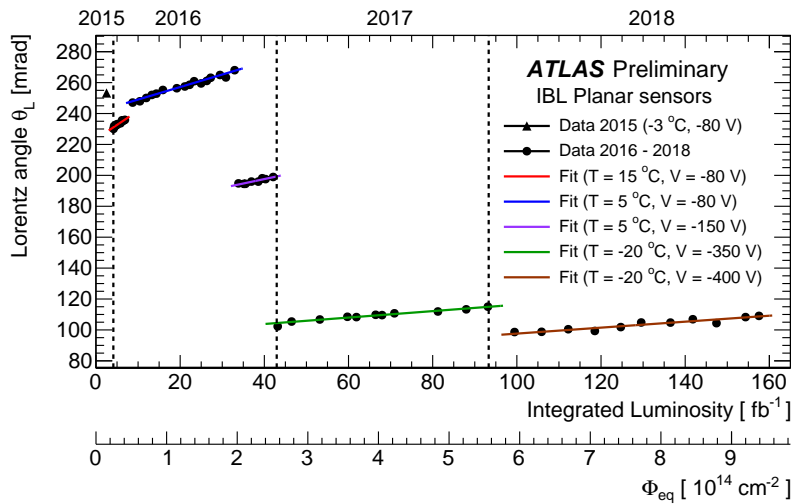


**Fig. 68:** The measured Lorentz angle during Run 2 in the ATLAS IBL

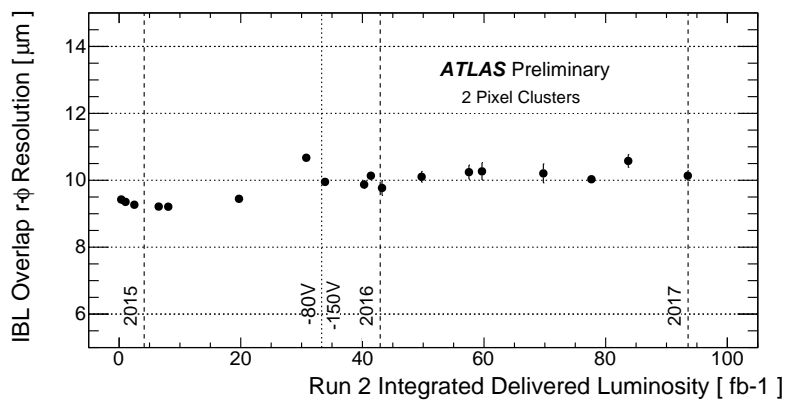
keeping the voltage constant, lower temperatures yield to smaller slopes. When keeping the temperature constant, higher voltages yield to smaller slopes.

### 5.3.6 Position resolution

The single cluster position resolution is sensitive to degraded charge information from charge trapping, mostly on the periphery of clusters due to lost hits. One challenge with *in situ* measurements of the single cluster position resolution is that they suffer from a large extrapolation/interpolation resolution that can mask subtle time-dependent effects. An alternative approach deployed by ATLAS for the IBL detector makes use of overlapping modules [14, 15]. In particular, the position resolution can be determined from a single layer for particles that traverse two modules on the same layer. Figure 69 presents a measurement of the corresponding resolution throughout most of Run 2 for the IBL detector. The slight worsening of the spatial resolution observed over the three years is correlated with the reduction of charge collection efficiency as a result of radiation damage. This may have important implications for flavour tagging

**Table 11:** Summary of the values for the intercepts and slopes obtained from linear fits to the Lorentz angle as a function of the fluence for fixed temperature  $T$  and high voltage  $V$ .

Temperature	Voltage	$\theta_L(\Phi_{\text{eq}} = 0)$ (Mrad)	$(\partial\theta_L/\partial\Phi_{\text{eq}})_{T,V}$ (Mrad·cm <sup>2</sup> )
15 °C	80 V	$223.5 \pm 1.0$	$(30.6 \pm 3.0) \cdot 10^{-14}$
5 °C	80 V	$240.9 \pm 0.7$	$(13.6 \pm 0.6) \cdot 10^{-14}$
	150 V	$174.6 \pm 3.6$	$(9.6 \pm 1.6) \cdot 10^{-14}$
−20 °C	350 V	$95.5 \pm 1.3$	$(3.5 \pm 0.3) \cdot 10^{-14}$
	400 V	$78.3 \pm 2.8$	$(3.2 \pm 0.4) \cdot 10^{-14}$

**Fig. 69:** The measured position resolution on the ATLAS IBL as a function of integrated luminosity during Run 2 [14, 15].

and other downstream track reconstruction tasks that depend on a precise position measurement on the innermost layer.

#### 5.4 Discussion and outlook

Measurements of silicon detector response to non-ionizing energy loss is essential for every facet of data collection, analysis, and future planning. The previous sections have shown that there is an extensive measurement program from ATLAS, CMS, and LHCb, with a variety of important and unforeseen results. However, there are also many challenges associated with performing and interpreting these results. While many of these challenges are not often discussed in public documentation, they are critically important for improving methods and planning for the future. This is not exhaustive.

1. *Leakage current:* on the measurement side, it is not 100% clear how to define the leakage current. In theory, the current should raise, plateau, and then raise again as the high voltage is increased from zero up through breakdown. The current at the plateau region is the theoretical definition of the leakage current. The left plot of Fig. 70 shows a typical IV scan. While the current does level off beyond some voltage, there is no region where it is flat. This results in (an often unaccounted for) uncertainty in the reported current. Furthermore, the current depends strongly on temperature, as shown in the right plot of Fig. 70. This leads to a challenge because the temperature on the sensors is often not known precisely. In many cases, the temperature is measured far from the sensors and inferred from simulations or auxiliary measurements. This affects both the leakage



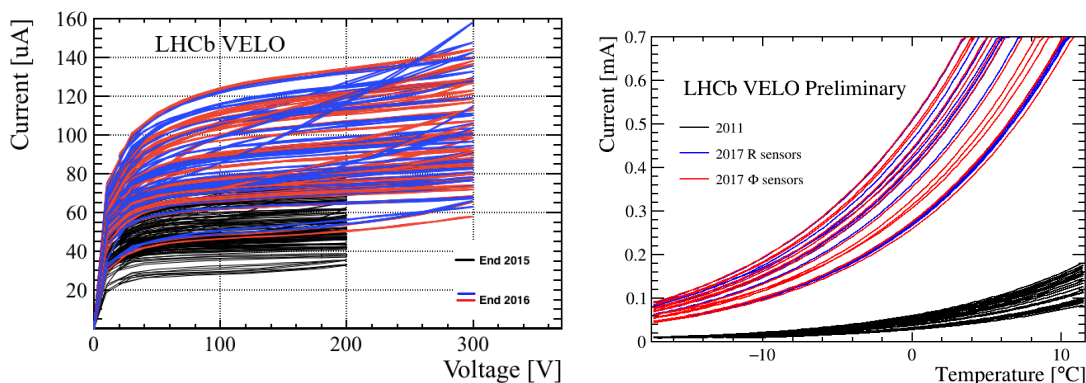


**Fig. 70:** Example current–voltage (IV) (left) and current–temperature (IT) (right) scans for the LHCb VELO detector [13].

current estimates and their interpretation because both require the measured temperature as input. A further complication is that the effective bandgap energy  $E_{\text{eff}}$  from Eq. 25 seems to anneal and may behave differently for charged/neutral hadron irradiation. For the interpretation, the  $\alpha_j$  values in Eq. 21 have a significant unaccounted uncertainty related to damage factors used to converge between proton or pion fluxes and 1 MeV  $n_{\text{eq}}$ . There is also ambiguity in how to model periods of non-constant temperature. Despite these challenges, the time dependence of the leakage current modelling appears to be accurate across experiments and across detector layers.

2. *Depletion voltage*: as with the leakage current, there is a large ambiguity in the definition of the full depletion voltage. For scans of the collected charge or cluster size, the actual values do not saturate, so an *ad hoc* definition must be used (often fitting two lines and taking the kink position). As the previous sections have highlighted, each experiment and detector subsystem has a different definition. In fact, the full depletion voltage is not even well defined at high fluence when the electric field can have regions of low field within the bulk. As most measurements of the depletion voltage require active collision conditions, they are performed infrequently to not interfere with data collection for physics analysis. This makes it difficult to constrain and tune simulation models. On the simulation side, there is currently no model that includes both annealing and non-trivial depth-dependent doping concentrations. This could be one reason why both ATLAS and CMS see significant deviations between model and measurement towards the end of Run 2. Fortunately, the simulations over-estimate the measurements and thus are conservative. Additional challenges with the predictions arise from the fact that the introduction rates are not well known for charged and neutral hadrons. There is a strong need for the community to develop an improved model for depletion voltage in Run 3 and beyond. The notion of full depletion may not be well-defined, but each detector needs to pick a bias voltage for safe and effective operations.
3. The other observables introduced in previous sections have similar challenges, with further complications on the interpretation because a full detector simulation is required.

Despite the challenges with the interpretation of the data presented in the chapter, there are a variety of important messages from the extensive measurement campaign from all of the LHC experiments. In particular:

- the silicon leakage current predictions are in general in good agreement with measurements at the LHC experiments. However, the simulated 1 MeV neutron equivalent fluence seems to underestimate the pixel data in the region 5–15 cm from the interaction point. The reason for this is not yet understood. Nonetheless, the uncertainties associated with the model predictions are now much better constrained and understood, giving increasing confidence of predictions at the LHC

upgrades. See also Section 4.5;

- the Hamburg model for annealing agrees with the time dependence of the leakage current data to within about 10% (ignoring the overall offset described in the previous bullet), although there are indications that it may no longer be precise enough at the end of the LHC. The depletion voltage data are harder to model and work will be required to make this a precise predictive tool for the future;
- despite the extensive radiation damage, track reconstruction remains relatively robust and the current impact on physics analysis is relatively minimal. As the probability of a charge to be trapped becomes  $\mathcal{O}(1)$ , radiation damage effects will be a non-negligible challenge for our tracking detectors;
- as various detectors have been or are being upgraded, there is a unique opportunity to stress test the detectors in order to take valuable diagnostic data. This was demonstrated by the LHCb experiment in their final high-voltage scan of the VELO detector before it was decommissioned.

To summarize, this section has reported various measurements of the silicon sensor response to non-ionizing radiation from collisions in the LHC. A variety of probes have resulted in a detailed diagnostic information that can be used for modifying models, guiding operation and upgrades, as well as improving the quality of offline reconstruction. Expanding and enhancing this measurement program into Run 3 and the HL-LHC will be critical for preserving and possibly enhancing physics analysis as radiation damage becomes even more prominent. Addressing the challenges outlined in this section will involve community collaboration and sharing of ideas, which has already begun as a result of the workshop series that inspired this report.

## References

- [1] G. Avoni *et al.*, *JINST* **13** (2018) P07017, doi:[10.1088/1748-0221/13/07/P07017](https://doi.org/10.1088/1748-0221/13/07/P07017).
- [2] M.P. Rauch, Ph.D. thesis, RWTH Aachen University, 2020, doi:[10.18154/RWTH-2020-05630](https://doi.org/10.18154/RWTH-2020-05630).
- [3] N. Tonon, [Search for the associated production of a single top quark and a Z or Higgs boson with the CMS experiment](#), Thèse de Doctorat, 2019STRAE022, Université de Strasbourg, 1er Octobre 2019.
- [4] M. Moll, [Radiation damage in silicon particle detectors: Microscopic defects and macroscopic properties](#), Ph.D. thesis, Hamburg Univ., 1999, DESY-THESIS-1999-040.
- [5] R.S. Harper, Radiation Damage Studies of Silicon Detectors and Searching for an Intermediate Mass Higgs Boson at ATLAS, PhD thesis, Univ. Sheffield, 2001.
- [6] ATLAS Collaboration, *JINST* **14** (2019) P06012, doi:[10.1088/1748-0221/14/06/P06012](https://doi.org/10.1088/1748-0221/14/06/P06012),
- [7] C. Abellan Beteta *et al.*, *JINST* **15** (2020) P08016, doi:[10.1088/1748-0221/15/08/P08016](https://doi.org/10.1088/1748-0221/15/08/P08016).
- [8] A. Chilingarov, Temperature dependence of the current generated in Si bulk. *JINST* **8** (2013) P10003, doi:[10.1088/1748-0221/8/10/p10003](https://doi.org/10.1088/1748-0221/8/10/p10003).
- [9] ROSE Collaboration, [3rd RD48 status report](#), CERN-LHCC-2000-009 (CERN, Geneva, 2009).
- [10] S.I. Parker, C.J. Kenney, J. Segal, *Nucl. Instrum. Methods Phys. Res.* **A395** (1997) 328, doi:[10.1016/S0168-9002\(97\)00694-3](https://doi.org/10.1016/S0168-9002(97)00694-3).
- [11] ATLAS Collaboration, [Measurement of radiation damage through leakage current monitoring of the ATLAS pixel detector](#), ATL-INDET-PUB-2019-001 (CERN, Geneva, 2019).
- [12] ATLAS Collaboration, [SCT radiation damage plots, prepared for Radiation damage workshop](#), ATL-SCT-2019-001; K Mochizuki, Sensor measurements with the ATLAS SCT, Radiation effects in the LHC experiments and impact on operation and performance, CERN, 11–12 Feb. 2019, [Indico](#).
- [13] K. Akiba *et al.*, *IEEE Trans. Nucl. Sci.* **65** (2018) 1127 doi:[10.1109/TNS.2018.2824618](https://doi.org/10.1109/TNS.2018.2824618).
- [14] ATLAS Collaboration, [IBL hit spatial resolution](#), ATL-PIX-2018-002 (CERN, Geneva, 2018).

- [15] ATLAS Collaboration, [IBL efficiency and single point resolution in collision events](#), ATL-INDET-PUB-2016-001 (CERN, Geneva, 2016).
- [16] ATLAS Collaboration, *JINST* **9** (2014) P08009, doi: [10.1088/1748-0221/9/08/P08009](https://doi.org/10.1088/1748-0221/9/08/P08009).
- [17] ATLAS Collaboration, [Luminosity determination in  \$pp\$  collisions at  \$\sqrt{s} = 13\$  TeV using the ATLAS detector at the LHC](#), ATLAS-CONF-2019-021 (CERN Geneva, 2019).



## 6 Impact of radiation on electronics and opto-electronics

*Editors: M. Bindi<sup>a</sup>, E. Butz<sup>b</sup>.*

*Contributing authors: M. Backhaus<sup>c</sup>; M. Bindi<sup>a</sup>; P. Butti<sup>d</sup>; E. Butz<sup>b</sup>; E. Chabert<sup>e</sup>; S. Chen<sup>f</sup>; J. Dickinson<sup>g</sup>; W. Erdmann<sup>h</sup>; J. Garcia Pascual<sup>i</sup>, R. Gerosa<sup>j</sup>; B. Haney<sup>f</sup>; H. Hillemanns<sup>k</sup>; K. Lantzsch<sup>l</sup>, A. LaRosa<sup>k</sup>; K. Padeken<sup>l</sup>; F. Pinto<sup>m</sup>; G. Pownall<sup>n</sup>; D. Robinson<sup>o</sup>; A. Rozanov<sup>p</sup>; J. Troska<sup>k</sup>; T. Weidberg<sup>q</sup>.*

<sup>a</sup>Georg August University of Göttingen, Germany

<sup>b</sup>Karlsruhe Institute of Technology, Germany

<sup>c</sup>ETH, Zürich, Switzerland

<sup>d</sup>SLAC, Stanford, USA

<sup>e</sup>Hubert Curien Pluridisciplinary Institute (IPHC), Strasbourg, France

<sup>f</sup>University of Pennsylvania, USA

<sup>g</sup>Fermilab, Batavia, USA

<sup>h</sup>PSI, Villingen, Switzerland

<sup>i</sup>IHEP, Beijing, China

<sup>j</sup>University of California San Diego, USA

<sup>k</sup>CERN, Geneva, Switzerland

<sup>l</sup>University of Bonn, Germany

<sup>m</sup>University of Seville, Spain

<sup>n</sup>DESY, Hamburg, Germany

<sup>o</sup>University of Cambridge, United Kingdom

<sup>p</sup>CPPM, Marseille, France

<sup>q</sup>University of Oxford, United Kingdom

In this chapter we will present the results of the impact of radiation on electronics and opto-electronics for two of the LHC experiments during Run 1 and Run 2. ATLAS results are presented in Section 6.1; CMS in Section 6.2. In Section 6.3 we will present a comparison between the two experiments, highlighting operational guidelines and proposing solutions to build the electronics and opto-electronics of the future LHC experiments.

### 6.1 ATLAS

Radiation effects from TID on the IBL front-end electronics will be described in Section 6.1.1; SEU/SET effects from highly ionizing particles in IBL and SCT detectors will be shown in Section 6.1.2 whilst impact on opto-electronics from SCT will be described in Section 6.1.3. Finally, results from TRT electronics will be presented in Section 6.1.4.

#### 6.1.1 TID effects in the IBL front-end chip

The IBL consists of 14 carbon fibre staves instrumented along 64 cm, 2 cm wide, and tilted in  $\phi$  by  $14^\circ$  surrounding the beam pipe at a mean radius of 33 mm from the beam axis and providing a pseudo-rapidity coverage of  $\pm 3$ . Each stave, with integrated CO<sub>2</sub> cooling, is equipped with 32 front-end chips bump bonded to silicon sensors. The IBL detector was designed to be operational until the end of the LHC Run 3, where the total integrated luminosity was expected to reach  $300 \text{ fb}^{-1}$ . The detector components are qualified to work up to 250 Mrad of TID.

---

This chapter should be cited as: Impact of radiation on electronics and opto-electronics, Eds. M. Bindi, E. Butz, DOI: [10.23731/CYRM-2021-001.87](https://doi.org/10.23731/CYRM-2021-001.87), in: Radiation effects in the LHC experiments: Impact on detector performance and operation, Ed. I. Dawson,

CERN Yellow Reports: Monographs, CERN-2021-001, DOI: [10.23731/CYRM-2021-001](https://doi.org/10.23731/CYRM-2021-001), p. 87.

© CERN, 2021. Published by CERN under the [Creative Commons Attribution 4.0 license](https://creativecommons.org/licenses/by/4.0/).

The IBL front-end chip, namely FE-I4B [1], was designed in 130 nm CMOS technology which features an array of  $80 \times 336$  pixels with a pixel size of  $50 \times 250 \mu\text{m}^2$ . Each pixel contains an independent, free running amplification stage with adjustable shaping, followed by a discriminator with independently adjustable threshold. The FE-I4B keeps track of the time-over-threshold (ToT) of each discriminator with 4-bit resolution, in counts of an external supplied clock of 40 MHz frequency. The FE-I4B operates by feeding the common power supply to analogue signal amplifiers and digital signal-process circuits, referred to as the low-voltage (LV) power supply and the clock input.

### 6.1.1.1 Observations during 2015 data taking

During the first year of the IBL operation in 2015, a significant increase of the LV current of the front-end chip and a detuning of its parameters (threshold and time-over-threshold) have been observed in relation to the received TID.

The average LV current of the IBL module groups (serving four FE-I4B chips) during data taking was stable at a value of 1.6–1.7 A until the middle of September 2015. Then, the current started to rise up significantly (see Fig. 71), and the change of the current during the period September–November 2015 was even more than 0.2 A within a single LHC fill, depending on the luminosity and duration of the fill. Due to safety concerns, after  $\sim 2 \text{ fb}^{-1}$  of integrated luminosity corresponding to  $\sim 580 \text{ krad}$  of TID, the IBL was switched off in early October 2015. The detector was kept off during two LHC fills for a total of  $\sim 240 \text{ pb}^{-1}$  of integrated luminosity, corresponding to  $\sim 70 \text{ krad}$  irradiation from the LHC beam. A complete return to the baseline of the LV currents was observed when the detector was powered up again. However, as soon as the LHC beam irradiation restarted with the detector being powered, the raising behaviour of the LV current appeared again with similar characteristics.

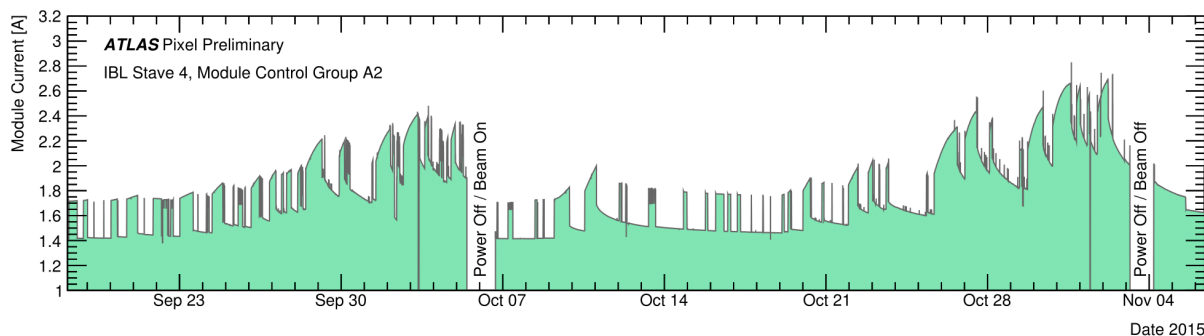


**Fig. 71:** LV current drift of an IBL module group (serving four FE-I4B chips) during 2015 data taking. There are two levels of the current depending on the front-end configuration: STANDBY (lower level, with pre-amplifiers off) and READY (higher level, with pre-amplifiers on). There are two long power-off periods on October 5–6 (with the LHC beam ON) and November 3–4 (during a LHC technical stop).

With the increase of the LV current, the temperature of IBL modules also changes (see Fig. 72). In addition, as shown for example in Fig. 73, the calibration of the FE-I4B chips for the analogue discriminator threshold and the target ToT drifted rapidly despite a frequent update of the calibration.

The increase of the LV current of the FE-I4B chip and the drifting of its tuning parameters were traced back to the generation of a leakage current in NMOS transistors induced by radiation. The radiation induces positive charges that are quickly trapped into the shallow-trench-isolation (STI) oxide at the edge of the transistor. Their accumulation builds up an electric field sufficient to open a source-drain channel where the leakage current flows. If the accumulation of positive charges is relatively fast, the formation of interface states is a slower process. The negative charges trapped into interface states start to compete with the oxide-trapped charges with a delay. This is what gives origin to the TID effect at low dose [3] which is discussed in more detail in Section 2.2.1.

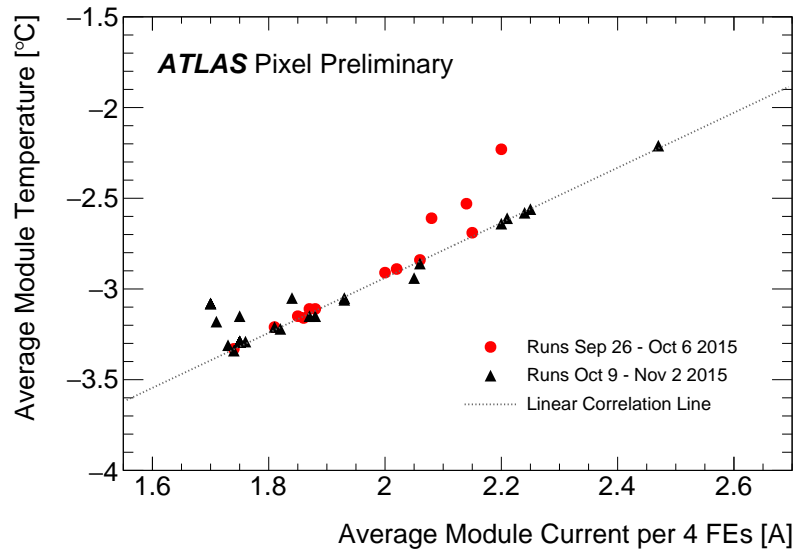


**Fig. 72:** Performance of the IBL modules during high luminosity proton–proton collision runs from September to November 2015, separated into the periods before (red circles) and after (black triangles) the long power-off on October 6. The average IBL module current (4 FE-I4B) is displayed against the average module temperature [2] and compared to a linear dependence.

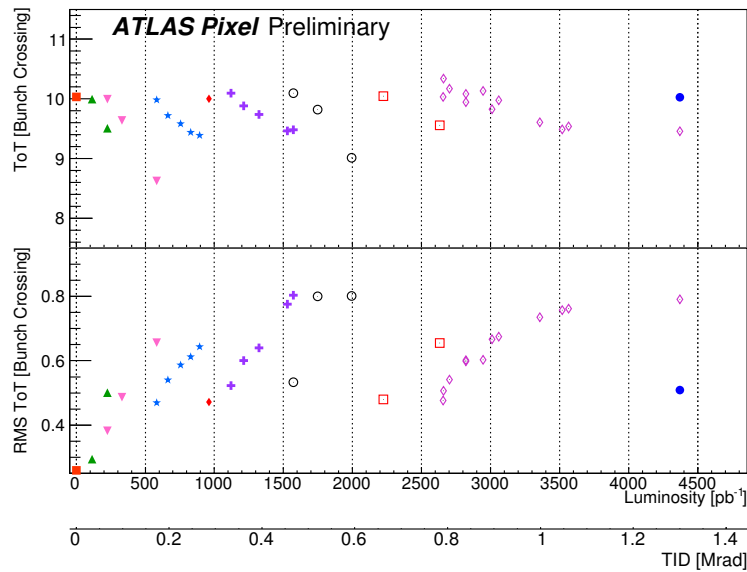


**Fig. 73:** The time-over-threshold (ToT) and its RMS as a function of the integrated luminosity or TID [2]. The detector was regularly retuned, and each marker type corresponds to a single tuning of the detector.

### 6.1.1.2 Irradiation test results

Dedicated laboratory measurements [4] of irradiated single transistors in 130 nm CMOS commercial technologies showed that the increase of the leakage current reaches its peak value between 1 Mrad and 3 Mrad. For higher TID the current decreases to a value close to the pre-irradiated one.

To reproduce and analyse the effects described above during the IBL operation, several irradiations and electrical tests were performed [2]. Since the current increase in NMOS transistors depends on dose rate and temperature, measurements under different temperature and dose rate conditions have been

carried out to qualify this dependency.

The first irradiation test aimed at measuring the boundary current (at a given temperature and dose rate) that the chip always approaches after annealing periods and re-irradiation. Figure 74 shows the increase of the current consumption of a single FE-I4B chip in data taking condition as a function of the TID. The temperature of the chip was 38 °C and the dose rate 120 krad h<sup>-1</sup>. After reaching the maximum of each peak the chip was annealed for several hours resulting in the observed partial recovery.

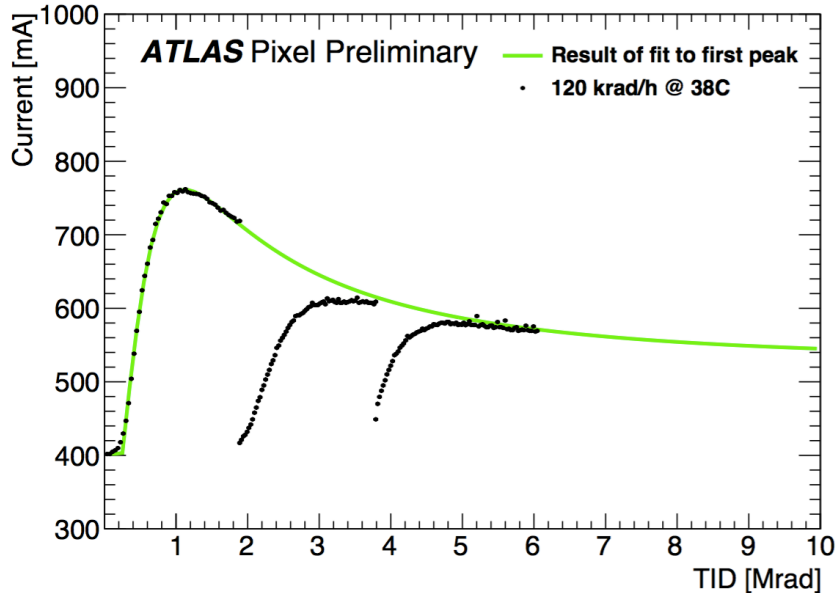


**Fig. 74:** Current consumption of a single FE-I4B chip in data taking condition as a function of the TID. The temperature of the chip was 38 °C and the dose rate 120 krad h<sup>-1</sup>. After reaching the maximum of each peak the chip was annealed several hours resulting in the observed partial recovery [2]. The fit performed on the first set of data (first peak) has been carried out by using the current parametrization described in Ref. [5].

In order to study the dependence of the LV current increase on temperature and dose rate several irradiation tests were performed by setting one of those variables and changing the other. Figure 75 shows the results of three different measurements, performed with three different and previously not irradiated chips. The dose rate was 120 krad h<sup>-1</sup> and the temperatures were 38 °C, 15 °C, and -15 °C. Before irradiation, the LV current of the three chips was 400 mA (38 °C), 360 mA (15 °C), and 380 mA (-15 °C). For comparison, Fig. 76 shows the result of two different measurements where the temperature was kept fix at 15 °C, while the dose rate set to 120 krad h<sup>-1</sup> or 420 krad h<sup>-1</sup>. Also in this case the tests were performed with different and previously not irradiated chips. The measurements described above revealed two facts:

- at a given dose rate the LV current increase is stronger at lower temperatures;
- at a given temperature, the LV current increase is stronger at higher dose rates.

To simulate the dose rate conditions of the 2015 and 2016 data taking, a first irradiation was performed at -15 °C and 120 krad h<sup>-1</sup>. This was followed by several hours of annealing and a second irradiation this time performed at 5 °C and 420 krad h<sup>-1</sup>. As shown in Fig. 77, the second LV current peak is lower than the first one, i.e., by increasing the operational temperature of the chip it was possible to keep the increase of the LV current below the boundary current given by the first irradiation. To verify that a temperature of 5 °C was safe for the IBL detector operation, a measurement at 10 krad h<sup>-1</sup> was performed. The maximum LV current increase was of the order of 250 mA, which gives a LV current



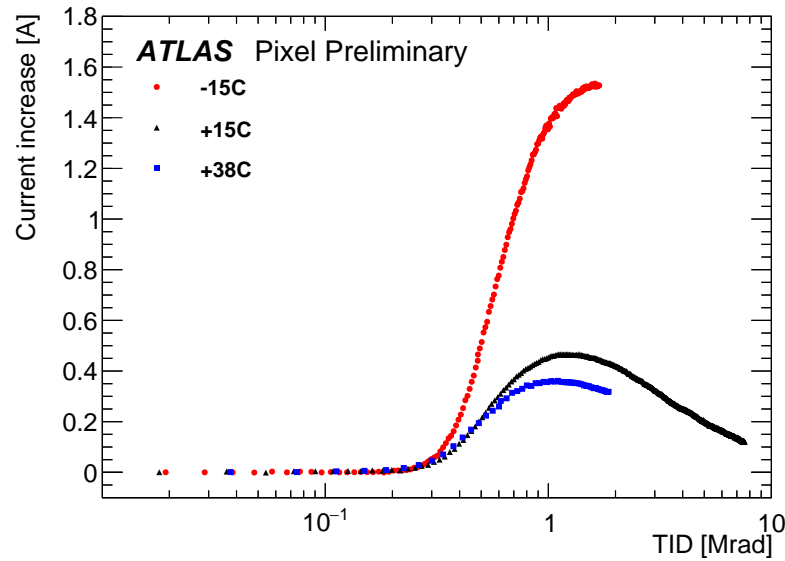


**Fig. 75:** Increase of the LV current of three single FE-I4B chips in data taking condition as a function of the TID ( $x$ -axis in log scale). Test measurements were carried out at 38 °C (blue), at 15 °C (black), and at –15 °C (red) with a dose rate of 120 krad h<sup>-1</sup>. A dose rate up to 10 krad h<sup>-1</sup> is expected in the experiment. The LV current of the single FE-I4B chips before irradiation were 400 mA (38 °C), 360 mA (15 °C), and 380 mA (–15 °C) [2].

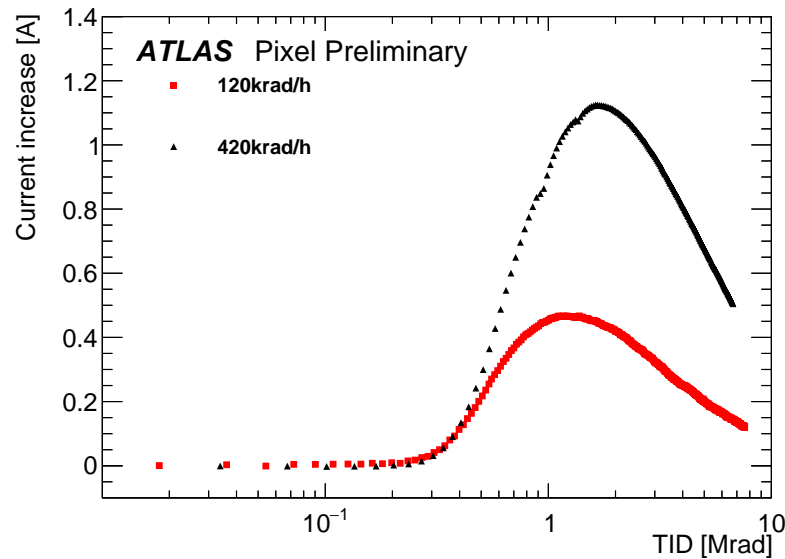


**Fig. 76:** Increase of the LV current of two FE-I4B chips in data taking as a function of the TID ( $x$ -axis in log scale). Test measurements were carried out at 15 °C with a dose rate of 120 krad h<sup>-1</sup> (red), and 420 krad h<sup>-1</sup> (black). A dose rate up to 10 krad h<sup>-1</sup> is expected in the experiment. The LV current of the single FE-I4B chips before irradiation were 380 mA (420 krad h<sup>-1</sup>) and 360 mA (120 krad h<sup>-1</sup>) [2].

increase of 1 A for a four-chip unit; this would not exceed the safety limit of the LV current originally set to 2.8 A. In principle, lower operational temperatures are favourable for the sensor performance and properties after irradiation and therefore preferred. Consequently, irradiation and electrical tests were

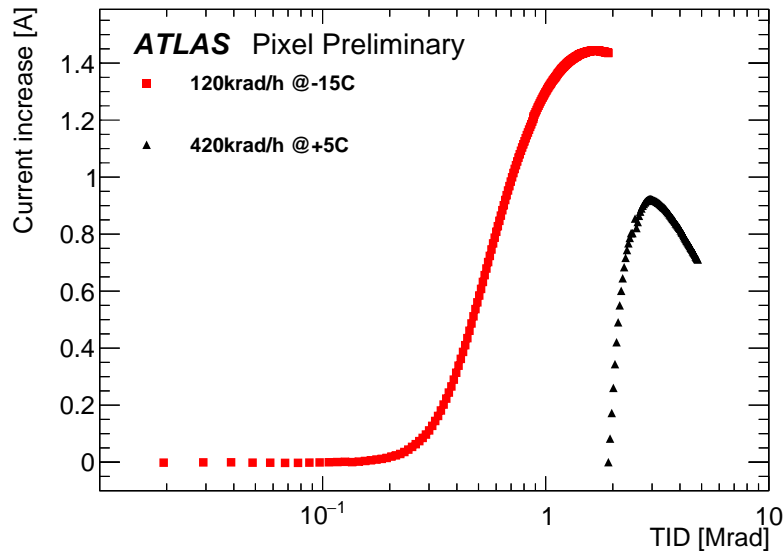


**Fig. 77:** Increase of the LV current of a single FE-I4B chip in data taking condition as a function of the TID ( $x$ -axis in log scale) during two consecutive irradiation campaigns in a lab measurement. Between the two irradiations several hours of annealing period at room temperature was performed, and resulted in the observed recovery. The TID of both irradiations is summed up. The LV current of a single FE-I4B chip before irradiation was 380 mA (first step) and 550 mA (second step) [2].

also performed at a temperature of  $0^{\circ}\text{C}$  to investigate the feasibility for a colder operation. In addition it was investigated the evolution of the maximum of the LV current peak under several irradiation steps followed, interleaved with periods of annealing. In this case the first two consecutive peaks of the LV current increase exceeded the maximum current allowed for a safe detector operation. Therefore, it was decided to set  $5^{\circ}\text{C}$  as minimum temperature for a safe and successful data taking.

Another effect was confirmed during the irradiation campaign of one FE-I4B chip with 16 MeV protons at room temperature (see Fig. 78). The chip was left without powering for 30 minutes in the beam, integrating a 2 Mrad dose (on top of the 9.2 Mrad of dose previously collected). As a result, the chip was completely annealed; this behaviour confirmed the observations with the IBL detector at LHC, with the return to baseline of the LV current consumption. The LHC data were taken with a module  $T \sim -7^{\circ}\text{C}$  on the 6 October 2015 (see Fig. 71). To be noticed that a similar effect was also observed during X-ray irradiation of CMS DC-DC converters (see Section 6.2).

### 6.1.1.3 Detector operation guidelines

Based on the observations during the first year of data taking in 2015 with the IBL detector, it was decided to raise the safety limit for the IBL LV currents from 2.8 A to 3 A for module groups of four chips, which means a maximum current consumption of 750 mA per chip. Since the average current consumption for a single FE-I4B chip is about 400 mA before irradiation, the increase of the current due to the TID effects cannot be higher than 350 mA per chip. Given the above results it was decided to increase the IBL operation temperature from  $-10^{\circ}\text{C}$  to  $15^{\circ}\text{C}$ . In addition, the digital supply voltage ( $V_D$ ) was lowered from 1.2 V to 1 V to decrease the LV current.

Thanks to dedicated measurements at  $5^{\circ}\text{C}$  and at a dose rate comparable to the LHC in 2016 ( $10\text{krad h}^{-1}$ ), it is proven that the current increase is of the order of 250 mA. With this a module group of four chips does not exceed the safety limit of 3 A. Therefore operating the IBL at  $5^{\circ}\text{C}$  is safe with respect to the expected luminosity in 2016. The temperature of the IBL cooling system was

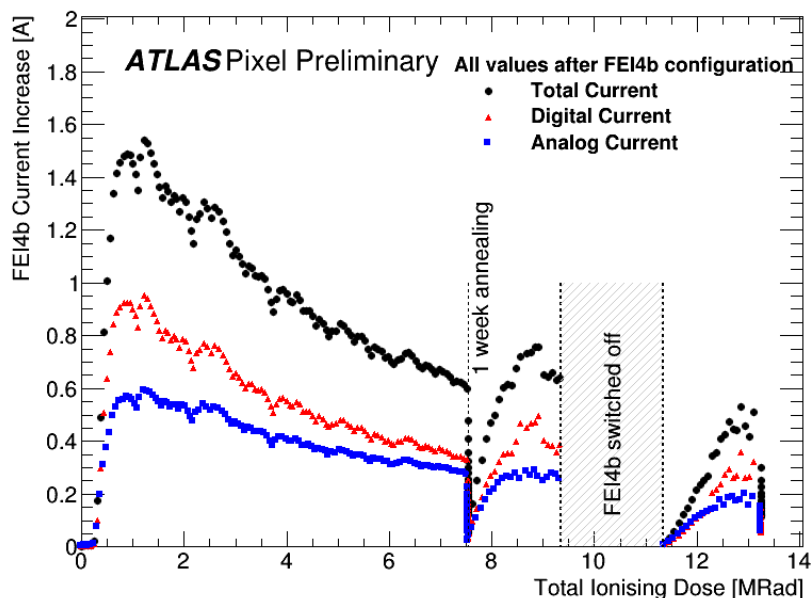


**Fig. 78:** LV current in a single FE-I4B chip during proton irradiation as a function of the TID delivered. The LV current is shown for the analogue and digital part of the FE-I4B chip, the sum of the two is also reported (total current). The LV current was monitored both during the irradiation and for about an hour afterward, showing an annealing effect. The FE-I4B chip was at room temperature and the dose rate was  $3 \text{ Mrad}\cdot\text{h}^{-1}$  for the first irradiation and  $4 \text{ Mrad}\cdot\text{h}^{-1}$  for the following campaign. The measurement was made in two steps, separated by one week in which the chip was not powered and left at room temperature. During the second irradiation, the chip was switched off for half an hour while the irradiation continued. In this measurement, the chip was irradiated with a 18 MeV proton beam [6].

lowered to a set point of  $5^\circ\text{C}$ . The digital supply voltage ( $V_D$ ) was raised from 1 V to 1.2 V, after an accumulated dose of  $\sim 4.3 \text{ Mrad}$  which, as the measurements show, is well beyond the high peak region for the current consumption. An overview of the mean LV current of the IBL FE-I4B chips as a function of integrated luminosity and TID during stable beam is shown in Fig. 79.

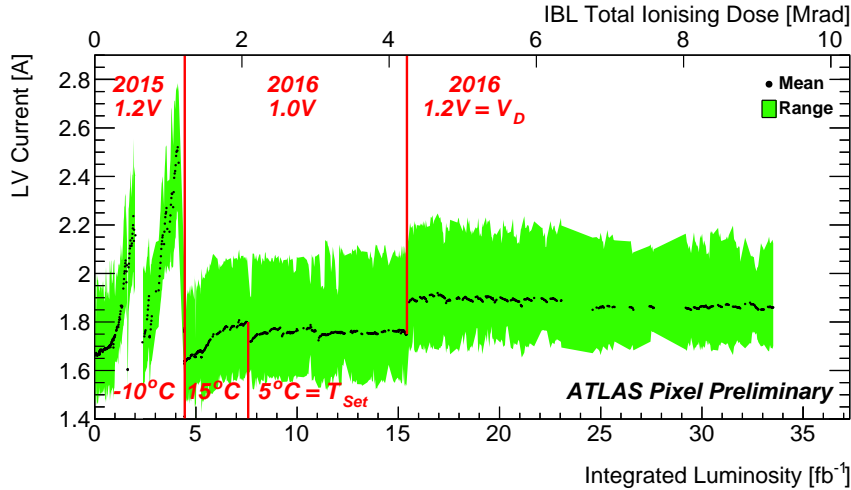
The LV currents are averaged for all modules across 100 luminosity blocks ( $\sim 100$  minutes), and the changes in digital supply voltage ( $V_D$ ) and the temperature ( $T_{\text{Set}}$ ) are highlighted. In addition, since the shift of the tuning parameters can be seen even at low dose rates and warmer temperatures, a re-tuning on a regular basis was performed.

#### 6.1.1.4 Observations collected at the end of Run 2

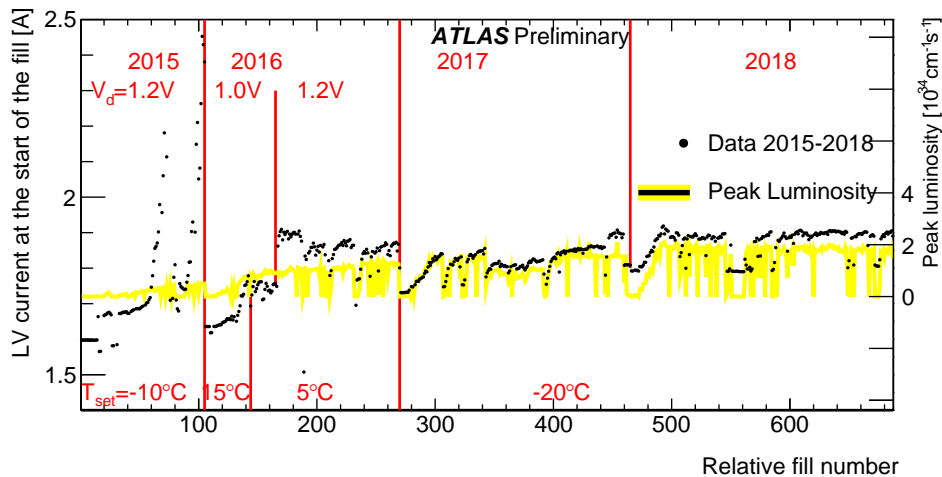
During the late years of Run 2 (2016–2018), the LHC instantaneous and integrated luminosity grow considerably respect to the previous years. The effect of the detector occupancy on the IBL LV currents became visible.

Figure 80 shows the average IBL LV current at the start of each stable beam period, whenever the FE-I4B pre-amplifiers were turned ON, for the entire Run 2 period. A clear correlation of the current consumption with the LHC peak luminosity was observed. This correlation became  $\sim 100\%$  for the difference between IBL LV currents at the start of each LHC fill ( $I_{\text{start}}$ ) and right before the fill, with amplifiers OFF ( $I_{\text{ampoff}}$ ), for 2017–2018 data (see Fig. 81). In this figure the TID effects are very small and the current difference is dominated by the chip digital activity proportional to the LHC peak luminosity.

Figure 82 shows the IBL LV current consumption during the inter-fill periods, when no beams were present in the machine and the FE-I4B pre-amplifiers were off. In this case, the only contribution comes from the integrated TID effect; such contribution became less and less effective, showing a sort



**Fig. 79:** Mean IBL LV current during stable beam against integrated luminosity and TID. Changes in digital voltage ( $V_D$ ) are highlighted. The set temperatures ( $T_{Set}$ ) of the modules correspond to actual module temperatures of about  $-5^\circ\text{C}$ ,  $20^\circ\text{C}$ , and  $10^\circ\text{C}$ . There were significant increases in LV current during 2015; this was addressed in 2016 by increasing the module temperatures and decreasing the digital voltage. The digital voltages were later increased back to decrease readout error frequency.



**Fig. 80:** Mean IBL LV current at the start of each stable beam fill (pre-amplifiers turned on)

of saturation on the LV currents in 2018 respect to the previous years.

Figure 83 shows the average IBL LV current consumption for FE-I4B chips with planar sensors that shares the same  $z$  coordinates. In total there are 56 FE-I4Bs per each  $z$  location. Higher current is present in the central part of the detector whilst a smaller impact is visible in the forward region. This increase of the current in the central  $z$  region is the sum of the TID effects and occupancy effects. The shape of the distribution is present during the entire Run 2 period.

#### 6.1.1.5 Summary

During the first year of data taking in 2015, a peculiar increase of the LV current of the FE-I4B chip and the detuning of its parameters (threshold and time-over-threshold) was observed in relation to the received total ionizing dose. It was tracked back to the generation of a leakage current in NMOS transistors induced by radiation. Dedicated irradiation and electrical tests of FE-I4B chips showed that the leakage

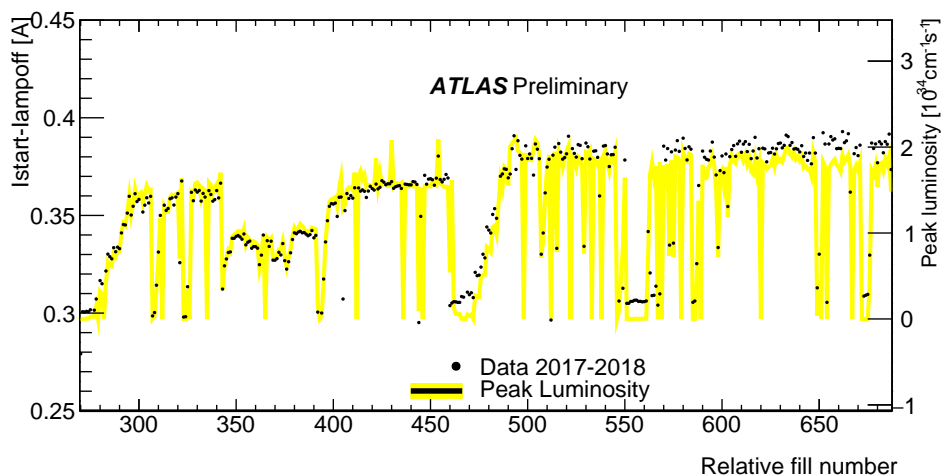


**Fig. 81:** Mean IBL LV current at the start of each stable beam fill ( $I_{\text{start}}$ ) (pre-amplifiers turned on) subtracted of the mean current right before the fill injection ( $I_{\text{ampoff}}$ ) (pre-amplifiers turned off).

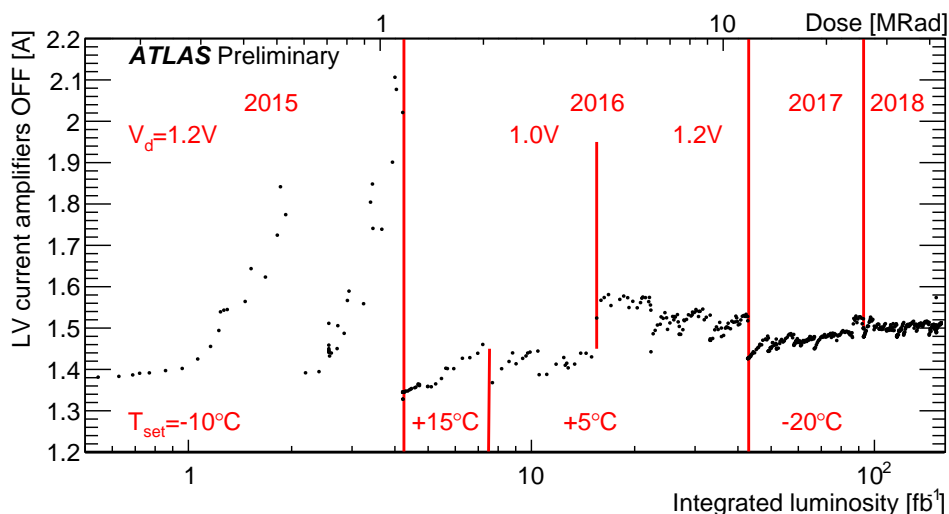


**Fig. 82:** Mean IBL LV current during the Run 2 inter-fill periods (pre-amplifiers turned off)

current reaches its peak value when the total ionizing dose is in the range of 1–3 Mrad, and above this the current decreases to a value close to the pre-irradiation one. This effect was shown to be temperature and dose rate dependent. Due to safety concerns, the IBL was temporarily powered off in October 2015 (during two LHC fills). A complete annealing of the LV currents was observed; this effect was confirmed in a dedicated test during the proton irradiation campaign. Thanks to the intensive irradiation studies it was possible to propose special detector settings (temperature and digital supply voltage) that could guarantee a successful data-taking in the following months.

With the increase of the integrated luminosity/dose at the end of Run 2 operation, a clear saturation of the LV current was observed. Furthermore, a minimal contribution of the LV current from the detector occupancy was also visible during the high luminosity fills (peak lumi  $> 10^{34} \text{ cm}^{-2} \text{ s}^{-1}$ ) in the years 2017–2018. A clear  $z$  dependence on the IBL LV currents was observed during Run 2, similar to the data obtained from sensor leakage current measurements and simulation presented in Chapters 5 and 7.

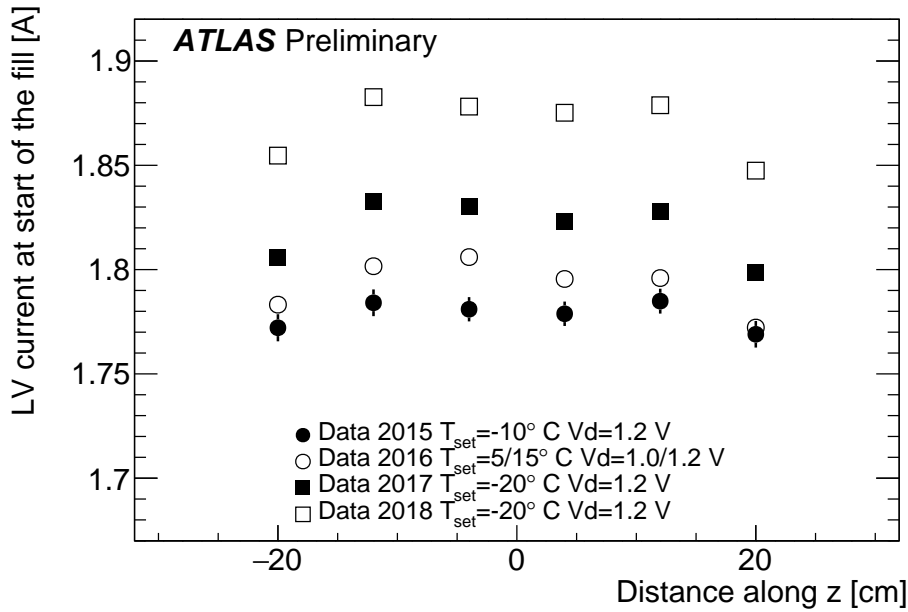


**Fig. 83:** Mean IBL LV current at the start of the stable beam fills during Run 2 (pre-amplifiers turned on) for different  $z$  regions.

### 6.1.2 SEU/SET studies on IBL and SCT detectors

An overall theoretical description of SEU/SET effects in electronics is given in Section 2.2. In this section we will present the experimental observations on the ATLAS IBL and SCT detector electronics, giving the results of detail studies performed during the LHC Run 1 and Run 2 periods [7], including the adopted mitigation strategies and the plans for the future operation in Run 3.

#### 6.1.2.1 SEU and SET measurement in IBL front-end chips

The readout integrated circuits in the ATLAS IBL detector are custom designed with SEU-hardened memory cells [8] (dual interlocked cells or DICE latches [9] and triple redundancy). These reduce the SEU rate, but do not completely eliminate it. The effects of SEUs were indeed visible in the behaviour of the FE-I4B during 2017, when the LHC peak luminosity increased further respect to 2016 and was constantly above  $1.5 \times 10^{34} \text{ cm}^{-2} \text{ s}^{-1}$ . Under these conditions, more frequent front end re-configurations were needed to preserve good data quality and data taking efficiency.

Impacted FEs can stop sending hits, become very noisy, or experience large drops/increases (up to  $\pm 100 \text{ mA}$ ) of the LV current consumption monitored from the detector control system (DCS) (see Fig. 84).

Since 2016, part of the SEU/SET effects was treated by occasional reconfiguration of the problematic modules. However, to minimize the impact of SEUs on ATLAS data taking, it was later decided to regularly reconfigure the global registers of the FE-I4B chips in the entire IBL.

Thanks to a joint effort of online software and firmware, it was possible to introduce this procedure without any additional dead time in ATLAS. Starting in August 2017, the global registers of the IBL FE-I4B chips were reconfigured every  $\sim 5 \text{ s}$ , improving the overall data acquisition (DAQ) efficiency and eliminating the low voltage current drops that were previously observed.

Unfortunately it was not possible to regularly reconfigure also the single pixel DICE latches in the FE-I4B since the needed software modifications were impacting the overall stability of the DAQ system. However, a test run was performed in July 2018 and can be used as proof of concept for future

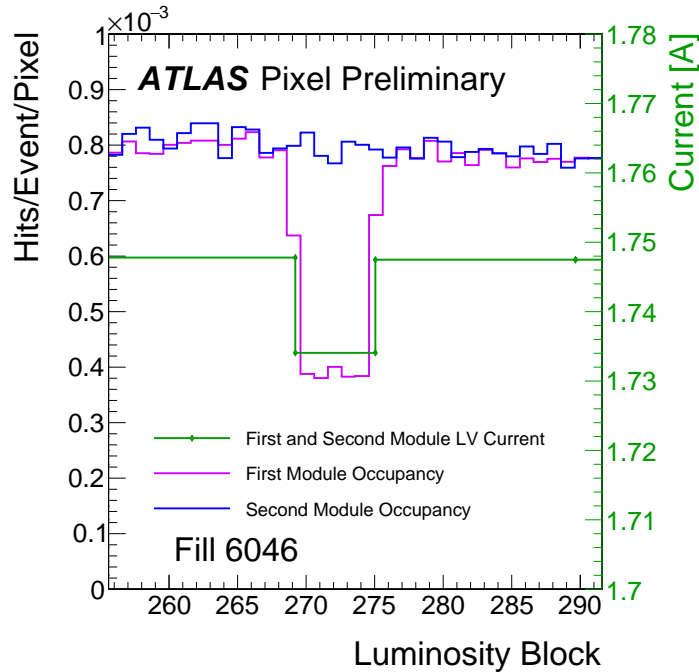


**Fig. 84:** Effects of SEU on FE-I4B global registers during a typical LHC fill; in this case, the peak luminosity reached  $1.5 \times 10^{34} \text{ cm}^{-2} \text{ s}^{-1}$ , and  $490 \text{ pb}^{-1}$  were delivered over the entire fill. During the data taking, at luminosity block (LB)  $\sim 268$ , a drop in the LV current consumption can be observed. At the same time, a drop in occupancy is observed in one of the two DAQ modules that share the same LV power supply. At LB  $\sim 277$ , the critical DAQ module was manually reconfigured, bringing the LV current consumption and hit occupancy back to their values before the SEU.

implementations.

The global configuration memory (GCM) of the FE-I4B, located at the end of the column area outside of the pixel matrix region, is implemented as a memory block of 32 words of 16 bits (512 bits in total). The design used for this global memory is based on the triplication of the DICE latch to further suppress SEU. Such triplication is not possible inside the pixel due to space constraints. An example of a fundamental parameter, vital for a proper chip functionality, is given by the global threshold, generated by a coarse and a fine DAC.

Each single pixel has instead a 13 bit configuration register, comprising a 1-bit enable flag, a 5-bit threshold tuning DAC (TDAC), a 4-bit ToT tuning DAC (FDAC), a 1-bit HitBus (input to logical OR of all pixel discriminators outputs in the matrix), and 2 bits for the selection of the charge injection capacitor. The ToT represents the time of a single pixel discriminator being over threshold and has a 4-bit resolution, in counts of an externally supplied clock, nominally 40 MHz, that corresponds to the LHC bunch crossing (BC) time of 25 ns.

The occurrence of SEUs during data taking modifies both single pixel and global front-end configurations: for the single pixel upset, quiet or noisy pixels can appear introducing buffer overflows and dead time in the FE-I4B; for what concerns the global register upset, lowering the global thresholds or changing other fundamental registers can impact severely the correct chip functionality.

Figure 85 shows the fraction of noisy pixels (meaning pixels that fire in correspondence with empty and well isolated bunches in the LHC ring) as a function of the single pixel TDAC, for a typical LHC fill in 2017. TDAC values for each pixel are taken from the initial pixel configuration. The pixels with more than 200 hits in this fill are defined as noisy. Low values of TDAC correspond to high thresholds.

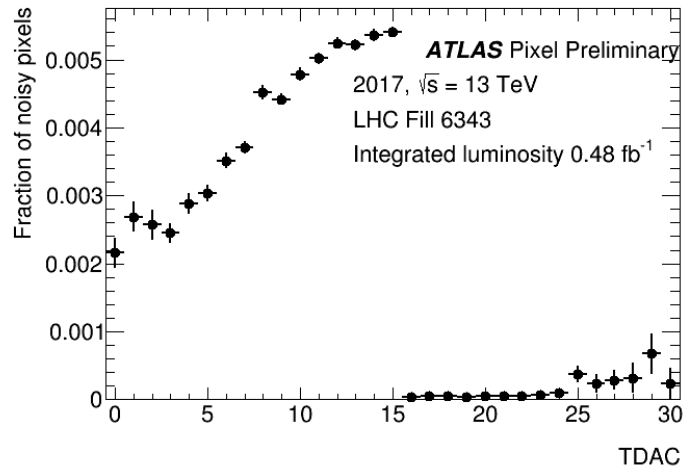


**Fig. 85:** Fraction of noisy pixels as a function of pixel TDAC during empty bunches of LHC fill 6343. TDAC values for each pixel are taken from the initial pixel configuration. The pixels with more than 200 hits in this fill are treated as noisy.

The higher fraction of noisy pixels with initial TDAC  $< 15$  indicates that some pixels become noisy due to the SEU flip  $0 \rightarrow 1$  of the most significant bit (MSB) of TDAC, which corresponds to lower the pixel threshold by  $\sim 1850 e$  (with  $2500 e$  being the typical discrimination threshold). No correlation of the noise with FDAC values was observed.

On the other hand, a pixel is defined to be quiet if it fired zero times in  $16 \text{ pb}^{-1}$  of data taking. A pixel can become quiet during data taking due to a flip on the Enable bit ( $1 \rightarrow 0$ ). The increasing fraction of quiet and noisy pixels versus integrated luminosity ( $\mathcal{L}$ ) for a typical LHC fill in 2018 in the eight forward 3D rings (each being an average over 14 FE-I4B with the same  $\eta$  coordinate) is shown in Fig. 86. Four  $\eta$  rings (A7\_1/2 and C7\_1/2) were regularly reconfigured, including the single pixel registers whilst the other four  $\eta$  rings (A8\_1/2 and C8\_1/2) were not reconfigured.

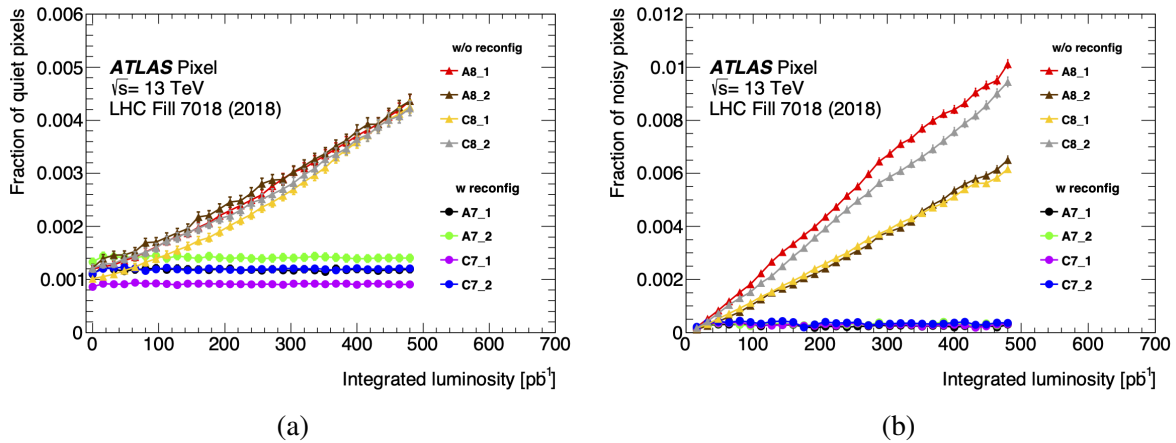


**Fig. 86:** Fraction of quiet (a) or noisy (b) pixels versus integrated luminosity in fill 7018 from 2018, shown in the eight 3D IBL  $\eta$  rings.

Module-to-module differences in the initial number of quiet pixels indicate different fractions of silent pixels, which fire zero times during the entire fill. The fraction of pixels that become quiet due to SEU is seen to increase linearly with integrated luminosity. The dependence of the number of quiet pixels as the function of luminosity was fitted with a linear function  $p_0 + p_1 \cdot \mathcal{L}$ , where the mean  $p_1$  is



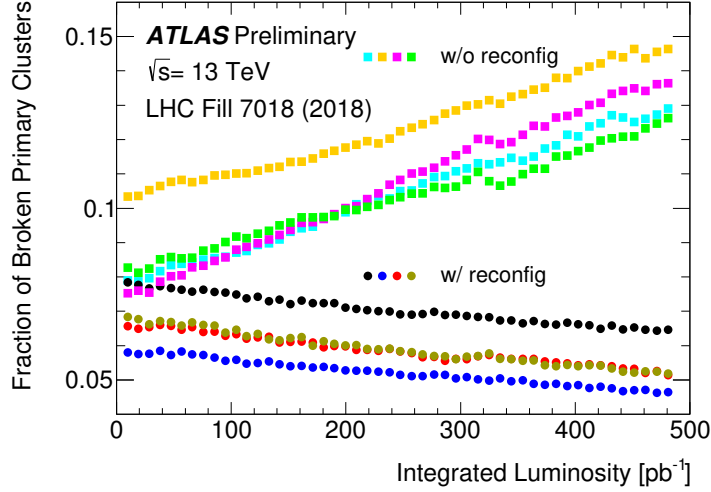


**Fig. 87:** Fraction of broken primary clusters versus integrated luminosity in fill 7018 from 2018, shown in the eight rings of 3D modules. Half of the modules were left without reconfiguration, whilst the other half were regularly reconfigured, including the single pixel registers.

$5.4 \pm 1.3 \times 10^{-3}$  fb.

The fraction of pixels that become quiet due to SEU ( $p_1 \cdot \mathcal{L}$ ) is equal to the ratio  $N_{\text{errors}} / N_{\text{latches}}$  in Eq. 29. The pixel latch SEU cross-section in FE-I4B is calculated with the ‘quiet-pixel-fraction’:

$$\sigma = \frac{p_1 \cdot \mathcal{L}}{\Phi}. \quad (29)$$

The predicted flux of hadrons with energy above 20 MeV with PYTHIA/FLUKA simulations in the extreme outside 3D sensor IBL module is  $\Phi = 0.91 \times 10^{13}$  hadrons ( $T > 20$  MeV)  $\text{cm}^{-2}$  per  $1\text{fb}^{-1}$  (see Table 6 in Chapter 4). The SEU cross-section is calculated to be  $(0.60 \pm 0.14) \times 10^{-15} \text{cm}^2$ , which is of the same order of magnitude as the test beam result [8].

The number of clusters produced by primary charged particles from a 13 TeV pp collision vertex (referred to as ‘primary clusters’) is proportional to luminosity. Quiet pixels can cause clusters to be broken. In the 3D modules, the average length of a primary cluster is nine pixels, so broken clusters are a very sensitive probe of quiet pixels caused by a flip of the SEU Enable bit from  $1 \rightarrow 0$ . If two clusters are separated by a one-pixel gap along  $z$  and  $\Delta\text{row}$  is no larger than three pixels, then these clusters are assumed to be broken from one long cluster. Background where two clusters are close together due to random coincidence is flat in  $\Delta\text{row}$ . Figure 87 shows the fraction of broken primary clusters versus integrated luminosity in fill 7018 from 2018, in the 8 rings of 3D modules. The rings where no single pixel reconfiguration was applied show the increase in the number of broken clusters with luminosity. On the other hand, rings where pixel reconfiguration was regularly done show a decrease of the fraction of broken clusters, that corresponds to a decrease of the fraction of quiet pixels visible in Fig. 86 (a).

Figure 88 shows the average fraction of quiet pixels in each chip ring after  $\sim 480 \text{pb}^{-1}$  of data taking in LHC fill 7018. It is compared with the PYTHIA/FLUKA simulation, which is normalized to the average fraction in data.

The FE-I4B provides the functionality to read back the content of the DICE latches by copying the latch content in the Shift Register (SR) for each double column and transmitting it back to the readout drivers (RODs). The SEU measurement scheme is to write to a register in the device being tested, let a certain fluence of particles traverse the device, and then read back the register. The fraction of pixels in which the bit state flips ( $\frac{N_i(0) - N_i}{N_i}$  ( $i = 0, 1$ )) after taking data of integrated luminosity  $\mathcal{L}$  depends on the

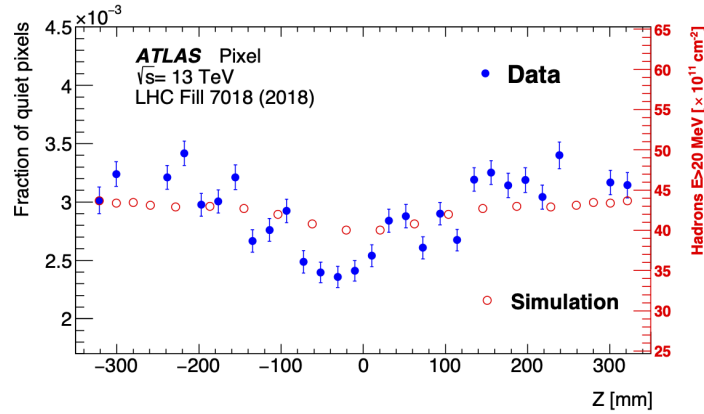


**Fig. 88:** Average fraction of quiet pixels in each IBL chip ring after  $\sim 480 \text{ pb}^{-1}$  of data taking in LHC fill 7018 of 2018, compared with PYTHIA/FLUKA simulations. Four points are missing due to the reconfiguration tests happening during that fill in four specific front-end rings.

probability of  $0 \rightarrow 1$  ( $P_{0 \rightarrow 1}$ ) and  $1 \rightarrow 0$  ( $P_{1 \rightarrow 0}$ ) transitions:

$$\frac{N_1(0) - N_1}{N_1} = P_{1 \rightarrow 0} \cdot \mathcal{L} \quad (30)$$

$$\frac{N_0(0) - N_0}{N_0} = P_{0 \rightarrow 1} \cdot \mathcal{L}. \quad (31)$$

Read back cannot be performed while a FE receives trigger signals, so there are only two read-backs for planar modules: before the start of the collisions and after beam dump. The first point is zero by construction.  $P_{0 \rightarrow 1}$  and  $P_{1 \rightarrow 0}$  are extracted from these measurements. This procedure allows for an independent measurement of the SEU probabilities for each of the 13 pixel latches.

The  $0 \rightarrow 1$  and  $1 \rightarrow 0$  transition probabilities have been measured for the pixel latch memories. The simulation of the SEUs in DICE memories [10–12] demonstrates that the dominant effect comes from glitches on the LOAD signal. The LOAD signal stores into the DICE latch the current content of the SR. In this case, the polarity of the transition depends on the actual values stored in the SR. The last bit (out of 13 bits) loaded into the SR is the output enable bit. As the enable bit is usually 1, this favours  $0 \rightarrow 1$  transitions.

These asymmetries were studied in detail during LHC fill 7334 with the read-back method. The probability of a pixel memory bit flip strongly depends on the value stored in the input SR. Pixel memory read-back results and chip simulations confirm that the FE-I4B SEEs are dominated by single event transient effects (SET), which create fake LOAD signals.  $0 \rightarrow 1$  flips in pixel memory are dominant when the SR is loaded with 1, and  $1 \rightarrow 0$  flips are dominant when SR is loaded with 0. The average rate of the SEU/SET bit flips in pixel memory of FE-I4B per  $\text{fb}^{-1}$  was studied in LHC fill 7334 as a function of the chip number. In Fig. 89 (a), the SR was set to 1, and  $0 \rightarrow 1$  flips dominate due to the SET on the LOAD line, while low rate  $1 \rightarrow 0$  flips are due to real memory SEU. In Fig. 89 (b), the SR was set to 0, and  $1 \rightarrow 0$  flips dominate. The values of the SR are refreshed several times during the LHC fill. The extrapolation of the measurement of the SEU rate with 24 GeV protons at CERN PS is shown with a blue line in Fig. 89 (b). During the CERN PS measurement, the value of the SR was not refreshed, which may explain the higher rate of bit flips due to SET contributions. Figures 89 (a) and (b) present different chips at slightly different locations, so part of the difference may come from chip-to-chip process variations, tuning, and particle flux differences.

In the same fill, the average rate of the SEU/SET bit flips in pixel memory was studied as a function of the bit number (0-12). In Fig. 90 (a), the SR was set to 1, and  $0 \rightarrow 1$  flips dominate due to the SET on the LOAD line, while low rate  $1 \rightarrow 0$  flips are due to real memory SEU. In Fig. 90 (b), the SR is set to 0,

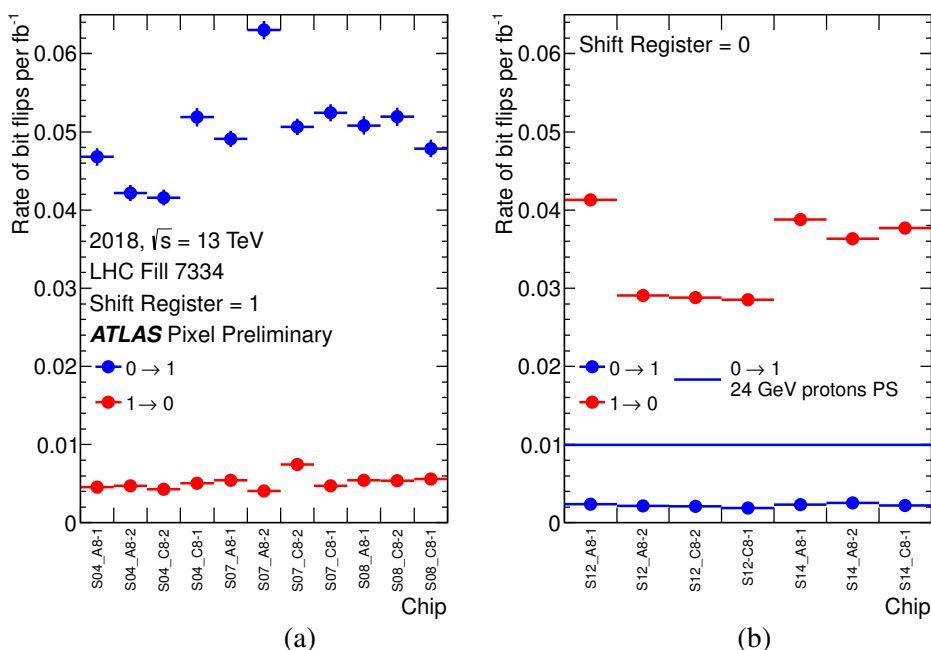


**Fig. 89:** In (a), the SR was set to 1, and  $0 \rightarrow 1$  flips dominate. In (b), the SR was set to 0, and  $1 \rightarrow 0$  flips dominate. The extrapolation of the measurement of SEU rate with 24 GeV protons on CERN PS is shown with blue line in (b).

and  $1 \rightarrow 0$  flips dominate. Flips in bit-8 (HitBus) are twice as frequent, probably due to specific layout of that memory bit.

During LHC fill 7333 the values of the global configuration memory were read back several times and compared with the initial setting. In Fig. 91, the cumulative fraction of SEU/SET bit flips in the global configuration memory of FE-I4B is shown as a function of integrated luminosity.

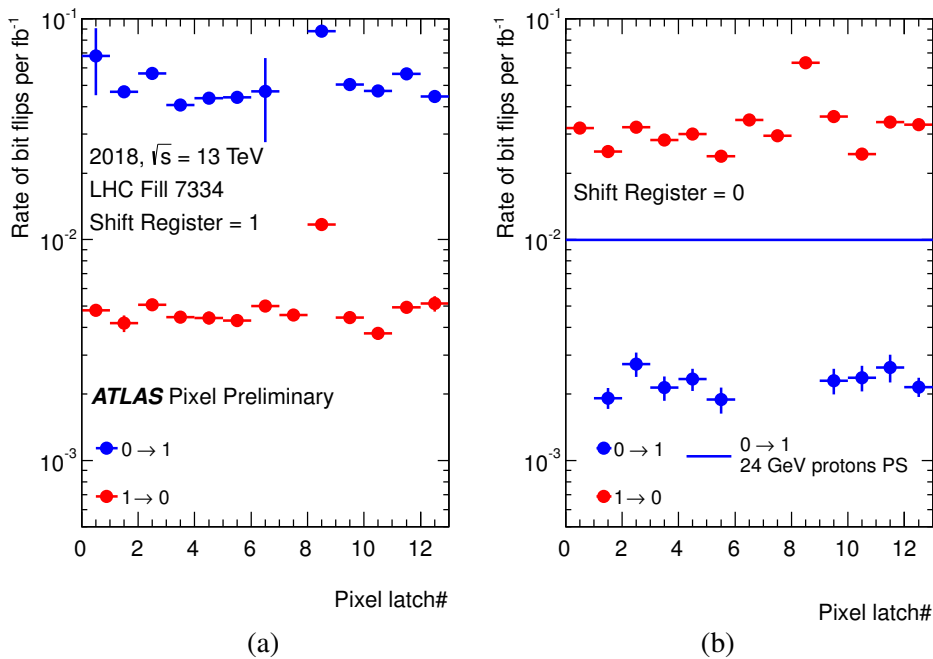
The high rate of  $0 \rightarrow 1$  flips is probably due to SET on the LOAD line with register value 1. The pattern 0xFFFF was loaded last into the SR. The values of the SR are refreshed several times during the fill. No  $1 \rightarrow 0$  real SEU transitions were observed during the fill due to the triply redundant memory design. For the calculation of SEE cross-sections, we use the average prediction of the flux of hadrons with energy above 20 MeV<sup>4</sup> in the two outer 3D IBL modules:  $91.0 \times 10^{11} \text{cm}^{-2} \text{fb}^{-1}$ . This flux was calculated from 13 TeV proton–proton minimum bias events generated using PYTHIA8 [14], applying the A3<sup>5</sup> tune to ATLAS data, and using NNPDF23LO Parton Density Functions (PDF) [15]. The flux of hadrons in the ATLAS detector was simulated using FLUKA version 2011.2x particle transport code [16]. The systematic error on the hadron flux was estimated to be  $\sim 30\%$ .

In Table 12, we summarize the measured rates and SEE cross-sections. The rates presented are averages over all available chips and 12 pixel memory bits, excluding the HitBus bit (which shows abnormal rates related to the special layout interconnecting all pixels in the matrix). The systematic errors on the SEE rates were calculated from the RMS spread of the rates in different IBL chips and in different pixel memory bits for SEU and SET dominated samples. SET cross-sections are greater than SEU cross-sections by a factor of 10. Some differences in  $0 \rightarrow 1$  and  $1 \rightarrow 0$  transitions are observed, but fall within the systematic errors. These variations are related to differences in the geometrical positions of the chips, differences in process variations, and differences in the mixture of SEU and SET effects.

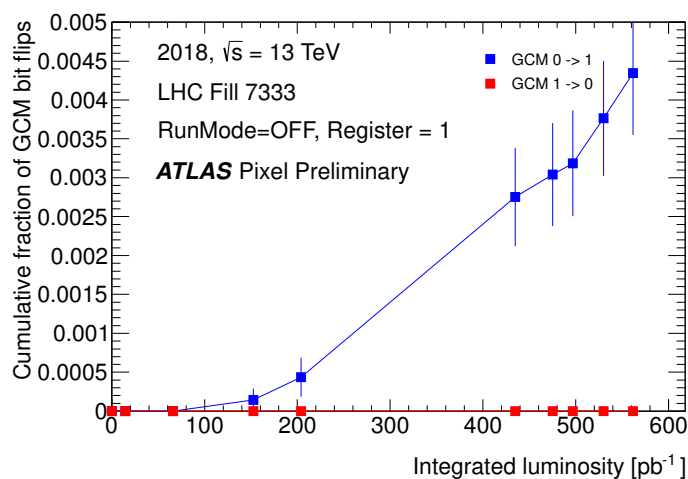
The measured cross-sections are compatible with the cross-sections measured with 24 GeV pro-

<sup>4</sup>The choice of 20 MeV hadron energy cut was justified in Ref. [13] by effective reduction of SEU effects below this energy.

<sup>5</sup>A3 is one of the tunes of PYTHIA8 Monte-Carlo generator to the ATLAS LHC data.



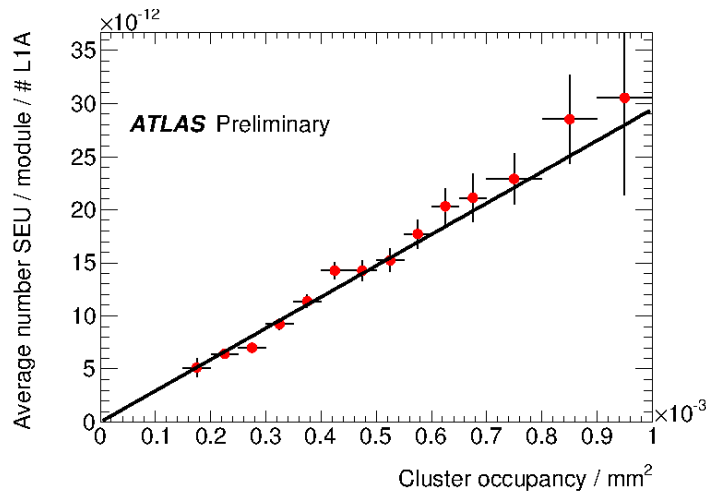
**Fig. 90:** Average rate of SEU/SET bit flips in pixel memory of FE-I4B per  $\text{fb}^{-1}$  in LHC fill 7334, as a function of bit number (0-12). In (a), the SR was set to 1, and  $0 \rightarrow 1$  flips dominate. In (b), the SR was set to 0, and  $1 \rightarrow 0$  flips dominate. The extrapolation of the measurement of the SEU rate with 24 GeV protons at CERN PS is shown with a blue line.



**Fig. 91:** Cumulative fraction of SEU/SET bit flips in the global configuration memory (GCM) of FE-I4B as a function of integrated luminosity in LHC fill 7333.

**Table 12:** Summary of measured rates and SEE cross-sections

Beam, SEE type	Transition	SR value	Rate per $\text{fb}^{-1}$ (%) (stat./syst.)	Cross-section $10^{-15} \text{ cm}^2$
LHC: mainly SEU	$0 \rightarrow 1$	0	$0.22 \pm 0.01 \pm 0.09$	$0.24 \pm 0.13$
LHC: mainly SEU	$1 \rightarrow 0$	1	$0.46 \pm 0.01 \pm 0.19$	$0.51 \pm 0.26$
LHC: mainly SET on LOAD line	$1 \rightarrow 0$	0	$3.07 \pm 0.02 \pm 0.80$	$3.39 \pm 1.34$
LHC: mainly SET on LOAD line	$0 \rightarrow 1$	1	$4.68 \pm 0.03 \pm 1.21$	$5.16 \pm 2.04$
24 GeV protons Mostly SEU with some SET admixture	$0 \rightarrow 1$	0	n.a.	1.10

**Fig. 92:** SEU rate per module versus module cluster occupancy. The line shows the result of a linear fit through the origin.

tons at CERN PS. So for future HL-LHC experiments, measurement of SEE cross-sections using the 24 GeV proton PS beam is recommended, and special attention should be paid to the optimization of chip design not only against SEU, but also against SET effects.

#### 6.1.2.2 SEU in SCT front-end chips

From test beam data single event upsets (SEU) are expected in the on-detector p-i-n diodes that receive the TTC data and in the ABCD ASICs. Extrapolations of the test beam results were used to compare with the measured *in situ* results [17].

#### *p-i-n diodes*

While no direct measurements of SEU rates could be performed *in situ*, the occurrence of SEUs led to a characteristic signature of synchronization errors [17]. The characteristic signature for a genuine SEU is the occurrence of a burst of events which fails this synchronization test. The correlation between the measured SEU rate and the cluster occupancy in a module in a given run is shown in Fig. 92. The cluster occupancy is a good proxy for particle flux, as the rate of noise hits is negligible.

The measured number of SEUs in a data set corresponding to an integrated luminosity of  $8.69 \text{ fb}^{-1}$  was 2504. The value of the SEU cross-sections determined from the test beams was used to predict the

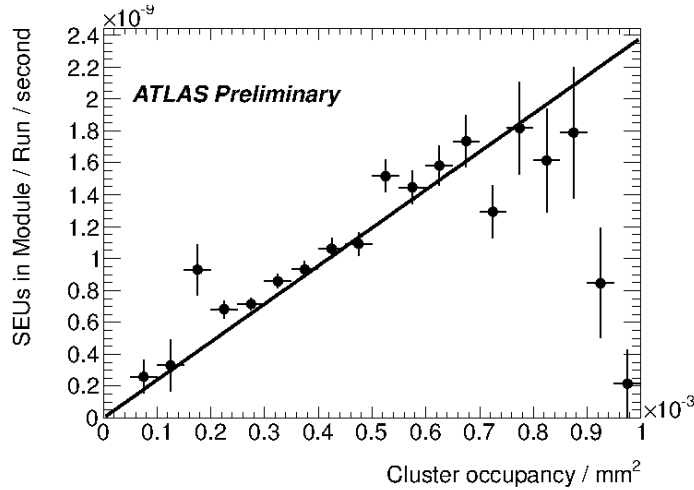


**Fig. 93:** Rate of SEUs in the ABCD DAC registers versus the module occupancy in a run

number of SEUs. The value determined was 1900 which is in reasonable agreement given the uncertainties in the extrapolation [17].

#### *ABCD registers*

SEUs in the ABCD registers cannot be directly identified during ATLAS operation. However, an indirect determination of SEUs in the ABCD register that sets the DAC value for the threshold is possible. The MSB is normally set to ‘1’ and if an SEU causes it to be flipped to a ‘0’ the threshold would become below the baseline. This would then result in a very high occupancy until the register was reset. This allowed the detection of SEU bursts. To demonstrate that these candidates are genuine SEUs, the rate was measured as a function of fluence. The results are illustrated in Fig. 93 and also show the expected linear relationship. The measured number of SEU events in a data set corresponding to  $20.3 \text{ fb}^{-1}$  was  $3046 \pm 100$ . Simple extrapolation of the measured SEU cross-sections at test beams gave a prediction of 1000 [17]. The discrepancy is probably a reflection of the uncertainties in the extrapolation of the SEU cross-sections with energy. Mitigation strategies including regular resets have reduced the data loss due to SEU to a negligible level.

### **6.1.3 Optical links studies in SCT**

The radiation damage in the optical links was measured *in situ* [18] and compared with extrapolations of test beam data [19], [20]. The radiation induced damage expected at the end of Run 3 can be accommodated in the links power budgets.

#### *6.1.3.1 VCSELs*

The optical power of the on-detector VCSELs was measured in special runs by measuring the photocurrents in the off-detector p-i-n diodes which received the light. The optical power decreased linearly with luminosity. The decrease in optical power was measured in different regions of the SCT that were exposed to different fluences. The results of these measurements [18] are summarized in a plot of the change in VCSEL output versus the fluence (see Fig. 94). Assuming that the threshold current and slope efficiency change linearly with fluence the results can be compared to test beam data with and without annealing. As these links have had more annealing time than used in the test beam studies, the plot indicates that the radiation damage is slightly larger than expected.

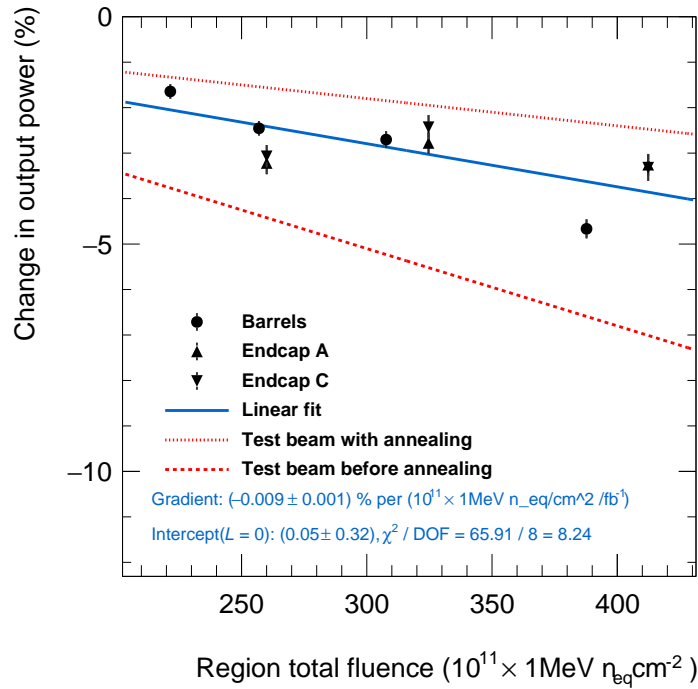


**Fig. 94:** Plot of the change in VCSEL output versus fluence for the different regions of the SCT

### 6.1.3.2 The p-i-n diodes

The radiation damage in the p-i-n diodes was studied *in situ* by measuring the photo-currents for the on-detector devices. The decrease in responsivity is not linear and tends asymptotically to a fixed value. The results of these fits are shown for one layer of the barrel in Fig. 95. The other regions gave similar results [18] and the weighted mean value for the asymptotic decrease of responsivity was  $R_{\infty}^{\text{eff}} = 0.731 \pm 0.027 \pm 0.046$ , which is in good agreement with the value of 0.71 obtained in test beam measurements [19].

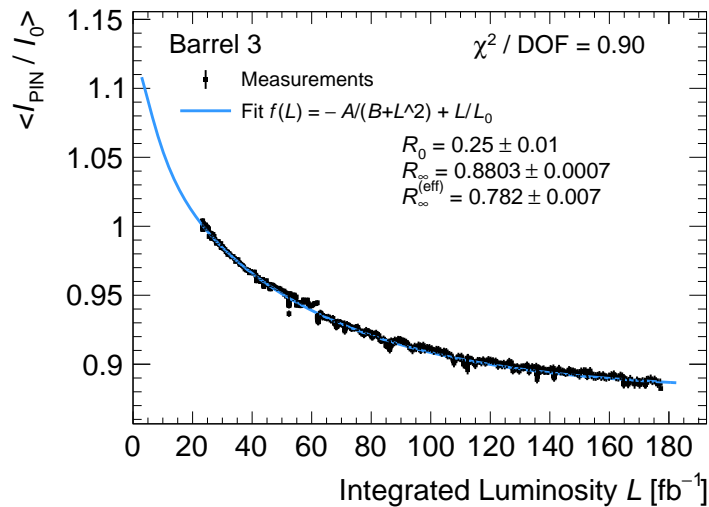


**Fig. 95:** On-detector p-i-n diodes. Each point represents the mean value for one day averaged over all modules in this layer. The value is the normalized mean value of the photo-current  $I_{\text{PIN}}$ .

#### 6.1.4 Irradiation effects in TRT electronics

The signals coming from the TRT straws are detected by custom designed electronics [24]. The analogue part of the electronics ‘amplifier, shaper, discriminator and baseline restorer’ (ASDBLR) performs the amplification, shaping, discrimination and base-line restoration against the long trailing signal caused by the drifting ions. ASDBLR is capable of detecting signals at two different thresholds: a tracking threshold about 200 eV (low-level level threshold), and the transition radiation threshold about 5 keV (high-level level threshold). The output is a ternary signal, with the first level indicating the time the input signal exceeded the low threshold and the second level indicating the time the input signal exceeded the high threshold. The digital readout chip for the TRT is the ‘drift time measurement/read out chip’ (DTMROC). A DTMROC receives the signals from two ASDBLR’s, that is from 16 straws. It samples each input eight times per 25 ns bunch crossing in 3.125 ns intervals. It also determines whether the high threshold was exceeded in each bunch crossing. The high and low thresholds for a ASDBLR are set by two registers in a DTMROC. DTMROCs are also capable of injecting test charge to ASDBLRs which is shaped similar to the integral of the expected ionization signal in a xenon filled straw in TRT. When a L1A signal is received, the data is sent from DTMROCs to the back-end consisting of the TRT Read-out Driver and subsequently the ATLAS central ROS system [25].

The TRT front-end electronics is susceptible to radiation damage caused by the intense particle flux coming from beam collisions. There are two important effects: irreversible radiation damage on the gain and the offset of the ASDBLR transistors, and the temporary radiation damage (SEU) in the DTMROCs.

##### 6.1.4.1 Effective threshold shift in ASDBLR

Transistors are sensitive to displacement damage from neutrons, protons, pions, and other interacting particles such as kaons. In ASDBLRs, this causes an increase in current at the base of the transistors of the pre-amplifiers, which lowers the gain [24]. The loss of gain can manifest itself both as a decrease in the gain of the amplifier and as a shift in the offset. Both of these effects can contribute to an effective shift in the low or high threshold. Extensive irradiation tests, to many tens of Mrad, were carried out on the electronics prior to the construction of ATLAS and no significant effects were to be expected in either Run 1 or Run 2. However, during Run 1, it was observed that the detection efficiency for  $Z \rightarrow ee$  decreased slowly during the run [26]. This was traced to a small shift in the effective high threshold. While similar shifts in the effective low threshold also occurred, it did not cause observable effects since the low threshold was adjusted regularly to maintain a constant noise occupancy. On the other hands, the high-level thresholds were not tuned time to time as it was expected that any small shifts that might occur would not affect the efficiency for electron identification.

This phenomenon, which was not observed in the former irradiations tests since they were performed only with higher dose, was investigated using a cobalt-60 source that produces gamma-rays at 1.17 MeV and 1.33 MeV at Brookhaven National Lab (BNL). Sets of TRT endcap front-end boards (triplet with 12 DTMROCs, 24 ASDBLRs, 192 ASDBLR channels) were irradiated with various doses: 30 krad which is roughly equivalent to the total Run 1 dose, 60 krad, and 500 krad. The metric of interest is the effective low-level threshold defined as the at the low-level threshold which the ASDBLR outputs would produce a 50% occupancy; measurements were made both with zero injected charge and with an injected charge from the DTMROCs with a pulse height corresponds to an ionization energy of typical low-level threshold hits (400 eV). Figure 96 shows the shift in the effective low-level threshold measured with and without charge injection. The observed shift, corresponding to an ionization energy of about 30 eV, after 30 krad is similar to that observed in the detector during Run 1. Tests to higher total dose rates showed no further shift up to 500 krad.

Measurements of the shift in the high-level threshold after irradiation at BNL were not recorded. However, a similar examination is performed in the ATLAS TRT by similarly measuring the 50% occupancy high-level threshold regularly over the time of Run 1 and Run 2. Figure 97 summarizes the



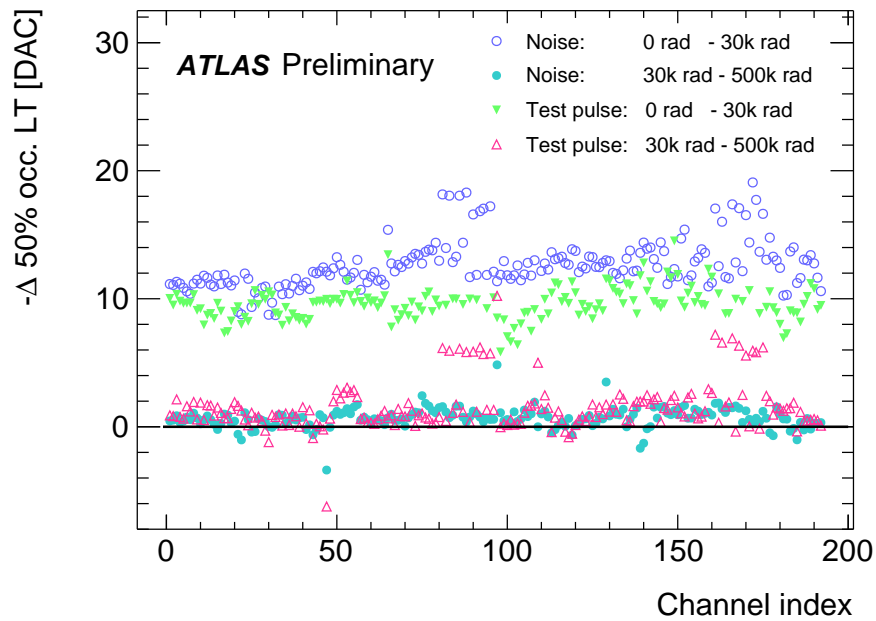


**Fig. 96:** The magnitude of negative shift in the effective low-level thresholds (LT) of ASDBLR chips after being irradiated by a  $\text{Co}^{60}$  source at BNL. The effective low-level threshold is determined as the DAC value that yields 50% occupancy for noise or a test pulse which corresponds to an ionization energy of 400 eV. The individual shifts of 24 ASDBLRs (192 channels) on a test board are shown. A shift of 12–13 DAC counts, corresponding to an ionization energy of about 30 eV is observed for both threshold definitions after an irradiation of 30 krad, which corresponds to the average dose accumulated in the inner layer of the TRT over the course of Run 1. No significant shift is seen for additional irradiations up to 500 krad, except for the three chips which saturated at about 60 krad.

chronological change of effective high-level threshold measured using the test pulse with the height equivalent to an ionization energy of 1.9 keV. The shift is clearly observed during Run 1 and was sufficient to cause the observed decrease in electron efficiency. The effect saturates after about 30 krad and there is no further shift during Run 2, which is consistent with what is found in the low-level threshold in the BNL experiment. Nonetheless, the high-level thresholds used for operation have been updated since the beginning of the Run 2 to compensate for any possible shift, calculated based on the extrapolated 50% occupancy threshold shift at the test pulse height equivalent to the transition radiation signal which is about 5 keV ionization energy equivalence.

#### 6.1.4.2 Single event upset in DTMROCs

When a charged particle or electromagnetic radiation traverses digital micro-circuitry, secondary ionization charges can cause internal logic elements to change their state (SEU ‘bit flips’). In the DTMROCs the bits that are susceptible to SEUs are:

- (1) straw hit data bits in the buffer;
- (2) event identifier bits associated with the straw data;
- (3) the bit flips in the registers storing the configuration information.

While the former two have relatively limited impact on the data taking either because only small subset of data is read out on the L1A or because they are frequently reset according to the LHC orbit, the SEUs on the configuration registers can cause serious impact. The general configuration and the threshold information are the most critical part of the configuration registers. Therefore they are triplicated and

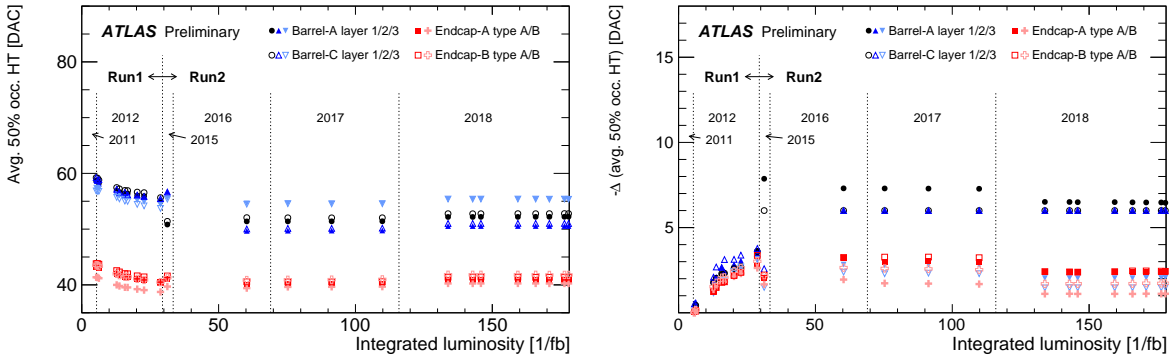


**Fig. 97:** (a) The effective high-level threshold (HT) of ASDBLR chips and (b) its decrease since the beginning of 2012, as function of integrated luminosity recorded in the ATLAS over the last year of the Run 1 (2012) and Run 2 (2015–2018). The HT is determined as the DAC value that yields 50% occupancy for a test pulse which corresponds to an ionization energy of 1.9 keV. Values are shown separately for the A side and C side of the detector for the three barrel layers and groups of endcap layers with type A and type B front-end boards, which largely correspond to the low-/high- $z$  part of the endcaps. All shown values are averaged over all channels in the respective detector part. The TRT active gas mixture of barrel layers 1 and 2 have been changed between Run 1 and 2015; and between 2015 and 2016. This required a change of the ASDBLR shaping, which resulted in a large change in the HT. The other changes to the HT during Run 2 are still being investigated, however, they are unrelated to radiation as the changes are independent of integrated luminosity.

automatically corrected using the parity logic in the DTMROCs. A polling scheme is also implemented in the TRT DAQ system to monitor and correct the DTMROC configuration registers. This is done by the TRT-TTCs requesting read back during the 199 bunch-crossing long beam gap booked at the end of the orbit, and compare the register information to the originally written configuration from the TRT-TTC. Any mismatch is logged in the database. The registers regarding to the general configuration and the thresholds are additionally re-written once the bit changes are detected. The polling is done sequentially and each DTMROC channel is fetched at about 10 Hz.

A SEU rate measurement has been performed utilizing this polling system during the  $\sqrt{s} = 7$  TeV operation in 2011, or the  $\sqrt{s} = 13$  TeV operation in 2015-16. After removing the events recorded due to the other known reasons such as bad communication between the TRT-TTCs and the DTMROCs, 46 and 1016 SEU events are observed in total during the  $\sqrt{s} = 7$  TeV operation in 2011 and the  $\sqrt{s} = 13$  TeV operation in 2015-16 respectively. Figure 98 shows the calculated SEU rate for the entire TRT as function of the average instantaneous luminosity in the various selected run period. A good linearity with respect to the instantaneous luminosity at the same centre-of-mass energy is found. The SEU cross-section per DTMROC chip is derived as  $(1.2 - 5.7) \times 10^{-14} \text{ cm}^2$  given the particle fluence in the TRT (charged and neutral hadrons with  $E > 20$  MeV:  $4.0 \times 10^{11} - 1.8 \times 10^{12} \text{ cm}^{-2}$  per  $1 \text{ fb}^{-1}$  of integrated luminosity depending on the position [27]), and the total number of chips (22 016). This is largely consistent with the measured SEU cross-section  $(0.8 - 1.2) \times 10^{-14} \text{ cm}^2$  for the DTMROC prototypes obtained using the 24 GeV proton test beam at the CERN PS irradiation facility [28].

## 6.2 CMS

The CMS tracking detector consists of the silicon pixel and silicon strip detectors. Together they provide charged particle tracking in the pseudo-rapidity range of  $|\eta| < 2.5$ . The original CMS pixel detector [30] was running during the years 2009–2012 and 2015–2016 and was replaced with the CMS Phase-1 pixel detector [31] during the extended year-end technical stop 2016/17.

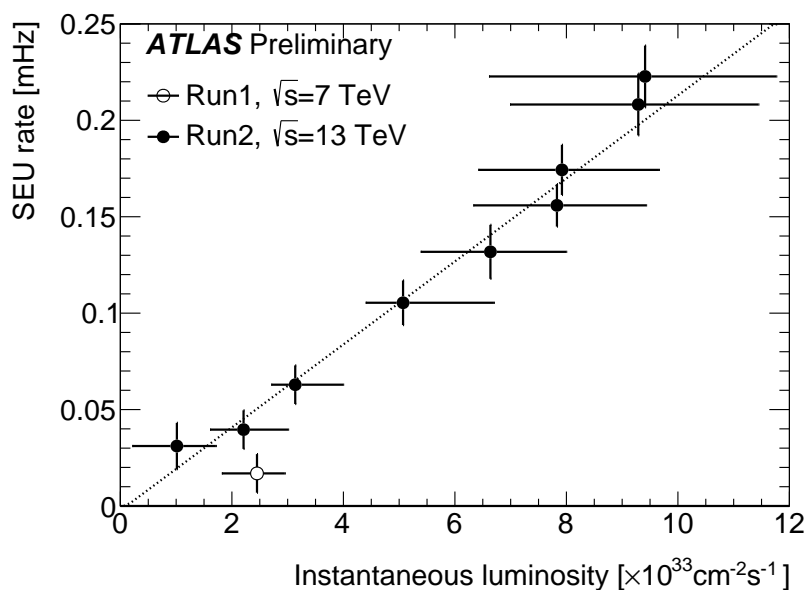


**Fig. 98:** Single event upset (SEU) rate in the DTMROCs measured as a function of the instantaneous luminosity observed in the ATLAS detector, using 2011 Run 1 data, collected at  $\sqrt{s} = 7$  TeV (hollow dots) and 2015–2016 Run 2 data, collected at  $\sqrt{s} = 13$  TeV (closed dots). The SEU rate is calculated for selected run periods for which the instantaneous luminosity is determined as the average over the respective period. The  $x$ -axis error bars represent the luminosity range from the different runs in the period. Only one point is shown for the  $\sqrt{s} = 7$  TeV result due to the limited data statistics. The observed SEU rate depends linearly on the instantaneous luminosity at the same centre-of-mass energy.

### 6.2.1 Radiation effects in the CMS pixel detector

The CMS pixel detector and its readout electronics have been described in Section 3.2.2.1. In the following some of the radiation effects observed in both the Phase-0 and Phase-1 pixel detectors will be described.

#### Evolution of low voltage currents

Figure 99 shows the evolution of the analogue low voltage currents in the CMS Phase-0 barrel pixel detector over its full lifetime. The current is averaged for all ROCs belonging to the layer in question. To be comparable, the current measurements are always taken 10 minutes into an LHC fill after it has reached stable proton collisions. Several distinct features can be seen in the plot. The current rises most steeply in the innermost layers in early Run 1 necessitating a recalibration of layers 1 and 2 already after few  $\text{fb}^{-1}$ . Another two recalibrations were performed during Run 1 on all layers afterwards. It can be seen that the increase per luminosity decreases over the course of the run from initially around  $0.4 \text{ mA}/\text{fb}^{-1}/\text{ROC}$  for layers 1 and 2 gradually decreasing to  $0.1 \text{ mA}/\text{fb}^{-1}/\text{ROC}$ . For layer 3 the initial increase is lower at around  $0.2 \text{ mA}/\text{fb}^{-1}$ . The analogue circuitry is powered via a bandgap reference voltage which increases with dose. This effect has been measured for the Phase-1 PSI46dig in Ref. [34] to be around 11% for TID expected for the lifetime of the Phase-1 detector with a 10% increase below 300 kGy. The increase reaches a plateau of around 14% for very high TIDs.

#### Radiation and SEU effects

The SEU cross-section in 250 nm technology which is used for the readout ASICs has been measured and protection measures have been put in place [33]. The large majority of SEUs in the ROCs will not be visible as they only affect small parts of the ASIC like single-pixel trim bits and do not affect the detector

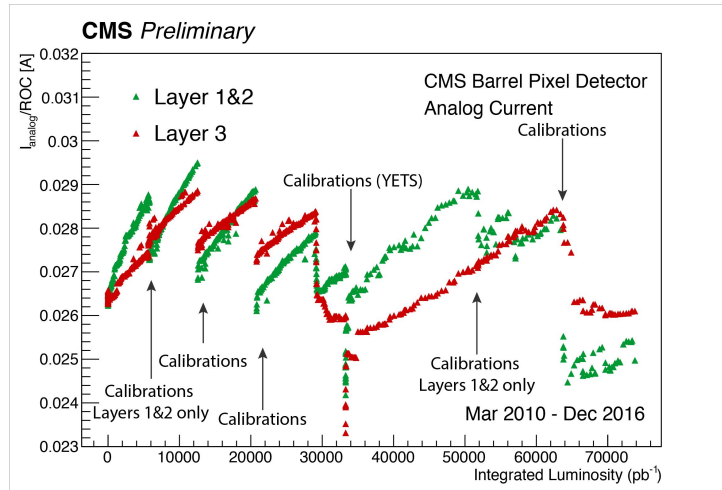


**Fig. 99:** Evolution of the analogue supply currents per ROC for the CMS Phase-0 pixel detector as a function of the integrated luminosity. Recalibrations, full or partial, are indicated as well as short technical stops (TS) and year-end technical stops (YETS).

response in a significant way. The data taking will be affected by SEUs when vital parts of the ASIC get affected which can happen with some probability. Also the TBM chips can be affected by SEUs in which case the readout to a group of ROCs is stopped. Both SEUs for single ROCs and TBMs get detected in the front-end driver (FED) that keeps a list of channels which do not send data. Once a programmable threshold of channels has been reached, a recovery procedure is initiated which will be described in more detail below. The threshold is adapted depending on the position in the detector and hence the potential impact on the data quality. The rate at which ROCs become fully inefficient in the Phase-0 detector was estimated from data to be around  $1/2\text{--}4\text{ pb}^{-1}$  for the PSI46 and about  $1/73\text{ pb}^{-1}$  for the TBM.

In the Phase-1 detector the TBM ASICs have been found to be more susceptible to SEUs because of a single non-protected transistor in the readout control. This condition cannot be recovered with a reprogramming of the chip but instead a power-on reset has to be issued. In 2017 the power cycling was performed using the DCDC converters of the Phase-1 detector. This procedure led to the discovery of the DCDC converter issue caused by a problem in the FEAST ASIC. The description of this problem is beyond the scope of this report, more details can be found in [35]. The rate at which TBM cores got stuck because of this problem was about  $0.7\%/100\text{ pb}^{-1}$  for BPIX layer 1, the worst affected region of the detector. During LS2, the innermost barrel pixel layer will be replaced. Improved versions of the readout ASICs will be deployed and the increased SEU susceptibility of the TBM will be removed for the newly installed modules. Figure 100 shows the evolution of inactive ROCs in the barrel layer 1 over a long (11 h) LHC fill with peak instantaneous luminosity around  $1.5 \times 10^{34}\text{ cm}^{-2}\text{ s}^{-1}$ .

The recovery from SEUs or SEU like effects is done by completely reprogramming the front-end ASICs. This can either be done specifically targeting affected detector regions or by performing a full reprogramming of the full detector. For the year 2018 the firmware of the front-end controllers, responsible for reprogramming of the detector modules, underwent a major revision. In the original firmware the amount of parallelism was limited by FIFO sizes and the structuring of the on-board memory. The new firmware features a segmented DDR memory and multiple segments per module with a maximum of 28 modules per channel. With the new firmware the time needed to perform pixel-level reprogramming of the detector modules decreased dramatically to only few seconds. This allowed to deploy a more complete recovery scheme for the 2018 run where a full pixel-level reprogramming of the modules was possible also in short interruptions of the data taking (making use of the CMS *soft error recovery* mechanism). In Fig. 101 the recovery time before and after the firmware update are compared. Here it is important to note that before the firmware update only a partial recovery was performed while with the

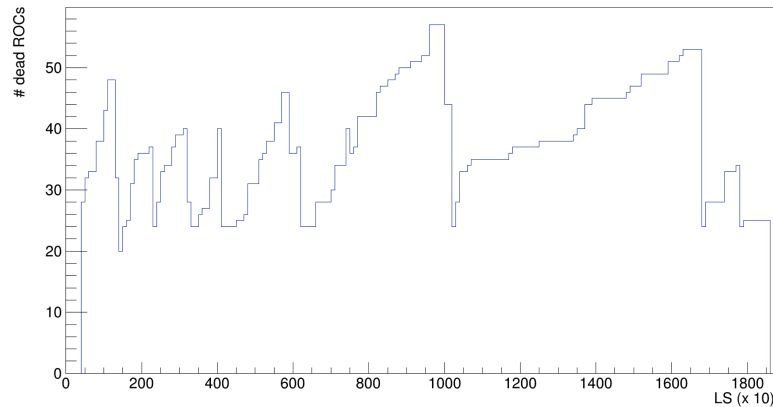


**Fig. 100:** The number of inactive ROCs as a function of time in BPIX layer 1 during a typical LHC fill in 2017. The number of inactive ROCs increases until a programmable threshold is reached, at which point the SEU recovery mechanism is activated and the ROCs are recovered. The SEU recovery mechanism can be activated several times during an LHC fill. The SEU rate depends on the instantaneous luminosity, which decreases over the time of the fill. In the fill used for this plot, the peak luminosity was around  $1.5 \times 10^{34} \text{ cm}^{-2} \text{ s}^{-1}$ . The typical rate for inactive ROCs is one in five minutes at an instantaneous luminosity of  $1.0 \times 10^{34} \text{ cm}^{-2} \text{ s}^{-1}$  for BPIX layer 1 modules. See Ref. [32].

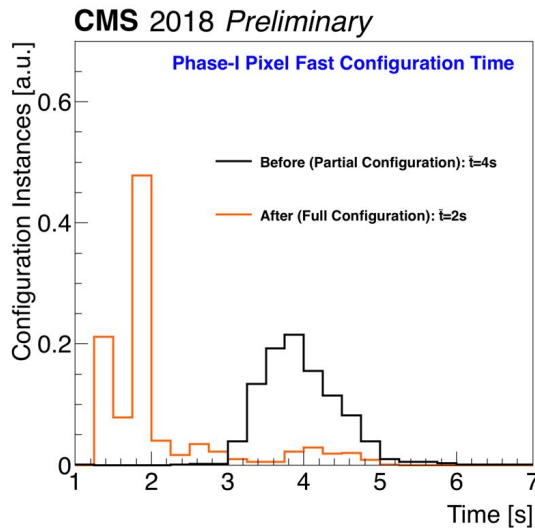


**Fig. 101:** Comparison of fast module configuration time before and after the PixelFEC firmware upgrade in 2018.

new firmware the full pixel-level reprogramming is carried out. The time needed for the full procedure with the new firmware is less than for the partial recovery with the old. For Run 3 a new scheme is being developed that will make use of fast reset commands to perform continuous reprogramming of pixel registers during a run.

### 6.2.2 Radiation effects in the CMS strip detector

The CMS strip tracker and the main components of its front-end electronics have been described in Section 3.2.2.2. In the following some of the radiation effects observed in the Front-End electronics of the system will be described.

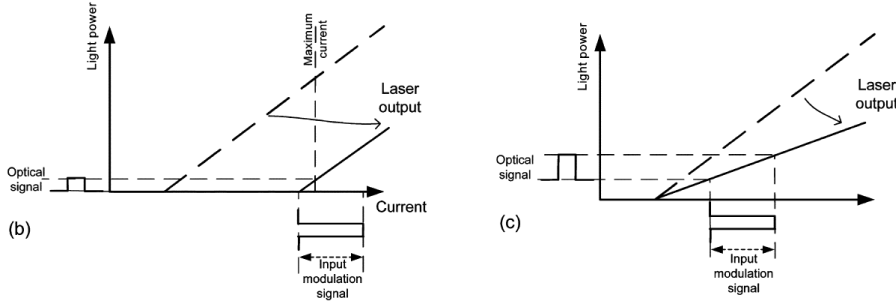


**Fig. 102:** Schematic laser light-current characteristics to illustrate the two main failure modes in the optical link system. Left: failure due to the laser threshold increasing beyond the maximum DC supply of the laser driver ASIC. Right: failure due to 50% loss of initial output efficiency. From Ref. [36].

### Radiation effects in the optical link system

The optical links of the strip detector are expected to undergo changes in their operational performance with increasing irradiation. Extensive tests prior to installation [36] suggest ample margin should be available at the end of life of the detector. Nonetheless, the performance of the optical links is continuously monitored also during operation. To this end, a calibration procedure normally used as optical link set up run, referred to as *gain scan* in the following, is used. The gain scan is a 2-dimensional scan of the gain and bias parameters of the LLD. The gain scan makes use of a feature of the APV25 chip which emits a digital ‘high’ signal (referred to as *tick mark*) every 70 clock cycles in the absence of a L1A. The height of this signal at the output is 800 mV differential ( $\pm 400$  mV) and it is stable to about 5% between APV chips. The height of the tick mark at the input of the FED is measured for all combinations of bias and gain settings.

The two main radiation effects on the optical link system are an increase in laser bias voltage and a decrease in gain [37] which are also illustrated in Fig. 102. The increase of threshold current is the more prominent effect and we will focus on it in the following. In Fig. 103 the threshold increase relative to a reference point in early 2016 is shown for two of the readout partitions of the strip tracker. The links are grouped by detector layer and the marker indicates the average threshold current increase for this layer. Each year is marked in a different colour, the operating temperature of the strip tracker was changed from  $-15^{\circ}\text{C}$  to  $-20^{\circ}\text{C}$  in early 2018. For each year also the start of high luminosity data taking is indicated. It can be seen that the threshold increases during periods of high luminosity production as can be expected. Annealing of the current is observed especially during year-end technical stops when the detector often is brought to room temperature for brief periods. The change to  $-20^{\circ}\text{C}$  is visible as an additional step down beyond the annealing, in some cases leading to threshold current below the ones from the reference point.

The expected change in threshold current with temperature can be parametrized as

$$I_{\text{th}} = I_{\text{th}}(0) \cdot \exp(\Delta T/T_0), \quad (32)$$

where  $I_{\text{th}}(0)$  is the characteristic current and  $T_0$  is the characteristic temperature. In order to try and obtain a measurement unaffected by different operating temperatures, the threshold current for different periods is scaled to a common reference. Various temperature measurements are available throughout the tracker but no direct measurement on the AOH is available. The temperature measurement on the front-end hybrid is taken as proxy and the rescaling to a common temperature for all time periods is performed. The result of this can be seen in Fig. 104. It can be seen that the trend seen in the non-rescaled figure is maintained but additional noise is observed, making the trend less clear. Two main effects are hypothesized to explain this effect currently, firstly the non-ideal proxy temperature on the front-end hybrid and the fact that the temperature measurements for technical reasons are not acquired directly during the gain scans but are chosen from suitable periods close in time. Especially the second

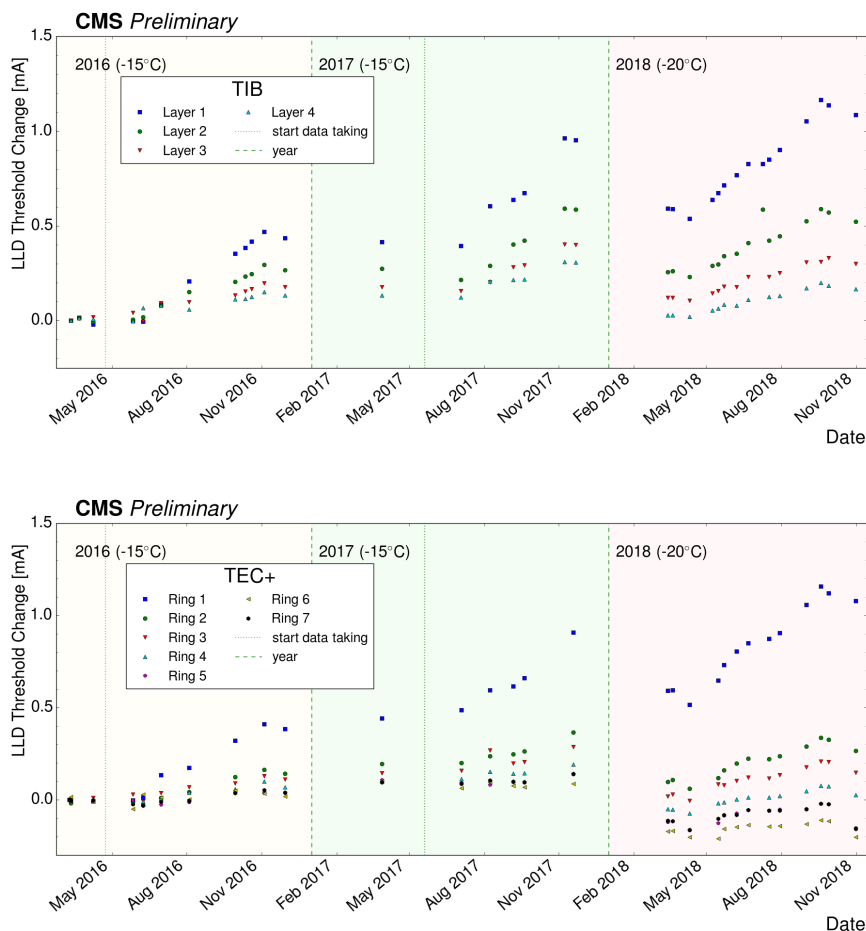


**Fig. 103:** Laser driver threshold increase as function of time for laser drivers in TIB (top) and TEC+ (bottom). Years are indicated in different colours, for each the start of high luminosity data taking is indicated in addition.

effect can lead to the additional spread as temperature data are taken from runs with potentially very different conditions.

The evolution of the threshold current is also compared to simulations. The data used are restricted to the running years 2016–2017 when the operating temperature of the strip tracker remained constant at  $-15^{\circ}\text{C}$ . The simulations are performed taking into account the luminosity delivered to CMS, split into 3.5 hours equivalent to irradiation duration in qualification tests [37]. The predicted damage (and hence threshold increase) is taken as the threshold increase at the qualification fluence of  $500\text{ fb}^{-1}$  scaled linearly to the luminosity delivered during the 3.5 hour block under consideration. The total damage is taken as the sum of the individual threshold increases also taking into account annealing based again on measurements in Ref. [37]. The comparison of the simulation to the gain scan data taking during 2016–2017 for the inner barrel is shown in Fig. 105. Very good agreement between data and simulation can be seen giving confidence in the adopted methodology and the predicted long-term behaviour of the optical links also during operating conditions. Further comparisons with data from other years are in preparation with the temperature scaling behaviour described above as one of the critical ingredients.

## 6. Impact of radiation on electronics and opto-electronics

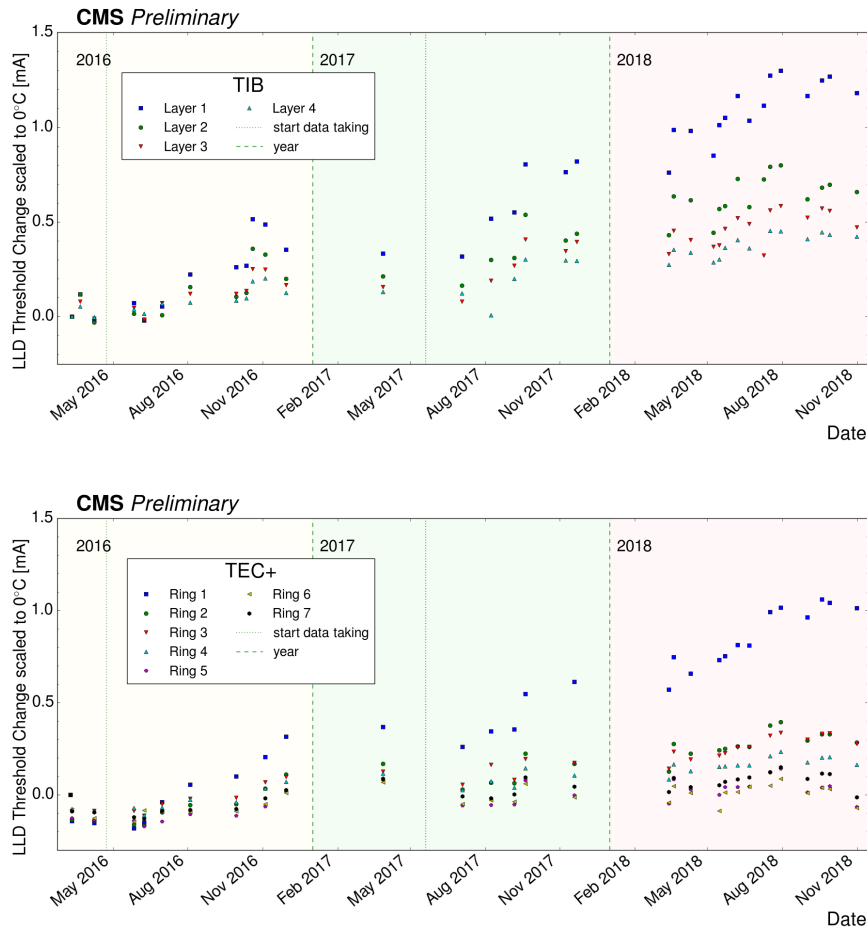


**Fig. 104:** Threshold current evolution as a function of time for the TIB partition (top) and TEC+ (bottom). The threshold current is scaled to  $0^{\circ}\text{C}$ . The increase is different by regions of equal radius, i.e., layers in the TIB and rings in the TEC.

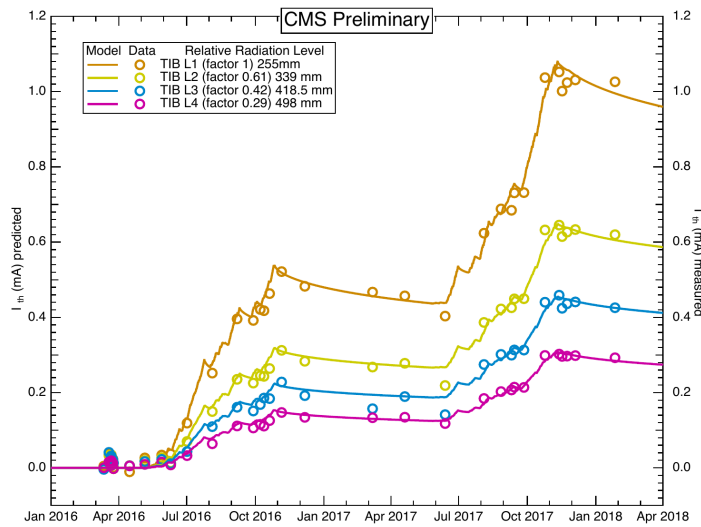


**Fig. 105:** Threshold current evolution as a function of time for the TIB subdetector compared to simulation.



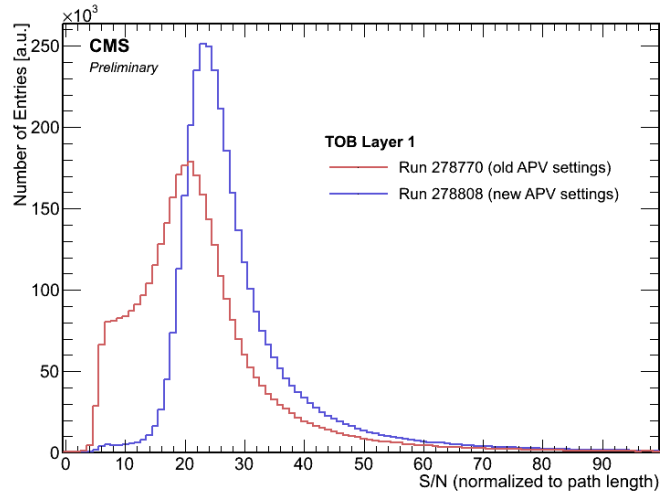


**Fig. 106:** Signal-to-noise distribution for hits on reconstructed particle tracks for two runs in 2016. The red curve comes from a run affected by the APV pre-amplifier saturation, the blue curve from a run with very similar conditions after the effect had been corrected.

#### *APV25 pre-amplifier saturation*

In late 2015 and early 2016 the strip tracker observed a loss of efficiency and a reduction of the signal-to-noise for clusters on particle tracks. The observed inefficiency finally reached levels of 10% of loss of hits on track for the most affected layer (outer barrel layer 1). While the initial hypothesis brought forward for the explanation of the effect was the passage of highly ionizing particles, it was subsequently found that the issue was caused by saturation effects in the APV25 pre-amplifier. The effect on the signal-to-noise distribution is illustrated in Fig. 106.

The red curve shows the signal-to-noise for clusters on tracker in the innermost layer of the outer barrel region. This is the region with 500  $\mu\text{m}$  thick sensors closest to the interaction region. Two main effects on the curve can be seen: an increased population of clusters at low signal-to-noise and a shifted most probable value (MPV) for the bulk of the distribution.

The root cause for this behaviour was finally traced to a larger than expected increase in decay time of the pre-amplifier when operating at low temperature (during LHC Run 1 the strip tracker was operated at  $+4^\circ\text{C}$  coolant temperature). The effect was removed by a change of the pre-amplifier feedback voltage (VFD) which very much reduced the decay time of the pre-amplifier. With this change, the hit efficiency was fully recovered even at beyond design instantaneous luminosities. The signal-to-noise distribution was also brought back to the expected Landau-like shape. This is again visible in Fig. 106, where the blue curve shows the signal-to-noise after the change of VFD. It can be seen that the MPV is shifted significantly compared to the pre-VFP change situation and also the population at low signal-to-noise has disappeared almost completely. The effect on the hit finding efficiency can be seen in Fig. 107. It can be seen that the saturation effect causes a drastic decrease in hit efficiency before the change of the VFP parameter while only a very slight decrease with increasing instantaneous luminosity is seen after the change.

One hypothesis is that the residual inefficiency is caused by actual highly ionizing particles (HIP). It has been shown [39] that charge depositions from HIPs can momentarily make the APV baseline drop very strongly and make the chip insensitive to further particle hits. This effect is recovered over the timescales of few tens of bunch crossings. An analysis is performed to identify events affected by highly ionizing particles. This is done in a run where non-zero suppressed data are recorded with the strip

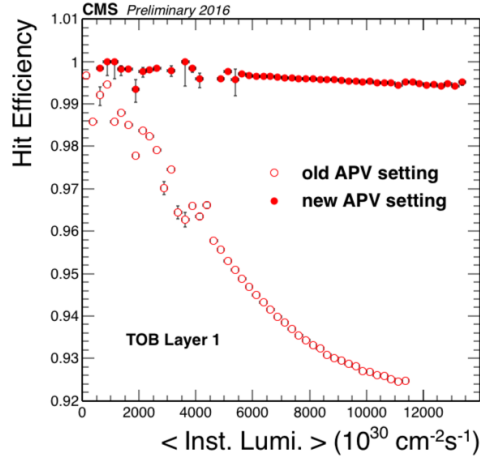


**Fig. 107:** Hit efficiency for clusters on tracks. The open points are data taken before the change of the APV pre-amplifier feedback voltage, and a clear decrease with increasing instantaneous luminosities can be seen. The full circles show data taken after the change. The inefficiency is much reduced and only a very slight decrease is seen as function of the luminosity [38].

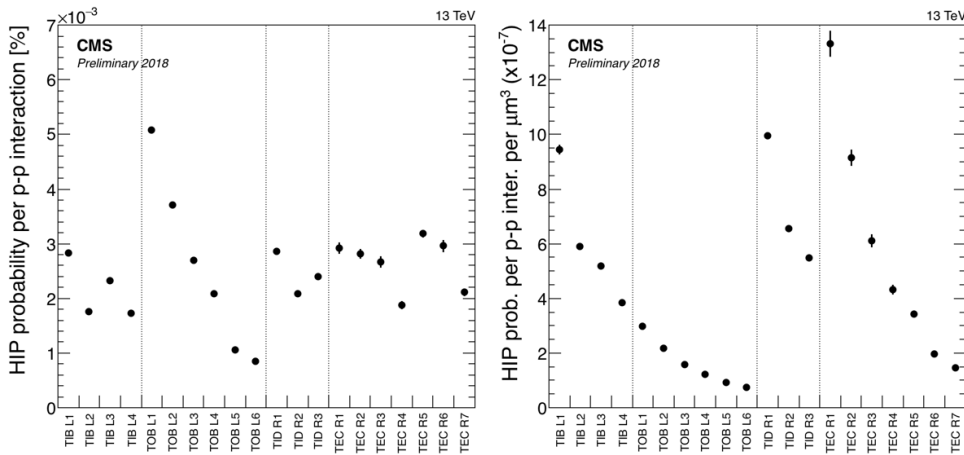


**Fig. 108:** Left: average probability of HIP event occurrence per pp interaction for different layers/rings of the silicon strip tracker. Right: average probability of HIP event occurrence per pp interaction normalized to unit detector volume for all layers/rings of the silicon strip tracker [38].

tracker during pp collision data taking<sup>6</sup>. Events affected by HIPs exhibit a strongly suppressed baseline of the APV25 with little variation between the strips. The probability of the occurrence of this type of events can be seen in Fig. 108 (left) for the different layers and rings of the strip tracker. It can be seen that the probability is again highest in the inner most layer of the outer barrel. To compensate for the effect of the sensor thickness and also the fact that the sensors with the same surface area can be read out by either 4 or 6 APV chips, the probability is normalized to a volume of  $1 \mu\text{m}^3$  read out by a given chip. This can be seen in Fig. 108 (right). It can be seen that with this normalization the probability follows a  $1/r^2$  behaviour for all regions of the detector.

The residual inefficiency as function of detector layer and event pile-up is shown in Fig. 109. It can be seen that the efficiency decreases linearly as function of increasing pile-up with the effect decreasing with increasing radius. This behaviour is consistent with a higher probability of HIP-like events occurring

<sup>6</sup>Due to the very large event size of about 14 MB the readout rate is strongly limited and thus this mode can only be used during special runs.

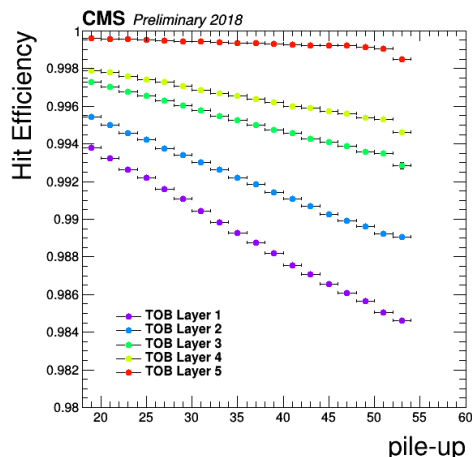


**Fig. 109:** Hit efficiency of silicon strip detectors from 5 TOB layers as a function of the pileup. Data from the long LHC fill 6714 (14 hours) taken in 2018 have been used. The number of colliding bunch crossings is 2544 and the peak pileup is 53.1 [38].

as function of radius and pile-up.

#### *Noise increase in runs with no sensor bias*

On a few occasions during LHC Run 2, the strip tracker observed high noise in the inner parts of endcap regions of the detector when the detector had been exposed to high luminosity beams but was fully switched off. The reasons for this configuration were for example infrastructure interruptions due to e.g., the cooling plants not being available. In order to investigate the origin of the failure a test was conducted during one of the last fills of the LHC Run 2. During this fill the powering status of modules of the inner rings of two endcap disks were changed. For one of the two endcaps, only the sensor bias voltage was turned off. For the other endcap the low voltage to the front-end electronics was turned off in addition to turning off the bias voltage. The results of this test can be seen in Fig. 110. It can be seen that high noise is present in both endcaps, i.e., irrespective of the powering status of the front-end electronics. The effect thus seems to come purely from the missing sensor bias. The effect decays with a timescale of several hours, its root cause is currently still unknown.

### 6.3 Discussion and outlook

The impact of radiation on tracker electronics at LHC has strong implications in the design and construction of the high-luminosity LHC detectors. The radiation effects on electronics can be separated in three main categories: TID, SEE and NIEL. A brief theoretical introduction was already given in Section 2.2. In this section we have shown the experimental observations of such effects on both electronics and opto-electronics. The operation of ATLAS and CMS trackers during the LHC Run 1 and Run 2 periods was strongly influenced by the unexpected behaviour of the detector electronics. The inner pixel layers of the two experiments were affected the most by the radiation damage.

In September/October 2015, ATLAS had to cope with a strong increase of the LV currents of the ROC (FE-I4B) in the newly installed IBL detector; this was caused by the generation of radiation induced current in NMOS transistors. CMS Pixel went through a complete replacement of the DC-DC converters (executed during the 2017–2018 winter shutdown), whose failures were also induced by the increase of leakage current in NMOS transistors.

The ATLAS IBL FE-I4B (130 nm CMOS technology) showed a strong drift of the LV currents and a de-tuning of the detector parameters, reaching a maximum of the effect between 1 and 3 Mrad.

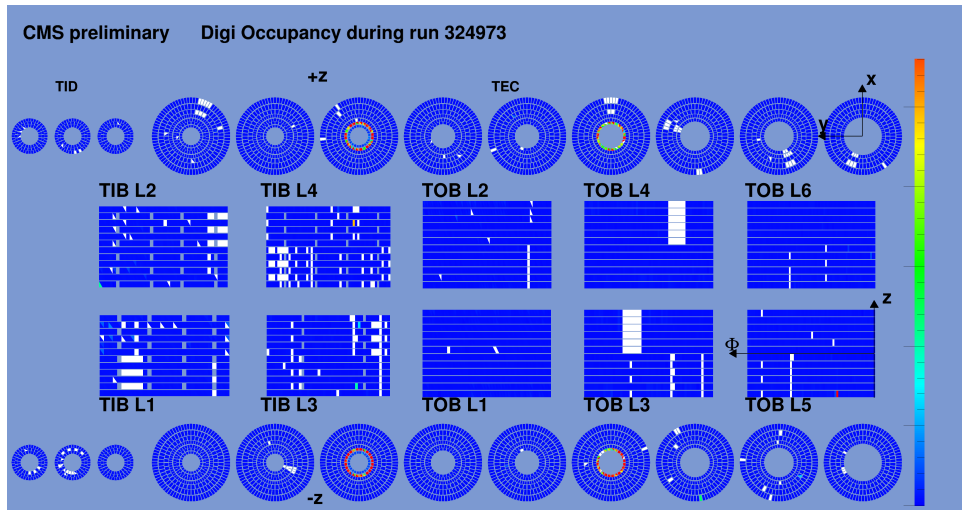


**Fig. 110:** Single strip occupancy from a run directly after dump of the LHC stable beams. Both sets of power groups in the positive and negative end caps which have been left without sensor bias only (TEC+) and without both sensor bias and front-end low voltage (TEC-) exhibit high occupancies.

The drift was characterized and reproduced during an X-ray irradiation campaign at CERN, where the dependency on parameters like dose rate, temperature and digital supply voltage was studied. Important guidelines were given to operate the detector safely, running temporarily at warmer temperature and lower digital supply voltage until the ‘TID bump’ was reached in 2016.

A similar but much less pronounced behaviour was observed in the analogue currents of the CMS pixel ROCs (PSI46v2, 250 nm CMOS technology), during Run 1 and at the beginning of Run 2 (before the replacement with the Phase-1 pixel detector chips (PSI46dig and PROC 600)). For the CMS pixel ROCs in the Phase-0 detector, a regular calibration was performed in order to contain the drift of the currents. For both cases, a plateau of the TID effects seems to be reached for high dose values  $> 300$  kGy (reached by the IBL detector during 2018); the increase was quantified to be  $\sim 14\%$  for the CMS Phase-1 pixel detector.

Furthermore, a beam annealing effect was observed in the ATLAS IBL FE-I4B chips in early October 2015, when the IBL was kept off and irradiated for a short time period (during two LHC fills). Such effect was reproduced during an irradiation campaign with 16 MeV protons and was observed during X-ray irradiation of CMS DC-DC converters. More systematic studies are needed for better understanding of this effect.

CMS observed SEU effects in the pixel detector. The most pronounced effect on data taking came from SEUs in the TBM chips of the Phase-1 detector. Because of an unprotected transistor their rate was greatly enhanced and in addition SEUs could result in the need for a power-on reset. These SEUs subsequently led to the discovery of the DC-DC converter problem during 2017. SEUs in the ROCs are also observed and the rates were quantified and found to be consistent with expectations. Particular emphasis was placed on the recovery mechanism. Actions were taken to mitigate the impact on the data quality and to limit the dead time in the DAQ system whenever a certain fraction of detector was affected. An upgrade of the control firmware for the 2018 run greatly reduced the recovery time needed.

The entire ATLAS tracker was affected by SEU, with different level of severity depending on the proximity and peculiarity of some of the electronics components. In the ATLAS IBL, SEUs were observed at rates close to the expectation based on previous tests in 24 GeV proton beam. SEUs in the global and local pixel configuration memories of FE-I4B chip were observed during LHC fills which had several consequences, including: module de-synchronization, current jumps, quiet modules, quiet pixels, noisy pixels, and broken clusters. Even in this case, a recovery mechanism was put in place in

2017, performing a regular reconfiguration of the FE-I4B global registers in the entire detector without introducing additional DAQ dead time. Furthermore, by read-back measurements and simulations of the electronics, it was demonstrated that SETs on the LOAD line of the DICE latch dominate the memory flips.

The ATLAS SCT observed and analysed the effects of SEU in their on-detector p-i-n diodes and in ROCs (ABCD). The macroscopic effect of such issues were respectively de-synchronization (bit flip in the trigger transmission) and noise (bit flip in the threshold value). Both measurements show a good agreement with the extrapolations from test beam results.

The ATLAS TRT also observed an effect on their ROCs (DTMROCs), in particular in the configuration registers. For this reason a continuous polling and rewriting of such registers was implemented in the DAQ system using the abort gap timing in the LHC orbit.

For what concerns the damage from NIEL, ATLAS TRT analogue electronics (ASDBLR, BiC-MOS DMILL radiation hard process) experienced a shift of the effective threshold cause by a loss of gain. This effect could be reproduced during an irradiation campaign at BNL and shows a saturation effect at about 30 kGy.

ATLAS SCT observed an effect on the opto-electronics, measuring the decrease of power of the on-detector VCSELs and a decrease of photo-current of the on-detector p-i-n diodes. Both effects are in good agreement with the test beam results even if the VCSEL optical power degradation seems a bit higher than expected considering the longer annealing periods during the LHC operation respect to the test beam campaigns.

CMS strips has also observed an impact of radiation on its optical links. The evolution of the optical link properties is monitored regularly during operations using optical link set up runs which scan gain and bias of the LLDs. As expected, a clear shift of the threshold current during Run 2 was seen. Important correction factors in this measurement come from the temperature and the fluence seen by the device. The data are compared to simulation for periods with constant operating temperature and very good agreement between data and simulation was found.

CMS observed occupancy dependent inefficiencies in the Strip Tracker during 2015 and 2016. This was eventually traced to saturation effects in the pre-amplifier of the APV25 chip caused by slower than anticipated discharge times at low temperatures. A change of a configuration register cured the problem. Residual dynamic inefficiencies which are observed as function of increasing instantaneous luminosity are likely caused by heavily ionizing particles (HIP). The rate of HIP-like events was measured in special runs with non-zero suppressed readout.

## References

- [1] M. Garcia-Sciveres *et al.*, *Nucl. Instrum. Methods Phys. Res* **A636** (2011) S155, [doi:10.1016/j.nima.2010.04.101](https://doi.org/10.1016/j.nima.2010.04.101).
- [2] ATLAS Collaboration, [Radiation induced effects in the ATLAS Insertable B-Layer readout chip](#), ATL-INDET-PUB-2017-001 (CERN, Geneva, 2017).
- [3] F. Faccio, G. Cervelli, *IEEE Trans. Nucl. Sci.* **52** (2005) 2413, [doi:10.1109/TNS.2005.860698](https://doi.org/10.1109/TNS.2005.860698).
- [4] L. Gonella, *et al.*, *Nucl. Instrum. Methods Phys. Res* **A582** (2007) 750, [doi:10.1016/j.nima.2007.07.068](https://doi.org/10.1016/j.nima.2007.07.068).
- [5] M. Backhaus, *JINST* **12** (2017) P01011, [doi:10.1088/1748-0221/12/01/P01011](https://doi.org/10.1088/1748-0221/12/01/P01011).
- [6] Braccini *et al.*, [The new Bern Cyclotron laboratory for radioisotope production and research](#), Proc. 2nd Int. Particle Conf., IPAC 2011, San Sebastian, Spain, September 4–9, 2011, pp. 3619–3621.
- [7] G. Balbi *et al.*, *JINST* **6** (2020) P06023, [doi:10.1088/1748-0221/15/06/P06023](https://doi.org/10.1088/1748-0221/15/06/P06023).
- [8] M. Menouni *et al.*, *JINST* **8** (2013) C02026, [doi:10.1088/1748-0221/8/02/C02026](https://doi.org/10.1088/1748-0221/8/02/C02026).
- [9] T. Calin *et al.*, *IEEE Trans. Nucl. Sci.* **43** (1996) 2874, [doi:10.1109/23.556880](https://doi.org/10.1109/23.556880).

- [10] F. Márquez *et al.*, *IEEE Trans. Nucl. Sci.* **62** (2015) 1609, doi:10.1109/TNS.2015.2456831.
- [11] E. López-Morillo *et al.*, *IEEE Trans. Nucl. Sci.* **65** (2018) 1943, doi:10.1109/TNS.2018.2840326.
- [12] F.R. Palomo *et al.*, Simulation of SET/SEU in microelectronics: AFTU software, Radiation Effects in the LHC Experiments and Impact on Operation and Performance, CERN, 11–12 February 2019, proc. in preparation (2020), [Indico](#).
- [13] M. Huhtinen and F. Faccio, *Nucl. Instrum. Methods Phys. Res* **A450** (2000), 155, doi:10.1016/S0168-9002(00)00155-8.
- [14] T. Sjöstrand *et al.*, *Comput. Phys. Commun.* **191** (20115) 159, doi:10.1016/j.cpc.2015.01.024, [arXiv:1410.3012](#) [hep-ph].
- [15] I. Dawson, Pos **Vertex2012** (2013) 015, doi:10.22323/1.167.0015.
- [16] A. Ferrari *et al.*, FLUKA: A multi-particle transport code, CERN-2005-010, INFN/TC-05/11, SLAC-R-773, (CERN, Geneva, 2005), doi:10.5170/CERN-2005-010.
- [17] A. Dafinca *et al.*, *JINST* **9** (2014) C01050, doi:10.1088/1748-0221/9/01/C01050.
- [18] I. Dawson *et al.*, *JINST* **14** (2019) P07014, doi:10.1088/1748-0221/14/07/P07014.
- [19] D.G. Charlton *et al.*, *Nucl. Instrum. Methods Phys. Res* **A456** (2001) 300, doi:10.1016/S0168-9002(00)00666-5.
- [20] J. Beringer *et al.*, *Nucl. Instr. Meth.* **A435** (1999) 375. doi:10.1016/S0168-9002(99)00570-7.
- [21] ATLAS TRT Collaboration, *JINST* **3** (2008) P02013, doi:10.1088/1748-0221/3/02/P02013.
- [22] ATLAS TRT Collaboration, *JINST* **3** (2008) P02014, doi:10.1088/1748-0221/3/02/P02014.
- [23] ATLAS TRT Collaboration, *JINST* **3** (2008) P10003, doi:10.1088/1748-0221/3/10/P10003.
- [24] ATLAS TRT Collaboration, *JINST* **3** (2008) P06007, doi:10.1088/1748-0221/3/06/P06007.
- [25] G. Crone *et al.*, *Nucl. Instrum. Methods Phys. Res* **A623** (2010) 534, doi:10.1016/j.nima.2010.03.061.
- [26] ATLAS Collaboration, [Particle identification performance of the ATLAS Transition Radiation Tracker](#), ATLAS-CONF-2011-128, (CERN, Geneva,2011).
- [27] ATLAS Collaboration, [Interactive web pages for radiation environment exploration of ATLAS](#) [ATL-SOFT-PUB-2020-003](#), 2020.
- [28] T. Åkesson *et al.*, Implementation of the DTMROC-S ASIC for the ATLAS TRT detector in a 0.25  $\mu\text{m}$  CMOS technology, 2002 IEEE Nuclear Science Symposium Conference Record, Norfolk, VA, USA, 2002, pp. 549-553 vol.1, doi: 10.1109/NSSMIC.2002.1239373.
- [29] F. Faccio *et al.*, SEU effects in registers and in a dual-ported static RAM designed in a 0.25 $\mu\text{m}$  CMOS technology for applications in the LHC, Proc. 5th Conference on Electronics for LHC Experiments, Snowmass (CO), USA, 20–24 Sep 1999, CERN-LHCC-99-033, CERN-99-09, (CERN, Geneva, 1999), pp.571-575, doi:10.5170/CERN-1999-009.571.
- [30] S. Chatrchyan *et al.* [CMS Collaboration], *JINST* **3** (2008) S08004, doi:10.1088/1748-0221/3/08/S08004.
- [31] A. Dominguez *et al.* [CMS Collaboration], CMS technical design report for the pixel detector upgrade, CMS-TDR-011, CERN-LHCC-2012-016, (CERN, Geneva, 2012), doi:10.2172/1151650.
- [32] CMS Collaboration, *JINST* **14** (2019) P10017, doi:10.1088/1748-0221/14/10/P10017.
- [33] H.-C. Kästli, *Nucl. Instrum. Methods Phys. Res* **A565** (2006) 188, doi:10.1016/j.nima.2006.05.038, [arXiv:physics/0511166](#).
- [34] J. Hoss *et al.*, *JINST* **11** (2016) C01003, doi:10.1088/1748-0221/11/01/C01003.
- [35] F. Faccio *et al.*, [Failure of DC-DC modules in the CMS pixel system during the 2017 run](#), (CERN, Geneva, 2018).
- [36] R. Macias *et al.*, *IEEE Trans. Nucl. Sci.* **52** (2005) 1488, doi:10.1109/TNS.2005.855812.
- [37] K. Gill *et al.*, *IEEE Trans. Nucl. Sci.* **49** (2002) 2923, doi:10.1109/TNS.2002.805422.

- [38] M. Jansova, [Search for the supersymmetric partner of the top quark and measurements of cluster properties in the silicon strip tracker of the CMS experiment at Run 2](#) Ph.D. thesis, University of Strasbourg, 2018.
- [39] CMS Tracker Collaboration, *Nucl. Instrum. Methods Phys. Res* **A543** (2005) 463, [doi:10.1016/j.nima.2004.11.049](https://doi.org/10.1016/j.nima.2004.11.049).





## 7 Simulating radiation effects and signal response in silicon sensors

*Editors:* M. Bomben<sup>a</sup>, J. Sonneveld<sup>b</sup>.

*Contributing authors:* M. Benoit<sup>c</sup>, M. Bomben<sup>a</sup>, E. Chabert<sup>d</sup>, T. Lari<sup>e</sup>, J. Llorente Merino<sup>f</sup>, B. Nachman<sup>g</sup>, L. Rossini<sup>h</sup>, P. Sabatini<sup>i</sup>, J. Sonneveld<sup>b</sup>, C. Suarez<sup>j</sup>, M. Swartz<sup>j</sup>, T. Szumlak<sup>k</sup>, A. Wang<sup>l</sup>.

<sup>a</sup>LPNHE & University of Paris, France

<sup>b</sup>Nikhef, Amsterdam, Netherlands

<sup>c</sup>Brookhaven National Laboratory (BNL), New York, USA

<sup>d</sup>Hubert Curien Pluridisciplinary Institute (IPHC), Strasbourg, France

<sup>e</sup>INFN, Milan, Italy

<sup>f</sup>Simon Fraser University, Burnaby, Canada

<sup>g</sup>Lawrence Berkeley National Laboratory, USA

<sup>h</sup>University of Milan and INFN, Milan, Italy<sup>7</sup>

<sup>i</sup>Institute for Corpuscular Physics (IFIC), Centro Mixto Universidad de Valencia - CSIC

<sup>j</sup>Johns Hopkins University, Baltimore, USA

<sup>k</sup>AGH University of Science and Technology, Krakow, Poland

<sup>l</sup>University of Wisconsin-Madison, USA

Simulating the effects of radiation on signal response in silicon sensors is crucial for accurately predicting detector performance throughout the lifetime of the experiment. This, in turn, improves the reconstruction accuracy of proton–proton collisions and helps maintain the experiment’s physics reach. In what follows, the strategies implemented by the LHC experiments to correctly simulate the evolution of silicon tracking performance with luminosity will be presented.

As already discussed in Section 2, the main macroscopic effects on silicon tracking devices resulting from radiation damage are: increase of leakage current, change of operational voltage, and signal loss. They are the result of phenomena happening at a microscopic level which are a consequence of the creation of defects that act as deep levels in the semiconductor energy gap. These levels can trap charged carriers – reducing the signal and modifying the electric field distribution inside the sensors. They also act as additional generation levels and these dynamics give rise to the aforementioned change in performance at a macroscopic level. These effects are further complicated by the temperature history, since the thermal motion in the silicon lattice leads to annealing phenomena that cause new defects to be formed or existing defects to dissociate.

The general parameterization of radiation damage simulation for silicon tracking detectors of LHC experiments should model the change of the electric field distribution in the silicon bulk and the signal loss with the accumulated luminosity. These two effects in turn also have an impact on other observables such as spatial resolution through modification of cluster sizes and Lorentz angle deflection.

Before presenting the details and results of the different LHC experiments, some general aspects of sensor simulations are discussed. Particles originating from collisions in the LHC deposit charge in silicon detectors by ionizing the silicon bulk: the deposited charge drifts through the sensor to an electrode, then the analogue signal is digitized, buffered and read out.

In general, for the LHC experiments the following are important to consider in simulation.

**Electric field:** as a result of radiation damage, the shape of the electric field inside the bulk of the sensor

This chapter should be cited as: Simulating radiation effects in silicon sensors and modelling charge response, Eds. M. Bomben, J. Sonneveld, DOI: [10.23731/CYRM-2021-001.123](https://doi.org/10.23731/CYRM-2021-001.123), in: Radiation effects in the LHC experiments: Impact on detector performance and operation, Ed. Ian Dawson,

CERN Yellow Reports: Monographs, CERN-2021-001, DOI: [10.23731/CYRM-2021-001](https://doi.org/10.23731/CYRM-2021-001), p. 123.

© CERN, 2021. Published by CERN under the [Creative Commons Attribution 4.0 license](https://creativecommons.org/licenses/by/4.0/).

<sup>7</sup>Now at DESY, Hamburg and Zeuthen, Germany

changes with fluence. Simulations of the three-dimensional profile of the electric field can be obtained with software based on technology computer-aided design (TCAD). Inputs for the electric field simulation are the sensor type, doping, and geometry, the irradiation fluence, the bias voltage, and the temperature.

**Lorentz angle:** the Lorentz angle  $\theta_L$  is the deflection angle for carriers in presence of an electric field  $\vec{E}$  and a magnetic field  $\vec{B}$ ; and is defined as the angle between the drift direction and the electric field. For a carrier travelling from an initial bulk depth  $z_i$ <sup>8</sup> to a final depth  $z_f$  inside the bulk of the sensor, the Lorentz angle  $\theta_L$  can be expressed by:

$$\tan \theta_L(z_i, z_f) = \frac{rB}{|z_f - z_i|} \int_{z_i}^{z_f} \mu(E(z)) dz, \quad (33)$$

where  $\mu$  is the charged carrier mobility,  $r$  is the Hall scattering factor,  $B$  is the magnetic field magnitude, and  $E(z)$  is the electric field as a function of the position. It is then possible to note that a change in electric field resulting from radiation damage will also impact the Lorentz angle, since the mobility depends on the electric field.

**Ramo potential and induced charge:** moving charges inside the bulk induce a signal onto the collecting electrodes. The induced signal can be calculated using the Shockley–Ramo theorem [1,2]. The induced signal by a charge  $q$  moving from the initial position  $\vec{x}_i$  to the final position  $\vec{x}_f$  is:

$$Q_{\text{induced}} = -q[\phi_w(\vec{x}_f) - \phi_w(\vec{x}_i)], \quad (34)$$

where  $\phi_w$  is the Ramo potential. The Ramo potential depends only on the geometry of the electrodes and the bulk thickness, and therefore it is evaluated once per geometry. The Ramo potential can be evaluated using TCAD tools replacing silicon with vacuum in the simulated structure so only electrodes are left.

**Charge trapping:** the charge carriers can be trapped by radiation-induced deep defects<sup>9</sup>, with a characteristic trapping time  $\tau$  that is proportional to the inverse of the radiation fluence  $\Phi$ :  $\tau = 1/(\Phi\beta)$ , where  $\beta$  is the trapping constant.

**Charge collection efficiency:** one important observable to monitor is the collected charge, which is reported as the most probable value of the cluster charge distribution. The charge collection efficiency (CCE) is defined as the ratio of the most probable value of the cluster charge distribution of a certain point in time against the value before irradiation. The evolution of CCE with luminosity is important to determine the sensor operational voltage: simulations of CCE vs. bias voltage for different radiation fluences are used to assure that the detector is collecting the largest possible amount of signal.

**Signal digitization:** charged particles crossing a detector produce electron–hole pairs that then drift towards the electrodes. The consequent charge induction on electrodes is the so-called *digitization* step in detector simulation.

In Fig. 111 a schematic view of the process flow presented above is shown.

While TCAD can be used for detailed simulations of silicon detectors, it is very demanding in computing time and is not easy to integrate in other tools, for example, Monte Carlo simulations. For this reason, TCAD is often used for the computation of the electric field in silicon sensors, and the resulting

<sup>8</sup>When referring to silicon sensors, the local coordinate  $z$  identifies the direction orthogonal to the collecting electrodes in planar technology and the one parallel to the columns axis in 3D technology.

<sup>9</sup>These defects are deep in the sense that the energy required to remove an electron or hole from the trap to the valence or conduction band is much larger than the characteristic thermal energy  $kT$ , where  $k$  is the Boltzmann constant and  $T$  is the temperature.

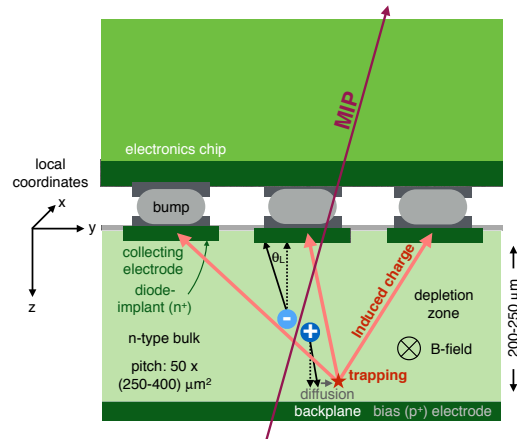


**Fig. 111:** An illustration of the digitization process for planar sensors [3]

field is then fed into other software that include drift-diffusion models of charge carriers, such as AllPix [4], KDetSim [5], and PixelAV [6–8]. AllPix2 [9] in addition allows for simulation of material effects in the experimental set-up such as multiple scattering and nuclear interactions.

Different implementations of sensor simulations are used by the large LHC experiments. In what follows, the implementations for ATLAS (7.1), CMS (7.2), and LHCb (7.3) are described. In Section 7.4 the different strategies of the LHC experiments are compared.

## 7.1 ATLAS

The ATLAS tracking system is described in more detail in Section 3.2. This section will focus on the simulation of radiation effects and charge transport in the sensors in the ATLAS pixel detector. Silicon sensor simulations of the ATLAS SCT are not discussed here.

The ATLAS pixel detector [11–13] contains hybrid pixel modules made by  $n^+$ -in- $n$  sensors bump bonded to custom front-end readout chips. In 2015, the now innermost barrel layer was added to the original detector; this new layer – called the insertable B-layer (IBL) [14, 15] – features thinner sensors (200 vs. 250  $\mu\text{m}$ ) with respect to all other layers as well as smaller cells (50  $\times$  250  $\mu\text{m}^2$ ; everywhere else the pixel pitch is 50  $\times$  400  $\mu\text{m}^2$ ). For more details on the ATLAS pixel detector see Section 3.2.1.1.

As the closest detector component to the interaction point, the pixel detector was subjected to a significant amount of radiation over its lifetime; as stated above, among the barrel layers, the IBL is the closest one to the beam pipe. The total fluence received during its lifetime has been of the order of  $\sim 1 \times 10^{15}$   $n_{\text{eq}}/\text{cm}^2$  at the end of Run 2 (corresponding to a luminosity delivered by the LHC of  $159 \text{ fb}^{-1}$ ), while a total fluence of  $1.8 \times 10^{15}$   $n_{\text{eq}}/\text{cm}^2$  is estimated by the end of Run 3 in 2023 (for a total estimated integrated luminosity of  $300 \text{ fb}^{-1}$ ). Figure 112 shows the fluence received by the four barrel layers as a function of the number of days since the start of Run 2.

In what follows, the details of a new digitizer model [3] that accounts for effects due to radiation damage will be presented. Section 7.1.1 presents the model used and each component used, and Section 7.1.2 presents the results of the simulation compared with data from Run 2.

### 7.1.1 ATLAS pixel digitizer model overview

In the digitization step [3] energy deposits are obtained from Geant4 [17] and saved in a list of position and energy, called *hits*. Radiation damage effects are modelled in this simulation step for ATLAS Pixel sensors. The algorithm which will be presented here was first developed on AllPix [4], a Geant4-based tool which allows an easy and fast simulation of silicon detector performance after radiation damage.

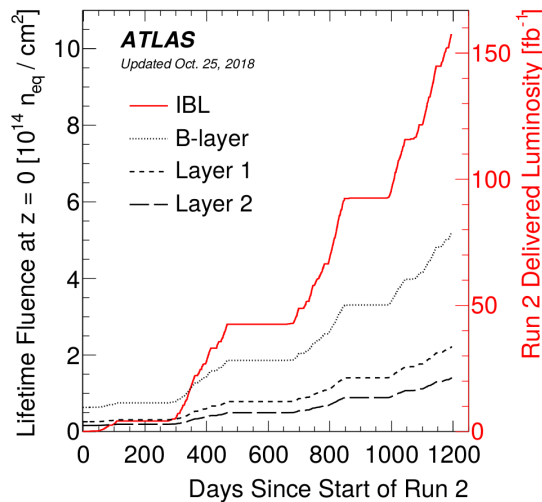


**Fig. 112:** Estimates of the lifetime fluence experienced by the four layers of the current ATLAS pixel detector as a function of time since the start of Run 2 (June 3, 2015) at  $z \sim 0$ . The IBL curve represents both the fluence on the IBL (left axis) as well as the delivered integrated luminosity in Run 2 (right axis). From Ref. [16].

Afterwards, the model was also implemented in the ATLAS common software Athena [18], in order to exploit the full-geometry description of the ATLAS detector, and check what the effects on physical quantities would be. The structure of the main algorithm in the two softwares is very similar.

The algorithm for simulating radiation damage within the ATLAS Athena digitizer is as follows:

- after charge deposition by Geant4, the digitizer takes in as input the charge and position of the various particles, as well as global information such as the electric field profile after radiation damage;
- groups of  $\sim 10$  charges are formed to be treated as a charge chunk to speedup the digitization;
- using the electric field distribution – based on voltage and fluence – the time for the charge chunk to drift to the electrode is evaluated;
- this drift time is compared to a randomly generated trapping time; the final bulk depth for the chunk is hence determined;
- deflections are calculated evaluating the average Lorentz angle along the path (using Eq. 33) and the contribution due to carrier diffusion, hence the final charge chunk position is determined;
- based on the initial and final charge positions, the induced charge on the electrode is then determined using the Ramo potential (Eq. 34).

#### *Geometry and condition configuration*

The first step of the software consists in the loading of all the geometry and operational parameters needed: thickness, pitch, tilt, fluence, trapping time, temperature, and magnetic field strength. Lookup tables are then loaded for Ramo potential, electric field maps, and Lorentz angle maps. Geant4 then generates the energy hits and these are converted into electron–hole pairs; the energy needed is about  $\sim 3.6$  eV for a pair. Charges are then drifted towards the electrodes, and, using the pre-loaded maps, the probability of being trapped is calculated, and then, using the Ramo potential, the induced charge on the electrodes is evaluated.

The different inputs to digitization are described in the following paragraphs.

## Fluence

Fluence is an important input for the simulations, in particular for the electric field determination. Leakage current is the observable used to relate luminosity to fluence. This is obtained from the measurement of leakage current compared with the predictions. Figure 113 (left) shows the predicted leakage current compared with data during Run 2. Figure 113 (right) shows the conversion factor from luminosity to fluence for the IBL, as a function of  $z$ , compared with predictions with Pythia8+ FLUKA [19, 20] and Pythia+Geant4. From a comparison among the different simulations an uncertainty of about 15 % is assumed for this conversion factor.

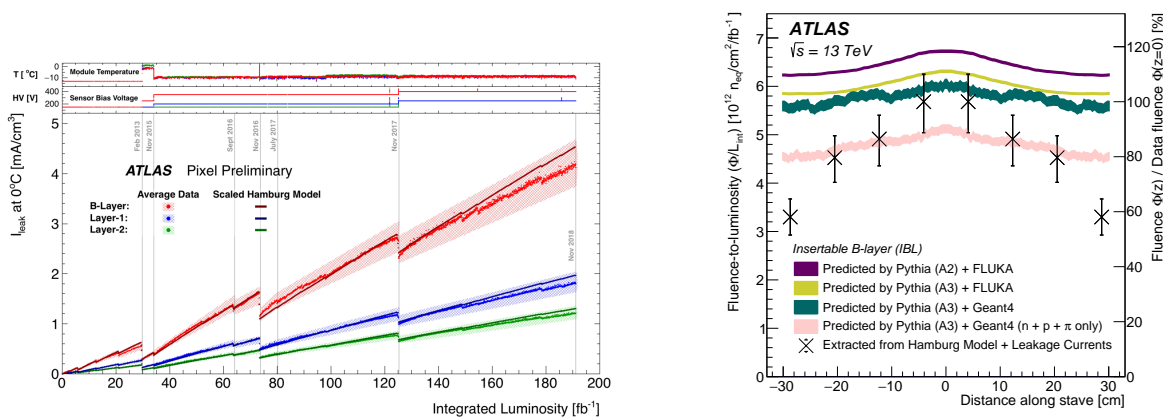


**Fig. 113:** Left: average measured leakage current data of a representative sample of modules in the ATLAS pixel detector barrel layers over the full period of operation. The leakage current data are normalized to  $0^\circ\text{C}$ ; the average module sensor temperature is shown in the top panel. From Ref. [21]. Right: the fluence-to-luminosity conversion factors (extracted from leakage current fits), as a function of  $z$ , compared with the Pythia+FLUKA and Pythia+Geant4 predictions. From Ref. [3].

## Electric field

Once the fluence level is known the electric field profile inside the silicon sensors can be calculated for different bias voltages using TCAD tools. The radiation damage models used in TCAD for simulating the electric field profile in the ATLAS pixel detector were the Chiochia model [22] for planar sensors and the Perugia model [23] for the 3D sensors. The Chiochia model features two traps, with one acceptor and one donor trapping centre, with energy levels at  $E_C - 0.525$  eV and  $E_V + 0.48$  eV for the conduction  $E_C$  and valence band energy level  $E_V$ , respectively. The Perugia model instead includes three trap levels: two acceptor and one donor, with energies:  $E_C - 0.42$  eV,  $E_C - 0.46$  eV, and  $E_V + 0.36$  eV, respectively. As explained in detail in Ref. [3], the values of trap parameters (energy, density, capture cross-sections) were varied to estimate the impact of these uncertainties on the simulated electric field and all the other observables depending on it.

The TCAD simulations are all performed at the temperature indicated by the authors of the radiation damage models used, i.e.,  $-10^\circ\text{C}$  for the planar sensors [22] and  $20^\circ\text{C}$  for the 3D sensors [23]. The reason for this choice is explained in detail for planar sensors in Ref. [3], and the same reasoning applies for 3D sensors. TCAD models only include a small number of effective states, and in reality the temperature dependence is reduced when a more complex (but computationally intractable) combination of states is present. Moreover, when assessing the impact on electric field predictions due to uncertainties from trap parameters as explained above, it was found that a variation of the trap energy level  $E_t$  by 10% of thermal energy  $k_B T$  is consistent with naive temperature variations that bracket all Run 2 operational temperatures ( $-15^\circ\text{C}$  to  $+20^\circ\text{C}$ ) [3]. Therefore, the impact on electric field prediction due to uncertainties from imperfect temperature-dependence parameterization in TCAD radiation damage models is already taken

into account by variations of values of TCAD radiation damage model trap parameters.

In order to save simulation time, many quantities derived from the electric field (such as the time for a charge to drift to an electrode) are also precomputed and saved as maps. Further details can be found in Ref. [3]. The two main parameters for generating maps are the fluence and the bias voltage. Typically, the electric field is computed only for a few benchmark pairs as it is not feasible to precompute all possible combinations. To be as flexible as possible, a new method has been developed to produce electric field maps for any (fluence, voltage) pair on the fly within the digitizer by interpolating existing electric field maps. This takes advantage of the fact that the electric field at a fixed sensor depth varies smoothly with fluence and voltage. Given a desired (fluence, voltage) pair an interpolation with cubic splines is first among available fluences to obtain various samples with the correct fluence but different voltages. Using these new samples the interpolation is repeated, this among voltages, to obtain the correct (fluence, voltage) target. Closure tests on this interpolation method were performed by comparing the precomputed maps with the interpolated maps. Example distributions of the electric field and  $dE/dx$  in Figure 114 show good agreement between the two. The electric field interpolation has now been added to the Athena [18] digitizer for planar sensors.

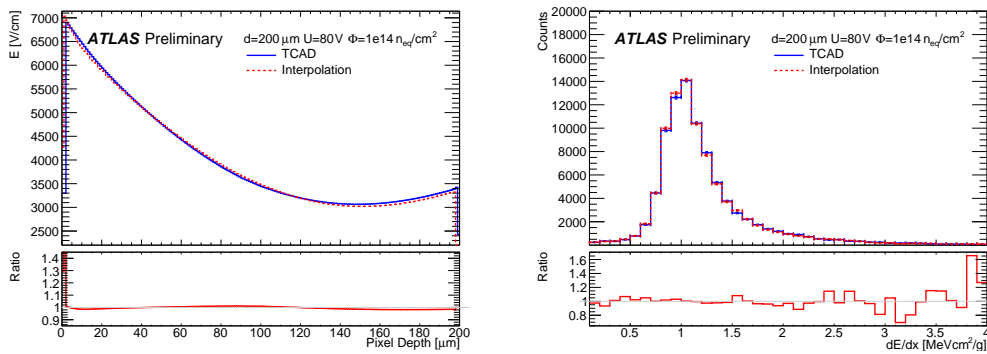


**Fig. 114:** Comparisons of the electric field and stopping power  $dE/dx$  for the interpolated maps and the maps generated directly from TCAD [24].

In addition to the more common planar pixel sensors, ATLAS also has 3D pixel sensors located at high  $\eta$  in the IBL. A radiation damage implementation for 3D sensors has been added to Athena too. The implementation is very similar to that of the planar sensors, despite the differing geometry.

To validate the Athena implementation muons have been simulated hitting the 3D sensors (with the planar sensors disabled). The simulated average  $dE/dx$  is plotted for a series of benchmarks, with fluences ranging from 0 to  $10^{16}$   $n_{eq}/cm^2$ . Figure 115 shows that the results from Athena agree well qualitatively with the results from standalone AllPix simulation, which itself has been validated against real test beam data.

### Lorentz angle

In the simulations, the Lorentz angle is calculated according to Eq. 33 and saved in maps which are loaded at the beginning for each geometry and condition set-up (fluence, bias voltage, and temperature).

The Lorentz angle has a direct impact on the cluster size, and it is therefore an important parameter to monitor. The Lorentz angle is obtained by fitting the transverse cluster size as a function of the incidence angle of the associated track, with a function  $F$  defined as:

$$F(\alpha) = [a \times |\tan \alpha - \tan \theta_L| + b/\sqrt{\cos \alpha}] \otimes G(\alpha|\mu = 0, \sigma), \quad (35)$$

where  $\alpha$  is the track incidence angle with respect to the normal direction of the sensor in the plane perpendicular to the magnetic field. The parameter  $\theta_L$  is the fitted Lorentz angle,  $G$  is a Gaussian prob-

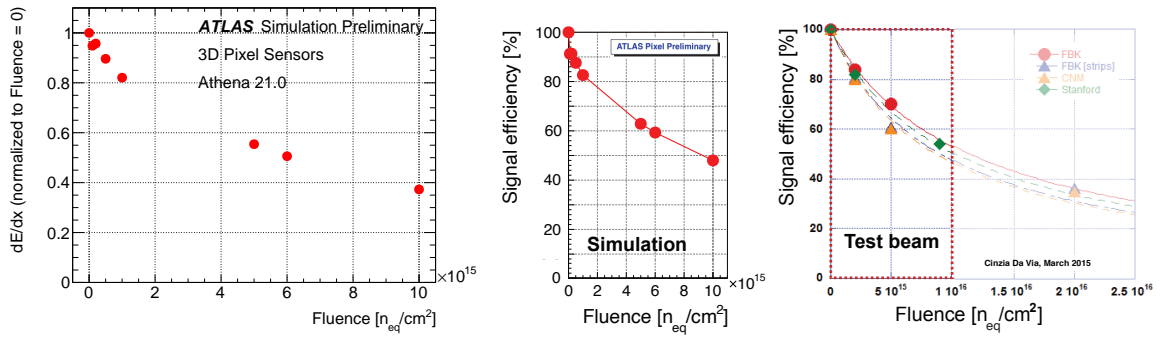


**Fig. 115:** Comparison of the charge collection efficiency vs. fluence for (left) the Athena simulation [25], (mid) the standalone AllPix simulation [26], and (right) real test beam data [27, 28].

ability distribution evaluated at  $\alpha$  with mean 0 and standard deviation  $\sigma$ , and  $a$  and  $b$  are two additional fit parameters related to the depletion depth and the minimum cluster size, respectively.

Figure 116 shows the mean transverse cluster size versus track incidence angle, in both data and AllPix simulation for integrated fluence at the end of 2016 and bias voltage of 80 V.

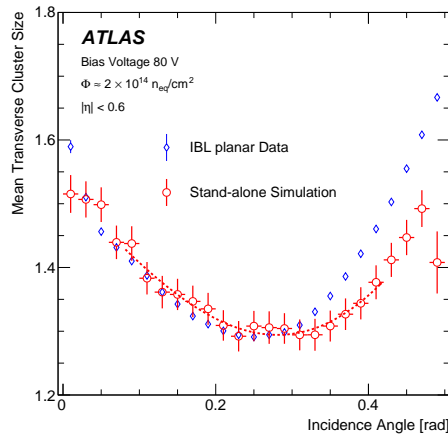


**Fig. 116:** The mean transverse cluster size versus transverse incidence angle near the end of the 2016 run (with about  $\sim 2 \times 10^{14} \text{ n}_{\text{eq}}/\text{cm}^2$  collected) with a bias voltage of 80 V compared with simulations from AllPix using the Chiochia model. From Ref. [3].

### Charge trapping

The trapping constants, i.e., the  $\beta$  values, have been taken from different measurements. It has been found that  $\beta$  depends on the type of irradiation, the temperature, and the annealing history, and on carrier type ( $e$ ,  $h$ ). The values used in the digitizer are an average from Refs. [29–31], with the uncertainties that account for differences in central value, irradiation type, and thermal history. The values used were:

$$\begin{aligned}\beta_e &= (4.5 \pm 1.5) \times 10^{-16} \text{ cm}^2/\text{ns}, \\ \beta_h &= (6.5 \pm 1.5) \times 10^{-16} \text{ cm}^2/\text{ns}.\end{aligned}$$

### Ramo potential and induced charge

Ramo potential maps are loaded at the beginning of each simulation, one for each geometry, and are used whenever a charge is trapped to estimate the induced charge in all the pixels in a  $3 \times 3$  matrix around the

closest pixel to the trapping position. These maps are evaluated with TCAD in order to solve the Poisson equation. Figure 117 shows a 2D projection of the Ramo potential for an IBL planar sensor.

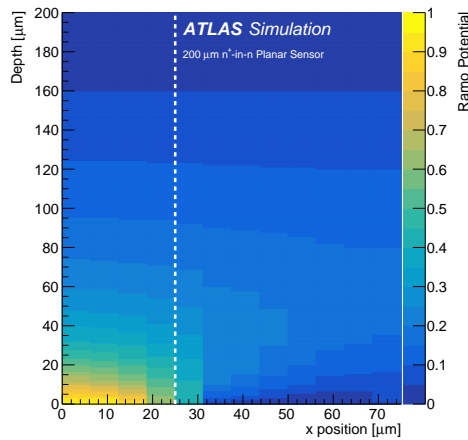


**Fig. 117:** A 2D projection in the  $z - x$  plane of the Ramo potential map for an ATLAS IBL planar module. The dashed vertical line (at  $25 \mu\text{m}$ ) indicates the edge of the primary pixel. From Ref. [3].

### 7.1.2 Validation with data

The evolution of the main performance parameters with fluence is simulated with AllPix, and the results are compared with collision data. This software is also used to predict future condition of the detector, in order to plan changes in the set-up to assure a high detection efficiency. In this section results obtained during the Run 2 with ATLAS detector are presented, in particular for the IBL system. During this time the bias voltage was increased to cope with radiation damage: the IBL sensors have been operated at 80 V in 2015, 150 V in 2016, 350 V in 2017, and 400 V in 2018.

In the following, the comparison between data and simulations is presented for charge collection efficiency (Section 7.1.2.1) and Lorentz angle (Section 7.1.2.2); results for mobility modelling are included too (see Section 7.1.2.3).

#### 7.1.2.1 Charge collection efficiency

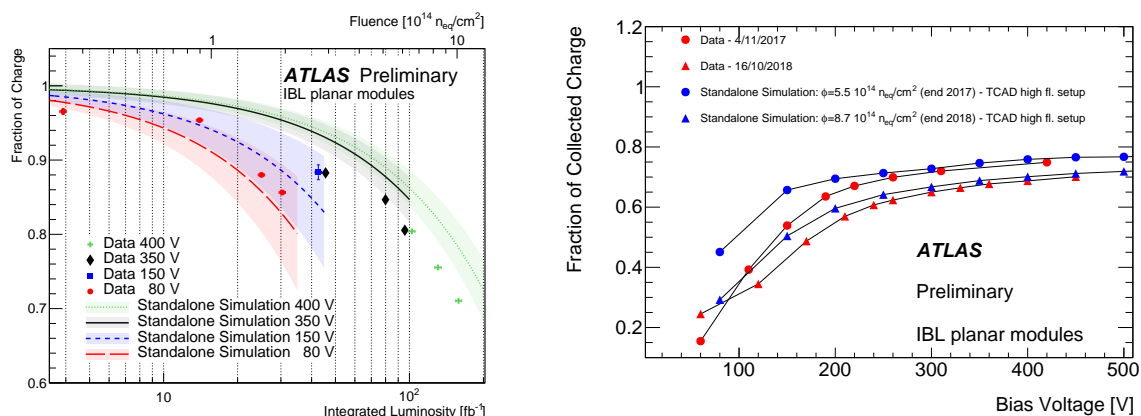
Figure 118 (left) shows the charge collection efficiency as a function of the delivered luminosity for central ( $|\eta| < 0.8$ ) IBL modules. Systematic uncertainties include fluence calculation and variation of the TCAD model and trapping parameters (simulations) and the drift in the charge calibration (data). Within uncertainties, the data and simulations are in agreement.

Figure 118 (right) shows the evolution of the collected charge as a function of the bias voltage in the IBL modules. Data and simulations are shown for the end of 2017 and 2018 for IBL modules. The data were taken in special runs where scans of bias voltages were performed. Again the simulation is in good agreement with data, both in trend and absolute value.

#### 7.1.2.2 Lorentz angle

The dependence of the Lorentz angle on fluence was simulated using the AllPix [4] package, with electric field maps produced using TCAD simulations based on the Chiochia radiation damage model [22]. Figure 119 shows the comparison of the Lorentz angle values obtained from a  $Z \rightarrow \mu\mu$  sample with the simulation. The vertical error bars on the data points represent the statistical uncertainties, while the error bars on the simulated points represent the statistical and systematic uncertainties on the simulation, obtained from variations on the simulated parameters [34].





**Fig. 118:** Left: charge collection efficiency as a function of luminosity [3]. Right: charge collection efficiency as a function of bias voltage [32].

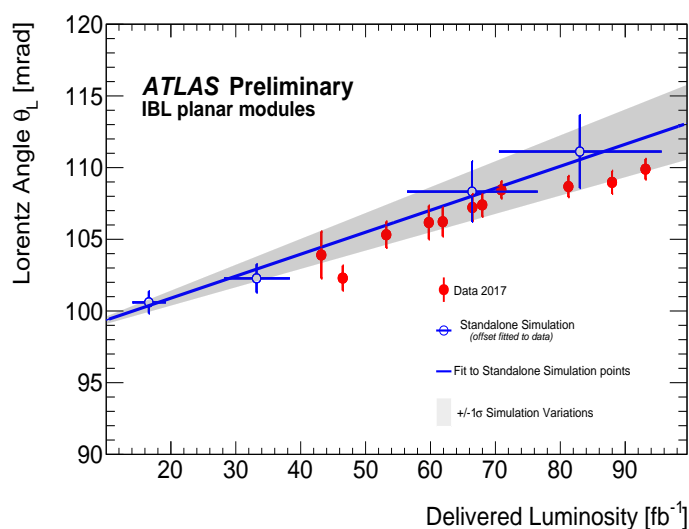


**Fig. 119:** Comparison of the evolution of the Lorentz angle with luminosity in data (red points) and in simulation (blue points) [34].

The slope of the linear fit in Fig. 119 is obtained from the simulated points, while the intercept is fitted from the data. A good agreement is observed between the data and the simulation within the uncertainties.

### 7.1.2.3 Mobility studies

The mobility  $\mu$  is defined as the ratio between the drift velocity of charge carriers in a silicon module and the electric field. As anticipated above, mobility is a function of temperature and electric field, and can be related to the value of the Lorentz angle by the value of the magnetic field

$$\tan \theta_L \sim \mu |\vec{B}|. \quad (36)$$

Thus, correctly modelling the Lorentz angle is equivalent to a good modelling of the mobility in the Monte Carlo simulation. Comparisons of the measured Lorentz angle with the Monte Carlo simulations during Run 1 showed discrepancies of about 10% on the value of  $\theta_L$  [37], so an investigation of the mobility models implemented in the simulations was carried out, with the goal of improving the data-MC agreement for Lorentz angle. At low electric fields, the mobility can be parameterized as a power

law of the temperature

$$\mu(T) = aT_n^{-b}; \text{ where } T_n = \frac{T}{300\text{K}}, \quad (37)$$

while the extrapolation to higher electric fields can be parameterized using the Thomas model [35]

$$\mu(T, E) = \mu_0(T) \left[ 1 + \left( \frac{\mu_0(T)E}{\nu_s(T)} \right)^\beta \right]^{-\frac{1}{\beta}}. \quad (38)$$

The parameters  $a$  and  $b$ , considered for the low-field parameterization in Eq. 37 can be found in Table 13 for both electrons and holes, while the parameters  $\nu$  and  $\beta$  for the high field extrapolation in Eq. 38 are summarized in Table 14 as a function of the temperature [37].

**Table 13:** Parameters for the low-field mobility parameterisation in Eq. 37

Low-field model	Parameter	Electrons	Holes
Jacoboni–Canali [38]	$a$ [cm <sup>2</sup> /(V·s)]	1533.7	463.9
	$b$	2.42	2.20
Canali [36]	$a$ [cm <sup>2</sup> /(V·s)]	1437.7	463.9
	$b$	2.42	2.20
Hamburg–Thomas [39]	$a$ [cm <sup>2</sup> /(V·s)]	1440(15)	474(10)
	$b$	2.260(7)	2.619(7)

**Table 14:** Parameters for the high-field extension of the mobility models, following the Thomas model in Eq. 38.

Extended model	Parameter	Electrons	Holes
Jacoboni–Canali [38]	$\nu_s$ (cm/s)	$1.07 \times 10^7 \times T_n^{-0.87}$	$8.34 \times 10^6 \times T_n^{-0.52}$
	$\beta$	$1.109 \times T_n^{0.66}$	$1.213 \times T_n^{0.17}$
Canali [36]	$\nu_s$ (cm/s)	$1.00 \times 10^7 \times T_n^{-0.87}$	$8.34 \times 10^6 \times T_n^{-0.52}$
	$\beta$	$1.109 \times T_n^{0.66}$	$1.213 \times T_n^{0.17}$
Hamburg [39]	$\nu_s$ (cm/s)	$1.054(38) \times 10^7 \times T_n^{-0.602(3)}$	$9.40(27) \times 10^6 \times T_n^{-0.226(2)}$
	$\beta$	$0.992(4) \times T_n^{0.572(3)}$	$1.181 \times T_n^{0.644(3)}$

A study of the different mobility models for unirradiated modules was performed using 2015 data. The results of the simulations using the models summarized in Tables 13 and 14 are compared with the data from the ATLAS Insertable B-Layer (IBL) in Fig. 120. Results show discrepancies between the data and the simulation using the Jacoboni–Canali model, while the Canali and Hamburg–Thomas models give a good description of the data.

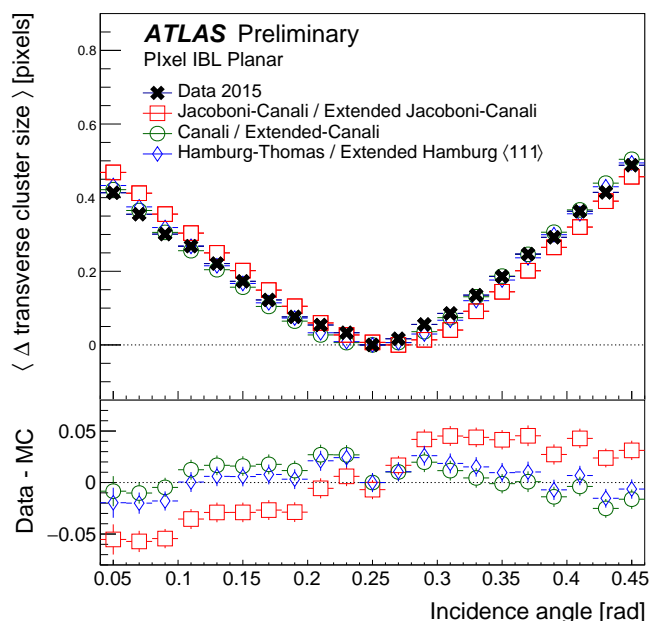


**Fig. 120:** Distribution of the cluster transverse size as a function of the incidence angle for data and different mobility models. The Jacoboni–Canali model shows important discrepancies with the data. From Ref. [37].

### 7.1.3 Summary

As the closest detector system to the interaction point, the ATLAS pixel system receives the most radiation fluence and dose. By the end of Run 2 the IBL sensors received an integrated radiation fluence up to  $10^{15}$  (1 MeV)  $n_{\text{eq}}/\text{cm}^2$ . The effects of radiation damage are being observed and measured, such as decreasing signal size and drifts in the Lorentz angle. A digitizer model implemented by ATLAS has been presented which models the effects of radiation damage [3]. It is based on Geant4 and uses TCAD simulation results as inputs for the electric field. Comparisons with data show reasonable agreement. These simulations help to make decisions about the operating working point for the future data taking period in order to ensure good online and offline performance of the ATLAS pixel detector, and to guide the design of the future detector at the HL-LHC.

For future ATLAS physics in Run 3 and the HL-LHC, understanding radiation damage effects will be crucial. The radiation damage digitizer will be a default component of the ATLAS simulations, helping to make accurate performance predictions with increasing luminosity. Future challenges include deciding the exact fluences to use as simulation inputs, and also ensuring that the digitizer will run fast enough for simulation production.

## 7.2 CMS

This section describes the modelling of the charge generation and transport in the silicon sensor of both the CMS pixel and CMS strip detector. Both systems have been described in more detail in Section 3.2.2.

### 7.2.1 CMS pixel detector

The CMS pixel detector uses  $285\ \mu\text{m}$  thick  $n^+ \text{-in-} n$  sensors with  $100 \times 150\ \mu\text{m}$  pixels. The sensors are estimated to be  $-14\ ^\circ\text{C}$  to  $-8\ ^\circ\text{C}$  when powered. The operational bias voltages at the end of Run 2 ranged from 250–450 V as shown in Table 2 in Section 3.2. For this detector, the modelling of radiation damage to the silicon sensors is performed with the standalone simulation software PixelAV [6–8] that is independent from the full CMS simulation framework CMSSW [40].

The detailed sensor simulation PixelAV simulates the passage of a pion ( $\pi$ ) through the sensor and incorporates the following elements:

- **charge deposition:** an accurate model of charge deposition by primary hadronic tracks uses the ‘exact’  $\pi - e$  elastic cross-sections of Bichsel [41], that depend on the electron energy, to determine the  $\pi$  mean free path. It takes into account the number of electron–hole pairs produced when the scattered electrons or ‘delta rays’ lose energy. The total number of electron–hole pairs is chosen from a Poisson distribution where the mean number of pairs is determined assuming that it takes 3.68 eV to produce a pair. The delta rays are propagated until they lose all energy or they leave the sensor;
- **electric field:** a realistic three-dimensional electric field profile resulting from the simultaneous solution of Poisson’s equation, carrier continuity equations, and various charge transport models is generated with the TCAD package. With as input the pixel cell geometry and material properties, TCAD predicts a non-uniform spatial distribution of space-charge density for computing charge propagation inside the sensor bulk. A temperature of 263 K was assumed in TCAD simulations;
- **charge transport:** the electrons and holes produced by the primary hadron drift to the sensor implants under the influence of the internal electric field and the external magnetic field. Charge carriers are transported by integrating the equations of motion:

$$\frac{d\vec{x}}{dt} = \vec{v} \quad (39)$$

$$\frac{d\vec{v}}{dt} = \frac{e}{m^*} \left[ q\vec{E} + qr_H\vec{v} \times \vec{B} - \frac{\vec{v}}{\mu(E)} \right]. \quad (40)$$

The electrons and holes drift with a carrier-dependent mobility ( $\mu$ ) that depends on the electric field ( $E$ ) and temperature. Here, the effective masses  $m^*$  are  $0.260 \cdot m_e$  for electrons and  $0.241 \cdot m_e$  for holes in silicon;

- **charge trapping:** when charge carriers are trapped they are captured for periods of time that are long as compared with the integrating time of the pre-amplifiers and are not detected with full efficiency. This trapping time is incorporated in the simulation by halting the propagation of that charge carrier according to the effective trapping times measured in Ref. [30]. The trapping constants used for electrons and holes in CMS simulation are tuned to measurements from data;
- **charge collection efficiency:** after all charge carriers have reached the boundary of the detector or have been trapped, the program counts the number of electrons that have been collected by each  $n^+$  implant. Then it calculates the additional charge induced on each pixel by trapped electrons and holes by approximating the detector as a parallel plate capacitor with a rectangular segment anode.

For each event, the simulation outputs the coordinates of the pion entry and direction, the generated number of electron–hole pairs, and two sets of signals for a pixel array. The first set includes only collected electrons and the second set includes collected electrons and induced signals from trapped charge. The final step consists in a simplified simulation of the electronics and readout system. First, a random noise is added to each pixel signal. Then, a function that simulates the analogue response of the ROC is applied to the total signal. The results of the PixelAV simulation are employed in the event reconstruction step of CMSSW. This is done by applying corrections from templates stored for sets of track angles and cluster charges to the total deposited charge in simulation and further correcting the position of the reconstructed pixel hit.

**Template reconstruction:** the PixelAV simulation was originally written to interpret beam test data from several un-irradiated and irradiated sensors. In CMS, the simulation is used to produce cluster projection shapes, also called ‘templates’, across measured cluster projections [42]. These templates are produced for different incident track angles ( $\cot \alpha, \cot \beta$ ) and hit positions defined with grids of eight

slices in local  $x$  and  $y$  coordinates within a pixel. They take into account the sensor geometry and are produced under certain conditions of fluence, temperature, bias voltage, and magnetic field. A single cluster template is created by repeatedly simulating the particle traversal for a certain incidence angle and position within a pixel using the PixelAV software. Parameters in PixelAV were originally taken from Ref. [22]. However, CMS has developed techniques to tune the PixelAV trapping parameters, as well as the TCAD donor and acceptor concentrations and the electron and hole trapping rates therein, from collision data through measurements of the charge collection vs. depth. The templates produced from the tuned PixelAV simulation are used to find the best fit and hence an estimate of the in-pixel hit position in both  $x$  and  $y$ . A template contains:

- the charge distribution in  $x$  and  $y$  for a charge bin;
- the average and maximum signals in the  $x$  and  $y$  projections as well as the expected RMS of the average signals;
- the averages of the minimum  $\chi^2$  functions in  $x$  and  $y$  to be used in the calculation of goodness of fit probabilities of in-pixel hit position and signals;
- the average correction to the average residuals to correct for effects like charge migration or signal fluctuating above or below readout threshold.

These templates were produced about every few  $\text{fb}^{-1}$  just after installation, when type inversion occurs, and later about every  $10\text{fb}^{-1}$  following periods of annealing or changes in detector parameters after calibration. This amounted to about twelve updates in the templates in a year. The templates are not only used to compute in-pixel hit position, but are also used to reweight the digitized cluster charge profile as a function of the production depth.

**Corrections in the pixel hit reconstruction:** the template-based reconstruction algorithm aims to get a better estimate of the pixel hit position by accounting for the charge sharing functions of the detector and how they are modified during large portions of its useful life. This is possible through the use of the projected pixel information stored in a template. The technique is based on fitting the now measured pixel cluster  $X$  and  $Y$  projections to the pre-determined cluster shapes or templates produced with PixelAV. Given a track with angles  $\alpha$  and  $\beta$  incident to the pixel module, the pre-determined cluster template is compared to the actual cluster produced by the track in question. A  $\chi^2$  minimization is performed with hit  $X$  and  $Y$  positions as floating variables. The in-pixel hit position is given by the  $X$  and  $Y$  coordinates which minimize the  $\chi^2$  comparison.

The cluster template technique was originally developed to optimally estimate pixel hit positions after radiation damage, but it was found that it performs better than standard CMS pixel hit reconstruction [43] even before irradiation [42]. The technique requires knowledge of the track direction, so it is used in the second pass of pixel hit reconstruction, when track incidence angles on detector modules are known. In the first pass of the reconstruction the standard technique is used. Results of this method are detailed in Ref. [44].

**Pixel cluster charge re-weighting** The pixel charge profile is defined as the normalized average pixel charge as a function of the production depth. For a non-irradiated, fully depleted detector, the pixel charge profile is expected to be flat as the detector is fully efficient and all the charge is collected. For an irradiated detector, on the other hand, charge collection losses are expected due to the trapping of carriers. The losses are larger for the charges released further from the readout plane. This behaviour is shown in Fig. 121 for different accumulated integrated luminosities during the data taking in 2017–2018. During the 2017 Extended Year-End Technical Stop, the barrel pixel detector was held at temperatures above  $10^\circ\text{C}$  for 53 days. The beneficial effect of the annealing during this period is clearly visible in the flattening of the pixel charge profile. At the beginning of 2018 data taking, the charge collection was additionally increased in Layer 1 by raising the bias voltage from 350 V to 400 V.

The cluster charge re-weighting (CCR) algorithm attempts to describe the effects of radiation damage and annealing. This algorithm modifies the charges in a cluster arising from a single simulated

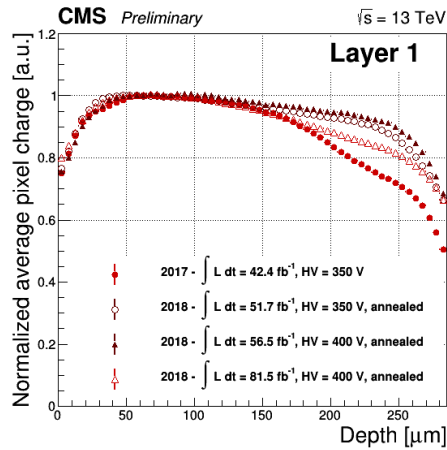


**Fig. 121:** Average pixel charge as a function of production depth [45]. The charge distribution is shown for the Layer 1 of the CMS barrel ip detector at the end of 2017 (HV = 350 V), at the beginning of 2018 data taking (HV = 350 and 400 V), and after  $30.0 \text{ fb}^{-1}$  of data collected in 2018. The selection includes tracks with  $p_T > 3 \text{ GeV}$ , pixel cluster charge  $< 1000 \text{ ke}^-$ , cluster size in  $y < 4$ , and hit position residuals  $< 100 \mu\text{m}$ .

hit such that a better description of the sensor response is obtained, while maintaining the randomized nature of the signal creation process. The method of CCR sets in at the end of the first part of the digitization process and is applied to clusters of pixel charges resulting from a single primary particle. Therefore, in CMSSW, the CCR is implemented before the charges in the pixels are summed and thresholds are applied, but after the cluster finding step.

To apply the CCR to a simulated cluster, the incidence angle and position of the corresponding primary particle and the module ID are used to find the most suitable cluster templates from the set of PixelAV templates. These are generated for various incidence angles and positions, as well as for different levels of irradiation. The templates are read from a database, and an interpolation is performed between the simulated particle parameters. The original  $_{x,y}$  induced charge of a pixel in the cluster is then scaled with the ratio  $w$  of the template pixel charges at the same position inside the cluster for an irradiated ( $t^{\text{irr}}$ ) and an un-irradiated sensor ( $t^{\text{unirr}}$ ). A matrix of  $13 \times 21$  pixels is defined, which covers the full cluster and has the particle hit position in its centre. For any pixel, specified by its pixel coordinate  $(x, y)$  with respect to the lower left pixel of this matrix, the reweighted charge signal  $_{x,y}$  is determined as

$$\text{signal}_{x,y} = \frac{t^{\text{irr}}_{x,y}}{t^{\text{unirr}}_{x,y}} \times \text{original}_{x,y}. \quad (41)$$

For pixel charges of the templates below a track-angle-dependent minimum charge<sup>10</sup>, no weights are computed, and instead the pixel charge is computed using the weight of the closest pixel with a weight.

One way to verify the effect of the CCR is to extract the collected charge as a function of the charge carrier creation depth from very long clusters. For unirradiated sensors, this profile is flat, and it is tilted for strongly irradiated sensors, as shown in Fig. 122. In the same figure, a preliminary distribution of the average charge profile shows that the CCR can reproduce this effect.

**Conclusion** The PixelAV simulation was developed to model pixel sensor physics as accurately as possible but its speed is not optimized to be included as part of the main CMS simulation framework. Therefore, its usage is limited to estimate the radiation damage effects in a standalone mode. Specifically,

<sup>10</sup>This helps to suppress low-charge clusters resulting from secondary electrons.

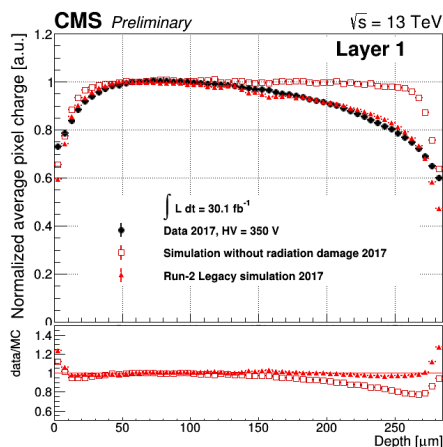


**Fig. 122:** Average pixel charge as a function of production depth for the Layer 1 of the CMS pixel barrel detector in 2017 [46]. The profile of the data collected (black) shows the losses expected due to the trapping of carriers as a function of depth. The charge simulation without the CCR algorithm is flat and shown in red squares. After applying the CCR algorithm a more accurate description of the simulated charge profile can be seen in red solid triangles.

it provides a more accurate estimate of the pixel hit position in the event reconstruction and is used to implement corrections to the simulated pixel cluster charge profiles. The latter is performed through a reweighting algorithm that includes more realistic modelling and irradiation effects. The simulation and the reconstruction are currently being synchronized by using templated cluster shapes generated from the same models. Preliminary cluster profiles measured in data and simulation show encouraging and promising results that reflect a more accurate estimate of the radiation damage effects.

### 7.2.2 CMS strip tracker

The CMS strip tracker has been in operation since the start of CMS in 2009. The strip sensors are of n-type silicon with  $p^+$  single-sided strips with a thickness of  $320 \mu\text{m}$  up to a radius of  $600 \text{ mm}$ , and  $500 \mu\text{m}$  at larger radii.

For the case of CMS strip tracker, the Geant4 package that describes the energy loss in the CMS tracker based on the interactions between the incoming particles and the bulk of the silicon sensor is not sufficient to simulate the signal collected in the real detector. For the proper modelling of radiation damage in the CMS strip tracker, an experiment-specific simulation of the signal and noise is required. This has been implemented within the CMS Software framework (CMSSW).

**Simulated hits:** for a given silicon strip module whose geometry is known, the simulation [47] starts from Geant4 hits providing information about the direction of the incoming particle, a hit position in the local coordinate frame and the total energy loss. The first step consists in dividing the trajectory of the incoming particle and randomizing the energy loss in each sub-path following a Landau distribution. The second step simulates the charge carrier drift including thermal diffusion. The underlying hypotheses are that the  $E$ -field is normal to the sensor plane and that there is no charge collection inefficiency. The next step emulates the effect of the inter-strip capacitance which induces charges on neighbouring strips of the one collecting the charge carriers. This is performed through a parameterization of the cross-talk effect assuming that for a given charge  $Q$  collected on a strip  $i$ , the signal observed on that strip will be  $x_0 \times Q$ , the two closest strips  $i \pm 1$  will measure a charge  $x_1 \times Q$  and the second ones ( $i \pm 2$ ) a charge  $x_2 \times Q$ . The parameters are constrained by the relationship  $x_0 + 2x_1 + 2x_2 = 1$ . The parameterization depends on the detector geometry and the readout mode of the APV25 (peak or deconvolution). To simulate the front-end electronics, a parameterization of the pulse shape is provided for both readout modes. It is

assumed that the detectors are synchronized and that the signal of ultra-relativistic particles are sampled at their maxima. Consequently, the signals collected for low  $\beta$  particles, loopers, as well as out-of-time pile-up effect induced by the electronic response are properly simulated. The above described simulation chain produces simulated hits (**SimHits**).

**Data digitization:** the next goal consists in simulating the digital data acquired by the back-end electronics (front-end driver, or FED), called the **digis**. Contributions from all particles, including in-time and out-of-time pileup, are taken into account. A list of bad components is extracted from an offline database and is used to suppress the signal for the corresponding channels. In order to describe the noise, it is required to randomize the summed signal according to the knowledge of the noise in each channel. The noise is also stored to and retrieved from a database. To simulate the optical chain response where gains vary between links, values of gains per APV stored in the database are used. The last elements in the readout chain are the FED where the digitization, a zero suppression and a cluster algorithm are performed. The signal processing in the FED is emulated in the CMSSW framework leading to 8-bit digis as provided by the FEDs during data-taking.

**Measurements in data:** to be as realistic as possible, quantities extracted from measurements in data are used to store estimates of observables in a database. During Run 2, the bad component list, the noise, the gains, the cross-talk parameters, and the APV signal shape were measured. These measurements have been used to either feed the database or to update parameters stored in configuration files. The noise is measured simultaneously with the pedestals during calibration runs where no collisions occur. The APV signal shape is measured with charge injection to estimate the electronic response. To simulate the observed signal, however, it has been required to convolute it with a physical signal simulated with external tools. The gains of the optical chains are measured using a reference signal with a fixed amplitude that marks the end of optically transmitted data words, called tickmark, in dedicated runs. The cross-talk parameters have been measured in cosmic runs both without magnetic field to avoid Lorentz deflection, as well as in non-zero-suppressed data-taking mode in order to avoid threshold effects.

All these quantities evolve with time and are updated accordingly. In order to validate the simulation, data/MC comparisons have been performed focusing on the most relevant quantities, mainly the cluster charge and width.

**Cluster charge:** The cluster charge is in general very well reproduced as a result of well-described gains. In the latest simulation campaign of the full Run 2 data, a simulation of the preamplifier has been introduced. It simulates the non-linear response of the pre-amplifier of the APV that was observed early in Run 2 (for a more detailed description of the effect, see Section 6.2.2). This effect is now propagated into the simulation and especially improves the description of the low charge contributions.

**Signal:** an improved description of the APV signal was achieved mainly with a reparameterization of the electronics. The change in the signal description in the simulation impacts the description of off-time signals such as out-of-time pileup and particles with a time of flight similar to that of a photon. The noise decreased with change of the operating temperature, that was changed from  $-15^{\circ}\text{C}$  to  $-20^{\circ}\text{C}$  at the start of 2018, but increased with irradiation. A new description of the noise improved the description of a drop in the signal-over-noise ratio that was measured in the data. This is shown on the left of Fig. 123. The improved noise description also has an impact on off-track clusters and the low charge description of the on-track clusters.

**Cross-talk:** cross-talk is related to the inter-strip capacitance which is affected by surface damages and depends on bias voltage. A comparison of the parameters for the barrel detectors are shown on the right in Fig. 123. The cluster width description has significantly been improved thanks to a new measurement of cross-talk parameters. While discrepancies still remain, they do weakly impact downstream quantities. The optical link gain decreased with time due to a loss of efficiency in the AOH and a loss of transparency in the optical fibres. The update of the gains helps to better describe the fraction of channels having signal saturating the 8-bit ADC.



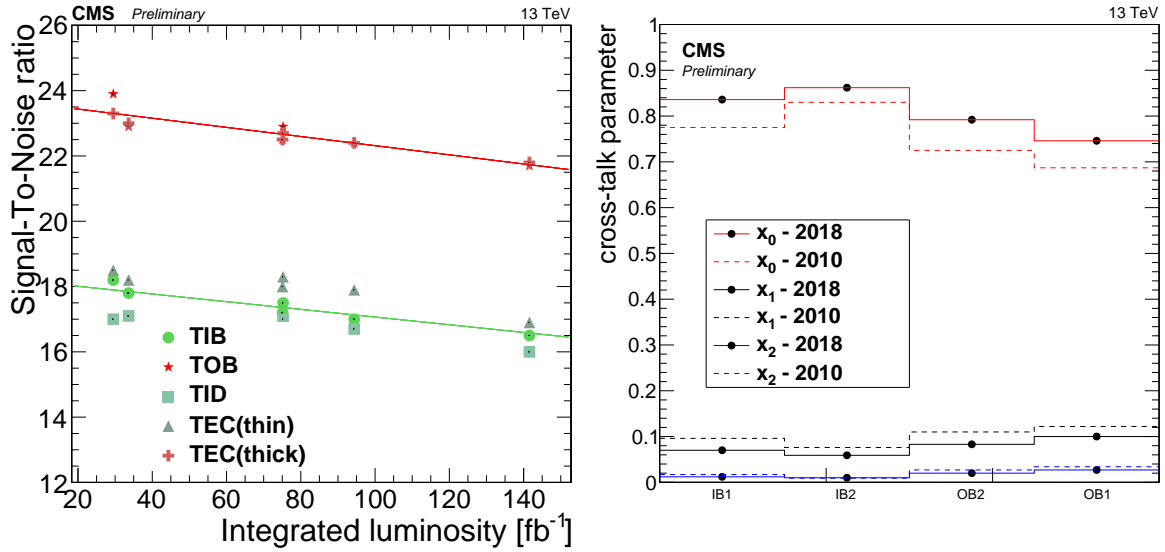


**Fig. 123:** Left: the evolution of the signal-over-noise ratio for modules belonging to different partitions [48]. Higher ratios correspond to the thick (500  $\mu\text{m}$ ) sensors. Right: cross-talk parameters for the four barrel silicon strip sensor geometries measured in Run 1 and Run 2 [49].

**Hit efficiency:** measurement of the hit efficiency as function of the pileup shows a linear dependence. The source of inefficiency has been identified as originating from heavy ionizing particles (HIP), or from inelastic nuclear interactions within the active volume. The inefficiency does not exceed 2% even at high pileup and for innermost layers. A simple approach to simulate inefficiency exists in the simulation but has not been used in the latest simulations.

**Conclusion:** the tracker simulation has been improved using the best knowledge we have on the detector through new measurements of observables and corresponding updates of the database and parameters. Moreover, a simulation of the preamplifier has been developed mainly to better describe the data in the first periods of 2016 where the silicon strip tracker suffered from dynamic inefficiencies. Beyond similar measurements that will need to be performed during Run 3, two kinds of further improvements could be foreseen. The inclusion of the HIP-induced hit inefficiency could be used in production. Moreover, as the detector will suffer even more from irradiation, a drop of charge collection efficiency is expected to be observable in the innermost layer. After a dedicated measurement, this effect could be injected into the simulation to even better describe the signal-over-noise ratio.

In general, the validation of the simulation shows that the track reconstruction and downstream algorithms are quite robust and do not require a very fine level of accuracy in the simulation.

### 7.3 LHCb

A more detailed description of the LHCb VELO detector is given in Section 3.2. The LHCb VELO detector has n-on-n silicon sensor pairs of 300  $\mu\text{m}$  thick. Each of the sensor pairs provides a single 3D measurement by employing both radial and concentric strip topologies, with a sensor pitch ranging from 35  $\mu\text{m}$  closest to the beam line to 101  $\mu\text{m}$  further away from the beam line. These innermost VELO sensors at 8 mm from the proton beams during stable beam conditions have seen fluences up to about  $\Phi_{\text{eq}} \sim 6.5 \times 10^{14}/\text{cm}^2$ . High-quality simulation is of major importance for LHCb experiment. The overall strategy is identical to each subdetector that exploits silicon-based devices and may differ in some details related mainly to the emulation of the readout electronics. The full processing chain leading to the production of simulated samples is divided into three independent stages:

1. generation of proton–proton interaction with a particular final state particles and their propagation through the detector (simulation phase);
2. simulation of the detector response (digitization phase);
3. detector output data decoding, track finding and fitting (reconstruction phase).

In the first and most time-consuming stage, the full truth information (a particle 4-momenta and its identification) is used by the LHCb Gauss application [50] to simulate the effects of the passage of particles through detector material. Gauss is interfaced with Geant4 [51] package that is dedicated to simulating with great precision effects such as energy loss or multiple scattering. The results are then stored in a specialized class called MCHit. The next stage, performed by the LHCb application Boole [52], uses the MCHit objects to perform the detector response simulation (see *Digitization* below). In addition, the output of Boole is formatted in an identical way it is sent out to processing in the trigger farm by the respective detectors. Finally, the LHCb Brunel application [53], simulating the full reconstruction process as performed by the LHCb tracking system, is used to produce high level objects like tracks and vertices. These, in turn, are stored in files formatted identically to the output format of the LHCb event building farm (so called Data Summary Tape). The Brunel application is data-type agnostic: that is, both simulated and collision data are processed in the same way. The simulated DST files can be further processed in an identical manner as real data are.

**Charge generation:** the MCHit objects that are produced by Gauss application and contain such data as sensitive material entry and exit points and energy loss are subsequently used to simulate detector hits. Using the deposited energy value for each particle, the corresponding number of electron-hole pairs are calculated. This generated charge is then distributed along a particle’s path within the silicon.

**Charge deposition:** the deposition process progresses in steps (where the number of steps is a tuneable parameter) and has three components: the constant core ionization, random ionization and high energy  $\delta$ -ray emission. The relative contribution of these three components is tuneable, although the high energy electron production is simulated in ‘a posteriori mode’.

**Delta ray emission:** the energy of emitted  $\delta$ -rays is recovered by comparing the total generated charge and distributed one — if the difference is larger than a given cutoff value, the emission process is simulated at a randomly chosen point on the particle’s path within active material.

**Charge propagation:** finally, the total distributed charge is normalized to the total generated charge for consistency. The distributed charges are then propagated through the sensitive material using a simple, fast projection method: the charge cloud is projected along the estimated particle trajectory direction and no additional secondary interactions are simulated. In case of the VELO the residual magnetic field is ignored, thus, no trajectory tilt is simulated. At each point, a random lateral diffusion is estimated by sampling a Gaussian distribution and then the charges are placed at the surface of the sensor.

**Charge collection:** at the stage of charge collection point, radiation damage effects are taken into account, if necessary, changing appropriately the depletion depth and as a result the collected charge distribution and taking into account the second metal layer effect. The charge distribution is adjusted by decreasing the active depth of the depleted bulk of the sensor using test beam data obtained for sensors irradiated with different fluences and bias voltages. The collected signal (in keV) measured as a function of the bias voltage at test beams was fitted with the model:

$$s_{eV} = A \times \sqrt{V_b + B}, \quad (42)$$

with  $s_{eV}$  the observed signal and  $V_b$  the bias voltage applied to the studied sensor. The charge distribution is adjusted using a lookup table of the charge loss as a function of the track position on the sensor, its distance to the strip implant and the track angle expressed in pseudorapidity.

In this pragmatic approach, a simple linear electric field is assumed, and no transient currents are simulated at the sensor collecting electrodes. Using local information on sensor segmentation topology

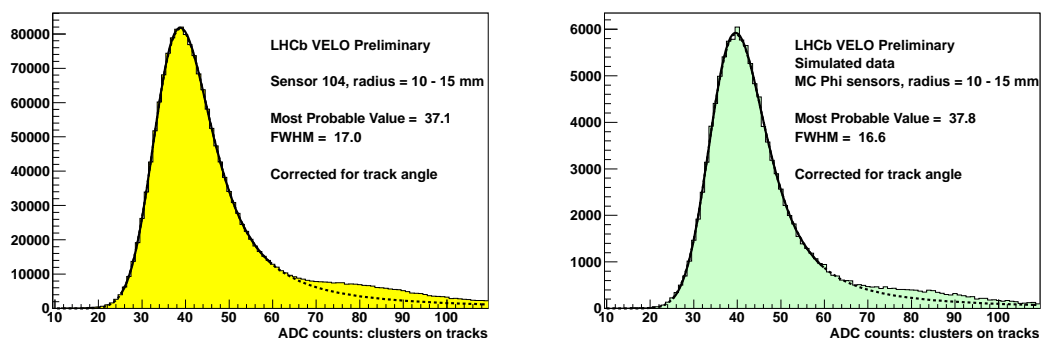


**Fig. 124:** Energy distribution, measured in arbitrary ADC counts, fitted with a model representing Landau convoluted with a Gaussian for a selected VELO sensor. Left hand-side plot is obtained using collision data whilst the right-side hand one presents simulated data. Plots are not normalized.

from a detector model description, a list of channels with collected charges is created.

**Digitization:** the list is next passed to the readout emulation code that adds electronic noise, introduces capacitive couplings between channels, perform digitization and finally applies activation cuts (zero suppression) and performs clusterization (hit reconstruction). The last step is the cluster data encoding into the format that is identical with the transport protocol of respective detectors (also called RawBank) that is the input data for the LHCb Brunel application for track reconstruction. In order to reproduce the clusterization and encoding exactly the emulation and calibration software were partially ported into the simulation platform [54].

**Simulation results:** the results of the simulation process can be broadly divided into two categories: low level, including Landau distribution of deposited energy and its dependency on the local position on a sensor, hit rates, occupancies etc.; and high level, such as track multiplicity, primary and secondary vertices, single hit resolution, vertex resolution, geometrical impact parameter resolution etc.

The latter set of variables need full track reconstruction to be performed. Some of these observables are frequently compared to the corresponding observables obtained from data. Specifically, the primary vertex resolution is monitored by means of lifetime measurements, the impact parameter resolution using selection algorithms, the spatial resolution using track fitting, and Landau distributions are measured using hit reconstruction and their association with tracks and radiation damage studies. Selected results are shown in Figs. 124 and 125, demonstrating well-simulated Landau curves and spatial single hit resolution.

**Summary:** the silicon simulation software is an essential part of the detector performance studies (including radiation damage effects) and physics analyses performed by LHCb collaboration. The quality of the simulated samples is continuously improved and cross-checked against the collision data. The constant maintenance and improvements of the simulation code, often using the feedback from measurements, is crucial.

## 7.4 Discussion and outlook

Thanks to the excellent luminosity performance of the LHC the effects of radiation damage are visible on silicon tracking sensors of the LHC experiments. The degradation of charge collection efficiency and spatial resolution was sizeable during Run 2, up to the point that it was necessary to modify detector conditions, changing bias voltage, threshold settings, temperature and more. While these measures allowed to keep collecting good data for physics, it was necessary to implement corrections to Monte Carlo simulations to take into account the modified performance of the silicon detectors. As presented in this Section, the LHC experiments implemented methods to correct MC simulations for the radiation

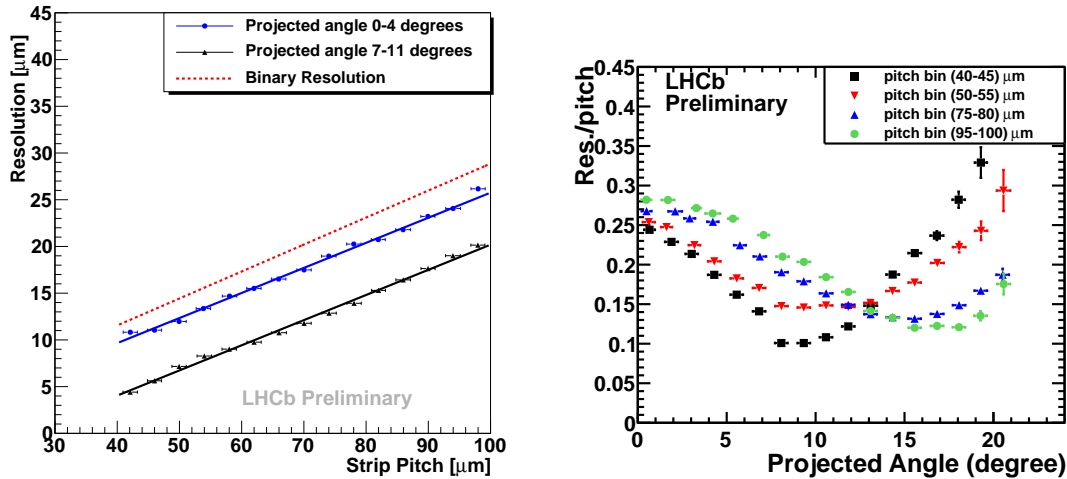


**Fig. 125:** Single hit spatial resolution measured for the LHCb VELO detector. Left: resolution as a function of the sensor pitch for two different track angles and compared to the binary resolution. Right: the resolution as a function of track angle for different pitch regions.

damage to silicon tracking sensors.

**ALICE**, like **ATLAS**, **CMS**, and **LHCb**, uses simulations of their pixel sensors for signal predictions in their sensors. However, radiation effects were not taken into account in these simulations, as their levels of radiation were quite low compared to those of the other three experiments; see also Sections 4 and 3.2.

**LHCb** implemented radiation damage in the step of charge collection by correcting for the depletion depth. The electric field is assumed to be linear. Charge loss is estimated from lookup tables with charge losses for different positions on a sensor, distances from implants and track angles. The lookup tables are based on models fitted to bias voltage scans in test beam data.

**ATLAS** calculates signal loss per pixel cell at the digitization step, that is, right after charge deposition by Geant4. This method relies on pre-calculated lookup tables for the needed quantities such as electric field, Lorentz angle, trapping rates, and Ramo potential; some of these are obtained using TCAD software. Such a strategy allows the calculation of radiation damage effects to be fast enough to be indeed included directly in the Monte Carlo simulation.

**CMS**, following a different approach with respect to **ATLAS**, applies *a posteriori* corrections to the Monte Carlo simulated events. The corrections are based on templates built from data using PixelAV and accurate silicon device simulations, the latter obtained using TCAD tools. The corrections are applied at cluster level, correcting for the signal amplitude and cluster shape. Trapping constants and donor and acceptor concentration parameters used in the TCAD and PixelAV software are derived from data.

Whereas in **ATLAS** parameters such as trapping parameters, electron and hole cross-sections in donor and acceptors, and existing models are used for parameters such as trapping rates and defects, **CMS** adjusts these parameters according to measurements from data around twelve times a year.

**Outlook** TCAD is widely used to compute the electric field for input to sensor simulation. This program, however, is proprietary, and computationally intensive. Simulations of charge transport could benefit from a viable open source alternative to TCAD. There are open source alternatives for technology computer aided design, but not with all capabilities that for example Silvaco or Synopsys have to offer. While for **CMS** the fitting of parameters to data seems to work quite well, it is not guaranteed that extrapolating such fitted parameters to future fluences would give a good prediction of a future detector's performance. **CMS** created new fits to data multiple times a year to accurately simulate charge transport

in the irradiated detector. Extrapolations to future datasets were made for making future predictions, but not for tracking and simulation for past datasets. Comparisons to data from LHC experiments is important, as irradiation of test beam devices that are often irradiated under controlled conditions can yield performance results deviating by large from radiation damage from LHC collisions. For example, PixelAV found that parameters derived from test beam data did not give an accurate description of the data taken during LHC operation. A model of radiation damage accurately modelling sensor responses as seen in LHC data would give more confidence in such a model being correct for future predictions. The community could benefit from such a description of radiation damage that would fit the data of all four LHC experiments. In addition, it would be beneficial to implement such a model in a framework that can be used to produce simulations of performance measurements so that it can be compared to both test beam and detector data.

## References

- [1] W. Shockley, *J. Appl. Phys.* **9** (1938) 635, doi:10.1063/1.1710367.
- [2] S. Ramo. *Proc. IRE* **27** (1939) 584, doi:10.1109/JRPROC.1939.228757.
- [3] M. Aaboud *et al.* [ATLAS Collaboration], *JINST* **14** (2019) P06012, doi:10.1088/1748-0221/14/06/P06012.
- [4] J. Idarraga and M Benoit, [The A11Pix simulation framework](#), last accessed July 12, 2020.
- [5] G. Kramberger, [KDetSim](#) – a simple way to simulate detectors, last accessed July 16th, 2020.
- [6] M. Swartz, [A detailed simulation of the CMS Pixel Sensor](#), CMS NOTE-2002/027, (CERN, Geneva, 2002).
- [7] V. Chiochia *et al.*, *IEEE Trans. Nucl. Sci.* **52** (2005) 1067, doi:10.1109/TNS.2005.852748, arXiv:physics/0411143.
- [8] M. Swartz *et al.*, *Nucl. Instrum. Meth.* **A565** (2006) 212, doi:10.1016/j.nima.2006.05.002, arXiv:physics/0510040.
- [9] S. Spannagel *et al.* *Nucl. Instrum. Meth.* **A901** (2018) 164, doi:10.1016/j.nima.2018.06.020
- [10] ATLAS Collaboration, *JINST* bf 3 (2008) S08003, doi:10.1088/1748-0221/3/08/S08003.
- [11] G. Aad *et al.* *JINST* **3** (2008) P07007, doi:10.1088/1748-0221/3/07/P07007.
- [12] [ATLAS inner detector: Technical design report, Vol. 1](#), ATLAS Collaboration, ATLAS-TDR-4, CERN-LHCC-97-16, (CERN, Geneva, 1997).
- [13] [ATLAS inner detector: Technical design report, Vol. 2](#), ATLAS Collaboration, ATLAS-TDR-5, CERN-LHCC-97-17, (CERN, Geneva, 1997).
- [14] ATLAS Collaboration, [ATLAS Insertable B-Layer technical design report](#), ATLAS-TDR-19, CERN-LHCC-2010-013 (CERN, Geneva, 2010).
- [15] ATLAS Collaboration, *JINST* **13** (2018) T05008, 10.1088/1748-0221/13/05/T05008.
- [16] ATLAS Collaboration, [Radiation damage in 2015-2017](#), PIX-2018-005, 2018.
- [17] S. Agostinelli *et al.*, *Nucl. Instrum. Meth.* **A506** (2003) 250, doi:10.1016/S0168-9002(03)01368-8, CERN-IT-2002-003.
- [18] ATLAS Offline Software, [ATLAS Athena Guide](#), last accessed July 12, 2020.
- [19] T. Sjöstrand *et al.*, *Comput. Phys. Commun.* **191** (2015) 159, doi:10.1016/j.cpc.2015.01.024, arXiv:1410.3012 [hep-ph].
- [20] A. Ferrari *et al.*, FLUKA: A multi-particle transport code (program version 2005), CERN Yellow Reports: Monographs, CERN-2005-010 (CERN, Geneva, 2005), doi:10.5170/CERN-2005-010.
- [21] ATLAS Collaboration, [Measurements and predictions of Pixel Detector leakage current](#), 2018.
- [22] V. Chiochia *et al.* *Nucl. Instrum. Meth.* **A568** (2006) 51, doi:10.1016/j.nima.2006.05.199, arXiv:physics/0506228.

- [23] F. Moscatelli *et al.*, *IEEE Trans. Nucl. Sci.* **63** (2016) 2716, [10.1109/TNS.2016.2599560](https://doi.org/10.1109/TNS.2016.2599560), [arXiv:1611.10138](https://arxiv.org/abs/1611.10138) [physics.ins-det].
- [24] ATLAS Collaboration, [ATLAS PIX-2018-004](#).
- [25] A. Zeng Wang and B. N. Philip Nachman [ATLAS Collaboration], [dE/dx simulation plots for Run 2](#), PIX-2018-004, 2018.
- [26] V Wallangen [ATLAS Collaboration], *PoS Vertex 2017* (2018) 050, [doi:10.22323/1.309.0050](https://doi.org/10.22323/1.309.0050).
- [27] G.F. Dalla Betta, *PoS IFD2014* (2015) 013, [doi:10.22323/1.219.0013](https://doi.org/10.22323/1.219.0013).
- [28] C. Da Via *et al.*, *Nucl. Instrum. Meth.* **A699** (2013) 18, [doi:10.1016/j.nima.2012.05.070](https://doi.org/10.1016/j.nima.2012.05.070).
- [29] O. Krasel *et al.*, *IEEE Trans. Nucl. Sci.* **51** (2004) 3055, [doi:10.1109/TNS.2004.839096](https://doi.org/10.1109/TNS.2004.839096).
- [30] G. Kramberger *et al.*, *Nucl. Instrum. Meth.* **A481** (2002) 297, [doi:10.1016/S0168-9002\(01\)01263-3](https://doi.org/10.1016/S0168-9002(01)01263-3), ATL-INDET-2002-006.
- [31] G. Alimonti *et al.*, [A study of charge trapping in irradiated silicon with test beam data](#), ATL-INDET-2003-014 (CERN, Geneva, 2003).
- [32] ATLAS Collaboration, [Charge Collection Efficiency as a function of integrated luminosity](#), 2017.
- [33] Synopsis Inc., [TCAD](#), last accessed July 12, 2020.
- [34] ATLAS Collaboration, [Radiation damage to the ATLAS pixel and Lorentz angle](#), PIX-2017-005, 2017.
- [35] D.M. Caughey and R.E. Thomas, *Proc. IEEE* **55** (1967) 2192, [doi:10.1109/PROC.1967.6123](https://doi.org/10.1109/PROC.1967.6123).
- [36] C. Canali *et al.*, *IEEE Trans. Electron Devices* **22** (1975) 1045, [doi:10.1109/T-ED.1975.18267](https://doi.org/10.1109/T-ED.1975.18267).
- [37] ATLAS Collaboration, [Modeling the mobility and Lorentz angle for the ATLAS Pixel Detector](#), ATL-INDET-PUB-2018-001 (CERN, Geneva, 2018).
- [38] C. Jacoboni *et al.*, A review of some charge transport properties of silicon, *Solid State Electron.* **20** (1977) 77, [doi:10.1016/0038-1101\(77\)90054-5](https://doi.org/10.1016/0038-1101(77)90054-5).
- [39] J. Becker *et al.*, *Solid State Electron.* **56** (2011) 104, [doi:10.1016/j.sse.2010.10.009](https://doi.org/10.1016/j.sse.2010.10.009), [arXiv:1007.4432](https://arxiv.org/abs/1007.4432) [physics.ins-det].
- [40] CMS Offline Software, [CMSSW](#), last accessed July 12, 2020.
- [41] H. Bichsel, *Nucl. Instrum. Meth.* **A562** (2006) 154, [doi:10.1016/j.nima.2006.03.009](https://doi.org/10.1016/j.nima.2006.03.009); H. Bichsel, *Rev. Mod. Phys.* **60** (1988) 663, [doi:10.1103/RevModPhys.60.663](https://doi.org/10.1103/RevModPhys.60.663).
- [42] M. Swartz *et al.*, *PoS Vertex 2007* 035, [doi:10.22323/1.057.0035](https://doi.org/10.22323/1.057.0035).
- [43] S. Cucciarelli, D. Kotlinski, T. Todorov, [Position Determination of Pixel Hits](#), CMS-NOTE-2002-049, (CERN, Geneva, 2002).
- [44] G. Giurgiu *et al.* [CMS Collaboration], [arXiv:0808.3804](https://arxiv.org/abs/0808.3804) [physics.ins-det].
- [45] Pixel Charge Profiles, [Performance plots for Phase 1 Pixel Detector, August 2018](#). Last accessed October 12, 2020.
- [46] Pixel Charge Profiles in Run-2 Data and Simulation, CMS Collaboration, May 2020, [CMS-DP-2020-026](#).
- [47] R. Ranieri, The simulation of the CMS Silicon Tracker, 2007 IEEE Nuclear Science Symposium Conference Record, Honolulu, HI, 2007, pp. 2434-2438, [doi:10.1109/NSSMIC.2007.4436649](https://doi.org/10.1109/NSSMIC.2007.4436649), [CMS-CR-2008-007](#).
- [48] Evolution of S/N during Run II, [CMS Silicon Strip Performance Results 2018](#). Last accessed October 12, 2020.
- [49] Silicon Strip Tracker Performance results 2018, CMS Collaboration, September 2018, [CMS-DP-2018-052](#).
- [50] LHCb Collaboration, [The Gauss project](#), last accessed July 12, 2020.
- [51] J. Allison *et al.*, *Nucl. Instrum. Meth.* **A835** (2016) 186, [doi:10.1016/j.nima.2016.06.125](https://doi.org/10.1016/j.nima.2016.06.125).
- [52] LHCb Collaboration, [The Boole project](#), last accessed July 12, 2020.

[53] LHCb Collaboration, [The Brunel project](#), last accessed July 12, 2020.

[54] L. Bel *et al.*, *J. Phys. Conf. Ser.* **898** (2017) 092046, [doi:10.1088/1742-6596/898/9/092046](https://doi.org/10.1088/1742-6596/898/9/092046).





## 8 Conclusions

The LHC experiments have been running successfully and taking data since 2010. Much experience has been gained in running detector systems in challenging radiation conditions, and the impact on operation and performance has been assessed in this report. In general, we find the impact of the radiation effects to be in accordance with initial design expectations. While some unexpected effects have been observed with challenging consequences, these were in general successfully mitigated against.

The simulation of radiation environments is crucial in the design phase of new hadron collider experiments or upgrades. We showed in Section 4 how the proton–proton collisions are now well described by Monte Carlo event generators such as PYTHIA, with inelastic cross-sections and particle production rates described at levels of precision typically less than 10%. The measurements made by the experiments, along with cosmic ray data, constrain significantly the predictions for particle production in future hadron colliders, such as the proposed 100 TeV Future Circular Collider at CERN. We also showed how Monte Carlo particle transport codes such as FLUKA and GEANT4 are being used to accurately simulate radiation backgrounds in and around the LHC experiments. In the initial design phase, factors of two to five were applied by some of the experiments to reflect the uncertainty in the simulations. Intensive benchmarking of the simulated predictions against detector measurements has led to a drastic reduction in such simulation ‘safety factors’. For example, today the ATLAS experiment applies a factor 1.5 on its simulated predictions of fluence and dose. This has big implications on the choice of technologies that can be used in the LHC experiment upgrades, which in turn has enormous cost benefits. An important caveat to this, however, is that the reliability and accuracy of the simulation results is highly dependent on the geometry and material description of the experiment implemented in the simulations. For radiation background studies, fine detail is often not required, but it is crucial to reproduce accurately the radiation and interaction lengths. A final comment on ‘lessons learned’ is relevant for detector upgrades in an experiment. It is vital to study the impact of introducing new detector systems and services into an existing experiment, otherwise unintended increases in radiation background levels can occur in some of the other systems leading to a reduction in detector lifetime.

In Section 5, we showed the many measurements related to radiation damage performed by the experiments. A variety of probes have resulted in a detailed diagnostic information that can be used for modifying models, guiding operation and upgrades, as well as improving the quality of offline reconstruction. For leakage current, existing models that were mostly developed at independent irradiation facilities describe the existing data reasonably well, while other probes like depletion voltage are less well modelled. Expanding and enhancing this measurement program into Run 3 and the HL-LHC will be critical for preserving and possibly enhancing physics analysis as radiation damage becomes even more prominent. Further developments of the existing models will be required to make the most use of future measurements and the existing data may provide powerful constraints on these models, including estimating uncertainties.

In Section 6, we discussed how the effects of radiation have impacted the electronic and optoelectronic systems. Several of the observed phenomena like single event effects and threshold or current increases are expected. For many of them the magnitude or probability is in line with simulations or pre-installation tests. Still, owing to the complexity of the systems there were surprises either due to unanticipated effects or larger than expected magnitude or probability of occurrence. The root cause in most cases has been identified and mitigating actions have been applied. It is still evident that even with the rigorous testing applied to any device installed in the detectors, surprises are always possible, and a

---

This chapter should be cited as: Conclusions, DOI: [10.23731/CYRM-2021-001.147](https://doi.org/10.23731/CYRM-2021-001.147), in: Radiation effects in the LHC experiments: Impact on detector performance and operation, Ed. Ian Dawson, CERN Yellow Reports: Monographs, CERN-2021-001, DOI: [10.23731/CYRM-2021-001](https://doi.org/10.23731/CYRM-2021-001), p. 147. © CERN, 2021. Published by CERN under the [Creative Commons Attribution 4.0 license](https://creativecommons.org/licenses/by/4.0/).

detailed understanding of the system is necessary to identify and compensate for these effects.

In Section 7, we showed how radiation damage measurements are being integrated into sensor simulation software by the LHC experiments to allow increasingly accurate sensor design and performance predictions. ATLAS and CMS both use TCAD simulations to model the non-linear electric fields created in the sensor by radiation induced defects. Trapping rates and defects are modelled, with ATLAS using parameters taken from the literature, and CMS preferring to fit their parameters to match their measured LHC data. This is then used as input into the sensor charge collection and digitization software. On the contrary, LHCb adopts a simpler and more direct strategy by assuming a linear electric field in the silicon sensor and correcting the signal collection according to the depth of the depleted region after radiation damage. Also discussed in Section 7 was the fact that models fitted to test beam data do not always accurately describe sensor performance after radiation damage in operation at the LHC. It is also unclear if the currently used fitting parameters can be used to extrapolate to the highest radiation levels of the HL-LHC and to perform accurate simulations of sensors for future predictions. Further investigations and modelling studies will likely continue well into the Phase II Upgrade.